Systematic Analysis of the Lock-Crisp-West Theorem in Electron-Positron Annihilation

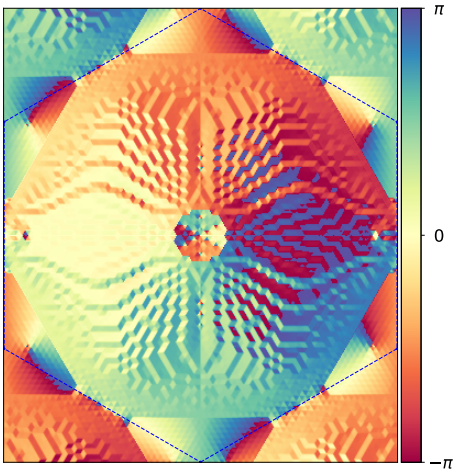

Dissertation

zur Erlangung des akademischen Grades
Dr. rer. nat.

eingereicht an der
Mathematisch-Naturwissenschaftlich-Technischen Fakultät
der Universität Augsburg

von

Markus Thomas Dutschke

Augsburg, Deutschland
Oktober 2018

Universität
Augsburg
University

Erster Gutachter: Prof. Dr. L. Chioncel
Zweiter Gutachter: Prof. Dr. K. Ziegler

Tag der mündlichen Prüfung: 12. Dezember 2018

Contents

Notation

Momentum Distributions

$\rho(\boldsymbol{p})$	Electron Momentum Distribution (EMD), page 47
$n(\boldsymbol{k})$	Electron Crystal Momentum Distribution (ECMD), page 47
$\rho^{2\gamma}(\boldsymbol{p})$	Two-Photon Momentum Distribution (TPMD), page 48
$n^{2\gamma}(\boldsymbol{k})$	Two-Photon Crystal Momentum Distribution (TPCMD), page 48
$\rho^{(2\gamma)}$	$\equiv \left\{\rho, \rho^{2\gamma}\right\}$
$n^{(2\gamma)}$	$\equiv \left\{n, n^{2\gamma}\right\}$
GMD	Generalized Momentum Distribution $\left\{\rho, \rho^{2\gamma}, n, n^{2\gamma}\right\}$, page 49

LCW Theorem

$\boldsymbol{p}$	momentum, page 9
$\boldsymbol{k}$	crystal momentum, page 9
$\boldsymbol{G}_{...}$	reciprocal lattice vector, page 56
$\{(G_x,G_y)\}$	x and y components of (all) reciprocal lattice vectors, page 65
$\rho(p_x,p_y)$	$\int \mathrm{d}p_z\, \rho(\boldsymbol{p})$, figure 3.1
$\rho(p_z)$	$\int \mathrm{d}p_x \mathrm{d}p_y\, \rho(\boldsymbol{p})$, figure 3.1
	analogous for $n(k_x,k_y)$ and $n(k_z)$

Operators

$\mathcal{D}^2_{\boldsymbol{d}}$	Second Directional Derivative (SDD) in direction $\boldsymbol{d}$, equation (3.43)
SDDmax	maximal absolute SDD over all direction $\boldsymbol{d}$, page 62
$\mathcal{D}^2_{\boldsymbol{n}}$	Second Directional Derivative in normal direction (SDDn), page 62
$I(r_{\mathrm{path}})$	cut through $I(x,y)$ along a given path, equation (3.50)
$\rho^{(2\gamma)}_{\circ}(p)$	rotational average of $\rho^{(2\gamma)}$, equation (3.52)
$\mathcal{A}\,\rho^{(2\gamma)}(p_x,p_y)$	anisotropy of $\rho^{(2\gamma)}$, equation (3.54)

Abbreviations

FS	Fermi Surface, page 9
BZ	Brillouin Zone, page 9
dHvA	de Haas-van Alphen, subsection 1.1.1
ARPES	Angle-Resolved PhotoEmission Spectroscopy, subsection 1.1.2
IMFP	Inelastic Mean Free Path, page 17
IA	Impulse Approximation, page 19
DDSCS	Double Differential Scattering Cross Section, page 19
ACAR	Angular Correlation of electron-positron Annihilation Radiation, subsection 1.1.4
CS	Compton Scattering, subsection 1.1.3
1D-ACAR	one-Dimensional ACAR, page 9
2D-ACAR	two-Dimensional ACAR, page 9
PSD	Position Sensitive Detector, page 22
DFT	Density Functional Theory, section 2.1
LDA	Local Density Approximation, page 37
LSDA	Local Spin Density Approximation, page 37
GGA	Generalized Gradient Approximation, page 37
APW	Augmented Plane Wave, page 39
LAPW	Linearized Augmented Plane Wave, page 39
MTA	Muffin Tin Approximation, page 40
ASA	Atomic Sphere Approximation, page 40
FP	Full-Potential, page 40
WDA	Weighted Density Approximation, page 43
LTM	Linear Tetrahedron Method, page 99
IPA	Independent Particle Approximation, page 52
IPM	Independent Particle Model, page 52
LCW	Lock-Crisp-West (theorem), equation (3.36)
2D-LCW	two-dimensional LCW (theorem), equation (3.40)
VP	Voronoi Plaquette, page 51
VP^{o}	interior of VP, page 118
RP	Rectangular Plaquette, page 77
MRI	Momentum Range of Interest, page 118
MEM	Maximum Entropy Method [83]

Expressions

ngridk	Elk internal parameter for LTM, page 99
Gaussian filter	folding with a Gaussian, page 106
momentum mesh spacing	spacing between the momentum grid, page 23
binning	histogram construction, page 23
projection	integration of one or two momentum components in ACAR spectra, page 9
convex shape effect	convex shape induced by back-folding a truncated spectrum, page 67
truncation artifacts	steps or kinks introduced by the LCW back-folding process due to the finite range issue, page 67
extrapolation artifacts	steps or kinks introduced by extrapolation, page 81
back-folding artifacts	all steps or kinks introduced by the LCW back-folding process, page 68

Abstract

The Lock-Crisp-West (LCW) theorem relates spectroscopic data in momentum space with the corresponding quantities in the repetitive crystal momentum space. The back-folding operation translates a measured distribution into the corresponding (periodic) distributions in the crystal. This is important in Angular Correlation of electron-positron Annihilation Radiation (ACAR) spectroscopy resolving one (1D-ACAR) or two (2D-ACAR) momentum components and in Compton scattering experiments. Besides its intuitive appearance, it turns out, that numerical implementations of the LCW theorem introduce artifacts. These can lead to misinterpretation of the back-folded data.

In this work we systematically analyze existing two-dimensional back-folding techniques and develop a new optimized back-folding strategy. This is applicable to 2D-ACAR spectra to extract Fermi surface features from a smaller momentum range (implying a lower number of experimental counts) than previous back-folding implementations. By this, we developed further an alternative to the commonly used tomographic methods, which perform the back-folding operation in three dimensions. While tomographic methods rely on data from several measured directions, our direct approach allows an analysis of the back-folded spectra from just one measured direction. We validate our results on 2D-ACAR data obtained from all-electron Full-Potential Linearized Augmented Plane Wave (FP-LAPW) calculations and experiments.

Introduction

Among the most common experimental techniques to gain insights about the **Fermi Surface (FS)** of materials are

Experiments

- Angular Resolved Photon Emission Spectroscopy (ARPES) [16, 17, 19],
- de Haas-van Alphen (dHvA) measurements [1–3, 15],
- Angular Correlation of electron-positron Annihilation Radiation (ACAR) [53, 60, 61] and
- Compton Scattering (CS) [30, 37].

ACAR and CS are especially useful for probing the electron crystal momentum distribution for materials with a short electronic mean free path [81], as ARPES and dHvA experiments usually fail in this case.

The **Lock-Crisp-West (LCW)** theorem [80, 81] is used in the context of Compton scattering and ACAR spectroscopy to **back-fold** the **Electron Momentum Distribution (EMD)** $\rho(\boldsymbol{p})$ measured in momentum space $\boldsymbol{p} \in \mathbb{R}^3$ into the crystal momentum space $\boldsymbol{k} \in$ **Brillouin Zone (BZ)**. To distinguish these quantities, $n(\boldsymbol{k})$ is called the **Crystal Momentum Distribution (CMD)**, representing the number of electrons at a certain crystal momentum $\boldsymbol{k}$. At zero temperature $n(\boldsymbol{k})$ has only integer values. Thereby, the Fermi surface sheets separate the regions of the $n(\boldsymbol{k})$ with different integer (at zero temperature) values.

LCW theorem

In experiments, however, it is not possible to resolve all three momentum components of $\rho(\boldsymbol{p})$ (without tomographic reconstruction from several measurements), but just two **(2D-ACAR)** or one (**1D-ACAR** and Compton scattering). Unresolved momentum components are implicitly integrated over by the experimental setup, which is often referred to as **projection** spectra. The LCW theorem in a dimensionally reduced version is still applicable in these cases.

Momentum integration

Berko's [60] 2D-ACAR setup is a further development of the 1D-ACAR technique of DeBenedetti [53]. In both methods positrons are used to annihilate electrons in the probe, resulting in annihilation radiation of (most probable) two photons. From the angle between these photons, $\rho^{2\gamma}$ is deduced.
In 1D-ACAR spectroscopy it was only possible to determine one momentum component of the photons on the detectors, i.e. $\rho^{2\gamma}(p_z)$. Developments in the size reduction of electronic detection devices in the 1970s, made the development of 2D-ACAR spectroscopy possible, where both spatial components of the photon impact are recorded on the detector, i.e $\rho^{2\gamma}(p_x,p_y)$.

2D-ACAR

Positron effects

The superscript '2γ' was introduced to symbolize, that information was gained on the basis of an annihilation process of an electron with a positron. The influence of the positron on the system under investigation can only be calculated approximately, but in general the 2γ-quantities are closely related to their purely electronic counterpart. Within the independent particle approximation, the electron-positron interaction is neglected (compare subsection 3.2.1) and the LCW theorem is used to derive the **Two-Photon Crystal Momentum Distribution (TPCMD)** $n^{2\gamma}(\boldsymbol{k})$ from the **Two-Photon Momentum Distribution (TPMD)** $\rho^{2\gamma}(\boldsymbol{p})$.
In the context of 2D-ACAR the two-dimensional version of the LCW theorem reads:

$$\rho^{2\gamma}(p_x, p_y) \equiv \int \mathrm{d}p_z \, \rho^{2\gamma}(\boldsymbol{p}) \quad \overset{LCW}{\Rightarrow} \quad n^{2\gamma}(k_x, k_y) \equiv \int \mathrm{d}k_z \, n^{2\gamma}(\boldsymbol{k}) \, .$$

Positron effects enhance the Fermi surface steps in $n^{2\gamma}(\boldsymbol{k})$. Hence, the Fermi surface can be identified by a kink (discontinuity/step in the first derivative) in $n^{2\gamma}(k_x,k_y)$ [126].

Compton scattering

The experimental setup of Compton scattering resolves only one momentum component $\rho(p_z)$. Due to the weak electron photon interaction [42], Compton scattering minimally alters the electronic structure of the system under investigation and allows a direct probing of $\rho(\boldsymbol{p})$. Without any approximations the LCW theorem is applicable

$$\rho(p_z) = \int \mathrm{d}p_x \mathrm{d}p_y \, \rho(\boldsymbol{p}) \quad \overset{LCW}{\Rightarrow} \quad n(k_z) = \int \mathrm{d}k_x \mathrm{d}k_y \, n(\boldsymbol{k}) \, .$$

Fermi surface detection

To deduce the exact shape and position (parameterization) of Fermi surface from the (projected) experimental data, i.e. $n(k_z)$ and $n^{2\gamma}(k_x,k_y)$, there are two options.
(i) The first is a reconstruction of $n^{2\gamma}(\boldsymbol{k})$ by **tomographic methods** [89–94]. In the case of 2D-ACAR, this takes several measurements along different crystallographic directions (for instance five in [93]).
(ii) The other, more direct, access to the Fermi surface parameterization is the **detection of kinks** in the spectrum. The steps in $n^{2\gamma}(k_x,k_y)$ at the Fermi surface, reduce to kinks due to the integration over momentum component.[1] Despite difficulties of identifying these kinks under the influences of experimental noise, experimental smearing and a finite momentum mesh, a direct analysis of the Fermi surface by just one measurement direction is possible. As this method is very sensitive to any artifacts (steps or kinks) in the data, this analysis depends on a careful application of the LCW back-folding operation.

LCW implementation

In literature only few comments on the application of the LCW theorem can be found without any description of algorithms or discussions of potential errors. As it turns out, the commonly used implementations [87,88] of the LCW theorem in its two-dimensional version suffer indeed from introducing artifacts in form of artificial kinks. The intensity of those artificial kinks is comparable with the intensity of the Fermi surface signatures and hence hampers a direct quantitative analysis of 2D-ACAR spectra.

[1] In the case of the double integration in $n(k_z)$, this reduces even to a discontinuity in the second derivative.

Aim of this work

The aim of this work is to formulate an implementation of the LCW theorem in its two-dimensional version, which is optimized with respect to artifacts. We will investigate the performance of this new implementation by analyzing 2D-ACAR data with the kink detection method to determine the Fermi surface.

Structure of this work

This work is structured as following: In part I we give an overview of the experimental and theoretical background of this work.

Analysis of LCW implementations

In part II we present a proof of the LCW theorem and discuss the properties of the different momentum distributions (i.e. EMD, ECMD, TPMD, TPCMD) in detail. Further we will systematically analyze the different techniques to LCW back-fold 2D-ACAR spectra and point out the different types of numerical artifacts, which were introduced. We further present a new set of techniques, designed to minimize these artifacts. This allows a more precise determination of important features based on kink detection. Simultaneously, these techniques allow a significant reduction of the measuring time, while still keeping the amount of artifacts significantly below other back-folding methods.

Application of optimized LCW

The new LCW back-folding algorithm is applied to different realistic systems in part III.
Silver is investigated, due to its almost spherical Fermi surface. The parameterization of this Fermi surface is investigated, while stepwise including theoretical and experimental effects to match the theoretical predictions with the experimental findings. This gives an overview of the different effects, being of importance, when analyzing the Fermi surface based on 2D-ACAR data. We further see the importance of some quantities, as for example the **Second Directional Derivative in normal direction (SDDn)** for Fermi surface detection.
Germanium acts as a benchmark system for the LCW back-folding algorithm. Due to its band gap, the expected back-folding result is a constant. Deviations from this are investigated in dependence of the used back-folding technique. Thereby, not only the direct result of back-folding is investigated, but also the quantities of interest, based on the findings in silver (for instance the SDDn). The predictions, made in part II, will be found to be fulfilled.
We apply our framework to **molybdenum**, as an element with a non-trivial Fermi surface, including features of very different sizes. We will analyze theoretical and experimental ACAR spectra and determine the majority of Fermi surface parameters. In comparison with other back-folding methods we see, that the new LCW back-folding algorithm improves the results of a quantitative analysis with the kink detection method. In this way FS signatures can be identified with a higher level of confidence, due to a reduced danger of confusing them with artifacts and vice versa.

Conclusion

The implications of the findings of this work for the experimental realization and promising further developments for the data analysis framework of ACAR spectra are pointed out in part IV.

Part I.

Experimental and Theoretical Background

1. Positron Annihilation Spectroscopy and Related Methods

1.1. Experimental Methods for Probing the Fermi Surface

Additional to positron annihilation spectroscopy, other experimental methods allow the probing of the Fermi surface as well. This section gives a brief overview of the most commonly used methods and their area of application.

1.1.1. The de Haas-van Alphen (dHvA) Technique

Method description

The dHvA effect [2] describes, how the magnetic moment of a probe is changing when applying an external magnetic field. By continuously increasing the external magnetic field H, one can observe an oscillating behavior in the inverse magnetization B^{-1} with a period of

$$\Delta\left(B^{-1}\right) = \frac{2\pi e}{\hbar S}\,. \tag{1.1}$$

Thereby, e denotes the electronic charge, $\hbar$ the Planck constant and S is a constant, which remains undefined at this point. The magnetization B of the probe is either determined by its rotation in a second external magnetic field (torque method [7]) or by the induction in a pickup coil [5, 6]. The peaks in the magnetization (giving rise to the oscillating behavior) appear, whenever an extremal (with respect to its area) orbit of the Fermi surface fulfills Landau's quantization condition [1]. An orbit is defined as a closed loop on the Fermi surface in the plane perpendicular to the magnetic field. The area of this orbit S is the constant in equation (1.1), which was not defined until now. It was Onsager [3] in 1952, who pointed out this connection to the extremal areas of the Fermi surface. An extensive overview of the field is given by Schoenberg in [4, 15].

(Dis)-Advantages

Since then the dHvA technique became one of the most powerful methods to investigate the Fermi surface. It is the most precise method to parameterize the Fermi surface. The drawback of the method is, that it relies on tomographic methods, such as Mueller's inversion scheme [8, 9], to translate the different detected orbits into a two or three dimensional model of the Fermi surface. From this model the parameters of the Fermi

surface can be extracted. The dHvA effect can only be measured at temperatures $T \leq 5\,\mathrm{K}$ and at strong magnetic fields [10]. Modern measurements are even performed in the range of millikelvin [14]. Further samples with a high purity are needed. Hence, the experimental setup requires a considerable amount of expertise and financial funding. Another shortcoming of the dHvA measurements is the appearance of spin splitting in the case of degenerate orbits due to the external magnetic field [11, 13]. Indicators for this effect can be found in the oscillation amplitude of the magnetization [12].

1.1.2. Angle-resolved Photoemission Spectroscopy (ARPES)

Method description

Based on the photoelectric effect, first observed by Hertz [16] and later explained by Einstein [17], in photoemission spectroscopy a probe is irradiated with soft x-rays. Two momentum components and the energy of the emitted electrons are measured simultaneously. The missing momentum component can be reconstructed by different methods from the information about the energy of the emitted electron. Due to its high resolution and the possibility to resolve (quasi) three momentum components of the electron momentum distribution, ARPES is a highly successful method for investigating the electronic structure of materials.

Conservation laws

The energy of the detected electron E_{kin} is given by

$$E_{\mathrm{kin}} = h\nu - \phi - |E_{\mathrm{B}}| \tag{1.2}$$

with $h\nu$ the energy of the incoming photon, ϕ the work function of the material and E_{B} the initial energy of the electron with respect to the Fermi level.
The momentum transfer from the photon to the electron is neglected, as its typical value is far smaller than the size of the Brillouin zone [20]. In a reduced zone scheme picture this condition writes

$$\boldsymbol{k}_{\mathrm{f}} - \boldsymbol{k}_{\mathrm{i}} = 0\,. \tag{1.3}$$

In an extended zone scheme representation this corresponds to a momentum change of a reciprocal lattice vector

$$\boldsymbol{p}_{\mathrm{f}} - \boldsymbol{p}_{\mathrm{i}} \in \{\boldsymbol{G}\}\,. \tag{1.4}$$

When detecting the emitted electron at a certain angle, $\boldsymbol{k}_{\parallel}$ (i.e. the momentum in the plane of the surface) fulfills condition (1.3). Due to the work function, however, the momentum component perpendicular to the surface $\boldsymbol{k}_{\perp}$ does not fulfill this condition.

Momentum reconstruction

As two momentum components and the energy of the initial state of the electron are known, complementary methods or model descriptions can be applied to deduce the missing momentum component $\boldsymbol{k}_{\perp}$. The possibilities thereby range from the nearly-free electron model to band structure calculations. As the angle resolution for momentum detection is given by the experimental setup, the possible momentum resolution depends on the photon energy.

In the theoretical description of ARPES experiments two approximations are used: Approximations

- The **independent-particle picture**, neglecting many body interactions
- The **sudden approximation** [23], assuming an instant scattering process, neglecting any interaction before and after the scattering process as well as any relaxation dynamics of the electronic structure.

Especially the sudden approximation is not necessarily fulfilled at low photon energies [24–26].

One can distinguish two different energy regions in ARPES experiments: (Dis)-Advantages
At high photon energies of 20-100 eV the **Inelastic Mean Free Path (IMFP)** of the electron is $\mathcal{O}(1)$ Å [18]. Hence, ARPES is extremely sensitive to the sample surface and prohibits the investigation of the bulk electronic properties. The momentum resolution varies between $0.05\,\text{Å}^{-1}$ (at $h\mu = 100\,\text{eV}$) and $0.008\,\text{Å}^{-1}$ (at $h\mu = 21.2\,eV$) [19, 20].
At low photon energies of $\approx$ 6 eV the IMFP increases by an order of magnitude to $\mathcal{O}(1)$ nm [18]. Zang [22] reports a Full Width Half Maximum (FWHM) value of $0.0071\,\text{Å}^{-1}$ for the momentum resolution at a photon energy of 6.994 eV. On the other side such low energetic photon beams may cause a breakdown of the sudden approximation and lead to a higher relative uncertainty of the work function ϕ [22]. An example for the dependence of ARPES spectra on the photon energy can be found in [27] (figure 1f), where it was used to investigate the topmost layer of Sr_2RuO_4 in different depths.
As a consequence of photon reflection on metals and short mean free paths, ARPES can not be used to measure the electronic structure of the bulk material. In the theoretical description of ARPES assumptions are included, which might lead to deviations in the excitation probability of the electron by Fermi's golden rule [21, 28] and the coupling of the final electronic state to surface plasmons [21, 29]. This is an additional source of uncertainty for the measured electronic structure.
In the experimental setup an ultra-high vacuum (lower than 10^{-11} torr) [20] and an extremely clean surface of the probe is required.
ARPES measurements further lack the possibility to investigate materials under pressure (due to the requirement of vacuum) or in magnetic fields (due to the Lorentz force acting on emitted electrons).

1.1.3. Compton Scattering (CS)

The scattering of a photon on an electron with and without initial momentum was studied by Compton and de Broglie [30, 31]. Figure 1.1 shows the scattering of a photon on a moving electron. The relevant quantities are given as: incoming photon (momentum $\hbar\boldsymbol{k_1}$, energy ω_1), outgoing photon (momentum $\hbar\boldsymbol{k_2}$, energy ω_2), the initial state of the electron (momentum $\boldsymbol{p}$, mass m), the final state of the electron (momentum $\boldsymbol{p} + \hbar\boldsymbol{K}$, mass m) and the photon scattering angle $\theta = \measuredangle(\boldsymbol{k_1},\boldsymbol{k_2})$. Background

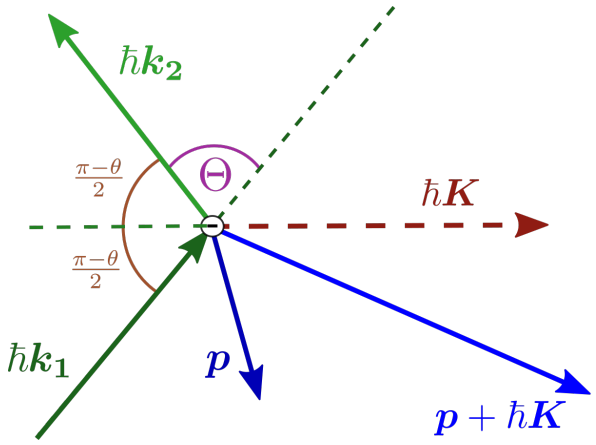

Figure 1.1.: Compton scattering: Definition of momenta

In an **independent-particle picture** (i.e. assuming a free electron) the photon transfers the momentum $\hbar\boldsymbol{K}$ and the energy $\Delta\omega$ on the electron

$$\hbar\boldsymbol{K} = \hbar\boldsymbol{k_1} - \hbar\boldsymbol{k_2} \tag{1.5}$$

$$\Delta\omega \equiv \omega_1 - \omega_2 = \frac{1}{2m}\left((\boldsymbol{p}+\hbar\boldsymbol{K})^2 - \boldsymbol{p}^2\right) . \tag{1.6}$$

Due to the large electron mass, the change of the length of the k-vector is negligible[1] (with respect to its total length) $k_1 \approx k_2$ and hence $K \approx 2k_1\cos\left(\frac{\pi-\theta}{2}\right)$. In this approximation equation (1.6) can be reformulated as

$$\Delta\omega = \frac{\sin(\theta/2)}{2m}\left[\left(\frac{2\omega_1-\Delta\omega}{c}\right)^2\sin(\theta/2) + 2\frac{2\omega_1-\Delta\omega}{c}p_z\right] , \tag{1.7}$$

where the relations $\cos\left(\frac{\pi-\theta}{2}\right) = \sin(\theta/2)$ and $\omega_i = \hbar k_i c$ with $i \in \{1,2\}$ were used. $p_z = \frac{\boldsymbol{pK}}{K}$ denotes the momentum component of the electron in $\boldsymbol{K}$-direction. By dropping terms of order $\mathcal{O}(\Delta\omega^2)$ [32], equation (1.7) simplifies to

$$\Delta\omega = \frac{2\omega_1\sin(\theta/2)\left(\frac{\omega_1}{mc^2}\sin(\theta/2)+\frac{p_z}{mc}\right)}{1+\frac{2\omega_1}{mc^2}\sin^2(\theta/2)+\frac{p_z}{mc}\sin(\theta/2)} . \tag{1.8}$$

Under the approximation $\frac{\omega_1}{mc^2} \ll 1$ (i.e. low energy of incoming photon compared to the rest energy of an electron) equation (1.8) writes in first order of $\frac{p_z}{mc}$ (i.e. non relativistic electron momentum)

$$\Delta\omega = 2\omega_1\sin(\theta/2)\frac{p_z}{mc} . \tag{1.9}$$

Validity These approximations (i.e. $\Delta\omega \ll \omega_1$ and $p_z \ll mc$) are fulfilled for metals with s and p valence electrons. The Fermi velocity v_F of those systems is of order $\mathcal{O}(10^6)\,\frac{\mathrm{m}}{\mathrm{s}}$ [136], which limits the energy shift of the scattered photons $\Delta\omega \approx 0.02\omega_1$, due to $p_z \leq m|\boldsymbol{v}_\mathrm{F}|$.

[1] In analogy to a ball bouncing off a wall in a perfectly elastic collision.

DuMond [32] used those findings to determine the Fermi velocity of beryllium with 0.5% accuracy.

Impulse approximation

The **Impulse Approximation (IA)** [34] is used to transfer DuMonds analysis to photons scattering in a crystal. It consists of 3 parts:
1) Indistinguishable electrons: This neglects the modification of surface electronic states and the influence of the lattice potential on the scattering process.
2) Instant scattering: This prevents any interaction of the electron with rest of the system during the scattering process. From the perspective of the photon the electron is quasi free. This condition excludes for example the resonance condition of Raman scattering [43].
3) No multiple scattering processes: The photon scatters with only one electron in the system and is not influenced by any other.

Method description

In modern Compton scattering experiments photons with an energy of 100-250 keV [43] are shot on a target. These energies have become accessible in the 1990s, due to the development of more performant synchrotrons. The reflected electron beam is measured in counts σ under a solid angle interval $\mathrm{d}\Omega$ and in an energy interval $\mathrm{d}\omega_2$. The underlying quantity $\frac{\mathrm{d}^2\sigma}{\mathrm{d}\Omega\,\mathrm{d}\omega_2}$is called **Double Differential Scattering Cross Section (DDSCS)** [2] and can be split into the Thomas-scattering cross section (describing the elastic scattering of the phonon on a free electron) and the dynamic structure factor (describing the transition probability of any electron into any available state, based on the product of the electron wave function with the plane wave of the incoming photon)

$$\frac{\mathrm{d}^2\sigma}{\mathrm{d}\Omega\,\mathrm{d}\omega_2} = (\mathrm{d}\sigma/\mathrm{d}\Omega)_{\mathrm{Th}}\, S(\boldsymbol{q} = \boldsymbol{k_1} - \boldsymbol{k_2}, \omega = \omega_1 - \omega_2)\,. \tag{1.10}$$

Within the impulse approximation and within the non-relativistic limit this can be calculated [41] to yield[3]

$$(\mathrm{d}\sigma/\mathrm{d}\Omega)_{\mathrm{Th}} = \left(\frac{e^2}{mc^2}\right)^2 (\hat{\boldsymbol{\epsilon}}_{\mathbf{1}} \cdot \hat{\boldsymbol{\epsilon}}_{\mathbf{2}}^{*})^2 \frac{\omega_2}{\omega_1} \tag{1.11}$$

$$S(\boldsymbol{q},\omega) = \frac{1}{(2\pi)^3}\frac{m}{\hbar q} J(p_z)\,. \tag{1.12}$$

Thereby, $\hat{\boldsymbol{\epsilon}}_{\boldsymbol{i}}$ denotes the polarization unit vectors of the incoming (i=1) and outgoing (i=2) photon. The **Compton profile** $J(p_z)$ is defined as the electron momentum distribution integrated over two momentum components

$$J(p_z) \equiv \int \mathrm{d}p_x \mathrm{d}p_y\, \rho(\boldsymbol{p}) \equiv \rho(p_z)\,. \tag{1.13}$$

[2] The mathematical notation $\frac{\mathrm{d}^2\sigma}{\mathrm{d}\Omega\,\mathrm{d}\omega_2}$ of the DDSCS implicitly includes the dependence on the solid angle segment $\mathrm{d}\Omega$ and the energy (of the scattered photon) interval $\mathrm{d}\omega_2$. The ω_1-dependence of the DDSCS is dropped, as ω_1 is kept constant during the experiment. The actual number of counts on a detector segment ΔS and in an energy interval ΔE is given as $\sigma = \int\limits_{\Delta S} \mathrm{d}\Omega \int\limits_{\Delta E} \mathrm{d}\omega_2 \frac{\mathrm{d}^2\sigma}{\mathrm{d}\Omega\,\mathrm{d}\omega_2}$.

[3] For a relativistic expression see [36].

By measuring the DDSCS under a solid angle Ω, we implicitly fix the variables $\boldsymbol{k_2}$, Θ and p_z. Also ω_2 follows by equation (1.9) or by a more general description of Compton scattering. In this way we statistically record the Compton profile

$$J(p_z) \propto \frac{\omega_1}{\omega_2} \frac{\mathrm{d}^2\sigma}{\mathrm{d}\Omega\, \mathrm{d}\omega_2}\Big|_{\omega_2=\omega_1\left(1-2\sin(\theta/2)\frac{p_z}{mc}\right)}, \tag{1.14}$$

giving direct access to the momentum distribution of the electrons.

(Dis)-Advantages

Due to the weak photon-electron interaction [43], CS is an excellent technique to measure the electron momentum distribution of a system. Therefore systems can be probed, independent of their IMFP.
On the other hand, Compton scattering experiments can only be performed at synchrotron facilities. Due to lack of ability to resolve more than one momentum component, complex tomographic methods are necessary for a reconstruction of the three-dimensional electron momentum distribution $\rho(\boldsymbol{p})$. Further it has a lower resolution than dHvA or ARPES measurements, making it only favorable in cases, where those techniques can not be applied.

Application

Compton scattering is used for measurements at room temperature [44] and for the investigation of systems with disorder [44]. Magnetic Compton scattering additionally allows to separate both spin channels $\rho^{\uparrow}$ and $\rho^{\downarrow}$ [38–40].

1.1.4. Angular Correlation of Electron-Positron Annihilation Radiation (ACAR)

Method description

In ACAR spectroscopy positrons are used to probe the electronic structure of a system (for details see sections 1.2 and 1.3.1). When the positron annihilates with an electron, two almost anti-parallel gamma quanta are emitted. This annihilation radiation is measured on two detectors, positioned at opposite sides of the probe. Deviations from the anti-parallel orientation of the two gamma quanta are due to momentum conservation in the annihilation process. As the positron thermalization time is much smaller than its lifetime, the positron does not contribute any momentum to the annihilation process. Hence, from the angle between the gamma quanta the electron momentum distribution is statistically recorded. The detectors can only resolve two spatial coordinates, so one momentum direction is integrated over

$$\rho^{2\gamma}(p_x,p_y) \equiv \int \mathrm{d}p_z\; \rho^{2\gamma}(p_x,p_y,p_z)\,. \tag{1.15}$$

The additional 2γ superscript takes positron related effects into account. In some approximations the positron influences can be neglected (compare section 3.1).
With the LCW theorem it is possible to deduce two components of the electron crystal momentum distribution $n(\boldsymbol{k})$, i.e. the occupation number in crystal momentum space

$$\rho^{(2\gamma)}(p_x,p_y) \quad \overset{\text{LCW}}{\rightarrow} \quad n^{(2\gamma)}(k_x,k_y)\,. \tag{1.16}$$

(Dis)-Advantages

Hence, ACAR spectroscopy provides an impression of $\int \mathrm{d}k_z\, n(\boldsymbol{k})$, which is proportional to the diameter of the Fermi surface in integration direction. Even though ARPES measurements can resolve the third momentum component and have a better resolution, ACAR measurements are experimentally more accessible and allow an investigation beyond the surface of the probe (the positron implantation depth is $\mathcal{O}(1)\,\mu$m [111, 112], where surface effects are absent). Further, measurements can be performed at room temperature [93] and for disordered systems [62, 63].
The drawbacks of ACAR spectroscopy are the resolution of $\approx 0.05\,$a.u., which is even lower than in Compton spectroscopy, and the influence of the positron on the electronic structure of the system under investigation (compare section 3.1). The implications of those drawbacks are systematically analyzed in chapters 5 and 7 for realistic systems.

1.2. Details about ACAR Spectroscopy

Agenda

We discuss the experimental realization of 2D-ACAR. After introducing the experimental setup we point out some difficulties arising during the measurement process and give mathematical descriptions, how to take them into account in a theoretical / numerical description.

1.2.1. Experimental Setup

Modern setup

Figure 1.2 shows a conceptual (distances and size relations are not maintained) drawing of the experimental setup. The positrons are created during the β^+-decay of Na^{22}. By an electromagnetic coil, the positrons are directed on the probe. They enter several μm until they thermalize (i.e. arriving in a low energetic state, depending on the temperature). After thermalization the positron annihilates with an electron, resulting in two gamma-quanta with almost anti-parallel orientation and an energy of $\approx 511\,\mathrm{keV}$, each. Energy and momentum conservation are the mechanisms, defining the corresponding momenta $\boldsymbol{p}_{\gamma,1}$ and $\boldsymbol{p}_{\gamma,2}$ and energies $E_{\gamma,1}$ and $E_{\gamma,2}$ of the annihilation radiation. The deviation from the anti-parallel is defined as

$$\Theta = \left| \pi - \sphericalangle \left(\boldsymbol{p}_{\gamma,1}; \boldsymbol{p}_{\gamma,2} \right) \right| . \tag{1.17}$$

Two detectors in a distance of $\mathcal{O}(10)\,\mathrm{m}$ from the annihilation spot, are used to detect the angular deviation, whenever they detect simultaneous events. At counting rates of $\mathcal{O}(10^2)\,\frac{1}{\mathrm{s}}$, a typical measurement with $\mathcal{O}(10^8)$ counts takes around a week.

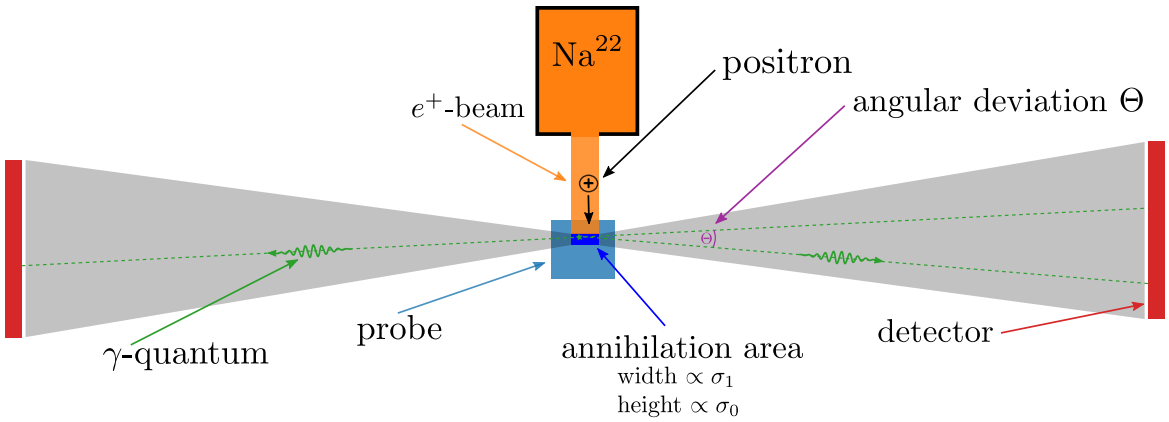

Figure 1.2.: Conceptual drawing of the experimental setup for 2D-ACAR. The quantities σ_0 and σ_1 refer to the experimental resolution, described in subsection 1.2.2.

Historic setups

The first ACAR experiment was set up by DeBenedetti in 1950 [53] in an one-dimensional version. Two **Position Sensitive Detectors (PSDs)** were oriented opposite of each other with respect to the probe and covered by a long slit mask.

The coincidence counting rate was measured in dependence of $\Theta_\perp$ (i.e. the annihilation angle component perpendicular to the long slit) by shifting one of the detectors. The decrease in size of electronic devices allowed an extension of this setup in the 1970s. Berko [60] was the first, who built a 2D-ACAR spectrometer in 1975, by using utilized multi-element scintillation counters as PSDs. Nowadays, utilized multi-element scintillation counters [69], anger cameras [71] and high density avalanche chambers [70] are used as PSDs.

Anger cameras

Anger cameras, for instance, consist of a single crystal connected to several photomultipliers [74]. The exact position of the photon on the detector is evaluated on a continuous scale from the signals arriving at the different photomultipliers [68]. By storing the incidence positions of each event in list-mode [71], a mapping ('binning') to a suitable momentum mesh can be performed, based on the full information of the experiment.

1.2.2. Experimental Resolution and Momentum Mesh

Definitions

In the following we want to point out problems related to the determination of the momentum components (p_x,p_y) of the photon pair. Thereby we want to distinguish between the two terminologies:
Momentum mesh refers to the numerical handling of momentum dependent data. $\rho^{2\gamma}(p_x,p_y)$ is statistically sampled on a continuous scale by the detector. For a statistical analysis it is necessary to assign the detected events to discrete momentum intervals (with a finite **momentum mesh spacing** between them). This process, being a two-dimensional histogram construction, is called **binning**. All averaging and interpolation issues can be assigned to the finite momentum mesh spacing. This is a common issue in numerical simulations and has no extraordinary implications on an experimental level. The implications for a numerical handling of the obtained data are found under the terminus finite resolution issue in subsection 4.1.1.
Experimental resolution denotes all effects of statistical uncertainty in the measuring process. This is responsible for smearing a delta peak shaped signal (in the real world) into a Gaussian (or similarly) shaped signal, coming from the PSD device.

Sources of Exp. Res.

In ACAR experiments there are several factors leading to this smearing of the measured momentum distribution. The main error sources are considered to be the uncertainty in the position of annihilation, the detector resolution and the thermal energy of the positron [74].
Thereby the experimental resolution is approximately a Gaussian distribution with a full width at half maximum of $(0.8, 1.3 * 0.8)$ mrad in (p_x,p_y). This corresponds to a standard deviation of

$$\begin{aligned} \sigma_0 &= 0.33973\,\text{mrad} = 0.04654\,\text{a.u.} \\ \sigma_1 &= 1.3\sigma_0 = 0.06051\,\text{a.u.} \end{aligned} \tag{1.18}$$

The different width in directions p_x and p_y origins from the spatial distribution of the detected positions. While σ_0 is determined by the implementation depth distribution

of the positron into the material, σ_1 characterizes the positron beam width (compare figure 1.2).

Gaussian blur

To mimic the experimental resolution, we use the **Gaussian blur** operation. This operation, common in image processing, represents the convolution of a function f with a Gaussian. In one dimension this reads

$$g(r) = \int \mathrm{d}\tilde{r}\, f(r)\, \frac{1}{\sqrt{2\pi}\sigma} e^{-(r-\tilde{r})^2/2\sigma}\,. \tag{1.19}$$

The definition for two-dimensions is analogous and can be found in equation (1.23).

Consequences

The consequence of the experimental resolution is a smearing on the one hand, but also a shift of Fermi surface signatures on the other hand. Figure 1.3 illustrates the effect of the experimental resolution on a test function $f(r)$ (compare equations (1.21), (1.22) and (1.32)). In the left column of figure 1.3 the test function and its blurred equivalent $b(r)$ is shown. The right column displays the curvature of $f(r)$ and $b(r)$. When a Gaussian blur is applied, a shift in the maximum of the curvature can be observed (compare maximum of the green curve and orange points with the blue peak). This is problematic, as the maximum curvature is in general used to identify the signature of the Fermi surface in a spectrum.

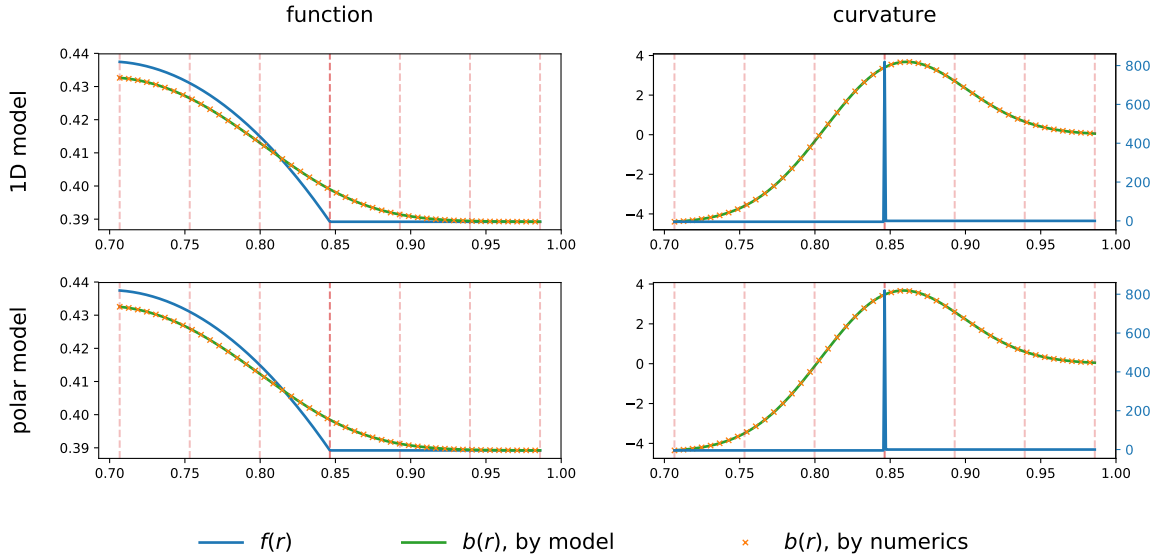

Figure 1.3.: Shift of kinks by Gaussian blur: Effect of experimental resolution (modeled by Gaussian blur in green and orange) on a test function (blue). The maximum of the curvature is shifted. Numerical results ('num') agree with the analytic description given in equations (1.25), (1.28) (1D model) and (1.36) (polar model).

Models

In the following we introduce two models to describe and correct the influence of experimental resolution on the position of kinks in a 2D-ACAR spectrum. We define the models to consist of a constant part and a quadratic part. They are merged

continuously in value, but have a kink (i.e. a discontinuity in the first derivative) at the connection. As presented in chapter 5, the ACAR spectrum of silver shows such a structure.

(Effective) One-Dimensional Model

Model description

To describe Fermi surface signatures in bach-folded 2D-ACAR spectra $n^{2\gamma}(k_x,k_y)$, we introduce the 'one-dimensional' model. For simplicity in the notation we use the coordinates x/y instead of the momenta p_x/p_y or k_x/k_y. The model is designed for situations, where the Fermi surface signature is a kink along a straight line (y direction). For generality, we define the standard deviations in the **longitudinal** and **transversal** directions

$$\sigma_\mathrm{l} \equiv \sigma_x$$
$$\sigma_\mathrm{t} \equiv \sigma_y\,.$$

The momentum region, where the model is an appropriate description, should cover a few sigma in both momentum directions. The 'one-dimensional' model consists of two touching half planes. One half plane is constant, while the other is described by a parabola with slope m and curvature c (with respect to x). The Fermi surface signature is modeled by the kink at the weld between the half planes. The formal definition of the model is given by

$$g(x,y) = m(x-x_0) + c(x-x_0)^2 \tag{1.20}$$
$$f(x,y) = f_0 + g(x,y)\,\Theta\left(s\,(x-x_0)\right) \text{ with } s \in \{1,-1\} \tag{1.21}$$
$$f(r) = f(x=r,y=0)\,. \tag{1.22}$$

The parameter s determines on what side of the kink the constant half plane is situated. The coordinate r is introduced to establish comparability with the polar model description in the next section. The term 'one-dimensional' refers to the independence of this description with respect to the y coordinate.

Analytical description

Applying a Gaussian blur to $f(x,y)$ results in

$$b(x,y) = \int_{-\infty}^{\infty} f(\tilde{x},\tilde{y}) \frac{1}{2\pi\sigma_\mathrm{l}\sigma_\mathrm{t}}\, e^{-(x-\tilde{x})^2/(2\sigma_\mathrm{l})}\, e^{-(y-\tilde{y})^2/(2\sigma_\mathrm{t})}\,\mathrm{d}\tilde{x}\mathrm{d}\tilde{y} \tag{1.23}$$
$$\begin{aligned} &= s\frac{m}{\sqrt{2\pi}\sigma_\mathrm{l}} \left(\sigma_\mathrm{l}^2 e^{-(x-x_0)^2/(2\sigma_\mathrm{l}^2)} s(x-x_0)\tilde{\Phi}(-s(x-x_0),\sigma_\mathrm{l})\right) \\ &+ \frac{c}{\sqrt{2\pi}\sigma_\mathrm{l}} \Big(s(x-x_0)\sigma_\mathrm{l}^2 e^{(x-x_0)^2/(2\sigma_\mathrm{l}^2)} \\ &\qquad + \left(\sigma_\mathrm{l}^2 + (x-x_0)^2\right)\tilde{\Phi}(-s(x-x_0),\sigma_\mathrm{l})\Big) \end{aligned} \tag{1.24}$$
$$b(r) = b(x=r,y=0)\,. \tag{1.25}$$

The $\tilde{\Phi}(x,\sigma_\mathrm{l})$ is defined as the integral from x to infinity of a Gaussian with standard deviation σ_l. This can be mapped to the error function ('erf') by

$$\tilde{\Phi}(x,\sigma_\mathrm{l}) = \int_x^\infty e^{-\tilde{x}^2/(2\sigma_\mathrm{l}^2)}\,\mathrm{d}\tilde{x} \tag{1.26}$$

$$= \sqrt{\frac{\pi}{2}}\sigma_\mathrm{l}\left(1 - \frac{2}{\sqrt{\pi}}\int_0^{x/(\sqrt{2}\sigma_\mathrm{l})} e^{-t^2}\,\mathrm{d}t\right) = \sqrt{\frac{\pi}{2}}\sigma_\mathrm{l}\left(1-\mathrm{erf}\left(\frac{x}{\sqrt{2}\sigma_\mathrm{l}}\right)\right) \tag{1.27}$$

The curvature of $b(r)$ along r (with $r_0 = x_0$) is given as

$$\partial_r^2 b(r) = s\frac{m}{\sqrt{2\pi}\sigma_\mathrm{l}}e^{-(r-r_0)^2/(2\sigma_\mathrm{l}^2)} + \frac{c}{\sqrt{2\pi}\sigma_\mathrm{l}}2\tilde{\Phi}(-s(r-r_0),\sigma_\mathrm{l})\,. \tag{1.28}$$

The condition $\partial_r^3 b(r) \stackrel{!}{=} 0$ leads to the position of the maximum in curvature at

$$r_{b,\,\max} = r_0 + \Delta r_\mathrm{kink} \tag{1.29}$$

$$\Delta r_\mathrm{kink} = -s\frac{c}{m}2\sigma_\mathrm{l}^2\,. \tag{1.30}$$

We see, that the quadratic term in the test function $f(r)$, compare equation (1.20), is responsible for the shift in curvature.

Polar Model

Limits of 1D model

While the 1D model is suitable for kinks running along a straight line, in practice many 2D-ACAR spectra will be approximately rotationally symmetric. Therefore a polar model, designed for kinks along a circular contour,

$$g(r) = m(r-r_0) + c(r-r_0)^2 \tag{1.31}$$

$$f(r) = f_0 + g(r)\Theta(s(r-r_0)) \tag{1.32}$$

with

$$s \in \{1,-1\} \tag{1.33}$$

$$r \in [0,\infty) \tag{1.34}$$

is preferable.

Derivation

The mathematical expression of the experimental resolution is not as compact as in the 1D model.

$$b(x,y) = \int_{-\infty}^{\infty} f(\sqrt{\tilde{x}^2+\tilde{y}^2})\frac{1}{2\pi\sigma_\mathrm{l}\sigma_\mathrm{t}}\exp\left(-\frac{(x-\tilde{x})^2}{2\sigma_\mathrm{l}^2} - \frac{(y-\tilde{y})^2}{2\sigma_\mathrm{t}^2}\right)\mathrm{d}\tilde{x}\,\mathrm{d}\tilde{y} \tag{1.35}$$

$$b(r) = f_0 + \int_{r_1}^{r_2}\mathrm{d}\tilde{r}\int_{-\pi}^{\pi}\mathrm{d}\tilde{\varphi}\;\frac{\tilde{r}g(\tilde{r})}{2\pi\sigma_\mathrm{l}\sigma_\mathrm{t}}\exp\left(-\frac{(r-\tilde{r}\cos(\tilde{\varphi}))^2}{2\sigma_\mathrm{l}^2} - \frac{(\tilde{r}\sin(\tilde{\varphi})^2}{2\sigma_\mathrm{t}^2}\right) \tag{1.36}$$

It turns out, however, that a straight forward numerical implementation of this formula is the preferable way to calculate $b(r)$. The analytic limits

$$r_1 = 0;\ r_2 = r_0 \qquad \text{for } s = -1 \tag{1.37}$$
$$r_1 = r_0;\ r_2 = \infty \qquad \text{for } s = 1 \tag{1.38}$$

are replaced by suitable numerical limits. A maximum integration range of $8\sigma_\mathrm{l}$ was chosen for all calculations in this work

$$r_1 = 0;\ r_2 = r_0 \qquad \text{for } s = -1 \tag{1.39}$$
$$r_1 = r_0;\ r_2 = r_0 + 8\sigma_\mathrm{l} \qquad \text{for } s = 1\,. \tag{1.40}$$

Typically the models are fitted in a fitting interval of 1-2 σ_l around r_0 to the experimental spectra. The chosen r_2 for $s = 1$ ensures, that also at the boundary of the fitting range, an environment of at least 6 σ_l is taken into account. The usage of a 100 and 51 mesh points trapezoidal integration for $\tilde{r}$ and $\tilde{\varphi}$ achieves a significantly higher accuracy in figure 1.3, than any analytic simplification of equation (1.36), due to the necessarily included approximations.

Validity

When investigating FS signatures, described by small radii r_0, both models start to differ significantly in their results. It is recommended in this case to use the polar model. For FS signatures, described by large radii on the other hand, the application of the 1D model is a reasonable approximation, yielding a mathematical compact expression. The task to define a critical radius r_crit, where the 1D model is a good approximation for $r_0 \geq r_\mathrm{crit}$, strongly dependents on the exact shape of the 2D-ACAR spectrum under consideration. A conservative estimate can be given by the condition, that the kink signature shall be approximately a straight line in a $\pm\sigma_\mathrm{t}$ range perpendicular to the x-axis at $x = r_0$, i.e. $\cos(\alpha) \approx 1$ with $\alpha = \arctan\left(\frac{\sigma_\mathrm{t}}{r_\mathrm{crit}}\right)$. This is fulfilled to an accuracy of 0.3% for $\alpha = 5°$. So, we arrive at the conservative estimate

$$r_\mathrm{crit} = \frac{\sigma_\mathrm{t}}{\tan(5°)} \approx 0.5\,\mathrm{a.u.} \tag{1.41}$$

Model Application

In this subsection we give a quick sketch about how to apply those fitting models. As back-folding enhances kink-features, it is preferable to investigate $n^{2\gamma}(k_\mathrm{path})$ instead of $\rho^{2\gamma}(p_\mathrm{path})$, where $(k/p)_\mathrm{path}$ denotes the parameterization of a path in the two-dimensional momentum space. Further, fitting the models not by value but by curvature to the experimental data points (compare page 108) is preferable, due to the stronger variations in this quantity. The fitting procedure yields f_0,m,c,x_0 / f_0,m,c,r_0 for the one-dimensional / circular model. The parameter s is chosen manually, as it just assigns the constant region to the left/right of the kink. The parameter x_0 / r_0 represents the position of the FS signature without the effect of experimental resolution. In the case of the polar model, the reference system has to be chosen such, that $r = 0$ marks the center of the polar symmetry.
An application for a realistic system (in analogy to figure 1.3) can be found in section 5.4.

1.2.3. Detection Probability

Overview

There are two effects influencing the recording of 2D-ACAR spectra. The first is the **geometric correction**, which takes into account the different cross sections of photon pairs with different angles to be detected.
Example: Assuming both detectors cover an angle of up to 3° from the perspective of the probe. To detect two photons with $\Theta = 6°$, both photons have to hit exactly on the border of the corresponding detector. There are significantly fewer possible scenarios to detect an annihilation event with this angle, than for $\Theta = 0°$. At $\Theta = 0°$, one photon can hit at any position of the detector, while the other photon will automatically hit the other detector in the anti-parallel direction. Hence, the cross section for detecting annihilation events is larger for small Θ, and is zero for $\Theta > 6°$.
The second effect is **counting statistics**, which describes the statistical fluctuation of the number of detected annihilation events under a certain (p_x,p_y). We shall see later, this is described by a Poisson distribution. In contrast to the geometric correction, the Poisson noise can not be analytically removed from the measured spectrum. A good signal-to-noise ratio can be established by recording a large number of total counts.

Geometric correction

The geometric correction is encoded in the so called **tent function** $f_{\text{tent}}(d)$. Here d denotes the distance between the hypothetical incident position at $\Theta = 0$ and the actual incident position

$$d = d_{\text{probe-detector}} \tan(\Theta)\,. \tag{1.42}$$

The total accessible area of the two photons on the detector for a given d (equivalent to a given angle Θ), is given as the overlap of two circles (the detectors are round) with radius r and distance $d \in [0,2r]$.

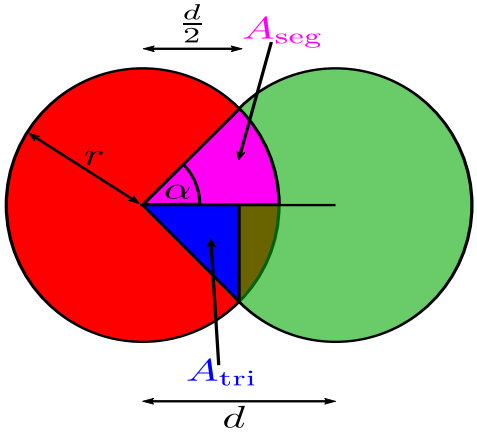

Figure 1.4.: Overlapping area of two circles

With basic geometric considerations (pointed out in figure 1.4) the overlap can be calculated as

$$A_{\text{overlap}}(d) = 4\,(A_{\text{seg}} - A_{\text{tri}}) = 2\alpha r^2 - rd\sin\alpha \tag{1.43}$$

$$\alpha = \arccos\left(\frac{d/2}{r}\right)\,. \tag{1.44}$$

The tent function (compare figure 1.5) is just the ratio of the accessible area at a given d and the maximal accessible area at $d = 0$

$$f_{\text{tent}}(d) = \frac{A_{\text{overlap}}}{r^2\pi} = \frac{1}{\pi}\left(2\alpha - \frac{d\sin\alpha}{r}\right) . \tag{1.45}$$

To perform the geometric correction, $\rho^{2\gamma}(p_x,p_y)$ has to be divided by the tent function.

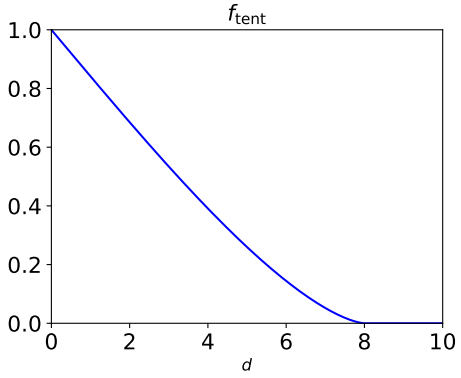

Figure 1.5.: Graphical representation of the tent function equation (1.45) for one dimension. The detector radius was taken as 4 a.u.

Because of the low positron density there is at most one positron at a time in the probe. Hence the annihilation events are independent of each other. Further we have a large number of channels/bins, which means that the probability of detecting an event in a specific bin is low.[4] The implication on the experimental counting statistics is, that the relative number of counts, detected for each momentum bin, resembles the long time limit up to a standard error. This error is approximately the square root of the number of detected events. Counting statistics

$$\sigma_{\text{Poisson}}(p_x,p_y) \approx \sqrt{\rho^{2\gamma}(p_x,p_y)} \tag{1.46}$$

Especially in the higher momenta regions (with a small number of counts) Poisson noise leads to an unfavorable signal-to-noise ratio. The geometric correction amplifies this issue additionally.

Figure 1.6 shows the effects of geometric correction and counting statistics at the example of a constant test spectrum[5] in subplot a. Figure 1.6b shows the recorded statistics Example

[4] Poisson distribution: According to the **law of rare events**, a binomial random variable (here 'annihilation event' or 'no annihilation event') can be approximated by a Poisson distribution when measured over a certain time interval. The λ-parameter of the Poisson distribution is equivalent to the expectation value for the count of events. The description as a Poisson distribution is only appropriate, when the probability p of the binomial distribution is small [221] (p: detection probability in a specific bin).

[5] This was chosen for demonstration purposes. A realistic $\rho^{2\gamma}(p_x,p_y)$ shows a high intensity in the center and decays for larger momenta, compare figure 4.4a.

by the detectors, due to the geometric correction. The influence of the counting statistics on the recorded spectrum is displayed in subplots c and e for measurements with 8 and 200 million counts.[6] The corresponding reconstructed spectrum $\rho^{2\gamma}_{\text{reconstr}}$ is presented in figure 1.6 d and f. The different scales in those subplots show, that the signal-to-noise ratio differs by a factor of 6. Further a stronger noise is found in the outer areas of $\rho^{2\gamma}_{\text{reconstr}}$ compared to the center.

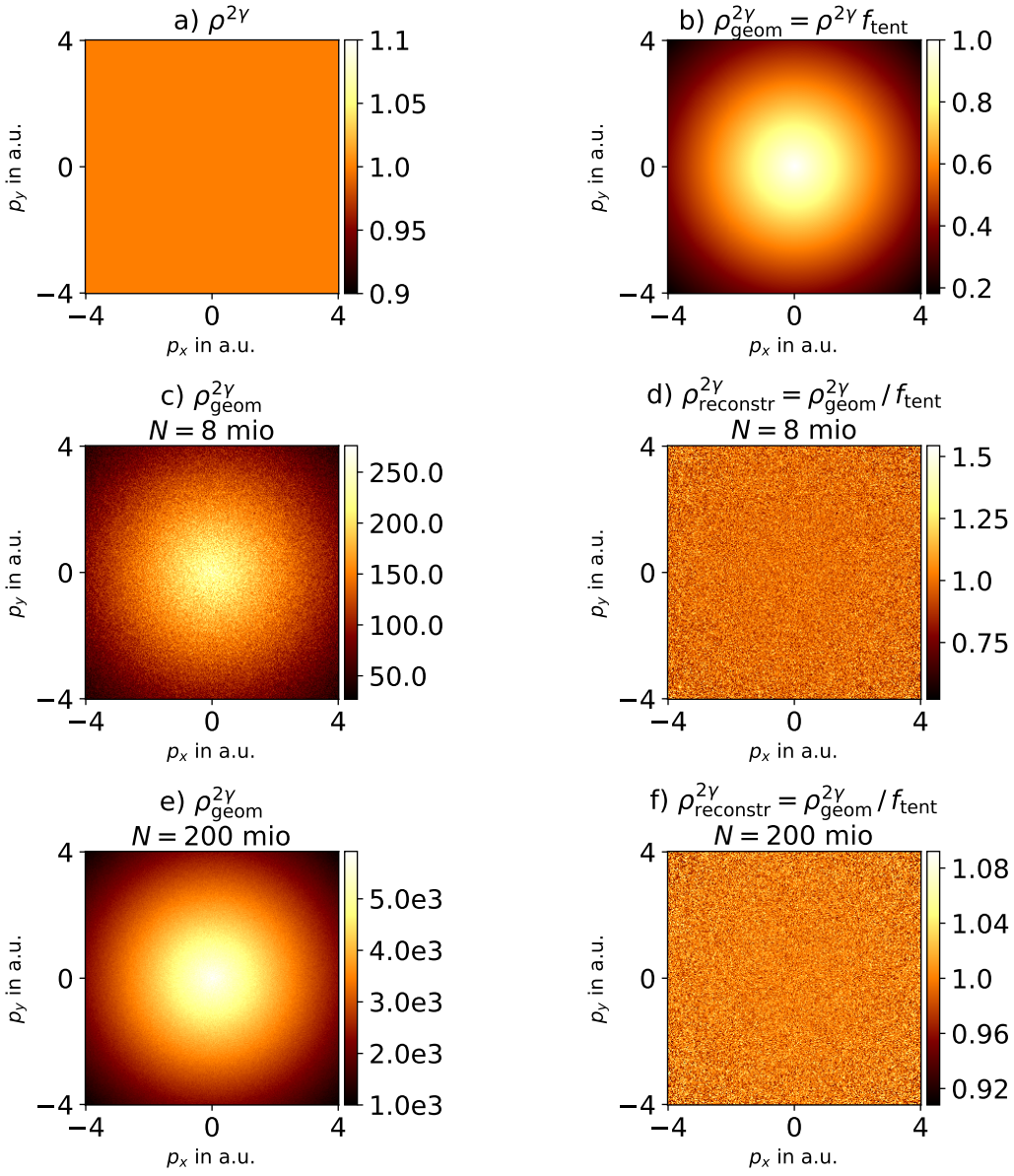

Figure 1.6.: Influence of geometric correction and counting statistics of 2D-ACAR spectra, model calculation:
Subplots d and f show the reconstruction of $\rho^{2\gamma}$ (subplot a) under the influence of Poisson noise amplified by the tent function (figure 1.5).

[6] These are two representative cases. The following references use 10-400 million counts [64–67, 203].

1.3. Experimental Background about Positrons

1.3.1. Properties of Positrons

History

Dirac mentioned in 1928 [95] a difficulty with a negative energy/charge branch of the "relativity wave equation". After a period of scientific discussions, following Oppenheimers [96] arguments, Dirac described in 1931 [97] this negative energy branch as 'uniformly filled' and 'completely unobservable'. He further pointed out, that if there were holes (which he called 'anti-electrons'), they would be a new kind of particle and rapidly recombine with electrons. Experimental evidence for these 'anti-electrons' was found by Anderson in 1932, when analyzing photographs of cosmic-rays. In his publication [98] Anderson introduced the modern term **positrons** for these particles.

Creation

Positrons can be produced by radioactive sources (as the result of β^+ decay) or in accelerators via **pair production**.
The most common radioactive sources for this purpose are ^{22}Na, ^{58}Co or ^{64}Cu. Positrons are emitted with a continuous spectrum of energy (conservation of energy during the emission is allowed by emission of one neutrino) with maximum energies, ranging from 0.5 to 1.5 MeV [113–116].
The creation of positrons by using pair production is more elaborate, as it requires thermal neutrons and hence a nuclear reactor. A description of the positron production process in the NEPOMUC facility (Technical University of Munich, Germany) can be found in [74, 99, 100]. With this setup positron rates of $10^9 \frac{1}{\mathrm{s}}$ [101] are possible.

Properties

Positrons have a thermalization time of $\mathcal{O}(10^{-12})$ s in solids (and $10^{-9} - 10^{-7}$s in some gases) and a lifetime of $\mathcal{O}(10^{-10})$ s in metals [103–105, 108, 110]. In the presence of vacancies their lifetime can increase [109].
Positrons most likely directly annihilate with an electron of opposite spin [74, 107]. There are however other decay processes, which might include the formation of a positronium (which is an unstable electron-positron bound state). The positron can be in the singlet or the triplet state, corresponding the vector summation of the electron and positron spin

$$|\boldsymbol{s}^{\mathrm{e}} + \boldsymbol{s}^{\mathrm{p}}| = \begin{cases} 0 & \text{(singlet)} \\ 1 & \text{(triplet)} \end{cases} . \tag{1.47}$$

Due to conservation of the total spin, the singlet configuration results in an even number of photons, while an odd number of photons is emitted from the annihilation of a triplet state [106]. The most probable annihilation scenarios of the positronium are two or three photons.

1.3.2. Other Experiments Including Positrons

The three conventional techniques, which use positrons to probe the bulk properties of solids, are ACAR (described before), Doppler broadening and positron lifetime spectrometry. All those techniques are based on the detection of γ rays with energies

$E_\gamma \approx 511\,\mathrm{keV}$, i.e. the rest masses of the electron and the positron. We want to give a quick sketch about the remaining two techniques at this point.

Doppler Broadening

Mechanism Doppler broadening spectroscopy measures the energy distribution of the electron-positron annihilation radiation. During the annihilation process, the momentum component of the electron in emitting (i.e. longitudinal) direction p_l directly adds to the 'zero momentum' $p_0 \equiv \frac{511\,\mathrm{keV}}{c}$ of both γ-quanta, where c denotes the speed of light. The transversal momentum component p_t only contributes by the Pythagorean theorem. The total momentum of the gamma quantum p_γ is hence given by

$$p_\gamma = \sqrt{(p_0 \pm \frac{p_\mathrm{l}}{2})^2 + \left(\frac{p_\mathrm{t}}{2}\right)^2}\,. \tag{1.48}$$

As $p_0 \gg p_{\mathrm{t/l}}$, the corresponding energy change by electron momentum components in longitudinal direction is amplified. Taking the energy of a γ-quantum as

$$E_\gamma \approx p_0 c \pm \frac{c p_\mathrm{l}}{2}\,, \tag{1.49}$$

electron momenta of 0.5 a.u. lead to a Doppler shift of $\frac{cp_\mathrm{l}}{2} \approx 1\,\mathrm{keV}$. Since the 1970s the energy resolution of commercially available detectors has reached this level, making Doppler broadening available as an experimental technique [107].

Method The width of different contributions to the 'annihilation line' at 511 keV can be used, to distinguish between core electron states (broadly distributed) and valence electron states (peaked distribution). One detector is enough to perform Doppler broadening measurements, which increases the sampling rate and opens new possibilities, when a specific experimental setup is needed [120]. In general this method is used to measure different properties of defects like concentration, spatial distribution and chemical variation at the defect site [122, 123]. Doppler broadening can also be performed in a two-detector setup [121], which improves the signal-to-noise ratio at the cost of a decreased counting rate.

Positron Annihilation Lifetime Spectrometry (PALS)

Setup In PALS, also called positron annihilation spectroscopy (PAS), the lifetime of positrons is investigated, to draw conclusions about their electronic environment. To measure the lifetime, a start signal and an end signal is needed. The start signal can be the 1.27 MeV γ-quantum, which is emitted a few picoseconds after the creation of the positron in the β^+ decay of Na^{22} [117–119]. The end signal is the annihilation radiation. Also the thermalization time of the positron is (in general) short compared to its lifetime.

Spectra The resulting spectrum (detected events N with a specific lifetime τ) is a linear combination of different decay modes i:

$$N(\tau) = \sum_i W_i e^{\lambda_i \tau} + B_i(\tau) \tag{1.50}$$

where B_i denotes a background noise, W_i the weight of the mode and λ_i its exponent. From a fit to such a model, information about the different components in the material can be gained. This method is especially useful to determine the density of defects in a probe.

2. Methods of Electronic Structure Calculations

Overview

The theoretical data for realistic systems in this work is based on an extension [190, 191] of the Elk Code [189], designed to obtain 2D-ACAR spectra. In this chapter we will discuss briefly the concept of **Density Functional Theory (DFT)** and the **Linearized Augmented Plane Wave (LAPW)** method, implemented in Elk. We will further point out the generalization to a two-component DFT [171], describing a positron in an electronic system.

History

Since the 1970s **ab-initio** DFT calculations have been used to investigate the electronic structure of materials. Moruzzi et. al. [210] used those methods to raise the standard of electronic structure calculations [209] back then. The DFT [145, 146, 149] has become the primary tool for calculating the electronic structure in condensed matter. It is also important in quantitative studies of molecules and other finite systems. Nowadays most of the basic properties of solids, such as the structural and cohesive properties, can be calculated without adjustments to the experimentally determined parameters [145].

Concept

In DFT the system under investigation (which is consisting of interacting particles) is mapped to a system of non-interacting particles described by a set of Schrödinger-like equations. These are called the **Kohn-Sham equations** [143]. The underlying central quantity, which is the same in both systems, is the electron density. DFT is hence based on a **single particle picture**, where correlations between particles are taken into account statically by the **exchange-correlation**-potential in the Hamiltonian.[1] This term can not be calculated exactly, but has to be approximated. The **local density approximation** and the **generalized gradient approximation** are two successful and widely used approaches.

Units

Throughout this chapter, we will use **Rydberg atomic units**

$$\frac{e}{\sqrt{2}} = 2m_{\mathrm{e}} = \hbar = 1\,. \tag{2.1}$$

This removes the prefactor $\frac{1}{2}$ from the kinetic energy and the Coulomb term for more compact expressions.

[1] There exist concepts, expanding the possibilities of DFT for an improved handling of correlation effects. The interested reader may therefore refer to [184–188].

2.1. Density Functional Theory for Purely Electronic Systems

Hohenberg-Kohn theorems

Hohenberg and Kohn gave two pioneering theorems in their publication [142]. **First**, the system (in particular the total energy and the external potential) is uniquely described by the electron density. So considering a system with N electrons, the problem is simplified from $\propto 3N$ to $\propto 3$ degrees of freedom. **Second**, the energy of the system is minimized only by the electron density of the ground state.
Those theorems are used to formulate the many-electron problem on the basis of energy functionals.
The total energy of the system is expressed as

$$E[n^\sigma(\boldsymbol{r})] = T[n^\sigma(\boldsymbol{r})] + \mathcal{V}[n^\sigma(\boldsymbol{r})] + \mathcal{V}_{\text{ee}}[n^\sigma(\boldsymbol{r})]\,, \tag{2.2}$$

where T is the kinetic energy, $\mathcal{V}$ is the external potential energy (including the ionic background) and $\mathcal{V}_{\text{ee}}$ contains the potential energy form electron-electron interaction. The spin index has to be interpreted as the tuple of the spin up and spin down quantity, as pointed out in the following for the electron density: $[n^\sigma(\boldsymbol{r})] \equiv \left[n^\uparrow(\boldsymbol{r}),n^\downarrow(\boldsymbol{r})\right]$.

Kohn-Sham equation

The **Kohn-Sham equation** is a single particle Schrödinger equation for some (at this point not specified) potential V_{eff}:

$$\{-\nabla^2 + V_{\text{eff}}(\boldsymbol{r}, [n^\sigma(\boldsymbol{r})])\}\Psi_j^\sigma(\boldsymbol{r}) = \epsilon_j \Psi_j^\sigma(\boldsymbol{r})\,. \tag{2.3}$$

This equation can be solved (at least up to a desired accuracy) and gives rise to a ground state solution $\Psi^\sigma_{\text{KS,GS}}$. From there the electron ground state density for the Kohn-Sham system follows directly as

$$n^\sigma_{\text{KS,GS}}(\boldsymbol{r}) = \left|\Psi^\sigma_{\text{KS,GS}}(\boldsymbol{r})\right|^2\,. \tag{2.4}$$

Kohn-Sham approach

The **Kohn-Sham approach** assumes, that there exists an effective potential V_{eff}, so that the corresponding $n^\sigma_{\text{KS,GS}}(\boldsymbol{r})$ is equivalent to the ground state electron density of the interacting system under investigation. To find the exact effective potential for a given system is a challenging and a - to this point - unsolved task. For a better understanding of the problem we split the effective potential into

$$V_{\text{eff}}(\boldsymbol{r}; [n^\sigma(\boldsymbol{r})]) = V_{\text{ext}}(\boldsymbol{r}) + V_{\text{H}}(\boldsymbol{r}; [n^\sigma(\boldsymbol{r})]) + V_{\text{xc}}(\boldsymbol{r}; [n^\sigma(\boldsymbol{r})])\,, \tag{2.5}$$

where V_{ext} and V_{H} have a simple physical description and V_{xc} summarizes contributions, which need to be handled approximately.

Separation of potentials

The V_{ext} denotes the external potential. In its simplest form this writes

$$V_{ext}(\boldsymbol{r'}) = -\sum_{\boldsymbol{R}} \frac{Z}{|\boldsymbol{r'} - \boldsymbol{R}|}\,, \tag{2.6}$$

where only the ionic background is taken into account. Further terms like an external magnetic field can be included in this term as well. The corresponding external energy functional is

$$E_{ext}[n^\sigma(\boldsymbol{r})] = \int \mathrm{d}\boldsymbol{r'}\, V_{ext}(\boldsymbol{r'}) n^\sigma(\boldsymbol{r'})\,. \tag{2.7}$$

The Coulomb potential V_H of the charge density at point $\boldsymbol{r}$ (with respect to the surrounding electron cloud) and the electrostatic Hartree energy E_H are given as[2]:

$$V_\mathrm{H}(\boldsymbol{r}; [n^\sigma(\boldsymbol{r})]) = \int \mathrm{d}\boldsymbol{r'} \frac{n^\sigma(\boldsymbol{r'})}{|\boldsymbol{r} - \boldsymbol{r'}|} \tag{2.8}$$

$$E_\mathrm{H}[n^\sigma(\boldsymbol{r})] = \int \mathrm{d}\boldsymbol{r}'\, V_H(\boldsymbol{r'}, [n^\sigma(\boldsymbol{r})]) n^\sigma(\boldsymbol{r'}) = \int \mathrm{d}\boldsymbol{r'}\mathrm{d}\boldsymbol{r''}\, \frac{n^\sigma(\boldsymbol{r'}) n^\sigma(\boldsymbol{r''})}{|\boldsymbol{r'} - \boldsymbol{r''}|}\,. \tag{2.9}$$

The exchange-correlation potential V_xc handles all other differences between the non-interacting system and the interacting one. This includes the electron-electron correlation and the exchange interaction (which corresponds to the symmetry restrictions of many particle states for indistinguishable particles). It can only be calculated approximately and is subject of continuous research. The early work of Wigner [151], investigating correlation effects in a homogeneous electron gas on a perturbative level, shall be mentioned in this context.

Exchange-correlation functionals

The number of possible expressions for V_xc is overwhelming. The **libxc library** (available at http://www.tddft.org/programs/libxc/functionals/, status 2018) is a comprehensive and continuously expanded collection of different exchange-correlation functionals [150]. If those functionals take only $n^\sigma(\boldsymbol{r})$ into account, they belong to the class of **Local Density Approximation (LDA)** functionals [154–156] or **Local Spin Density Approximation (LSDA)** functionals [152, 153] (in the case of spin dependence). **Generalized Gradient Approximation (GGA)** functionals [157–159] additionally take the gradient of the electron density $\nabla n^\sigma(\boldsymbol{r})$ into account. LDA and GGA are the two most famous classes of exchange-correlation functionals.

2.1.1. Self-Interaction Correction and Exchange-Correlation Hole

Self-interaction

By working purely with an electron density based description, the Hartree energy (2.9) does not take into account the fact, that an electron can not interact with itself [145, 148,155]. This means that one specific electron contributes simultaneously to the terms $n^\sigma(\boldsymbol{r'} = \boldsymbol{r_1})$ and $n^\sigma(\boldsymbol{r''} = \boldsymbol{r_2})$ in equation (2.9) for $\boldsymbol{r_1} \neq \boldsymbol{r_2}$. Hence, the contribution of this electron to $n^\sigma(\boldsymbol{r_2})$ has to be subtracted before calculating E_H.

[2] This term gives rise to the self-interaction correction [148], as casually speaking the electron at point $\boldsymbol{r}$ should be subtracted from the cloud before calculating the Coulomb potential. This is described in the next section.

Exchange-correlation hole

Practically, this effect is not considered in the Hartree term V_{H} but in the exchange correlation term V_{xc}. This leads to

$$V_{\mathrm{xc}}\left(\boldsymbol{r},[n^{\sigma}(\boldsymbol{r})]\right)=\int \mathrm{d}\boldsymbol{r'}\,\frac{n_{\mathrm{xc}}(\boldsymbol{r},\boldsymbol{r'}-\boldsymbol{r})}{|\boldsymbol{r}-\boldsymbol{r'}|} \tag{2.10}$$

$$E_{\mathrm{xc}}\left(\boldsymbol{r},[n^{\sigma}(\boldsymbol{r})]\right)=\int \mathrm{d}\boldsymbol{r}\,n^{\sigma}(\boldsymbol{r})V_{\mathrm{xc}}\left(\boldsymbol{r},[n^{\sigma}(\boldsymbol{r})]\right)\,, \tag{2.11}$$

where n_{xc} denotes the correction to the electron density. Perdew and Zunger [155] showed within the LSDA, that this correction is approximately the Coulomb interaction of the corresponding orbital.[3] Per definition, n_{xc} is negative and obeys the normalization condition

$$\int \mathrm{d}\boldsymbol{r'}n_{\mathrm{xc}}(\boldsymbol{r},\boldsymbol{r'}-\boldsymbol{r})=-1\,. \tag{2.12}$$

So, in total one electron is subtracted from the electron density. This correction, due to inter electronic repulsion, is often interpreted as a positively charged **exchange-correlation hole** 'in front' of an uncorrected electronic background.

Canceling of anisotropy

Due to the isotropy of the Coulomb repulsion, the potential of the exchange-correlation hole can be expressed as

$$V_{\mathrm{xc}}\left(\boldsymbol{r},[n^{\sigma}(\boldsymbol{r})]\right)=\int \mathrm{d}\boldsymbol{R}\,\frac{n_{\mathrm{xc}}(\boldsymbol{r},\boldsymbol{R})}{|\boldsymbol{R}|}\,. \tag{2.13}$$

The isotropic integration cancels all contributions except the spherical symmetric part of $n_{\mathrm{xc}}(\boldsymbol{r},\boldsymbol{R})$ [144]. So when expanding the exchange-correlation hole into spherical harmonics

$$n_{\mathrm{xc}}(\boldsymbol{r},\boldsymbol{R})=\sum_{l=0}^{\infty}\sum_{m=-l}^{l}\rho_{lm}(\boldsymbol{r},\boldsymbol{R})Y_{lm}\left(\frac{\boldsymbol{R}}{|\boldsymbol{R}|}\right)\,, \tag{2.14}$$

only the $l=m=0$ contribution survives

$$V_{\mathrm{xc}}\left(\boldsymbol{r},[n^{\sigma}(\boldsymbol{r})]\right)=\sqrt{4\pi}\int \mathrm{d}R\,R^{2}\frac{\rho_{00}(\boldsymbol{r},\boldsymbol{R})}{R}\,. \tag{2.15}$$

We used $R=|\boldsymbol{R}|$ and $\int \mathrm{d}\Omega\,Y_{lm}\left(\frac{\boldsymbol{R}}{R}\right)=\frac{1}{\sqrt{4\pi}}\delta_{l,0}\delta_{m,0}$. Hence, not the exact shape of the exchange-correlation hole but only its isotropic part is relevant for the self-interaction contribution to the exchange-correlation energy.

Estimated size

From the normalization condition (2.12) the radius of the exchange correlation hole can be estimated as [4]

$$r_{xc}\approx\left(-\frac{3}{\sqrt{4\pi}\rho_{00}}\right)^{\frac{1}{3}} \tag{2.16}$$

[3] Hence, the self-interaction correction introduces an orbital dependent effective potential. For simplicity we do not introduce an orbital index for $n^{\sigma}(\boldsymbol{r})$ at this point.

[4] Note that $\rho_{00}<0$, due to equations (2.12) and (2.14).

under the assumption of an exchange-correlation hole with a homogeneous density

$$n_{\mathrm{xc}}(\boldsymbol{r},\boldsymbol{R}) = \begin{cases} \rho_{00} & \text{for } R \leq r_{xc} \\ 0 & \text{for } R > r_{xc}\,. \end{cases} \tag{2.17}$$

The LSDA describtion of n_{xc} is based on a homogeneous electron liquid approach. Due to the canceling of anisotropic terms in V_{xc}, the LSDA gives a remarkable precise description, even for electrons in a periodic potential. This is also true for systems with very strong density variations, so that a homogeneous electron liquid ansatz does not appear to be suitable [144].

2.1.2. Solving the Kohn-Sham Equation

To solve the Kohn-Sham equations (2.3) for a crystal, a basis has to be chosen to express the eigenstates $|\Psi_{j,\boldsymbol{k}}\rangle$ Motivation

$$|\Psi_\alpha\rangle = \sum_n a_{\alpha n}|\phi_n\rangle \equiv \boldsymbol{a}_\alpha\,. \tag{2.18}$$

Due to translational symmetry in the crystal, α denotes a tuple of band index and crystal momentum $(j,\boldsymbol{k})$. For simplicity we omitted the spin index σ. The secular equation for the Hamiltonian writes

$$\boldsymbol{H}\boldsymbol{a}_\alpha = E_\alpha \boldsymbol{S}\boldsymbol{a}_\alpha \tag{2.19}$$
$$H_{nm} = \langle\phi_n|\boldsymbol{H}|\phi_m\rangle \tag{2.20}$$
$$S_{nm} = \langle\phi_n|\phi_m\rangle\,. \tag{2.21}$$

As the Hamiltonian Self-consistency

$$\boldsymbol{H} = \left\{-\nabla^2 + V_{\mathrm{eff}}\left(\boldsymbol{r},[n(\boldsymbol{r})]\right)\right\} \tag{2.22}$$

depends on the solution of the secular equation by

$$n(\boldsymbol{r}) = \sum_{\mathrm{occ}.\alpha} |\Psi_\alpha(\boldsymbol{r})|^2\,, \tag{2.23}$$

this problem has to be solved self-consistently. The computational complexity of this task can be simplified, by choosing a proper basis [161,166]. This can be achieved by the concept of **Augmented Plane Waves (APW)** and its expansion, the **Linearized Augmented Plane Wave (LAPW)** method.

Augmented Plane Wave Method

The concept of the APW method was formulated by Slater in 1937 [138]: In the region $\mathcal{S}$, close to a nucleus, the wave functions of the Kohn-Sham equation can be expected to be similar to those of an isolated atom. In the interstitial region $\mathcal{I}$ (being the APW basis set

complementary space), the wave functions are expected to be less influenced by the nuclei, giving rise to a plane wave representation. These ideas are expressed in the ansatz

$$\phi_{j,\boldsymbol{k}}^{\mathrm{APW}}(\boldsymbol{r}) = \begin{cases} \sum_{l,m} A_{j,lm} u(r,E_{j,l}) Y_{lm}(\hat{\boldsymbol{r}}) & \text{for } \boldsymbol{r} \in \mathcal{S} \\ \frac{1}{(2\pi)^3} \sum_{\boldsymbol{G}} c_{j,\boldsymbol{G}+\boldsymbol{k}} e^{i(\boldsymbol{G}+\boldsymbol{k})\boldsymbol{r}} & \text{for } \boldsymbol{r} \in \mathcal{I} \end{cases} \tag{2.24}$$

for the wave function $\Psi_j^\sigma(\boldsymbol{r})$ in the Kohn-Sham equation (2.3) with expansion coefficients $A_{j,lm}$ and $c_{j,\boldsymbol{G}+\boldsymbol{k}}$. $u(r, E_{j,l})$ is the **regular solution** of

$$\left[-\frac{\mathrm{d}^2}{\mathrm{d}r^2} + \frac{l(l+1)}{r^2} + V(r) - E_{j,l}\right] r u(r,E_{j,l}) = 0 \qquad \text{for } \boldsymbol{r} \in \mathcal{S}\,, \tag{2.25}$$

where $E_{j,l}$ is the eigenvalue of $\Psi_{j,\boldsymbol{k}}$ (compare equations (2.18) and (2.19)) and $V(r)$ the spherical component of the potential in $\mathcal{S}$ [166].

Approximations

The concept of splitting $\mathbb{R}^3$ into $\mathcal{S}$ and $\mathcal{I}$ is called the **Muffin-Tin Approximation (MTA)**. This approximation can be avoided by methods, based on multiple-scattering theory (as for instance in modern versions [176–183] of the **Korringa-Kohn-Rostoker** [174, 175] method), but was used in the context of this work. After applying the MTA, the situation can be further simplified to the **Atomic Sphere Approximation (ASA)** or treated in the **Full-Potential (FP)** description. The ASA assumes, that the potential is radial symmetric (i.e. $V(r)$) within the spherical volume $\mathcal{S}$. This approximation is used for the factorization of radial and angular part in equation (2.24) and for $V(\boldsymbol{r}) \to V(r)$ in equation (2.25). FP calculations also take the anisotropy of the atomic potential into account.[5]

Continuity condition

To establish continuity at the boundary between $\mathcal{S}$ and $\mathcal{I}$, the following condition [147] has to be fulfilled between the expansion coefficients $A_{j,lm}$ and $c_{j,\boldsymbol{G}+\boldsymbol{k}}$:

$$A_{j,lm} = \frac{i^l}{2\pi^2 u(R,E_{j,l})} \sum_{\boldsymbol{G}} c_{j,\boldsymbol{G}+\boldsymbol{k}}\, j_l(|\boldsymbol{G}+\boldsymbol{k}|R)\, Y_{lm}^*(\boldsymbol{G}+\boldsymbol{k})\,, \tag{2.26}$$

where R is the radius of $\mathcal{S}$ and j_l the spherical Bessel function of first kind.

Issues

The problem with the APW method is the self-consistent determination of the parameters $E_{j,l}$. Instead of simply diagonalizing $\boldsymbol{H}$, a set of energies $\{E_{j,l}\}$ has to be found first, simultaneously fulfilling equations (2.19) and (2.25). This can be achieved, for instance, by solving $\det(\boldsymbol{H} - E_\alpha \boldsymbol{S}) = 0$ as a function of the energy parameters $\{E_{j,l}\}$ [141,147,166,167]. From a computational perspective this is extremely demanding, which can be avoided by using the LAPW method.

Linearized Augmented Plane Wave Method

Concept

First proposed by Andersen in 1975 [160], the LAPW method was shortly later applied

[5] There exists some confusion in the nomenclature of MTA, ASA and FP. In some cases MTA is used instead of ASA.

by Koelling and Arbman [161]. In the LAPW approach the derivative of $u(r,E_{j,l})$ with respect to $E_{j,l}$ is calculated

$$\dot{u}(r,E_{j,l}) \equiv \frac{\mathrm{d}u(r,E_{j,l})}{\mathrm{d}E_{j,l}}\,. \tag{2.27}$$

We therefore differentiate equation (2.25) to

$$\left[-\frac{\mathrm{d}^2}{\mathrm{d}r^2} + \frac{l(l+1)}{r^2} + V(r) - E_{j,l}\right] r\dot{u}(r,E_{j,l}) = ru(r,E_{j,l})\,. \tag{2.28}$$

The ansatz for the wave function is chosen as

$$\phi^{\mathrm{LAPW}}_{j,\boldsymbol{k}}(\boldsymbol{r}) = \begin{cases} \sum\limits_{l,m} \left[A_{j,lm}u(r,E_{j,l}) + B_{j,lm}\dot{u}(r,E_{j,l})\right] Y_{lm}(\hat{\boldsymbol{r}}) & \text{for } \boldsymbol{r} \in \mathcal{S} \\ \frac{1}{(2\pi)^3} \sum\limits_{\boldsymbol{G}} c_{j,\boldsymbol{G}+\boldsymbol{k}} e^{i(\boldsymbol{G}+\boldsymbol{k})\boldsymbol{r}} & \text{for } \boldsymbol{r} \in \mathcal{I}\,, \end{cases} \tag{2.29}$$

for $u(r,E_{j,l})$ and $\dot{u}(r,E_{j,l})$ at a fixed $E_{j,l} = E^{\mathrm{init}}_{j,l}$. The expansion coefficients $A_{j,lm}$ and $B_{j,lm}$ are chosen to establish continuity in $\phi^{\mathrm{LAPW}}_{j,\boldsymbol{k}}(\boldsymbol{r})$ and $\frac{\mathrm{d}\phi^{\mathrm{LAPW}}_{j,\boldsymbol{k}}(\boldsymbol{r})}{\mathrm{d}r}$ at the boundary of the muffin-tin.

Error estimation

It can be shown [161], that the error made by choosing $E^{\mathrm{init}}_{j,l}$ instead of the real value

$$\epsilon = \frac{\langle \Psi_{j,\boldsymbol{k}} | \boldsymbol{H} | \Psi_{j,\boldsymbol{k}} \rangle}{\langle \Psi_{j,\boldsymbol{k}} | \Psi_{j,\boldsymbol{k}} \rangle} \tag{2.30}$$

is proportional to $(E^{\mathrm{init}}_{j,l} - \epsilon)^2$ in $\phi^{\mathrm{LAPW}}_{j,\boldsymbol{k}}$ and proportional to $(E^{\mathrm{init}}_{j,l} - \epsilon)^4$ in

$$E^{\mathrm{LAPW}}_{j,l} = \frac{\langle \Psi^{\mathrm{LAPW}}_{j,\boldsymbol{k}} | \boldsymbol{H} | \Psi^{\mathrm{LAPW}}_{j,\boldsymbol{k}} \rangle}{\langle \Psi^{\mathrm{LAPW}}_{j,\boldsymbol{k}} | \Psi^{\mathrm{LAPW}}_{j,\boldsymbol{k}} \rangle}\,, \tag{2.31}$$

where $\Psi^{\mathrm{LAPW}}_{j,\boldsymbol{k}}$ is an eigenvalue of the Hamiltonian calculated by replacing $E_{j,l} \to E^{\mathrm{init}}_{j,l}$ in equations (2.25) and (2.28).

Implementation

By using (2.29) as a basis for (2.18), an analytic expression for the matrix elements of the Hamiltonian H_{nm} (2.20) can be derived. The computational time needed for the LAPW approach can be estimated to be two orders of magnitude smaller compared to the APW method [161]. Historically the LAPW method opened the path to further developments like fully self-consistent [162,163] and full-potential [164] calculations. A review of LAPW results, concerning surface calculations from that time, was given by Wimmer [165].

2.2. Two-Component Density Functional Theory

Introduction

To simulate ACAR experiments, it is necessary to take the positron into account as well. From a DFT perspective this is a challenging problem, as the electron density $n^{\mathrm{e}}(\boldsymbol{r})$ and the positron density $n^{\mathrm{p}}(\boldsymbol{r})$ influence each other dynamically. Until today, this dynamic electron-positron correlation is simplified to a static model, where the purely electronic state of the system is calculated and the positron density is calculated in this rigid setting.

Validity

This approach is surely reasonable for delocalized positrons, as the positron density is low and so is the influence on the electron density in the background. For localized positron states (as occur in the case of vacancies in the probe) however, the assumption of a rigid electron density is questionable.

Kohn-Sham equations

To describe the dynamics of the electron and positron densities, we arrive (in analogy of the purely electronic DFT framework, compare equation (2.3)) at a set of two coupled Kohn-Sham equations [170, 171, 173] (spin index σ is omitted).

$$\text{electrons: } \Big\{ -\nabla^2 + V_{\mathrm{ext}}(\boldsymbol{r}) + V_{\mathrm{H}}^{\mathrm{ep}}\left(\boldsymbol{r}, [n^{\mathrm{e}}(\boldsymbol{r}),n^{\mathrm{p}}(\boldsymbol{r})]\right) + \frac{\delta E_{\mathrm{xc}}[n^{\mathrm{e}}(\boldsymbol{r})]}{\delta n^{\mathrm{e}}(\boldsymbol{r})} + \frac{\delta E_{\mathrm{c}}^{\mathrm{ep}}\left[n^{\mathrm{e}}(\boldsymbol{r}),n^{\mathrm{p}}(\boldsymbol{r})\right]}{\delta n^{\mathrm{e}}(\boldsymbol{r})} \Big\} \Psi_j^{\mathrm{e}}(\boldsymbol{r}) = \epsilon_j^{\mathrm{e}} \Psi_j^{\mathrm{e}}(\boldsymbol{r}) \tag{2.32}$$

$$\text{positrons: } \Big\{ -\nabla^2 - V_{\mathrm{ext}}(\boldsymbol{r}) - V_{\mathrm{H}}^{\mathrm{ep}}\left(\boldsymbol{r}, [n^{\mathrm{e}}(\boldsymbol{r}),n^{\mathrm{p}}(\boldsymbol{r})]\right) + \frac{\delta E_{\mathrm{xc}}[n^{\mathrm{p}}(\boldsymbol{r})]}{\delta n^{\mathrm{p}}(\boldsymbol{r})} + \frac{\delta E_{\mathrm{c}}^{\mathrm{ep}}\left[n^{\mathrm{e}}(\boldsymbol{r}),n^{\mathrm{p}}(\boldsymbol{r})\right]}{\delta n^{\mathrm{p}}(\boldsymbol{r})} \Big\} \Psi_j^{\mathrm{p}}(\boldsymbol{r}) = \epsilon_j^{\mathrm{p}} \Psi_j^{\mathrm{p}}(\boldsymbol{r}) \tag{2.33}$$

with

$$V_{\mathrm{H}}^{\mathrm{ep}}\left(\boldsymbol{r}, [n^{\mathrm{e}}(\boldsymbol{r}),n^{\mathrm{p}}(\boldsymbol{r})]\right) = \int \mathrm{d}\boldsymbol{r'} \frac{n^{\mathrm{e}}(\boldsymbol{r'}) - n^{\mathrm{p}}(\boldsymbol{r'})}{|\boldsymbol{r} - \boldsymbol{r'}|} \,. \tag{2.34}$$

The Coulomb potential $V_{\mathrm{H}}^{\mathrm{ep}}$ is extended by the positron density term (compared to equation (2.8)) and $E_{\mathrm{c}}^{\mathrm{ep}}$ denotes the electron-positron correlation energy. These two equations describe the full dynamics of the interplay of electrons and positrons in a fixed ionic background. From a computational perspective however, this setup is by far more difficult to compute than the self-consistent solution of the purely electronic problem. As only the $E_{\mathrm{c}}^{\mathrm{ep}}$-term is responsible for this coupling, it is therefore interesting to investigate it in more detail. It will turn out during this investigation, that within some approximations the electron-positron Kohn-Sham equations can, indeed, be decoupled.

Electron-positron correlation

The electron-positron correlation energy can be expressed as

$$E_{\mathrm{c}}^{\mathrm{ep}}\left[n^{\mathrm{e}}(\boldsymbol{r}),n^{\mathrm{p}}(\boldsymbol{r})\right] = -\int_0^1 \mathrm{d}\lambda \int \mathrm{d}\boldsymbol{r}\mathrm{d}\boldsymbol{r'} \, \frac{n^{\mathrm{p}}(\boldsymbol{r}) n_0^{\mathrm{e}}(\boldsymbol{r'}) \left[g_{\mathrm{d}}\left(\boldsymbol{r},\boldsymbol{r'}, n^{\mathrm{p}}(\boldsymbol{r}), n^{\mathrm{e}}(\boldsymbol{r'}), \lambda\right) - 1\right]}{|\boldsymbol{r} - \boldsymbol{r'}|} \,, \tag{2.35}$$

where n_0^{e} denotes the electron density of a purely electronic system (without a positron present) [173]. The electron-positron interaction is switched on by the integration from $\lambda = 0$ to $\lambda = 1$. This arises from a coupling constant integration, a general tool used in perturbation theories.

Approximations

In the **Weighted Density Approximation (WDA)** [169] and the limit $n^{\mathrm{p}}(\boldsymbol{r}) \to 0$ the displaced charge pair-correlation function g_{d} [168] is replaced by the pair-correlation function of a homogeneous system $g_{\mathrm{d}}^{\mathrm{h}}$

$$g_{\mathrm{d}}\left(\boldsymbol{r},\boldsymbol{r'},n^{\mathrm{p}}(\boldsymbol{r}),n^{\mathrm{e}}(\boldsymbol{r'}),\lambda\right) \to g_{\mathrm{d}}^{\mathrm{h}}\left(|\boldsymbol{r}-\boldsymbol{r'}|,\tilde{n}^{\mathrm{p}}(r)\to 0,\tilde{n}^{\mathrm{e}}(r'),\lambda\right) . \tag{2.36}$$

The tilde character marks weighted densities, defined by obeying the sum rule

$$\int_0^1 \mathrm{d}\lambda \int \mathrm{d}\boldsymbol{r'}\, n_0^{\mathrm{e}}(\boldsymbol{r'}) \left[g_{\mathrm{d}}^{\mathrm{h}}\left(|\boldsymbol{r}-\boldsymbol{r'}|,\tilde{n}^{\mathrm{p}}(r)\to 0,\tilde{n}^{\mathrm{e}}(r'),\lambda\right) - 1 \right] = 1 . \tag{2.37}$$

The $g_{\mathrm{d}}^{\mathrm{h}}$ has a compact analytical form [172, 173]

$$g_{\mathrm{d}}^{\mathrm{h}}\left(|\boldsymbol{r}-\boldsymbol{r'}|,\tilde{n}^{\mathrm{p}}(r)\to 0,\tilde{n}^{\mathrm{e}}(r'),\lambda\right) = \frac{\lambda^3 \exp\left(\frac{-\lambda|\boldsymbol{r}-\boldsymbol{r'}|}{a(\tilde{n}^{\mathrm{e}}(r'))}\right)}{8\pi\left[a(\tilde{n}^{\mathrm{e}}(r'))\right]^3 \tilde{n}^{\mathrm{e}}(r')} + 1 \tag{2.38}$$

$$a(x) = (1+41.87x)^{-\frac{1}{3}} . \tag{2.39}$$

Decoupling the KS equations

With those two approximations (i.e. $n^{\mathrm{p}}(\boldsymbol{r}) \to 0$ and the WDA) the Kohn-Sham equations 'decouple' (in the sense, that they do not dynamically influence each other) to

$$\text{electrons: } \left\{ -\nabla^2 + V_{\mathrm{ext}}(\boldsymbol{r}) + V_{\mathrm{H}}^{\mathrm{e}}\left(\boldsymbol{r},[n^{\mathrm{e}}(\boldsymbol{r})]\right) + \frac{\delta E_{\mathrm{xc}}[n^{\mathrm{e}}(\boldsymbol{r})]}{\delta n^{\mathrm{e}}(\boldsymbol{r})} \right\} \Psi_j^{\mathrm{e}}(\boldsymbol{r}) = \epsilon_j^{\mathrm{e}} \Psi_j^{\mathrm{e}}(\boldsymbol{r}) \tag{2.40}$$

$$\begin{aligned}\text{positron: } \Big\{ &-\nabla^2 - V_{\mathrm{ext}}(\boldsymbol{r}) - V_{\mathrm{H}}^{\mathrm{e}}\left(\boldsymbol{r},[n^{\mathrm{e}}(\boldsymbol{r})]\right) + \frac{\delta E_{\mathrm{xc}}[n^{\mathrm{p}}(\boldsymbol{r})]}{\delta n^{\mathrm{p}}(\boldsymbol{r})} \\ &+ \epsilon_{\mathrm{c}}^{\mathrm{ep}}\left(\boldsymbol{r},[n^{\mathrm{e}}(\boldsymbol{r}),n^{\mathrm{p}}(\boldsymbol{r})]\right) \Big\} \Psi_j^{\mathrm{p}}(\boldsymbol{r}) = \epsilon_j^{\mathrm{p}} \Psi_j^{\mathrm{p}}(\boldsymbol{r})\end{aligned} \tag{2.41}$$

with

$$V_{\mathrm{H}}^{\mathrm{e}}\left(\boldsymbol{r},[n^{\mathrm{e}}(\boldsymbol{r})]\right) = \int \mathrm{d}\boldsymbol{r'} \frac{n^{\mathrm{e}}(\boldsymbol{r'})}{|\boldsymbol{r}-\boldsymbol{r'}|} \tag{2.42}$$

$$\epsilon_{\mathrm{c}}^{\mathrm{ep}}\left(\boldsymbol{r},[n^{\mathrm{e}}(\boldsymbol{r}),n^{\mathrm{p}}(\boldsymbol{r})]\right) = -\int_0^1 \mathrm{d}\lambda \int \mathrm{d}\boldsymbol{r'} \frac{n_0^{\mathrm{e}}(\boldsymbol{r'}) \left[g_{\mathrm{d}}^{\mathrm{h}}\left(|\boldsymbol{r}-\boldsymbol{r'}|,\tilde{n}^{\mathrm{p}}(r)\to 0,\tilde{n}^{\mathrm{e}}(r'),\lambda\right) - 1 \right]}{|\boldsymbol{r}-\boldsymbol{r'}|} . \tag{2.43}$$

Two-component DFT scheme

Equation (2.40) is now independent of the positron density. For this reason it is solved first, and equation (2.41) can be solved after inserting the electron density from the previous equation. The decoupled Kohn-Sham equations are in general solved in momentum space. The positron density is calculated under the assumption that the positron is in its ground state, i.e. $\mu \equiv (j,\boldsymbol{k}) = (0,0)$.

TPMD Based on the static electron and positron densities the electron-positron interaction is reintroduced by the so called enhancement factor γ (compare [126,129] and section 3.1). With the electron-positron annihilation condition $\boldsymbol{r}^{\mathrm{e}} = \boldsymbol{r}^{\mathrm{p}} = \boldsymbol{r}$ (compare subsection 3.2.1) the two-photon momentum density is given as

$$\rho^{2\gamma}(\boldsymbol{p}) = \sum_{\mathrm{occ.}(j,\boldsymbol{k})} \left| \int \mathrm{d}\boldsymbol{r}\, e^{-i\boldsymbol{p}\boldsymbol{r}} \psi^{\mathrm{e}}_{j,\boldsymbol{k}}(\boldsymbol{r}) \psi^{\mathrm{p}}_{0}(\boldsymbol{r}) \sqrt{\gamma_{j,\boldsymbol{k};0}(\boldsymbol{r},\boldsymbol{r})} \right|^2 . \tag{2.44}$$

This allows to calculate ACAR spectra from the electron and the positron wave functions, obtained by the eigenstates of the secular equation (2.19).

Part II.

Methods to Analyze the Annihilation Spectra

3. Lock-Crisp-West Back-folding

3.1. Momentum Densities

Agenda

This section gives a qualitative overview of the different momentum dependent densities, relevant for this work. While their physical interpretation is pointed out here, a mathematical description can be found in subsection 3.2.1.

ECMD

The **Electron Crystal Momentum Distribution (ECMD)** $n(\boldsymbol{k})$ is a fundamental quantity in condensed matter physics. When integrated over a small interval, $n(\boldsymbol{k})\,\mathrm{d}\boldsymbol{k}$ is the number of electrons per unit cell within this crystal momentum range. The $n(\boldsymbol{k})$ consists of individual contributions from each band j

$$n(\boldsymbol{k}) = \sum_j n_j(\boldsymbol{k})\,. \tag{3.1}$$

At zero temperature $n(\boldsymbol{k})$ has only integer values, as

$$n_j(\boldsymbol{k}) = \begin{cases} 1 \text{ if occupied} \\ 0 \text{ if unoccupied}\,. \end{cases} \tag{3.2}$$

The Fermi surface separates volumes of $n(\boldsymbol{k})$ containing a different number of filled bands. Completely filled bands increase the value of $n(\boldsymbol{k})$ by 1 for all $\boldsymbol{k}$-points in the BZ. They are often not taken into account, as the focus is (in general) on identifying the Fermi surface by steps in $n(\boldsymbol{k})$.

EMD

The Fourier components of the electron density in real space $n(\boldsymbol{r})$ are called **Electron Momentum Distribution (EMD)** $\rho(\boldsymbol{p})$. The $n(\boldsymbol{k})$ can be constructed out of $\rho(\boldsymbol{p})$ by the **Lock-Crisp-West (LCW)** theorem (see subsection 3.2.1). The $\rho(\boldsymbol{p})$ has its highest intensity around the central region ($\boldsymbol{p} \approx 0$) and decays with a power law at large momenta [46, 50, 52].
As becomes clear with equation (3.35), $\rho(\boldsymbol{p})$ has steps at the mirror images of the Fermi surface centered around all reciprocal lattice vectors. The summation of all mirror images results in the Fermi surface steps of $n(\boldsymbol{k})$.
There is a qualitative difference between contributions from valance bands and from core states. As core states are more localized in real space, they more broadly distributed in momentum space. Hence, the large momenta region of $\rho(\boldsymbol{p})$ is dominated by core state contributions [37].

Symmetry selection rules

Along different symmetry directions electron bands with a certain irreducible representation can not contribute to $\rho(\boldsymbol{p})$. This leads to a set of **symmetry selection**

rules [75, 77], making it possible to assign contributions to $\rho(\boldsymbol{p})$ along those lines to a certain subset of bands.

Momentum limits

The limits $p \approx 0$ and $p \gg 0$ of $\rho_j(\boldsymbol{p})$ can be calculated in an atomic orbital ansatz and depend on the band character. In leading order we find [48, 50]

$$\lim_{p\to 0} \rho(p) \propto |p^l|^2 \tag{3.3}$$

$$\lim_{p\gg 0} \rho(p) \propto |p^{-l-4}|^2 \,. \tag{3.4}$$

with azimuthal quantum number l. So, in the region of low momenta $\rho(p)$ bands with d- and f-character are suppressed, due to the large exponent $\rho_\mathrm{d}(p \to 0) \propto p^4$ and $\rho_\mathrm{f}(p \to 0) \propto p^6$ (compare Mijnarends in [47]). Hence, Fermi signatures from those bands are not expected to be found in this region. At large momenta bands with d- and f-character, again, contribute less intensity to $\rho(p)$. For reasons of normalization (compare equation (3.8)) the signal of those bands is found in the intermediate momenta regime. Typical intermediate values are $p \approx 2\,\mathrm{a.u.}$ (compare for instance [49]), but the validity of the atomic orbital ansatz depends on the investigated system and is more justified for tightly bound core states than for valance states.

Positron influences

In 2D-ACAR experiments the **Two-Photon Momentum Distribution (TPMD)** $\rho^{2\gamma}(p_x,p_y)$ is measured. This corresponds to $\rho(p_x,p_y)$, but additionally takes positron related influences into account. Dependent on the used approximation, this includes a product of the electron wave function with the positron wave function and an interaction term (enhancement), for details see equation (3.11). The LCW theorem can be used to derive the **Two-Photon Crystal Momentum Distribution (TPCMD)** $n^{2\gamma}(k_x,k_y)$ from $\rho^{2\gamma}(p_x,p_y)$, in analogy to the purely electronic case. Again, Fermi surface signature can be identified by kinks in the back-folded spectrum $n^{2\gamma}(k_x,k_y)$. The positron related effects even emphasize those kinks [126].

Properties

As the core electrons are localized in the positively charged ion environment, it is less likely for them to annihilate with a positron [45]. The ratio of those annihilation probabilities is system dependent. In [131] ratios between 2 for chromium and 13 for aluminum were reported. Based on the fact, that the positron wave function suppresses large momentum contributions, the core contributions are more distorted than the valance contributions. As they do not yield any information about the Fermi surface, in general core contributions are removed from the measured spectra (for example by energy filters on an experimental level or by tail fitting on a data processing level).

The large momenta asymptotic behavior of $\rho^{2\gamma}(\boldsymbol{p})$ (a detailed description can be found in [51]) is smaller compared to $\rho(\boldsymbol{p})$, as the positron wave function decays with increasing momentum modulus as well. In general $\rho^{2\gamma}(\boldsymbol{p})$ is assumed to decay exponentially, but due to the finite size of the detectors in the experimental setup of ACAR and the low counting rates, this is not systematically investigated.

The symmetry selection rules for $\rho(\boldsymbol{p})$, apply for $\rho^{2\gamma}(\boldsymbol{p})$ as well, under the assumption that the positron ground state is Γ_1 symmetric [76, 77]. This symmetry is given in the cubic groups [78], but can be broken, for example by vacancies [79].

When referring commonly to $\rho^{(2\gamma)} \equiv \{\rho, \rho^{2\gamma}\}$ or $n^{(2\gamma)} \equiv \{n, n^{2\gamma}\}$, we call those **Generalized Momentum Densities (GMDs)**. We summarize those, due to their commonalities. For instance all four quantities have steps at the position of the Fermi surface (or its mirror images). Generalized momentum densities

Such a clear distinction is usually not made between ρ, $\rho^{2\gamma}$, $\rho^{(2\gamma)}$, n, $n^{2\gamma}$, $n^{(2\gamma)}$ and GMDs (compare also page 5), so deviating expressions can be found in literature. Due to the focus of this work on the LCW theorem, a clear notation is necessary.

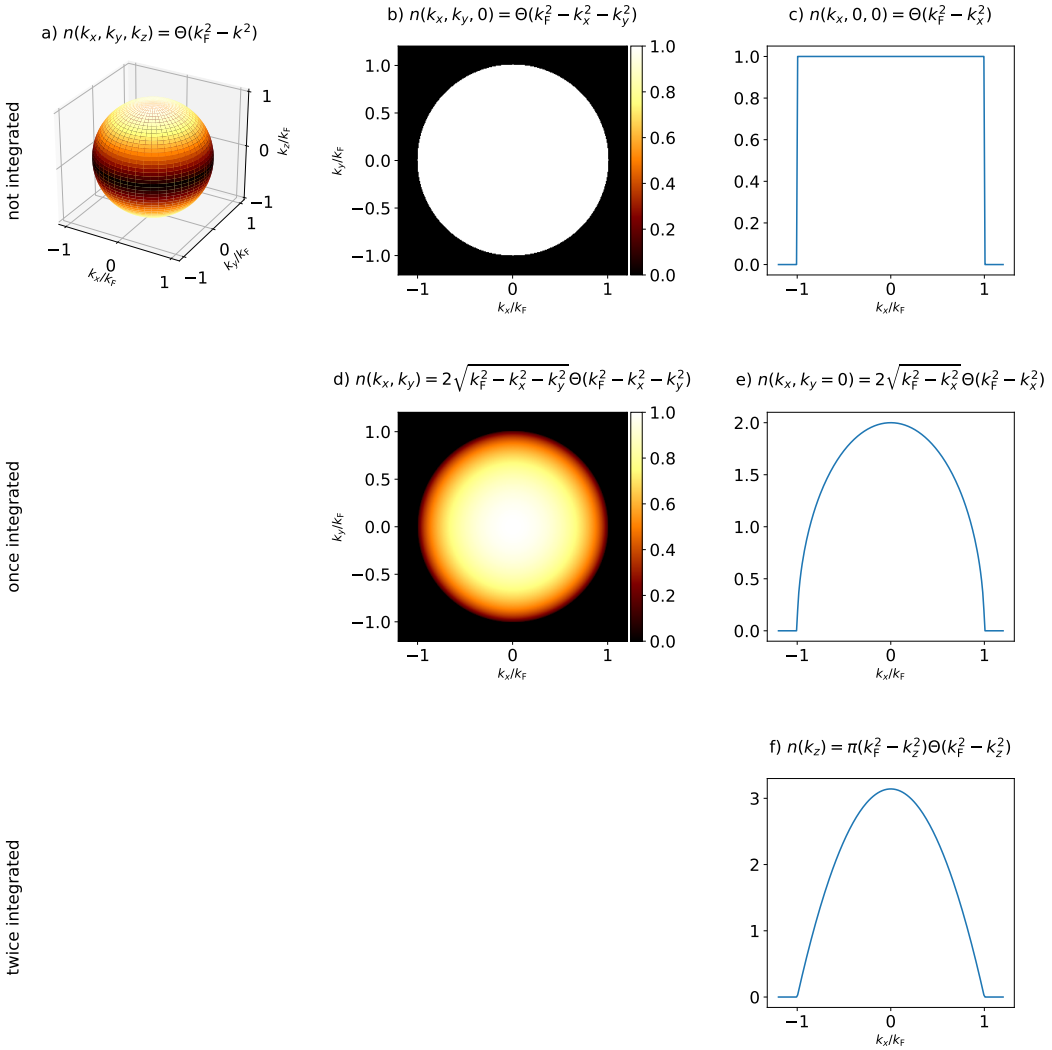

Figure 3.1.: Illustrative example of $n(\boldsymbol{k})$, integrated $n(\boldsymbol{k})$ and cuts through $n(\boldsymbol{k})$ in one to three dimensions for a Fermi sphere. The color values in the middle column and the y-values in the right column are given in multiples of $n^{\mathrm{e}}_{\mathrm{val}} / \frac{4\pi}{3} k_{\mathrm{F}}^3$, compare normalization convention (3.10).

In the scope of this work, we will refer to different momentum integrated versions of the GMDs. The used notation shall be illustrated at the example of a free electron gas in figure 3.1. Notation

Subplot a shows the complete three-dimensional representation of the Fermi sphere

$n(\boldsymbol{k})$ or $n(k_x,k_y,k_z)$. Values inside the sphere are $n_{\mathrm{val}}^{\mathrm{e}}/\,\frac{4\pi}{3}k_{\mathrm{F}}^3$, the others are 0. The coloring corresponds to subplot d for illustrative purposes.
It is sometimes useful to investigate cuts through GMDs, which can be either by a plane or along a line. Subplot b and c show cuts through the Fermi sphere at $k_z = 0$ and along the k_x axis.
As 2D-ACAR measurements can only resolve two momentum components, we introduce a shorthand notation for the integration over momentum components

$$n^{(2\gamma)}(k_x,k_y) \equiv \int \mathrm{d}k_z \; n^{(2\gamma)}(k_x,k_y,k_z) \tag{3.5}$$

$$n^{(2\gamma)}(k_z) \equiv \int \mathrm{d}k_x \mathrm{d}k_y \; n^{(2\gamma)}(k_x,k_y,k_z)\,. \tag{3.6}$$

The once and twice integrated examples can be found in figure 3.1 d and f. In the context of ACAR and Compton scattering the integration is also called **projection**.
Figure 3.1e shows the once integrated spectrum $n(k_x,k_y)$ along a path in $\boldsymbol{k}$-space (here the k_x-axis). This representation makes it easier to identify kinks, as identifying them from a color gradient is difficult. In the scope of this work we will mainly refer to once integrated spectra and cuts through them (figure 3.1 d and e).

Fermi surface signatures

Due to the integration of the momentum component p_z, the Fermi surface step (subplots b and c) reduces to a kink (subplots d and e). By following $n^{(2\gamma)}(k_x,k_y)$ along a certain path $\boldsymbol{k}_{\mathrm{path}}(\lambda)$, a kink is found at λ, if there exists at least one point $\mathcal{P}$, which is projected onto $\boldsymbol{k}_{\mathrm{path}}(\lambda)$ and with the normal of the Fermi surface $\boldsymbol{n}_{\mathrm{Fermi}}$ at this point being parallel to the direction along the path

$$\lim_{\lambda' \overset{<}{\to} \lambda} \frac{\partial n^{(2\gamma)}\left(\boldsymbol{k}_{\mathrm{path}}(\lambda')\right)}{\partial \lambda'} \neq \lim_{\lambda' \overset{>}{\to} \lambda} \frac{\partial n^{(2\gamma)}\left(\boldsymbol{k}_{\mathrm{path}}(\lambda')\right)}{\partial \lambda'}$$

$$\Leftrightarrow$$

$$\exists \mathcal{P} \in \mathrm{FS} : \; \mathcal{P} - \boldsymbol{k}_{\mathrm{path}}(\lambda) \parallel \hat{k}_z \quad \wedge \quad \frac{\mathrm{d}\boldsymbol{k}_{\mathrm{path}}(\lambda)}{\mathrm{d}\lambda} \parallel \boldsymbol{n}_{\mathrm{Fermi}}(\mathcal{P})\,. \tag{3.7}$$

For brevity we call this a **kink**. Subplot e gives thereby an easier access (by eye) to determine the position of the Fermi surface.

Disturbing issues

The task to identify Fermi surface signatures becomes more challenging under the following influences:

- smooth $\boldsymbol{k}$-dependent modulation of $n_j^{2\gamma}(\boldsymbol{k})$ (positron influences, figure 3.2),
- experimental counting noise (compare subsection 1.2.3),
- experimental resolution (compare subsection 1.2.2) and
- the finite momentum spacing of $\rho(p_x,p_y)$ (compare subsection 1.2.2).

Normalization

The normalization condition of $n(\boldsymbol{k})$ is given as

$$\sum_{\boldsymbol{k}\in 1.\mathrm{BZ}} n(\boldsymbol{k}) = n^{\mathrm{e}}\,, \tag{3.8}$$

with n^{e} the number of electrons per unit cell. Ignoring core states, we arrive at a slightly modified version of the normalization condition

$$\sum_{\boldsymbol{k}\in 1.\mathrm{BZ}} n(\boldsymbol{k}) = n^{\mathrm{e}}_{\mathrm{val}}\,, \tag{3.9}$$

with $n^{\mathrm{e}}_{\mathrm{val}}$ valence electrons per unit cell.

Normalization convention

In the case of $\rho^{2\gamma}(\boldsymbol{p})$ and $n^{2\gamma}(\boldsymbol{k})$ the normalization conditions (3.8) and (3.9) do not hold anymore. This is due to the overlap of the electron with the positron wave function (from an independent particle perspective) and due to the different annihilation probabilities of valance and core states. For simplicity and to be able to compare GMDs among each other, we will normalize all GMDs to one

$$\begin{aligned}\int \mathrm{d}p_x\mathrm{d}p_y\, \rho^{(2\gamma)}(p_x,p_y) &= 1\\ \int_{\mathrm{VP}} \mathrm{d}k_x\mathrm{d}k_y\, n^{(2\gamma)}(k_x,k_y) &= 1\,,\end{aligned} \tag{3.10}$$

where the **Voronoi Plaquette (VP)** denotes a specific irreducible symmetry unit of the periodic $n^{(2\gamma)}(k_x,k_y)$. A more detailed introduction of the VP is given later in section 4.1.

Enhancement

The electron and the positron are in general described by a common electron-positron wave function

$$\psi^{\mathrm{ep}}_{j,\boldsymbol{k}}\,(\boldsymbol{r}^{\mathrm{e}},\boldsymbol{r}^{\mathrm{p}}) = \psi^{\mathrm{e}}_{j,\boldsymbol{k}}(\boldsymbol{r}^{\mathrm{e}})\psi^{\mathrm{p}}_{\mu}(\boldsymbol{r}^{\mathrm{p}})\sqrt{\gamma_{j,\boldsymbol{k};\mu}(\boldsymbol{r}^{\mathrm{e}},\boldsymbol{r}^{\mathrm{p}})}\,. \tag{3.11}$$

The factor γ thereby describes the electron-positron **enhancement** [124–129], coming from the electron-positron interaction. The exact description of enhancement is under continuous investigation and different approximations are made, usually omitting one or more of the arguments $\{j,\boldsymbol{k},\mu,\boldsymbol{r}^{\mathrm{e}},\boldsymbol{r}^{\mathrm{p}}\}$ [130–134].
We want to give a simplified picture, describing the electron-positron interaction: *The positron will induce a cloud of electrons around it. These are mainly electrons close to the Fermi level, due to their higher mobility. Besides an increased annihilation probability for those electrons, this means, that the electronic structure of the material is mainly affected around the Fermi level.*
Enhancement generally leads to an increase in $n^{2\gamma}(\boldsymbol{p})$ (compared to $n(\boldsymbol{p})$) directly below the Fermi level. The intensity of $n^{2\gamma}$ at lower momenta is hence reduced by normalization. This tendency can be seen very clearly in model systems, for instance in the homogeneous electron gas results of Drummond (see figure 2 bottom in [133]).[1]

[1] Drummond's results have to be transfered to our case of a periodic potential. The crucial commonality is, that at zero temperature electron momenta are limited to the Fermi momentum k_{F}.

IPM In this context, the **Independent Particle Model (IPM)** or **Independent Particle Approximation (IPA)** assumes $\gamma_{j,\boldsymbol{k};\mu}(\boldsymbol{r}^{\mathrm{e}},\boldsymbol{r}^{\mathrm{p}}) = 1$, meaning that the electron and the positron wave function factorize in real space and do not influence each other dynamically (compare equation (2.44)). The IPM is a sever approximation and is used to separate positron effect, which originate from the positron wave function, from positron effects, due to enhancement. The IPM explains why the experimental setup is insensitive to the contributions from some areas in real space, where the positron wave function has a low amplitude.

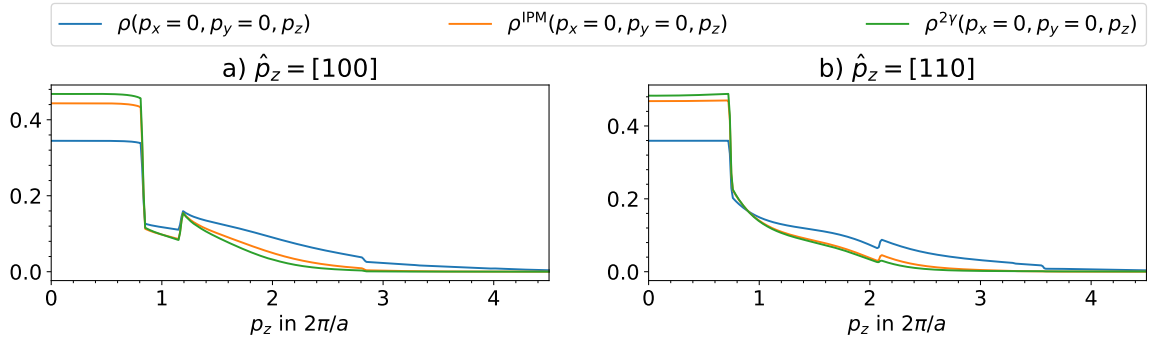

Figure 3.2.: Positron effects in silver along different directions:
The major positron effect is an increase of intensity at small momenta in $\rho(\boldsymbol{p})$. Additional enhancement effects can be seen in subplot a at $p = 1.2\,\frac{2\pi}{a}$ and in subplot b at $p = 0.8\,\frac{2\pi}{a}$. The corresponding $n(k_x,k_y)$, $n^{\mathrm{IPM}}(k_x,k_y)$ and $n^{2\gamma}(k_x,k_y)$ can be found in figure 5.5.

Lattice effects Lattice effects lead to deviations from Drummond's simple picture, as seen in the results for silver in figure 3.2. The most significant change from $\rho \to \rho^{\mathrm{IPM}} \to \rho^{2\gamma}$ is the shift of spectral weight to lower momenta.
When analyzing the influence of taking the positron wave function into account, i.e. considering ρ^{IPM} instead of ρ, large momenta are suppressed. This is due to the low amplitude of the positron expansion coefficients for high momenta. Because of normalization, the intensity at low momenta increases.
Note: It is thereby a tempting misconception to argue: The $\Psi^{\mathrm{p}}(p \gg 0)$ *is small, hence* $\rho^{\mathrm{IPM}}(p \gg 0) = |\Psi^{\mathrm{p}}(p \gg 0)|^2 \cdot |\Psi^{\mathrm{e}}(p \gg 0)|^2$ *(wrong!) is suppressed. This argument is based on the wrong equation above, which (nevertheless) often leads to qualitatively right results. The electron-positron wave function product can only be calculated in real space.*
Our argument is based on equations (3.30) *and* (3.35)*, where the positron expansion coefficients* $A_{\boldsymbol{G_2}}$ *determines the amplitude of* ρ^{IPM}*.*
When including enhancement $\rho^{\mathrm{IPM}} \to \rho^{2\gamma}$, the higher positron density in between the ions induces an increase in the electron density there. This means a more uniform distribution in real space, corresponding to an additional localization in momentum space.
An increase of intensity below the Fermi surface (as in Drummond's data) can be seen

in figure 3.2a at $p = 1.2\,\frac{2\pi}{a}$ and in figure 3.2b at $p = 0.8\,\frac{2\pi}{a}$ (considering the shift in spectral weight to lower densities).

3.2. Lock-Crisp-West Theorem

Concept

In ACAR spectroscopy photons are measured, which contain information about the momentum distribution of the electrons within a crystal. The momentum of those photons is not limited to the first Brillouin zone, but can take any value of $\boldsymbol{p} \in \mathbb{R}^3$. The number of photons detected at a certain momentum $\rho^{2\gamma}(p_x,p_y)$ is proportional to the Fourier components of $n^{2\gamma}(\boldsymbol{r})$ (integrated along the p_z-component). The Lock-Crisp-West theorem [80] relates $\rho^{2\gamma}(\boldsymbol{p})$ to the electron momentum distribution in crystal momentum space $n^{2\gamma}(\boldsymbol{k})$. By setting the positron wave function to a constant in the following proof, a simplified version of the LCW theorem is derived, relating $\rho(\boldsymbol{p})$ with $n(\boldsymbol{k})$ (see also appendix A).

Original proof

Originally [80] the LCW theorem was shown in an one-dimensional version within an one-particle picture, the independent particle approximation and a spatially constant positron wave function. Also the approximate validity for a non-constant positron wave function was discussed. We will prove the LCW theorem in a more general formulation and discuss these cases separately.

3.2.1. Proof

Definitions

Electron-positron wave function

As pointed out earlier, the electron-positron wave function is given as

$$\langle \boldsymbol{r}^{\mathrm{e}},\boldsymbol{r}^{\mathrm{p}}|\psi^{\mathrm{ep}}_{j,\boldsymbol{k};\mu}\rangle = \psi^{\mathrm{e}}_{j,\boldsymbol{k}}(\boldsymbol{r}^{\mathrm{e}})\psi^{\mathrm{p}}_{\mu}(\boldsymbol{r}^{\mathrm{p}})\sqrt{\gamma_{j,\boldsymbol{k};\mu}(\boldsymbol{r}^{\mathrm{e}},\boldsymbol{r}^{\mathrm{p}})} \tag{3.12}$$

The tuple $(j,\boldsymbol{k})$ thereby refers to the Bloch state representation of the electron. For completeness, we want to point out its Fourier transformed explicitly

$$\langle \boldsymbol{p}^{\mathrm{e}},\boldsymbol{p}^{\mathrm{p}}|\psi^{\mathrm{ep}}_{j,\boldsymbol{k};\mu}\rangle = \int \mathrm{d}\boldsymbol{r}^{\mathrm{e}}\mathrm{d}\boldsymbol{r}^{\mathrm{p}}\, e^{-i\boldsymbol{p}^{\mathrm{e}}\boldsymbol{r}^{\mathrm{e}}-i\boldsymbol{p}^{\mathrm{p}}\boldsymbol{r}^{\mathrm{p}}}\langle \boldsymbol{r}^{\mathrm{e}},\boldsymbol{r}^{\mathrm{p}}|\psi^{\mathrm{ep}}_{j,\boldsymbol{k};\mu}\rangle\,. \tag{3.13}$$

Annihilation condition

For the annihilation process to take place, the electron and the positron need to meet at the same spatial point $\boldsymbol{r}$. We therefore introduce the **pair representation** of the electron-positron wave function

$$\langle \boldsymbol{r}|\tilde{\psi}^{\mathrm{ep}}_{j,\boldsymbol{k},\mu}\rangle \equiv \langle \boldsymbol{r},\boldsymbol{r}|\psi^{\mathrm{ep}}_{j,\boldsymbol{k},\mu}\rangle\,. \tag{3.14}$$

As one spatial degree of freedom is removed by the annihilation condition, the consequence is, that the momenta of electron and positron sum up to the pair momentum $\boldsymbol{p}^{\mathrm{ep}} = \boldsymbol{p}^{\mathrm{e}} + \boldsymbol{p}^{\mathrm{p}}$. This is illustrated by the following equation

$$\langle \boldsymbol{p}^{\mathrm{e}},\boldsymbol{p}^{\mathrm{p}}|\boldsymbol{r},\boldsymbol{r}\rangle = e^{-i\boldsymbol{p}^{\mathrm{e}}\boldsymbol{r}-i\boldsymbol{p}^{\mathrm{p}}\boldsymbol{r}} = e^{-i(\boldsymbol{p}^{\mathrm{e}}+\boldsymbol{p}^{\mathrm{p}})\boldsymbol{r}} = \langle \boldsymbol{p}^{\mathrm{e}}+\boldsymbol{p}^{\mathrm{p}},0|\boldsymbol{r},\boldsymbol{r}\rangle = \ldots = \langle 0,\boldsymbol{p}^{\mathrm{e}}+\boldsymbol{p}^{\mathrm{p}}|\boldsymbol{r},\boldsymbol{r}\rangle\,. \tag{3.15}$$

The pair wave function in momentum representation, hence writes

$$\langle \boldsymbol{p}^{\mathrm{e}}, \boldsymbol{p}^{\mathrm{p}} | \psi^{\mathrm{ep}}_{j,\boldsymbol{k};\mu} \rangle \Big|_{\substack{\boldsymbol{r}^{\mathrm{e}}=\boldsymbol{r} \\ \boldsymbol{r}^{\mathrm{p}}=\boldsymbol{r}}} = \int \mathrm{d}\boldsymbol{r} \langle \boldsymbol{p}^{\mathrm{e}}, \boldsymbol{p}^{\mathrm{p}} | \boldsymbol{r}, \boldsymbol{r} \rangle \langle \boldsymbol{r}, \boldsymbol{r} | \psi^{\mathrm{ep}}_{j,\boldsymbol{k};\mu} \rangle \tag{3.16}$$

$$= \int \mathrm{d}\boldsymbol{r} e^{-i(\boldsymbol{p}^{\mathrm{e}}+\boldsymbol{p}^{\mathrm{p}})\boldsymbol{r}} \langle \boldsymbol{r} | \tilde{\psi}^{\mathrm{ep}}_{j,\boldsymbol{k},\mu} \rangle \equiv \langle \boldsymbol{p}^{\mathrm{ep}} | \tilde{\psi}^{\mathrm{ep}}_{j,\boldsymbol{k},\mu} \rangle \,. \tag{3.17}$$

Ansatz

An electron-positron pair operator is represented in second quantized form by Two-particle operator

$$\hat{\mathcal{A}}^{\mathrm{ep}} = \sum_{\mu_1,\mu_2} \sum_{\boldsymbol{k_1},\boldsymbol{k_2}} \sum_{j_1,j_2} \langle \psi^{\mathrm{ep}}_{j_1,\boldsymbol{k_1};\mu_1} | \hat{\mathcal{A}}^{\mathrm{ep}} | \psi^{\mathrm{ep}}_{j_2,\boldsymbol{k_2};\mu_2} \rangle \; \hat{a}^{\dagger}_{j_1,\boldsymbol{k_1}} \hat{b}^{\dagger}_{\mu_1} \, \hat{b}_{\mu_2} \hat{a}_{j_2,\boldsymbol{k_2}} \tag{3.18}$$

where $\hat{a}^{\dagger}_{\dots}$/ $\hat{a}_{\dots}$ and $\hat{b}^{\dagger}_{\dots}$/ $\hat{b}_{\dots}$ are the creation/annihilation operators for an electron and a positron.

The TPMD is expressed as TPMD

$$\rho^{2\gamma}(\boldsymbol{p}) = \langle \Omega | \hat{\rho}^{2\gamma}_{\boldsymbol{p}} | \Omega \rangle \,. \tag{3.19}$$

where $|\Omega\rangle$ is the **pair ground state**. The operator $\hat{\rho}^{2\gamma}_{\boldsymbol{p}}$ is given in its second quantized representation

$$\hat{\rho}^{2\gamma}_{\boldsymbol{p}} = \sum_{\mu_1,\mu_2} \sum_{\boldsymbol{k_1},\boldsymbol{k_2}} \sum_{j_1,j_2} \langle \psi^{\mathrm{ep}}_{j_1,\boldsymbol{k_1};\mu_1} | \left(\frac{1}{(2\pi)^3} \int \mathrm{d}\boldsymbol{r}^{\mathrm{e}} \mathrm{d}\boldsymbol{r}^{\mathrm{p}} \, | \boldsymbol{r}^{\mathrm{p}}, \boldsymbol{r}^{\mathrm{e}} \rangle \delta(\boldsymbol{r}^{\mathrm{e}} - \boldsymbol{r}^{\mathrm{p}}) \langle \boldsymbol{r}^{\mathrm{e}}, \boldsymbol{r}^{\mathrm{p}} | \right)$$
$$\times \left(\sum_{\boldsymbol{p}^{\mathrm{e}},\boldsymbol{p}^{\mathrm{p}}} | \boldsymbol{p}^{\mathrm{p}}, \boldsymbol{p}^{\mathrm{e}} \rangle \delta_{\boldsymbol{p}^{\mathrm{e}}+\boldsymbol{p}^{\mathrm{p}},\boldsymbol{p}} \langle \boldsymbol{p}^{\mathrm{e}}, \boldsymbol{p}^{\mathrm{p}} | \right) | \psi^{\mathrm{ep}}_{j_2,\boldsymbol{k_2};\mu_2} \rangle \; \hat{a}^{\dagger}_{j_1,\boldsymbol{k_1}} \hat{b}^{\dagger}_{\mu_1} \, \hat{b}_{\mu_2} \hat{a}_{j_2,\boldsymbol{k_2}} \tag{3.20}$$

and measures the spatial overlap from electron-positron pair products with pair momentum $\boldsymbol{p}$. With equation (3.17) this simplifies to matrix elements, which are diagonal with respect to the pair momentum

$$\rho^{2\gamma}(\boldsymbol{p}^{\mathrm{ep}}) = \langle \Omega | \sum_{\mu_1,\mu_2} \sum_{\boldsymbol{k_1},\boldsymbol{k_2}} \sum_{j_1,j_2} \langle \tilde{\psi}^{\mathrm{ep}}_{j_1,\boldsymbol{k_1};\mu_1} | \boldsymbol{p}^{\mathrm{ep}} \rangle \langle \boldsymbol{p}^{\mathrm{ep}} | \tilde{\psi}^{\mathrm{ep}}_{j_2,\boldsymbol{k_2};\mu_2} \rangle \; \hat{a}^{\dagger}_{j_1,\boldsymbol{k_1}} \hat{b}^{\dagger}_{\mu_1} \, \hat{b}_{\mu_2} \hat{a}_{j_2,\boldsymbol{k_2}} \; | \Omega \rangle \tag{3.21}$$

Approximation

We use the IPM for further simplification. By setting $\gamma_{j,\boldsymbol{k};\mu}(\boldsymbol{r}^{\mathrm{e}}, \boldsymbol{r}^{\mathrm{p}}) = 1$, equation (3.12) reduces to IPM

$$\langle \boldsymbol{r}^{\mathrm{e}}, \boldsymbol{r}^{\mathrm{p}} | \psi^{\mathrm{ep}}_{j,\boldsymbol{k};\mu} \rangle \overset{\mathrm{IPM}}{\rightarrow} \langle \boldsymbol{r}^{\mathrm{e}} | \psi^{\mathrm{e}}_{j,\boldsymbol{k}} \rangle \langle \boldsymbol{r}^{\mathrm{p}} | \psi^{\mathrm{p}}_{\mu} \rangle \,. \tag{3.22}$$

This implies, that the pair ground state of the system Ω can be expressed as a product of the Fermi sea $|\Omega_{\mathrm{F}}\rangle$ and the positron state $|\Omega_{\mathrm{P}}\rangle$

$$|\Omega\rangle = |\Omega_{\mathrm{P}}\rangle \cdot |\Omega_{\mathrm{F}}\rangle \,. \tag{3.23}$$

The positron is assumed to be thermalized to its ground state $\mu = 0$

$$|\Omega_{\mathrm{P}}\rangle = \hat{b}_0^\dagger |0\rangle \,. \tag{3.24}$$

Hence, the expectation value with respect to Ω in equation (3.21) simplifies to

$$\langle\Omega|\hat{a}^\dagger_{j_1,\boldsymbol{k_1}}\hat{b}^\dagger_{\mu_1}\,\hat{a}_{j_2,\boldsymbol{k_2}}\hat{b}_{\mu_2}|\Omega\rangle = \langle\Omega_{\mathrm{P}}|\hat{b}^\dagger_{\mu_1}\,\hat{b}_{\mu_2}|\Omega_{\mathrm{P}}\rangle\,\langle\Omega_{\mathrm{F}}|\hat{a}^\dagger_{j_1,\boldsymbol{k_1}}\hat{a}_{j_2,\boldsymbol{k_2}}|\Omega_{\mathrm{F}}\rangle \tag{3.25}$$

$$= \delta_{\mu_1,0}\delta_{\mu_2,0}\,\langle\Omega_{\mathrm{F}}|\hat{a}^\dagger_{j_1,\boldsymbol{k_1}}\hat{a}_{j_2,\boldsymbol{k_2}}|\Omega_{\mathrm{F}}\rangle \,. \tag{3.26}$$

Bloch expansion

To simplify the $\langle\tilde{\psi}^{\mathrm{ep}}_{j_1,\boldsymbol{k_1};\mu_1}|\boldsymbol{p}^{\mathrm{ep}}\rangle\langle\boldsymbol{p}^{\mathrm{ep}}|\tilde{\psi}^{\mathrm{ep}}_{j_2,\boldsymbol{k_2};\mu_2}\rangle$-term in equation (3.21), we independently expand the electron and the positron wave function by Bloch's theorem into

$$\langle\boldsymbol{r}|\psi^{\mathrm{e}}_{j,\boldsymbol{k}}\rangle = \sum_{\boldsymbol{G_1}} \frac{B_{j,\boldsymbol{G_1}+\boldsymbol{k}}}{(2\pi)^3} e^{i(\boldsymbol{G_1}+\boldsymbol{k})\boldsymbol{r}} \tag{3.27}$$

$$\langle\boldsymbol{r}|\psi^{\mathrm{p}}_{\mu=0}\rangle = \sum_{\boldsymbol{G_2}} \frac{A_{\boldsymbol{G_2}}}{(2\pi)^3} e^{i\boldsymbol{G_2}\boldsymbol{r}} \,, \tag{3.28}$$

where the summation $\sum_{\boldsymbol{G}_{...}}$ is performed over all reciprocal lattice vectors $\boldsymbol{G}_{...}$.
As the electron-positron wave function is chosen as a simple product state in the IPM, it can be expressed in terms of Fourier coefficients as

$$\langle\boldsymbol{r},\boldsymbol{r}|\psi^{\mathrm{ep}}_{j,\boldsymbol{k}}\rangle = \langle\boldsymbol{r}|\psi^{\mathrm{e}}_{j,\boldsymbol{k}}\rangle\langle\boldsymbol{r}|\psi^{\mathrm{p}}_{0}\rangle = \sum_{\boldsymbol{G}} \frac{C^{\mathrm{ep}}_{j,\boldsymbol{G}+\boldsymbol{k}}}{(2\pi)^3} e^{i(\boldsymbol{G}+\boldsymbol{k})\boldsymbol{r}} \tag{3.29}$$

$$C^{\mathrm{ep}}_{j,\boldsymbol{G}+\boldsymbol{k}} = \sum_{\boldsymbol{G'}} \frac{A_{\boldsymbol{G'}} B_{j,\boldsymbol{G}+\boldsymbol{k}-\boldsymbol{G'}}}{(2\pi)^3} \,, \tag{3.30}$$

where the substitutions $\boldsymbol{G} = \boldsymbol{G_1} + \boldsymbol{G_2}$ and $\boldsymbol{G'} = \boldsymbol{G_2}$ were used. Even though $\Psi^{\mathrm{ep}}_{j,\boldsymbol{k}}$ has a Bloch (similar) form, the coefficients $C^{\mathrm{ep}}_{j,\boldsymbol{k}}$ are not normalized. The momentum representation follows as

$$\langle\boldsymbol{p}^{\mathrm{ep}}|\tilde{\psi}^{\mathrm{ep}}_{j,\boldsymbol{k}}\rangle \equiv \int \mathrm{d}\boldsymbol{r} e^{-i\boldsymbol{p}^{\mathrm{ep}}\boldsymbol{r}} \langle\boldsymbol{r},\boldsymbol{r}|\psi^{\mathrm{ep}}_{j,\boldsymbol{k}}\rangle = \sum_{\boldsymbol{G}} C^{\mathrm{ep}}_{j,\boldsymbol{G}+\boldsymbol{k}} \delta_{\boldsymbol{G}+\boldsymbol{k},\boldsymbol{p}^{\mathrm{ep}}} \,. \tag{3.31}$$

With equations (3.26) and (3.31) equation (3.21) simplifies to

$$\rho^{2\gamma}(\boldsymbol{p}^{\mathrm{ep}}) \approx \rho^{\mathrm{IPM}}(\boldsymbol{p}^{\mathrm{ep}}) = \sum_{\boldsymbol{G_1},\boldsymbol{G_2}} \sum_{\boldsymbol{k_1},\boldsymbol{k_2}} \sum_{j_1,j_2} C^{\mathrm{ep}}_{j_1,\boldsymbol{G_1}+\boldsymbol{k_1}} \delta_{\boldsymbol{p}^{\mathrm{ep}},\boldsymbol{G_1}+\boldsymbol{k_1}}\; C^{\mathrm{ep}*}_{j_2,\boldsymbol{G_2}+\boldsymbol{k_2}} \delta_{\boldsymbol{p}^{\mathrm{ep}},\boldsymbol{G_2}+\boldsymbol{k_2}}$$
$$\times \langle\Omega_{\mathrm{F}}|\hat{a}^\dagger_{j_1,\boldsymbol{k_1}}\hat{a}_{j_2,\boldsymbol{k_2}}|\Omega_{\mathrm{F}}\rangle \,. \tag{3.32}$$

Theorem

Natural orbitals

The expectation value with respect to the Fermi sea can be diagonalized in the orbital index by using Löwdin's **natural spin-orbital representation** [139, 140]

$$\langle\Omega_{\mathrm{F}}|\hat{a}^\dagger_{j,\boldsymbol{k_1}}\hat{a}_{j',\boldsymbol{k_2}}|\Omega_{\mathrm{F}}\rangle = n_{j,\boldsymbol{k_1};j',\boldsymbol{k2}}\;\delta_{j,j'} \,. \tag{3.33}$$

Thereby j and j' are now natural spin-orbitals and $n_{j,\boldsymbol{k_1};j',\boldsymbol{k_2}}$ is the one-particle (electron) density matrix. The diagonal elements of $n_j(\boldsymbol{k}) \equiv n_{j,\boldsymbol{k};j,\boldsymbol{k}}$ are the occupation numbers of each state.

Because $\boldsymbol{k}_{...}$ denotes momenta of the first Brillouin zone and $\boldsymbol{G}_{...}$ reciprocal lattice vectors, the Kronecker deltas in equation (3.32) can be simplified by the relation Splitting momenta

$$\delta_{\boldsymbol{p},\boldsymbol{G_1}+\boldsymbol{k_1}} = \delta_{\boldsymbol{G_p},\boldsymbol{G_1}}\delta_{\boldsymbol{k_p},\boldsymbol{k_1}} \tag{3.34}$$

with $\boldsymbol{p} \equiv \boldsymbol{p}^{\mathrm{ep}} = \boldsymbol{G_p} + \boldsymbol{k_p}$.

This relation reduces the number of indices in the expression (3.32) drastically to Simplified TPMD

$$\rho^{2\gamma}(\boldsymbol{p}) \approx \rho^{\mathrm{IPM}}(\boldsymbol{p}) = \sum_j |C^{\mathrm{ep}}_{j,\boldsymbol{p}}|^2 \; n_j(\boldsymbol{k_p})\,. \tag{3.35}$$

The band-resolved occupation number $n_{j,\boldsymbol{k_p}}$ in this expression is periodic in $\boldsymbol{p}$ with the periodicity of the reciprocal lattice. It is responsible for the afore mentioned **mirror images** of the Fermi surface steps around the reciprocal lattice vectors, while the $|C^{\mathrm{ep}}_{j,\boldsymbol{p}}|^2$ determines the amplitude of $\rho^{2\gamma}(\boldsymbol{p})$ (and of the mirror steps).

With $n_{j,\boldsymbol{k_p}} = n_{j,\boldsymbol{k_{G+p}}}$ and by a shifted summation over all $\boldsymbol{G}$, we arrive at the most general form of the **Lock-Crisp-West theorem** [80]. For simplicity and to stick to the common notation, we skip the explicit indication of the IPM, such that we use the superscript '2Γ' instead of 'IPM'. Therefore the LCW theorem LCW

$$\sum_{\boldsymbol{G}} \rho^{2\gamma}(\boldsymbol{G}+\boldsymbol{p}) = \sum_j \sum_{\boldsymbol{G}} |C^{\mathrm{ep}}_{j,\boldsymbol{G}+\boldsymbol{k_p}}|^2 \; n_j(\boldsymbol{k_p}) \equiv \sum_j n_j^{2\gamma}(\boldsymbol{k_p}) \tag{3.36}$$

is only valid approximately. This can be seen as a 'recipe' to construct the $n^{2\gamma}(\boldsymbol{k})$ out of $\rho^{2\gamma}(\boldsymbol{p})$.

3.2.2. Simplifications of the LCW Theorem

Lock, Crisp and West showed [80] the approximate $\boldsymbol{k_p}$ independence of $|C^{\mathrm{ep}}_{j,\boldsymbol{G}+\boldsymbol{k_p}}|^2$ in a tight binding model. Rabou [81] however presented examples of realistic systems where $|C^{\mathrm{ep}}_{j,\boldsymbol{G}+\boldsymbol{k_p}}|^2$ changes significantly with $\boldsymbol{k_p}$. Smooth modulation

The implication of Rabou's finding is, that there might be cases with such a strong modulation of $|C^{\mathrm{ep}}_{j,\boldsymbol{G}+\boldsymbol{k_p}}|^2$, that this modulation might be mistaken as a FS step in $n^{2\gamma}$, as $n^{2\gamma}$ is only available on a discrete momentum mesh. This issue would appear in an even more subtle way in 2D-ACAR data, because of the p_z-integration.

In the context of this research no such cases were found. Also no further analyses of that issue were published since then. For that reason $|C^{\mathrm{ep}}_{j,\boldsymbol{G}+\boldsymbol{k_p}}|^2$ is in general assumed to be slowly varying in $\boldsymbol{k_p}$ [86].

No positron The expression of the LCW theorem can be simplified further by assuming a spatially constant positron wave function

$$\langle \boldsymbol{r}^{\mathrm{p}} | \psi^{\mathrm{p}} \rangle = \frac{1}{V_{\mathrm{BZ}}} \quad \Leftrightarrow \quad A_{\boldsymbol{G_2}=0} = \frac{(2\pi)^3}{V_{\mathrm{BZ}}} \wedge A_{\boldsymbol{G_2}\neq 0} = 0 \tag{3.37}$$

$$\Rightarrow \quad C^{\mathrm{ep}}_{j,\boldsymbol{G}+\boldsymbol{k_p}} = B_{j,\boldsymbol{G}+\boldsymbol{k_p}} \,, \tag{3.38}$$

i.e. $\rho^{2\gamma} \rightarrow \rho$. In this approximation the normalization condition of the Fourier coefficients $\sum\limits_{\boldsymbol{G}} |B_{j,\boldsymbol{G}+\boldsymbol{k_p}}|^2 = 1$ removes all positron related influences

$$\sum_{\boldsymbol{G}} \rho(\boldsymbol{G}+\boldsymbol{p}) = \sum_{j} n_j(\boldsymbol{k_p}) \,. \tag{3.39}$$

This result is also valid for Compton scattering, where no positron is present at all.

Prefactor The $\rho^{(2\gamma)}(p_x,p_y)$ is only recorded statistically in ACAR and Compton spectroscopy. Therefore, it is only possible to determine this quantity up to a prefactor, which has to be determined by the normalization condition (3.10).

2D-LCW For 2D-ACAR spectroscopy, the LCW theorem finds its application in a two-dimensional version (**2D-LCW**)

$$\sum_{(G_x,G_y)} \rho^{2\gamma}(G_x+p_x,G_y+p_y) = \sum_{j} n_j^{2\gamma}(k_{p,x},k_{p,y}) \,. \tag{3.40}$$

The summation over $\boldsymbol{G}$ is reduced to a summation of the x-y-projection (G_x,G_y) of each reciprocal lattice vectors. This corresponds to a summation over a projected lattice, where all reciprocal lattice vectors are shifted along the p_z direction into the p_x-p_y-plane.
We will present a numerical implementation for the 2D-LCW theorem in the next chapter.

3.2.3. Comments on the LCW Theorem

Approximations In the following, we explicitly want to point out the assumptions used in the proof of the LCW theorem:

- Independent particle model, equation (3.22):
  The expression of the electron-positron wave function product as a simple product of the separate wave function is a serious approximation. In general the positron wave function will be influenced strongly by the electron cloud. In contrast to that, the positron will modify the electron cloud only in its direct vicinity.

- Bloch's theorem, [135–137]:
  Bloch's theorem is applied to the electron and the positron wave function independently.

Electrons: While independent-particle type models fulfill the precondition for Bloch's theorem (i.e. a periodic potential), this is not the case for systems with strong electron-electron interaction. From the perspective of one electron, the potential induced by the other electrons will not be periodic, as the surrounding electrons will show a reduced density in the vicinity of the electron under consideration.
Positron: The same is true for a screening cloud of electrons, which is expected to form around the positron and which violates the precondition of a periodic potential also in this case. This effect can only be considered beyond the independent particle approximation.

Besides these strict mathematical assumption, there are a few more assumptions included, referring to the experimental setup.

Further disturbing effects

- Periodicity of the lattice:
  The crystal lattice is assumed to be perfect and clean (again for the Bloch's theorem to hold). Of course, this is an assumption as well. The strong influence on the positron state by vacancies is exploited in positron lifetime spectroscopy (compare subsection 1.3.2)

- Finite temperature:
  At finite temperatures thermalized positrons are in energetically higher states, than the ground state. The additional momentum from the positron leads to a smearing of the measured $\rho^{2\gamma}$ spectrum. This smearing is approximately isotropic and is hence modeled by folding $\rho^{2\gamma}(\boldsymbol{p})$ with a Gaussian.

- High positron density:
  The following considerations refer to much higher positron densities than currently possible.[2] As the proof of the LCW theorem is completely based on an **one positron assumption**. We want to discuss briefly possible implications that could occur in future experiments.
  a) Distortion of the lattice: The added positively charged cloud increases the lattice constant. As the reciprocal lattice vectors $\boldsymbol{G}$ change accordingly, this effect should be considered in the summation over $\boldsymbol{G}$ in the LCW theorem.
  b) Modification of the electronic structure: While the influence of one positron on the electronic structure can still be modeled by an enhancement factor, positrons at a higher density might alter the system under investigation qualitatively. In an extreme case a high density of positrons could even introduce a positron sublattice between the ion positions and thereby create a completely different physical system.
  c) Positron ground state: As there are multiple positrons in the probe, simultaneously, also energetically higher states are occupied (Pauli principle). This means, that the assumption of the positron to be in its ground state is no fulfilled for all annihilation events. Similar to the case of finite temperatures, this leads to

[2] The currently realizable maximum number of positrons in a probe is 0.1, meaning one positron over a tenth of the time (for details compare section 1.3.1). As the capacities of modern positron sources continuously increases [101,102], 'high positron density effects' might contribute at a certain point.

non-zero momentum contribution $\boldsymbol{p}^{\mathrm{p}}$ from the positron to the electron-positron pair momentum.

History of LCW

After establishing the first 1D-ACAR experiment in 1950 [53], materials with a spherical Fermi surface were investigated [54, 56]. Soon the Fermi surface radius could be extracted from the measured spectra [54]. In a next step, copper gained attention, due to its spherical Fermi surface with additional neck features [55, 57, 59]. Cooper [35] pointed out very clearly the relation between the position of the Fermi surface and periodically appearing steps in the measured spectrum. By performing model calculations for lithium in an atomic (free electron) and in a lattice (Bloch waves) ansatz, he presented a pair of $\rho(\boldsymbol{p})$ and $n(\boldsymbol{k})$ for a simple system.
Inspired by those findings, Lock, Crisp and West proposed more then 20 years after the first 1D-ACAR experiment the LCW theorem. The confirming and preceding work of Berko [55] as well as the complementary work of Mijnarends [58] should be mentioned in the historic context as well.

Is the LCW theorem trivial?

As the construction 'recipe' of the LCW theorem is identical to the construction of the repeated zone scheme out of the extended zone scheme (for dispersion relations), the LCW theorem might appear trivial (especially considering its application in Compton scattering). The main difference is, that the reduced zone scheme is obtained by reducing the translational invariant solutions of the Schrödinger equation in momentum space to an irreducible zone. In contrast, the LCW theorem describes the construction of $n^{2\gamma}(\boldsymbol{k})$ from the electron-positron annihilation spectrum. Even though the relation can be made a posteriori (within the approximation of a constant positron wave function), in the pioneering research of ACAR and Compton scattering the LCW theorem was not obvious.
Before the novel interpretation of 1D-ACAR spectra gained by the LCW theorem, the common interpretation is best described with Murray's words [59]:
"Except for the effect of high Fourier components and core annihilations, an angular correlation measurement [...] essentially maps out cross-sectional areas of the occupied regions of k space in the first [Brillouin] zone."
In a mathematical formulation this writes

$$\rho^{2\gamma}(k_z) = \int \mathrm{d}k_x \mathrm{d}k_y \, n(\boldsymbol{k}). \qquad \lightning$$

This (wrong) formulation, indeed, can be used to find FS steps in the first BZ, but does not provide proper cross-sections of the Fermi volume.
People were close to the discovery of the LCW theorem for almost the complete time span since the first ACAR experiment. This can be seen from various publications [35, 55]. With the LCW theorem in mind, the reader can literally back-fold the given graphs of $\rho^{(2\gamma)}$ by eye, to construct $n^{(2\gamma)}$.

3.3. Momentum Density Related Operators

In this section we introduce some tools to analyze GMDs and their integrated versions. We will discuss their implementation and the information they reveal about the spectrum under consideration. Applications on realistic systems can be found in chapters 5,6 and 7. Agenda

Even though the application of some of the tools is not explicitly presented in this work (for example Canny edge detection [212]), they played an important role to identify situations of interest and getting an overview of the data under consideration. Application

3.3.1. Second Directional Derivative

We use the second directional derivative (SDD) to identify kinks in 2D-GMDs (i.e. one dimension is integrated over). The SDD is a standard quantity in computer science, especially in image processing. For generality we stick to the commonly used expressions, and denote the 2D-GMDs as **images** Purpose

$$I(x,y) \in \left\{\rho^{(2\gamma)}(p_x,p_y), n^{(2\gamma)}(k_x,k_y)\right\} . \tag{3.41}$$

The SDD measures the curvature of I along a certain path in the (x,y) plane. As the second derivatives diverges at kinks, this quantity will have extrema at the signatures of the Fermi surface.

The **directional derivative** of a multivariate function $f(\boldsymbol{x})$ along a direction $\boldsymbol{d}$ is mathematically defined as Definition

$$\mathcal{D}_{\boldsymbol{d}} f(\boldsymbol{x}) \equiv \lim_{h\to 0} \frac{f(\boldsymbol{x}+h\boldsymbol{d}) - f(\boldsymbol{x})}{h} . \tag{3.42}$$

The **Second Directional Derivative (SDD)** is the two-fold application of the directional derivative along the same direction.

$$\mathrm{SDD}_{\boldsymbol{d}}(I(x,y)) \equiv \mathcal{D}^2_{\boldsymbol{d}} I(x,y) \tag{3.43}$$

Applications can be found for instance in figures 5.3 and C.6. To derive a general expression for the SDD we define a straight path

$$\boldsymbol{r}(\lambda) \equiv (x(\lambda),y(\lambda)) = (x,y) + \lambda(d_x, d_y) \tag{3.44}$$

with $|(d_x,d_y)| = 1$ and parameterization λ. We calculate now the second derivative of I at the starting point of path $\boldsymbol{r}(\lambda)$

$$\mathcal{D}^2_{\boldsymbol{d}} I\,(x,y) \equiv \frac{\partial^2 I\,(\boldsymbol{r}(\lambda))}{\partial\lambda^2}\Big|_{\lambda=0} \tag{3.45}$$

$$= \frac{\partial}{\partial\lambda}\left(\frac{\partial I\,(\boldsymbol{r}(\lambda))}{\partial x(\lambda)}\frac{\partial x(\lambda)}{\partial\lambda} + \frac{\partial I\,(\boldsymbol{r}(\lambda))}{\partial y(\lambda)}\frac{\partial y(\lambda)}{\partial\lambda}\right)\Big|_{\lambda=0} \tag{3.46}$$

$$= \ldots = I_{xx}d_x^2 + 2I_{xy}d_xd_y + I_{yy}d_y^2 , \tag{3.47}$$

where the subscript x/y denotes the derivative in x/y direction. Higher order derivatives are denoted by multiple subscripts. The order, in which the derivatives are performed, is not relevant in this context.

$$I_x \equiv I_x(x,y) \equiv \frac{\partial I(x,y)}{\partial x} \tag{3.48}$$

$$I_{xy} \equiv (I_x)_y = I_{yx} \tag{3.49}$$

Special cases

Two cases are of special interest:

- The **Second Directional Derivative in normal direction (SDDn)** , calculated by $\mathcal{D}^2_{\boldsymbol{n}} I(x,y)$ with $\boldsymbol{n} = -\nabla I(x,y)/|\nabla I(x,y)|$.

- The **maximal Second Directional Derivative (SDDmax)**, calculated by $\max_\theta |\mathcal{D}^2_{\boldsymbol{d}(\theta)} I(x,y)|$ with $\boldsymbol{d} = (\cos\theta, \sin\theta)$.

The former is a popular quantity in the field of corner detection [211], [213] and especially in the context of zero crossing edge detectors [214]. The latter does not suffer from numerical instabilities at local extrema, and hence will turn out to be more useful in some cases (for example in figure 6.1, compare equation (6.4))

3.3.2. Canny Edge Detector

Advantages

The Canny edge detector [212] belongs to the class of Gaussian edge detectors and has a better signal-to-noise ratio compared to zero crossing edge detectors [214]. Its popularity and robustness make it easily applicable to ACAR data. Edge detection methods use techniques to follow edge signals in areas with a low edge intensity based on clear signals of the same edge in other areas. This feature can be an advantage and a disadvantage at the same time.

Disadvantages

There are two major disadvantages of using general edge detection methods in the context of Fermi surface detection.
First, these give only a discrete measure (in the sense of edge or no edge) at a certain point. For the application of Fermi surface detection, though, complex overlap patterns of different sheets can not be resolved. Due to the integration in one direction, different features show different edge intensities, depending on the shape of the Fermi volume.
Second, the definition of an edge is different in picture processing compared to the task of analyzing integrated momentum quantities. In picture processing, the edge is (roughly speaking) defined to be in the center of the area with the steepest descent. For Fermi surface detection however, the point of interest is the very end of this steep descent, where the curvature reaches a maximum.

Take home message

Canny edge detection is a complementary method to the SDD. The SDD reveals a more complex picture, leaving it to the analyst to distinguish the intensity of different features under consideration. The Canny edge detector, gives a good first impression on a new dataset within a simplified picture.

3.3.3. Cuts, Rotational Average and Anisotropy

The examples presented in the right column of figure 3.1 can be generalized to cuts along custom paths, as seen for instance in figure 5.3. A cut $I(k_{\text{path}})$ along a given path $\boldsymbol{k}_{\text{path}}(k_{\text{path}})$ through an image $I(x,y)$ is given in short notation as Cuts

$$I(k_{\text{path}}) \equiv I\left(\boldsymbol{k}_{\text{path}}(k_{\text{path}})\right) . \tag{3.50}$$

We always ensure, that paths resemble the same distance as given in the argument

$$\left| \frac{\partial \boldsymbol{k}_{\text{path}}(k_{\text{path}})}{\partial k_{\text{path}}} \right| = 1 . \tag{3.51}$$

The parameter k_{path} is in general chosen such, that the starting point of the path denotes the origin $\boldsymbol{k}_{\text{path}}(0) = (0,0)$, compare figure 5.4 paths (a) - (e). Exceptions are made to highlight certain symmetries as for paths (f) and (f') in figures 5.3 and 5.4, where $k_{\text{path}} = 0$ denotes the center of the VP edge.

The rotational average of a spectrum gives a measure, how fast it decays for large momenta. This can be used to estimate the intensity of LCW back-folding artifacts, as illustrated in section 4.2. As this analysis method applies only to $\rho(p_x,p_y)$ and $\rho^{2\gamma}(p_x,p_y)$, we do not use the abstract image notation I. The **rotational average** is given by Rotational average

$$\rho_{\circ}^{(2\gamma)}(p) = \frac{1}{2\pi} \int_0^{2\pi} \mathrm{d}\phi \, \rho_{\phi}^{(2\gamma)}(p) . \tag{3.52}$$

where $\rho_{\phi}^{(2\gamma)}(p)$ is the representation of $\rho^{(2\gamma)}$ in polar coordinates

$$\rho_{\phi}^{(2\gamma)}(p) = \rho^{(2\gamma)}\left(p\cos(\phi), p\sin(\phi)\right) . \tag{3.53}$$

The **Anisotropy** Anisotropy

$$\hat{\mathcal{A}}\,\rho^{(2\gamma)}(p_x,p_y) \equiv \frac{\rho^{(2\gamma)}(p_x,p_y) - \rho_{\circ}^{(2\gamma)}(\sqrt{p_x^2+p_y^2})}{\rho_{\circ}^{(2\gamma)}(p_x,p_y)} . \tag{3.54}$$

visualizes the signatures of the Fermi surface, by showing only deviations from the isotropic background, relative to the signal strength of the background. In this way a picture of the Fermi surface is extracted - even for larger momenta, where the signal-to-noise ratio is less favorable. The anisotropy can be used to evaluate the quality of a 2D-ACAR spectrum, even during the measurement process. Different definitions of the anisotropy of 2D-ACAR spectra are used in literature [72–74].

4. Lock-Crisp-West Theorem from a Numerical Perspective

In this chapter we will present the underlying difficulties in the implementation of 2D-LCW back-folding as presented in equation (3.40). Depending on the exact implementation, different kinds of artifacts are introduced by the back-folding process. We will characterize those artifacts and discuss strategies for artifact reduction. Agenda

4.1. Issues with a Numerical Implementation

The summation over all $\{(G_x,G_y)\}$ forms a regular pattern of projected points on the x-y plane. We call this pattern **projected lattice**. In subsection 4.3.2 we give a recipe, how a **primitive basis ($\boldsymbol{p_1}, \boldsymbol{p_2} \in \mathbb{R}^2$)** consisting of two vectors can be constructed to replicate the projected lattice $\{(G_x,G_y)\}$. For the purpose of this chapter, we reformulate equation (3.40) as Problem reduction

$$\sum_{n_1,n_2} \tilde{\rho}\left((k_x,k_y) + n_1\boldsymbol{p_1} + n_2\boldsymbol{p_2}\right) = \tilde{n}(k_x,k_y) \quad \text{with } n_1,n_2 \in \mathbb{Z}\,. \tag{4.1}$$

Here $\tilde{\rho}$ and $\tilde{n}$ denote 2D-GMDs $\rho^{(2\gamma)}(p_x,p_y)$ and $n^{(2\gamma)}(k_x,k_y)$ or more generally spoken, the two-dimensional input and output of the LCW algorithm. We use this notation so separate the implementation of equation (4.1) from the physical quantities used in the examples. Due to their specific definition, restricted to this chapter, we drop the arguments of $\tilde{\rho}$ and $\tilde{n}$ in the flowing text, when convenient.

As the summation runs over all points of the projected lattice, $\tilde{n}$ is by construction periodic in $\boldsymbol{k}$-space. It is therefore sufficient to consider only an irreducible plaquette in crystal momentum space. We introduce the **Voronoi Plaquette (VP)** around a point of the projected lattice (**projection point**) as the manifold of all (k_x,k_y)-points, which are closer to this projection point, than to any other.[1] In figure 4.1 we show different possible shapes of VPs. As the VP is defined by the projection points $\{(G_x,G_y)\}$, it can also be constructed in momentum space (p_x,p_y). Symmetry considerations

[1] The VP is the 'Brillouin zone' of the projected lattice. To avoid confusion with the Brillouin zone in three dimensions, we choose this more general wording. Two properties of the VP shall be pointed out here: 1) It is not possible to construct the VP out of a 2D-cut through the three dimensional Brillouin zone and vice versa. 2) The wording 'VP' instead of 'Brillouin zone' does not imply, that the projected lattice can be irregular.

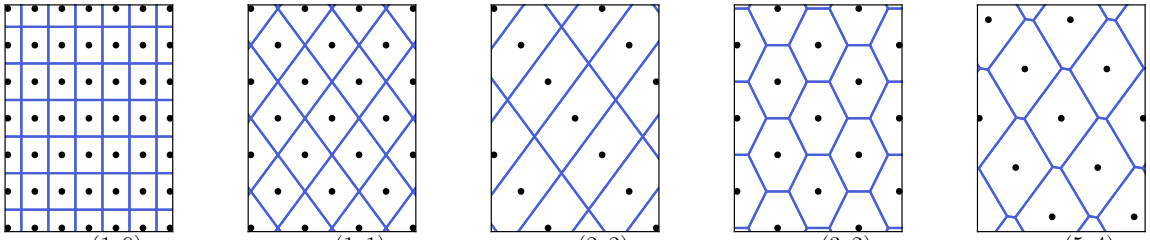

Figure 4.1.: Voronoi plaquette construction (blue lines) for different projection patterns (black dots).

Numerical issues

Coming back to equation (4.1), we observe two factors, which might lead to difficulties in a numerical implementation. These are the **finite resolution issue** and the **finite range issue**, as discussed in the following subsections:

4.1.1. Finite Resolution Issue

Discrete mesh

The finite resolution issue addresses the fact, that $\tilde{\rho}$ is only known on a discrete mesh. In general an interpolation becomes necessary, when trying to shift $\tilde{\rho}$ in equation (4.1) by a linear combination of $\boldsymbol{p_1}$ and $\boldsymbol{p_2}$, which is not an integer multiple of the momentum mesh spacing. As we will see in figure 4.2, the interpolation process blurs and shifts Fermi surface signatures.

Solution

The finite resolution issue can be circumvented by choosing the momentum mesh spacing of $\tilde{\rho}$ in both directions to be an integer multiple $\mathbb{N}$ of the greatest common divisor of all projection points (or of the constructing vectors $\boldsymbol{p_1}$ and $\boldsymbol{p_2}$)

$$\Delta p_{x/y} = \mathbb{N} \gcd\left(p_{1,x/y}, p_{2,x/y}\right) . \tag{4.2}$$

Effect of interpolation

If $\tilde{\rho}$ is not available in a suitable resolution, we interpolate to a suitable mesh before applying the back-folding algorithm. The result will be a smoothing and a shift of steps and kinks in the data, as illustrated in figure 4.2. As the original meshing does not capture the position of kinks exactly, this information can not be taken into account for the interpolation process.[2] Interpolation should therefore be avoided, whenever possible. A higher order interpolation was not used to avoid overshooting, which might lead for instance to negative $\tilde{\rho}$ values.[3]

[2] As mentioned already in subsection 3.2.2, it is not even possible to find out, if there is a kink at all between data points on a discrete mesh or, if the spectrum changes smoothly.

[3] An option, which might be interesting to investigate in future is to interpolate with Piecewise Cubic Hermite Interpolating Polynomials (PCHIP). This avoids overshooting, but has to be generalized to two-dimensions. Another custom designed interpolation scheme for integrated momentum densities is discussed in the outlook (part IV).

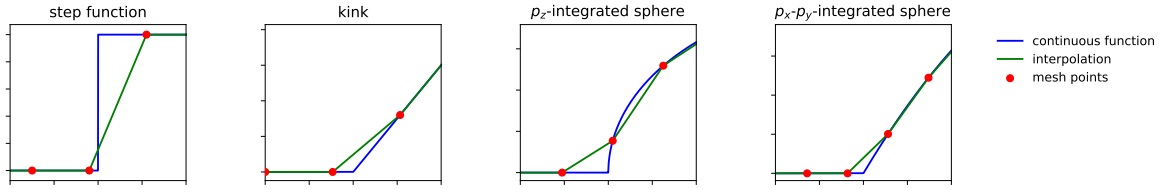

Figure 4.2.: Illustration of the smoothening of steps and kinks by interpolation: The blue line represents the original function, which is only known at discrete points (red circles). When using linear interpolation, the result will be points on the green line. The position of the step/kink will be shifted and the resulting curve will be smoother (in the sense of smaller values of the second numerical derivative).

4.1.2. Finite Range Issue

Truncation Artifacts

As $\tilde{\rho}$ is given on a limited rectangular momentum range, we define

$$-p_{x,max} \leq p_x \leq p_{x,\max} \tag{4.3}$$
$$-p_{y,max} \leq p_y \leq p_{y,\max} \tag{4.4}$$
$$p_{\max} = \min\left(p_{x,\max}, p_{y,\max}\right) . \tag{4.5}$$

The maximal momentum range $p_{\max}$ is thereby a measure of the amount of available information. It is (implicitly) assumed, that $\tilde{\rho}(p_x,p_y) = 0$ outside of this limited momentum range, when back-folding $\tilde{\rho}$ by equation (4.1). This introduces a step into $\tilde{n}$, where $\tilde{\rho}$ contributed finite values on the one side and zero on the other (compare figure 4.5 b and c). These steps can be mistaken as signatures of the Fermi surface. In subsection 4.2.1 back-folding methods are discussed, which introduce artificial kinks instead of artificial steps. We will refer to both, steps and kinks, as **truncation artifacts**.

Convex shape effect

Another consequence of the truncation issue is an induced change of shape by the information, which is not taken into account. Because the $\tilde{\rho}$ decays faster than linearly, the amount of lost intensity in the back-folded spectrum is larger at the boundaries of the VP than in the center. The result is a convex shape of $\tilde{n}$ (**convex shape effect**), which is stronger for small $p_{\max}$. It is a subtle question, how large the momentum region of $\tilde{\rho}$ has to be, to reduce the convex shape effect to a certain level. The answer depends on the crystal symmetry, the band structure of the investigated material and especially on the role of positron effects (wave function, enhancement). An estimate of the convex shape effect can be obtained, by comparing the back-folding result of the spectrum under consideration ($p_{\max} = p_1$) with the one from an extrapolated spectrum (compare subsection 4.2.2) ($p_{\max} = p_1 + \Delta$)

$$\tilde{n}(k_x,k_y)\Big|_{p_{\max}=p_1+\Delta} - \tilde{n}(k_x,k_y)\Big|_{p_{\max}=p_1} . \tag{4.6}$$

Applying the cutoff schemes, presented in subsection 4.2.1, on the two spectra $\tilde{\rho}\Big|_{p_{\max}=p_1(+\Delta)}$ before back-folding is thereby recommended, to reduce the artifact intensity. The extrapolation range Δ should be increased until some convergence (similar

to germanium in figure 6.1) is achieved in the equation above. An appropriate value for $p_1 + \Delta$ should be found at 15 a.u. for $\rho(p_x,p_y)$ and 6 a.u. for $\rho^{2\gamma}(p_x,p_y)$.

Following sections

Truncation artifacts and the convex shape effect always appear commonly in back-folded spectra and sometimes interfere with each other in an unpredictable way. For an example see the behavior of the circular cutoff scheme in the germanium benchmark (figures 6.1 and D.1). There exist concepts to overcome the implications of the finite range issue. While the effects of truncation artifacts can be reduced by cutoff schemes (compare subsection 4.2.1) extrapolation is used to compensate the convex shape effect (compare subsection 4.2.2).

4.1.3. Overview of back-folding Methods

Units

For simplicity we (mostly) drop the units $\frac{2\pi}{a}$, when referring to momentum coordinates in this chapter.

Motivation

As pointed out in section 3.1, the diameter of the Fermi surface is mapped onto the back-folded 2D-ACAR spectrum $n^{2\gamma}(k_x,k_y)$. In this chapter we will demonstrate the formation of **back-folding artifacts** using the experimental 2D-ACAR spectrum $\rho^{2\gamma}(p_x,p_y)$ of molybdenum (projected along the [110] direction) as an example.
Note: Back-folding artifacts are separated into two groups: Truncation artifacts (compare subsection 4.1.2) and extrapolation artifacts (compare subsection 4.2.2).

FS of molybdenum

To distinguish FS signatures from back-folding artifacts, we give an overview of the expected FS signatures in figure 4.3. We shift a discussion about the shape of the Fermi surface and an interpretation of our results to chapter 7. At this point we want to identify advantages and disadvantages of different back-folding methods.

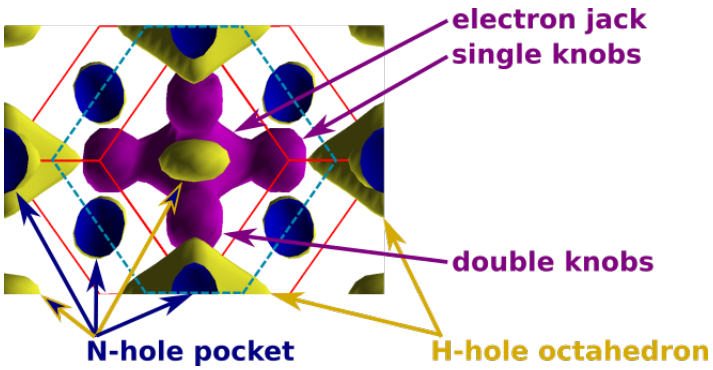

Figure 4.3.: Fermi surface of Mo along the [110] direction, Elk calculation:
Definition of Fermi surface features for the analysis of different back-folding methods. Red lines: Brillouin zone contours, blue dashed lines: Voronoi plaquette

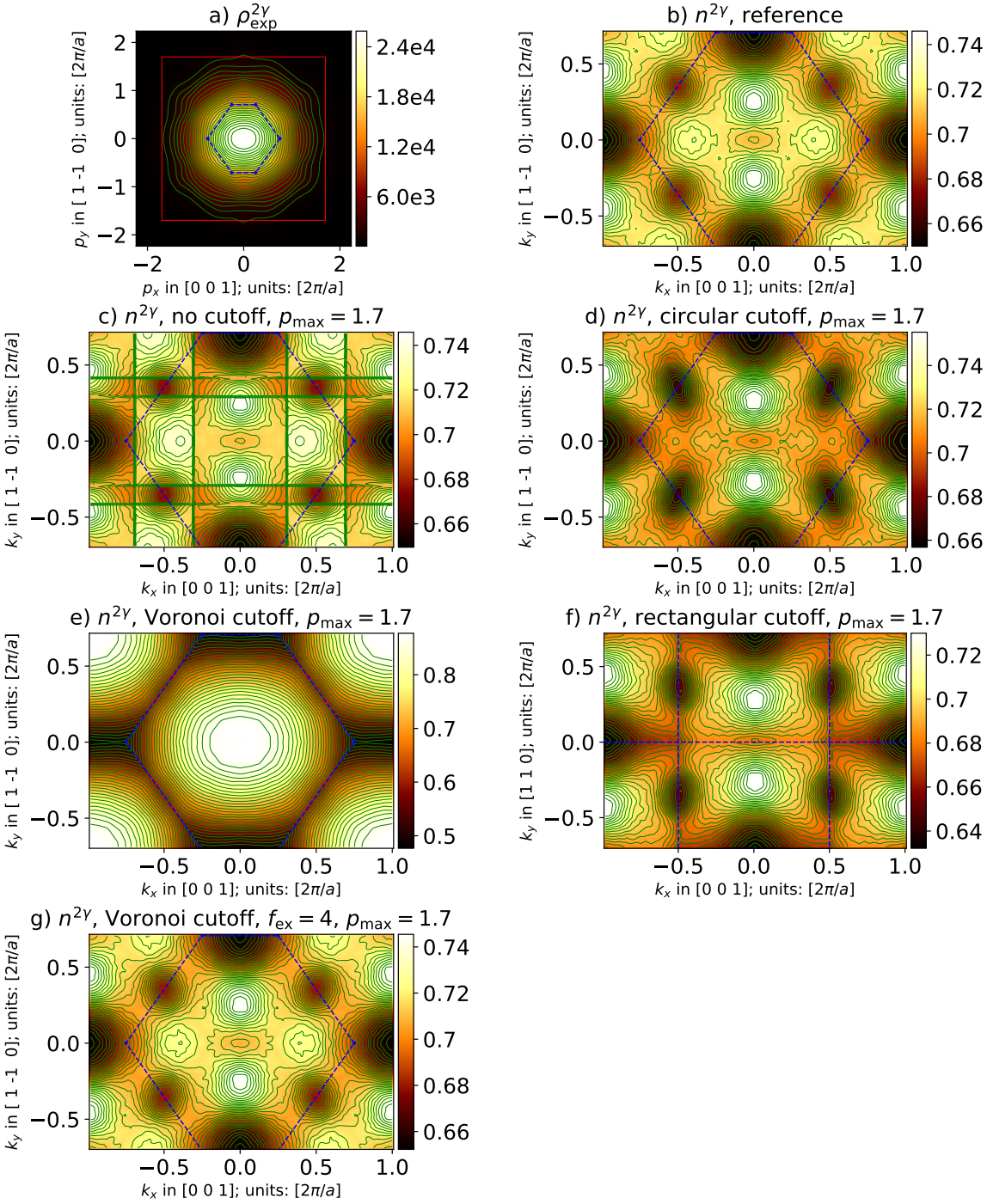

Figure 4.4.: Results for different cutoff methods in LCW back-folding applied on the experimental spectrum of molybdenum.
a) $\rho^{2\gamma}_{\mathrm{exp}}$ according to [203]. The red frame marks $\rho^{2\gamma}_{\mathrm{t1.7}}$.
b) Back-folding result of $\rho^{2\gamma}_{\mathrm{exp}}$. Different back-folding methods give similar results in this case (compare right column of figure B.1).
c-g) Result for back-folding $\rho^{2\gamma}_{\mathrm{t1.7}}$ with different methods, compare section 4.2.

Reference result

In figure 4.4a we present the experimental 2D-ACAR spectrum of molybdenum $\rho^{2\gamma}_{\text{exp}}(p_x,p_y)$ [203]. Commonly used back-folding methods show good agreement with each other, when applied on this dataset. An example is presented in subplot b and should be taken as a reference.

Back-folding methods

To evaluate the performance of different back-folding methods in figure 4.4 c-g, we apply these on a truncated version of $\rho^{2\gamma}_{\text{exp}}$ with $p_{\max} = 1.7$ (denoted $\rho^{2\gamma}_{\text{t1.7}}$ and indicated by the red frame in subplot a). This additional truncation leads to strong method specific deviations from the reference for currently used back-folding methods (subplots c-f). The origin of those deviations will become clear during the discussion of cutoff procedures in subsection 4.2.1.
Subplot g shows the application of a set of newly developed methods on the same truncated spectrum. We see an excellent agreement with the reference, clearly outperforming the currently used methods. The concepts in use to achieve this result will be presented in section 4.2.

No cutoff

In figure 4.4c a naive implementation of equation (4.1) without any cutoff scheme is shown. We see, that this is similar to the reference, but heavily corrupted by horizontal and vertical edges. The rectangular areas in between are shifted among each other in intensity. We can still identify the main structures, but the shape of the N-pockets ($k_x = \pm 0.5, k_y = \pm 0.3$) and the single knobs of the electron jack ($k_x = 0.4$; $k_y = 0$) are heavily distorted.

Circular cutoff

Subplot d shows the result of the circular cutoff. This is in less agreement with the reference but does not include the rectangular artifact pattern. The 4 projections of the eight N-hole pockets ($k_x = \pm 0.5, k_y = \pm 0.3$) are oriented in the wrong direction. Further the projection of the two N-hole pockets at the origin ($k_x = 0, k_y = 0$) is too small and the double knob structure ($k_x = 0, k_y = \pm 0.25$) is slightly overemphasized. This cutoff scheme is one of the schemes currently in use to perform LCW back-folding, for instance in [71, 73].

Voronoi cutoff

The Voronoi cutoff in subplot e shows by far the worst agreement with the reference. None of the features is reproduced. This scheme was newly developed in the context of this work and is the favorable cutoff in case of large $p_{\max}$, while performing poor for small $p_{\max}$. A more detailed illustration will follow in sections 4.2.1 and 6.2.

Rectangular cutoff

The result of the rectangular cutoff, presented in subplot f, is dominated by horizontal ($k_y = 0, \pm \frac{1}{\sqrt{2}}$) and vertical ($k_x = \pm 0.5$) lines. In contrast to subplot c these lines are not step functions but kinks. This leads to a heavy distortion of most signatures: The N-hole pockets point in vertical direction; the single electron knobs are vanished; and the H-hole octahedron ($k_x = \pm 1$; $k_y = 0$ and $k_x = 0$; $k_y = \pm \frac{1}{\sqrt{2}}$) is too spiky in horizontal direction. For a reason explained in subsection 4.2.1, a different irreducible plaquette than the VP is used here. This cutoff scheme is the other one currently in use to perform LCW back-folding, for example in [203].

Voronoi and extrapolation

In subplot g we present the combination of the newly developed extrapolation technique for 2D-ACAR with the Voronoi cutoff. This combination successfully circumvents truncation artifacts and the convex shape effect. The result is in much better agreement with the reference compared to any other method. Only slight deviations can be observed comparing the N-hole pocket projection at the origin.

Conclusion

It might be surprising, that common LCW back-folding methods perform so poorly in our example. The truncation of $\rho^{2\gamma}_{\text{exp}}$ to such a small p_{max} however, is a serious implication and is usually not given for experimental data. This extreme example illustrates two points:
1) The general structure of back-folding artifacts. We can use this information to critically review other results in ACAR spectroscopy with larger p_{max} and hence less intense back-folding artifacts (see for example figure B.1).
2) It is possible to obtain a reasonable $\tilde{n}$ from far less data (i.e. smaller p_{max} and hence less experimental counts) than expected. This is useful for analyzing noisy ACAR spectra, while simultaneously opening the path to reduced measurement times and more precise results.

4.2. Concepts to Overcome Numerical Issues

4.2.1. Cutoff Schemes

Overview

It is a common strategy for avoiding the formation of sharp edges in $\tilde{n}$ (and hence for improving the result of back-folding), to apply a cutoff on $\tilde{\rho}$. The mechanism behind the formation of those edges will be illustrated under the key word 'no cutoff'. Further, we will explain the underlying concepts of the circular cutoff, the rectangular cutoff and the Voronoi cutoff.

No Cutoff

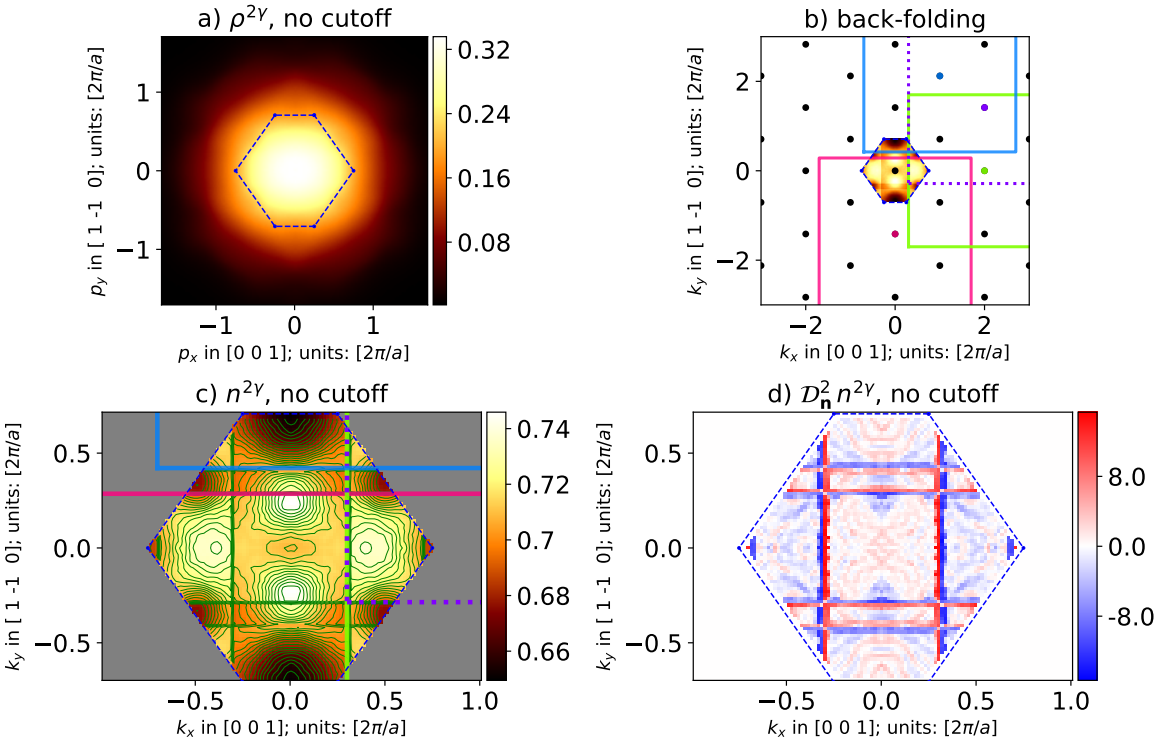

Figure 4.5.: Artifact formation for molybdenum, no cutoff, compare figure 4.4c:
a) shows the input ($p_{\max} = 1.7\frac{2\pi}{a}$) with the corresponding Voronoi plaquette.
b) shows the construction of $n^{2\gamma}$, where the input is replicated to all points of the projected lattice (black dots). The resulting boundary positions for a few examples are shown as the colored lines, passing through the Voronoi plaquette.
c) is a closeup of the Voronoi plaquette in subplot b with added contour lines.
d) is the SDDn of subplot c, showing the FS signatures and back-folding artifacts.

Reminder edge formation

As pointed out already in subsections 4.1.2 and 4.1.3, the direct application of equation (4.1) generates horizontal and vertical steps. They correspond to the boundaries of $\rho^{2\gamma}$, where known data points with finite values are separated from the unknown part of $\rho^{2\gamma}$

(set to zero). The formation of the sharp edges is shown in figure 4.5. We see clearly that all steps in $n^{2\gamma}$ correspond to the boundaries of $\rho^{2\gamma}$ centered around a projection point.

As we can see in figure B.1 a and b, the truncation artifacts get weaker but remain clearly visible with increasing $p_{\max}$. From experience, the truncation artifacts from this method are not obvious for $p_{\max} \geq 3.0\,\text{a.u.}$ in ACAR data (corresponding to $2.9\,\frac{2\pi}{a}$ for molybdenum). In section 6.2 we analyze this systematically and find, that using any of the following cutoff scheme, reduces the intensity of truncation artifacts by an order of magnitude. Evaluation

Circular Cutoff

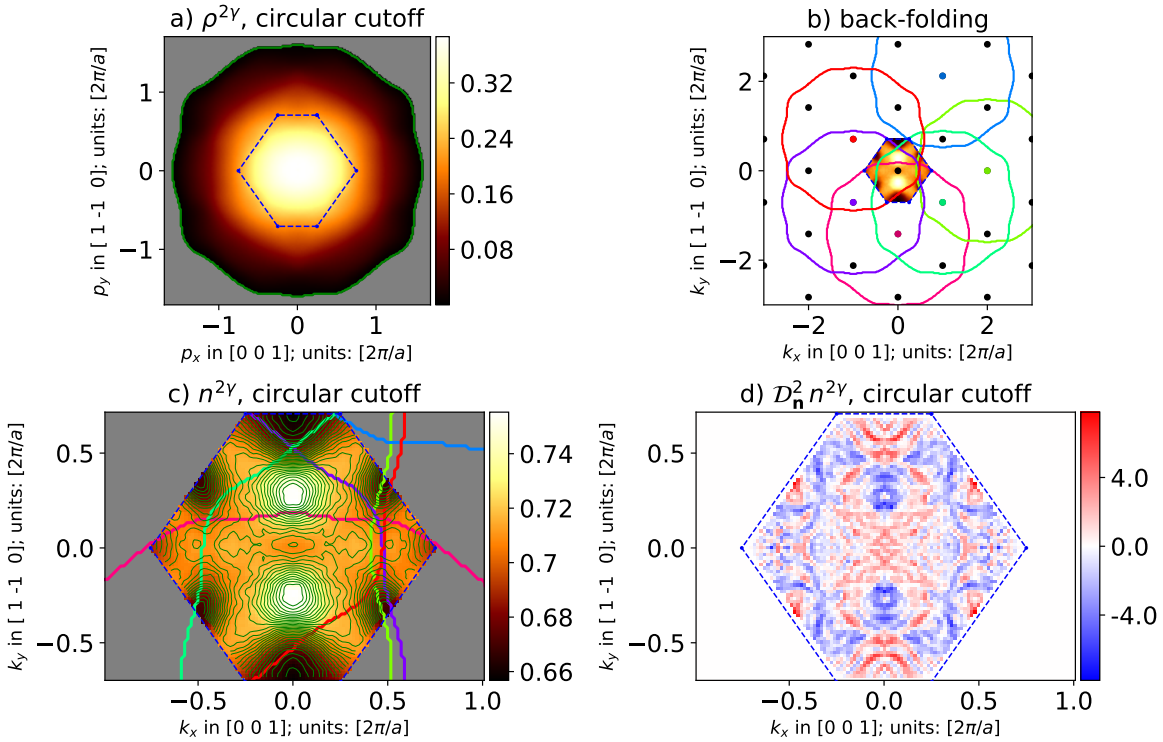

Figure 4.6.: Artifact formation for molybdenum, circular cutoff, compare figure 4.4d:
a) shows the input ($p_{\max} = 1.7\frac{2\pi}{a}$) with the corresponding Voronoi plaquette. The gray area represents the data points, which were replaced by zero by applying the cutoff.
b) shows the construction of $n^{2\gamma}$, where the input is replicated to all points of the projected lattice (dot pattern). Some truncation artifacts, introduced in the VP during the back-folding process, are pointed out as colored lines.
c) is a closeup of the Voronoi plaquette in subplot b with added contour lines.
d) is the SDDn of subplot c, showing the FS signatures and back-folding artifacts.

To perform the circular cutoff, we first identify the maximum inner circle for the known Concept

momentum range of $\tilde{\rho}$. Second, we subtract $\tilde{\rho}_{\max}$, i.e. the maximum of $\tilde{\rho}$ from outside of the maximum inner circle, from $\tilde{\rho}$. Hence, outside of the circle all values are either zero or negative. Negative values can also occur inside the maximum inner circle. Third, we set all negative values of $\tilde{\rho}$ to zero

$$\tilde{\rho}(p_x,p_y) \to \max\left(0, \tilde{\rho}(p_x,p_y) - \max_{\boldsymbol{q}\in\mathbb{O}} \tilde{\rho}(q_x,q_y)\right) \tag{4.7}$$

$$\mathbb{O} = \left\{\boldsymbol{q} : q \geq \min(p_{x,\max}, p_{y,\max})\right\}. \tag{4.8}$$

This cutoff generates a continuously to zero decaying spectrum with approximately circular shape. In this way the steps at the boundaries are transformed to kinks.

Artifact formation

The corresponding truncation artifacts can be seen in figure 4.6c. We see, how the N-hole pockets ($k_x = \pm 0.5, k_y = \pm 0.3$) are forced pointing in vertical direction by two artifact lines (lime green and red) parallel to each other at the position of the pocket. Further the overemphasis of the double knobs ($k_x = 0, k_y = \pm 0.25$) and the triangular form of the H-hole octahedra at ($k_x = 0$; $k_y = \pm\frac{1}{\sqrt{2}}$) is explained by the overlap and gap regions of the spectra from the dark green and dark blue projection points (compare figures 4.4 d vs b).

Evaluation

Comparing the results for this method, presented in figure B.1 c and d, with the reference in B.1j, only minimal differences can be found. Therefore, the circular cutoff produces a stable (for increasing $p_{\max}$ from 2.1 to 2.24, but not with respect to noise) and correct back-folding result.

Disadvantages: kinks and shifts

Besides its obvious success for larger $p_{\max}$ and its simplicity, this cutoff bears two major disadvantages:
1) By producing kinks as truncation artifact the circular cutoff can alter $\tilde{n}$ strongly but at the same time in a subtle way, as seen at the shape of the N-hole pockets in figure 4.6c. When using this cutoff scheme, the possibility of such overlap patterns should always be considered. Results should hence be double checked with a slightly changed $p_{\max}$ parameter. This issue becomes more important for small $p_{\max}$, as the resulting kink at the boundaries of the cutoff is stronger.
2) The second complication is the shift of $\tilde{\rho}$. As the shift is defined by just one point in the $\max\tilde{\rho}(q_x,q_y)$-term, it is highly sensible to noise and details of the spectrum. This makes it hard to compare two different $n^{2\gamma}(k_x,k_y)$ for materials with similar electronic structures.

Voronoi Cutoff

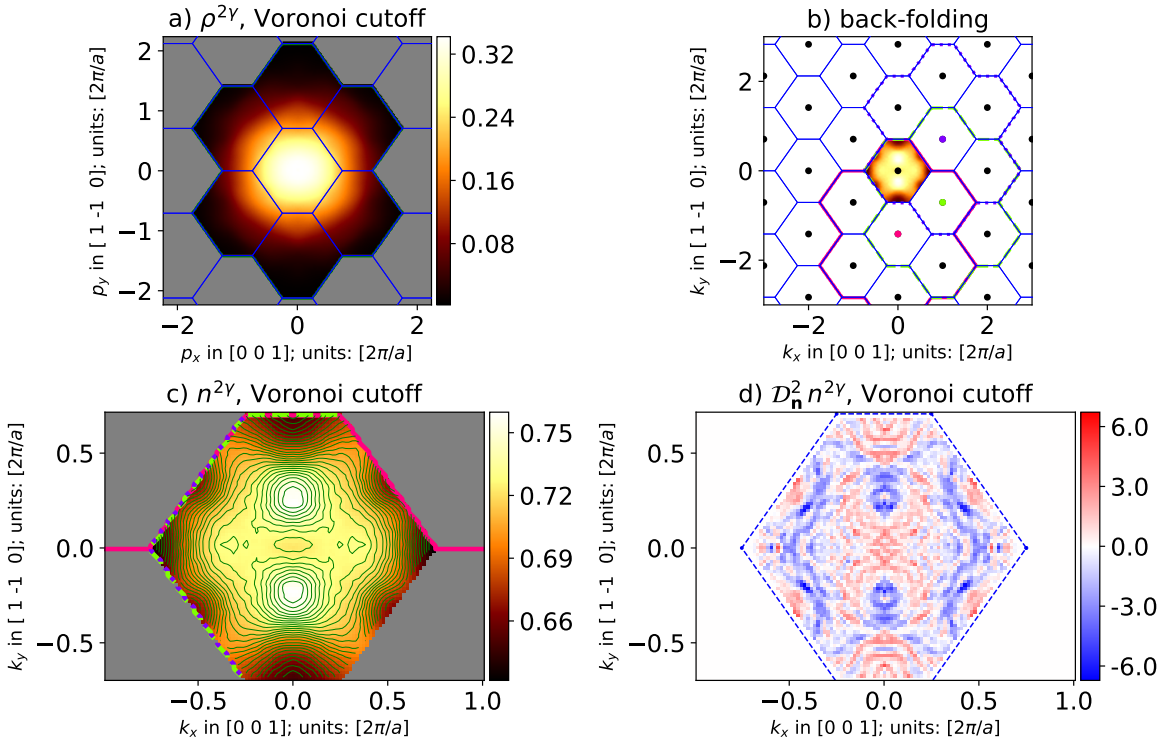

Figure 4.7.: Artifact formation for molybdenum, Voronoi cutoff, compare figure 4.4e:
a) shows the input ($p_{\max} = 2.24\frac{2\pi}{a}$) with the corresponding Voronoi plaquette. The gray area represents the data points, which were put to zero by applying the cutoff.
b) shows the construction of $n^{2\gamma}$, where the input is replicated to all points of the projected lattice (dot pattern). Apparently only contributions to the complete VP are considered.
c) is a closeup of the Voronoi plaquette in subplot b with added contour lines.
d) is the SDDn of subplot c, showing the FS signatures and back-folding artifacts.

Concept

The Voronoi cutoff handles truncation artifacts in a more organized way. By taking only complete VPs into account, all truncation artifacts are collected at the boundaries of the VP. Due to translational and mirror symmetries, $n^{2\gamma}$ can be replicated to cover the full crystal momentum space without introducing steps. To avoid an overweighting of **anisotropic contributions** along the $p_y \approx \pm p_x$ direction, we consider only complete VPs, which are closer to the origin than any incomplete VP.[4] We do so by comparing the Euclidean distance to the corresponding projection point. The resulting Voronoi cutoff consists of putting all $\tilde{\rho}(p_x,p_y) = 0$ if (p_x,p_y) is in an incomplete or anisotropic VP (compare figures 4.7a and 4.8).

[4] Tests on Ge and Mo showed little difference between taking the anisotropic VPs into account or not.

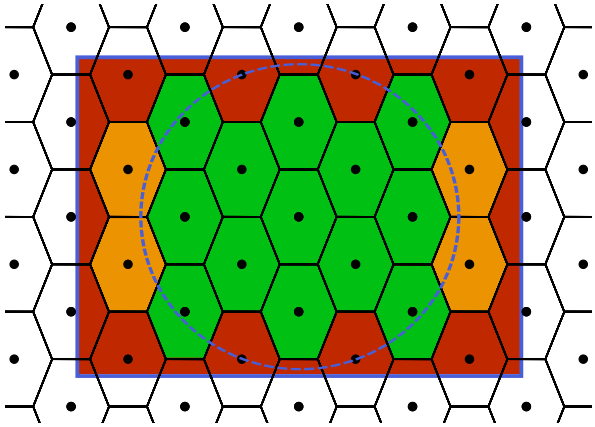

Figure 4.8.: Concepts of the Voronoi cutoff:
The values of $\tilde{\rho}$ in incomplete (red) and anisotropic (orange) VPs are set to zero.

Disadvantages

The drawback of this cutoff is the big loss of data points, as can be seen in figure 4.7a. The cutoff reaches even points at $(p_x \approx \pm 1.2, p_y = 0)$. Therefore, the Voronoi cutoff suffers from two issues: 1) Due to the convex shape effect there is an extremely sharp kink along the boundary of VP. 2) Even for comparably large $p_{\max}$, the cutoff scheme ignores such a big portion of data, that important signatures are missing.

Evaluation

Figure B.1f (equal to 4.7c) shows clearly the consequences of issue 2. We see that the single knobs of the electron-jack ($k_x = 0.4$; $k_y = 0$) are not reproduced, the N-hole pockets ($k_x = \pm 0.5, k_y = \pm 0.3$) are prolonged along the VP boundary and the H-hole octahedra ($k_x = \pm 1$; $k_y = 0$ and $k_x = 0$; $k_y = \pm \frac{1}{\sqrt{2}}$) are distorted by a strong kink along the VP. These artifacts origin from the missing contributions of the VPs situated at ($p_x \approx \pm 2$, $p_y = 0$) to $\rho^{2\gamma}(p_x,p_y)$.
In figure 4.7 even a larger $p_{\max} = 2.24$ was chosen compared to the other cutoff schemes (i.e. $p_{\max} = 1.7$ in figures 4.5, 4.6 and 4.9). For $p_{\max} = 1.7\frac{2\pi}{a}$ only the central VP is left after applying the Voronoi cutoff, leading to the back-folding result presented in figure 4.4e. By comparing figures 4.4e, B.1e and B.1f, we see how the back-folded $n^{2\gamma}$ evolves with one, four and six VPs (compare figure 4.7a) taken into account.

Rectangular Cutoff

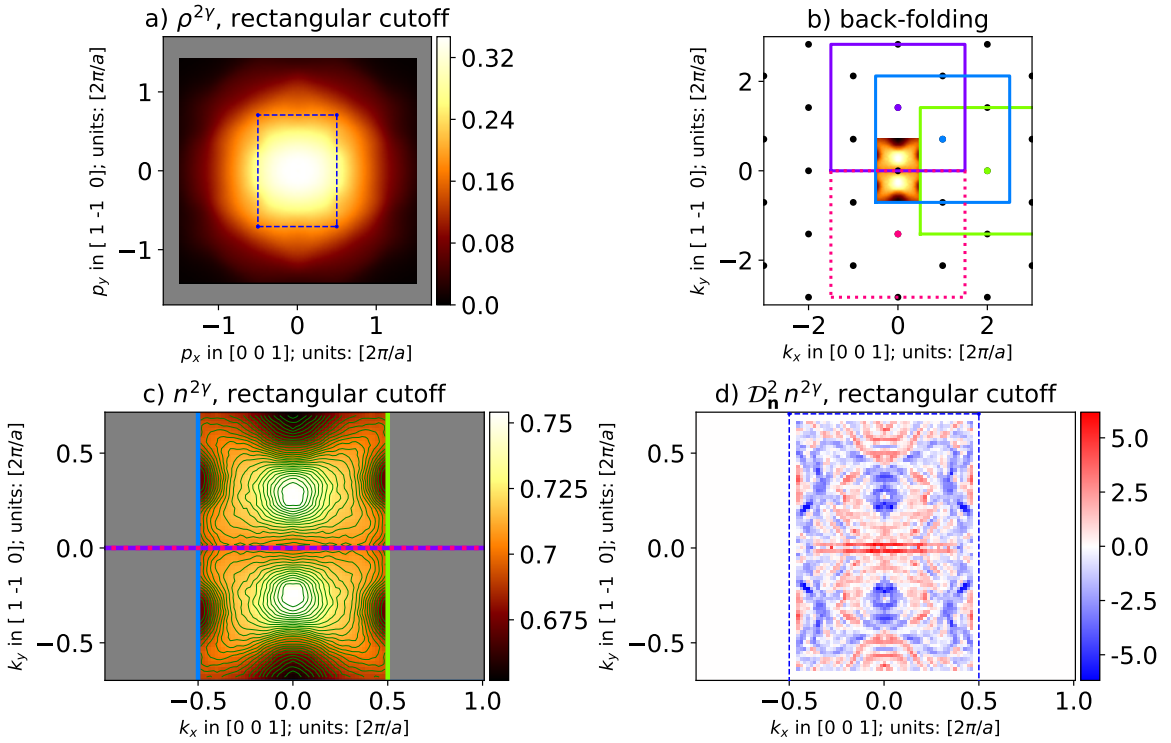

Figure 4.9.: Artifact formation for molybdenum, rectangular cutoff, compare figure 4.4f:
a) shows the input ($p_{\max} = 1.7\frac{2\pi}{a}$) with the corresponding rectangular irreducible plaquette. The gray area represents the data points, which were put to zero by applying the cutoff.
b) shows the construction of $n^{2\gamma}$, where the input is replicated to all points of the projected lattice (dot pattern). Some truncation artifacts, introduced in the RP during the back-folding process, are pointed out as colored lines.
c) is a closeup of the Voronoi plaquette in subplot b with added contour lines.
d) is the SDDn of subplot c, showing the FS signatures and back-folding artifacts.

Concept

The concept of the rectangular cutoff [87], illustrated in figure 4.9, is to truncate $\tilde{\rho}$ slightly in both directions, such that contributions from different projection points are merged without gaps or overlaps (see subplot b). We define the **Rectangular Plaquette (RP)** (i.e. all edges are situated along the p_x- and p_y-directions) on the projected lattice, similar to the construction of the VP.
We choose the width Δx of the RP to be the largest p_x-component of the primitive basis $\boldsymbol{p_1}, \boldsymbol{p_2}$ and the height Δy accordingly

$$\Delta x = \max(p_{1,x}, p_{2,x}) \tag{4.9}$$
$$\Delta y = \max(p_{1,y}, p_{2,y})\,. \tag{4.10}$$

Analogous to the VP, the RP is centered around each projection point and the cutoff is performed by taking only complete RPs into account for the LCW back-folding operation

$$\tilde{\rho}(p_x,p_y) \to \begin{cases} \tilde{\rho}(p_x,p_y) & \text{if } |p_x| \leq p_{x,\text{cut}} \text{ and } |p_y| \leq p_{y,\text{cut}} \\ 0 & \text{otherwise} \end{cases} \tag{4.11}$$

$$p_{x,\text{cut}} = \left\lfloor \frac{p_{x,\,\max}}{\frac{\Delta x}{2}} \right\rfloor \frac{\Delta x}{2} \quad \text{and} \quad p_{y,\text{cut}} = \left\lfloor \frac{p_{y,\,\max}}{\frac{\Delta y}{2}} \right\rfloor \frac{\Delta y}{2}\,. \tag{4.12}$$

Here $\lfloor \ldots \rfloor$ denotes the floor function. This means, that $\tilde{\rho}$ is truncated with a symmetric rectangular shape, with its length and width being a multiple of the length and width of the RP (compare figure 4.9a). The back-folding result is the area of the RP. Truncation artifacts appear at the RP boundaries and, dependent on the situation, at $k_x = 0$ and $k_y = 0$.

Discussion For a specific combination of $\boldsymbol{p_1}$,$\boldsymbol{p_2}$ and $p_{\max}$ this cutoff becomes equivalent to the Voronoi cutoff. Similarly to the Voronoi cutoff, it suffers from the convex shape effect and from strong kinks along the irreducible plaquette boundaries. In contrast to the Voronoi cutoff, the rectangular cutoff can introduce additional kinks on the k_x and k_y axis, while having less intensity at the kinks along the boundaries of the irreducible plaquette.

Artifact positions In figure 4.9b the dark blue and the pink dashed cutoff boundaries both introduce a step at $k_y = 0$. Due to symmetry, they sum up to a continuous spectrum with a kink. In the same way the artifacts at $k_x = \pm 0.5$ and $k_y = 0, \pm\frac{1}{\sqrt{2}}$ are created. This explains our finding in figure 4.4f, which is just the periodic repetition of figure 4.9c.

Evaluation How the observed artifacts evolve with increasing $p_{\max}$ can be seen in figures B.1 g and h. As the truncation artifacts become weaker from subplots g to h, their appearance becomes more subtle. While in subplot g the artifact along $k_y = 0$ can still be identified, this is not possible in subplot h anymore. Small distortions of the N-hole pocket ($k_x = 0$; $k_y = 0$) and the single knobs ($k_x = 0.4$; $k_y = 0$) remain. It should be mentioned here, that Kaiser's original back-folding code [87] was used for a better comparison with literature values (figure B.1h is equivalent to figure 2 top in [203]). As this code operates on an even momentum mesh, interpolation issues might have occurred, being responsible for minor differences between figures B.1h and the reference B.1j. It becomes apparent however, that these differences are stronger at the typical artifact positions of the rectangular cutoff scheme. A more detailed investigation follows in section 7.3.

4.2.2. Extrapolation

Skeptical discussion By extrapolating $\tilde{\rho}$, we simultaneously reduce the truncation issue (as the step at the boundary of an extrapolated $\tilde{\rho}$ is smaller) and the convex shape effect. Even though extrapolation is in general known to generate misleading results, we strongly

recommend to extrapolate $\tilde{\rho}$ before back-folding. The reason is that, as seen before at the examples of different cutoff schemes in subsection 4.2.1, we zero-padded all data points outside of the known range of $\tilde{\rho}$ in the numerical implementation of equation (4.1). This corresponds to an extreme rough extrapolation, which can be improved by any educated guess.

Requirements

We shall develop an extrapolation scheme, interfering as little as possible with the back-folding procedure by fulfilling the following requirements:

- The extrapolation scheme should not introduce any artificial steps or kinks.
- The extrapolated data should be continuously decaying.
- The extrapolation should be robust to noise at the larger momenta of $\tilde{\rho}$.
- No attempt to model $\tilde{\rho}$ exactly (i.e. including for instance Fermi surface signatures, repairing noise, ...) should be made, as this would introduce a bias into our data.

Concept

We extrapolate by fitting a function to $\tilde{\rho}((p_x,p_y) \in \mathbb{B})$ at each boundary mesh point

$$\begin{aligned}\mathbb{B} \equiv \{(p_x,p_y) : (|p_x| = p_{x,\max} \wedge |p_y| \leq p_{y,\max}) \\ \vee \ (|p_x| \leq p_{x,\max} \wedge |p_y| = p_{y,\max})\} \ ,\end{aligned} \tag{4.13}$$

which decays either exponentially or by a power law. Each function consists of two fitting parameters: An amplitude and a decay rate. The latter is the same for all functions and is deduced from the values of $\tilde{\rho}((p_x,p_y) \in \mathbb{T})$ in the higher momentum region $\mathbb{T}$, compare equation (4.21). The amplitude is determined for each function individually by fitting it to its boundary point. The **extrapolation grid** is a concentric set of lines, starting (in prolongation) at the origin and passing through the points of $\mathbb{B}$, where the afore mentioned functions are defined on. All data points, which are situated in between the extrapolation grid lines, are constructed by linear interpolation on a straight line parallel to the corresponding boundary of $\tilde{\rho}$. As seen in figure 4.10 the extrapolation result is a steadily decaying function, showing the same characteristics as $\tilde{\rho}$ at its boundaries. In this case, we see a broad central peak structure being replicated in vertical direction, while a narrow multi-peak structure is extrapolated in horizontal direction.

Algorithm

This extrapolation process is described in algorithmic form as following: We consider $\tilde{\rho}$ as an image, where the pixels correspond to the momentum mesh points. We map the most outer row/column of pixels to a frame, consisting of an array of discrete values along this path. We increase the frame size by two pixels in each direction and scale the values with the appropriate scaling behavior. We map this extended frame back to $\tilde{\rho}$ (covering now one additional row/column in each direction), where the exact values at the new pixel positions are determined by linear interpolation.

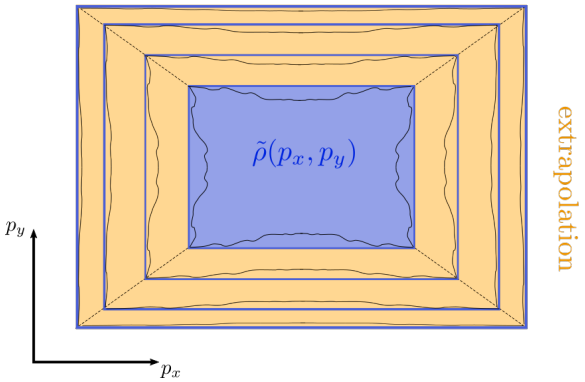

Figure 4.10.: Scheme of the extrapolation algorithm:
Blue shaded area denotes the known data, the yellow shaded area is the extrapolation area. The values of $\tilde{\rho}$ at its boundaries are symbolized by the wiggly black lines. Those are stretched (in p_x/p_y) direction and reduced in value by extrapolation.

Scaling models

We extrapolate $\tilde{\rho}$ according to its scaling behavior based on the absolute momentum $p = |(p_x,p_y)|$.

Exponential decay:

$$\tilde{\rho}(p) \propto e^{-\mu p} \tag{4.14}$$

$$\tilde{\rho}(p_x,p_y) = \tilde{\rho}(b(p_x,p_y))e^{-\mu(|p-b(p_x,p_y)|)} \tag{4.15}$$

$$\mu = -\left\langle \frac{\ln\tilde{\rho}(\boldsymbol{p_1}) - \ln\tilde{\rho}(\boldsymbol{p_2})}{p_1 - p_2} \right\rangle_{\boldsymbol{p_1},\boldsymbol{p_2}} \tag{4.16}$$

Power law decay:

$$\tilde{\rho}(p) \propto p^{-\mu} \tag{4.17}$$

$$\tilde{\rho}(p_x,p_y) = \tilde{\rho}(b(p_x,p_y)) \left(\frac{p}{|b(p_x,p_y)|} \right)^{-\mu} \tag{4.18}$$

$$\mu = -\left\langle \frac{\ln\tilde{\rho}(\boldsymbol{p_1}) - \ln\tilde{\rho}(\boldsymbol{p_2})}{\ln p_1 - \ln p_2} \right\rangle_{\boldsymbol{p_1},\boldsymbol{p_2}} \tag{4.19}$$

with

$$\text{boundary points:} \quad b(p_x,p_y) = \begin{cases} \left(p_{x,\max}, \frac{p_{x,\max}}{p_x} p_y\right) & \text{for } \frac{p_y}{p_x} \leq \frac{p_{y,\max}}{p_{x,\max}} \\ \left(\frac{p_{y,\max}}{p_y} p_x, p_{y,\max}\right) & \text{otherwise} \end{cases} \tag{4.20}$$

$$\text{tail region:} \quad \mathbb{T} = \left\{ (p_x,p_y) : p \geq (1 - r_{\text{tail}}) p_{\max} \right\}, \tag{4.21}$$

where $r_{\text{tail}} \in (0,1]$ defines the tail ratio. The condition $\mu > 2$ is imposed for the power law decay, as this avoids divergence at $p = 0$ ($\mu > 1$) and ensures that $\tilde{\rho}$ is normalizable. We define the extrapolation scaling factor $f_{\text{ex}} > 1$ as the ration of $p_{\max}$ after and before back-folding.

Monte Carlo

As the number of data points in the tail region $|\mathbb{T}|$ is of the order of 10^5, the evaluation of μ with all combinations of $\boldsymbol{p_1}, \boldsymbol{p_2} \in \mathbb{T}$ (i.e. $|\mathbb{T}|^2$ operations) is not practical. We hence calculate μ by Monte Carlo averaging

$$\Big\langle f(\boldsymbol{p_1},\boldsymbol{p_2})\Big\rangle_{\boldsymbol{p_1},\boldsymbol{p_2}} \equiv \frac{1}{|\mathbb{M}|}\sum_{(\boldsymbol{p_1},\boldsymbol{p_2})}^{\mathbb{M}} f(\boldsymbol{p_1},\boldsymbol{p_2}) \tag{4.22}$$

$$\mathbb{M} = \Big\{\boldsymbol{p_1},\boldsymbol{p_2} \text{ randomly chosen from } \mathbb{T}\times\mathbb{T} \text{ with } |p_1 - p_2| \geq \delta p_{\min}\Big\} \tag{4.23}$$

with $|\mathbb{M}| = |\mathbb{T}|$ samples. The minimum momentum distance $\delta p_{\min}$ is needed, to avoid divergent contributions from equations (4.16) and (4.19) for $\ln\tilde{\rho}(\boldsymbol{p_1}) \gg \ln\tilde{\rho}(\boldsymbol{p_2})$ and $p_1 \approx p_2$. Practically the parameters $\delta p_{\min} = 0.1 r_{\text{tail}} p_{\max}$ and $r_{\text{tail}} = 0.2$ were chosen.

Scaling behavior

Of course, finding the exact scaling behavior (exponential, power law or some other) depends on the exact physical information, represented by $\tilde{\rho}$. $\tilde{\rho}$ representing momentum densities this not a trivial task and subject of current investigations [52]. As stated earlier in this chapter, the target of the extrapolation is not to model $\tilde{\rho}$ as precise as possible (being beyond the possibilities of this extrapolation algorithm anyway), but to reduce truncation artifacts and the convex shape effect.

Evaluation

In figures B.2 and B.3 we compare both scaling models for the calculated [189] 2D-ACAR spectrum of Molybdenum, $\tilde{\rho} = \rho^{2\gamma}$. We use theoretical data for this demonstration, as higher momenta regions $p_{\max} > 3.5\,\text{a.u.}$ are accessible.
Both figures show $\rho^{2\gamma}(p_x,p_y)$ (subplot a) and the reference back-folding result (subplot b) in the first row. The other rows present data based on extrapolation of the red boxed area in subplot a for different scaling parameters μ. The optimal scaling parameter according to equations (4.16) and (4.19) is presented in the second row. In the third row $\mu = 0.1/2.1$ represents a very small exponents, while $\mu = \infty$ in the last row corresponds to zero-padding. As all spectra are normalized after extrapolation, also deviations inside the red box occur in subplots c, f and i. The right column shows the deviation of the back-folding results (subplots d, g and j) with respect to the reference in percent. The exponential extrapolation gives a better agreement with the reference $\rho^{2\gamma}$ (figure B.2e), than the extrapolation by a power law (figure B.3e).[5] Because of this finding, we use exponential scaling for extrapolation in this work.

Extrapolation artifacts

The condition to extrapolate $\tilde{\rho}$ continuously at the boundary, can lead to **extrapolation artifacts**. The first type of extrapolation artifacts, thereby occurs at the boundary between the known and the extrapolated data points. This is a kink, as the extrapolated data was only matched by value but not by slope. The strength of the kink is the difference of the slope at the end of the known spectrum and the slope of the matched model decay (equation (4.14) or (4.17)). However, in all investigated cases this type of artifacts was negligible compared to the Fermi surface signatures.

[5] We experimented also with hybrid extrapolation models, weighting the exponential scaling and power law scaling extrapolation results according to their capability to reproduce the values of $\tilde{\rho}(p_x,p_y)$ in the tail region $(p_x,p_y) \in \mathbb{T}$. As the improvement was minor and for sake of simplicity, we did not follow this path any further.

Extrapolation artifacts of the second type occur, when steps or kinks (for instance Fermi surface signatures) touch the boundaries $\mathbb{B}$ of $\rho^{2\gamma}(p_x,p_y)$. They appear as shadow images of the corresponding step or kink, starting at the boundary of the original spectrum and following a concentric line with decreasing intensity.

Illustration

This is illustrated based on theoretical data in figure 4.11.[6] We therefore extrapolate a spectrum with a strong Fermi surface signature (from the H-hole octahedron, as we will see later) touching the boundary of the spectrum ($p_x = \pm 0.9$; $p_y = \pm 1.1$). The input for the extrapolation is marked by a red frame and is identical in subplots a and b (showing the SDDn). To identify missing Fermi surface signatures and extrapolation artifacts, we compare subplot a (reference) with subplot b (extrapolated) outside of the framed area. As expected, all Fermi surface signatures in the extrapolated region are missing and we find the extrapolation artifacts (second type) from the H-hole octahedron along the concentric extrapolation grid line at $(p_x,p_y) = (\pm 0.9, \pm 1.3)$ and $(p_x,p_y) = (\pm 0.1, \pm 1.3)$. Extrapolation artifacts of the first type, would appear as a kink along the red frame, but can not be found. The second row shows the back-folding result of both spectra. We see differences in the color scale. Also the edges of the H-hole octahedron at $k_x = \pm 0.25$; $k_y = \pm 0.6$ are more blurry in the extrapolated case. By analyzing the SDDn, displayed in the third row, we see clearly, that edge intensity is lost at these points. The extrapolation artifacts can be observed at $k_x = \pm 0.1$; $k_y = \pm 0.45$, where the edge of the H-hole octahedron is interrupted in the extrapolated case. To make comparison easier, we also show the back-folding results of the truncated spectrum (red frame) in subplots g and h.

Circumvention

Extrapolation artifacts only appear in extreme cases. In the investigations of the extrapolation process they could be found only at very small $p_{\max} = 1.2$ for the theoretical spectra of transition metals. Transition metals have the property of strong Fermi surface signatures in the region of intermediate momenta, due to the d- and f-character of their valance bands, as pointed out in section 3.1 and in [47, 48, 50].

These artifacts were not observed when extrapolating experimental 2D-ACAR data, due to the experimental resolution and the Poisson noise. The experimental resolution leads to a smoothing of the data, especially at the boundaries of $\rho^{2\gamma}_{\text{exp}}(p_x,p_y)$, where the relative intensity of the Fermi surface signatures is weaker (due to the higher intensity of continuous core contributions to $\rho^{(2\gamma)}_{\text{exp}}(p_x,p_y)$). The Poisson noise, introduces low intensity extrapolation artifacts everywhere in the extrapolated area of $\rho^{2\gamma}_{\text{exp}}(p_x,p_y)$, but these are just added to an irregular noise pattern in $n^{2\gamma}_{\text{exp}}(k_x,k_y)$ by the back-folding operation.

No attempts are needed to avoid extrapolation artifacts. In the rare cases, where those artifacts appear, the SDDn of the extrapolated spectrum reveals them immediately. A correction should not be made, however, as any modification of kinks at the boundaries, would introduce artifacts at another position.

[6] For clearness we zoomed into subplots a and b. The real $p_{\max}$ is situated at 3.6.

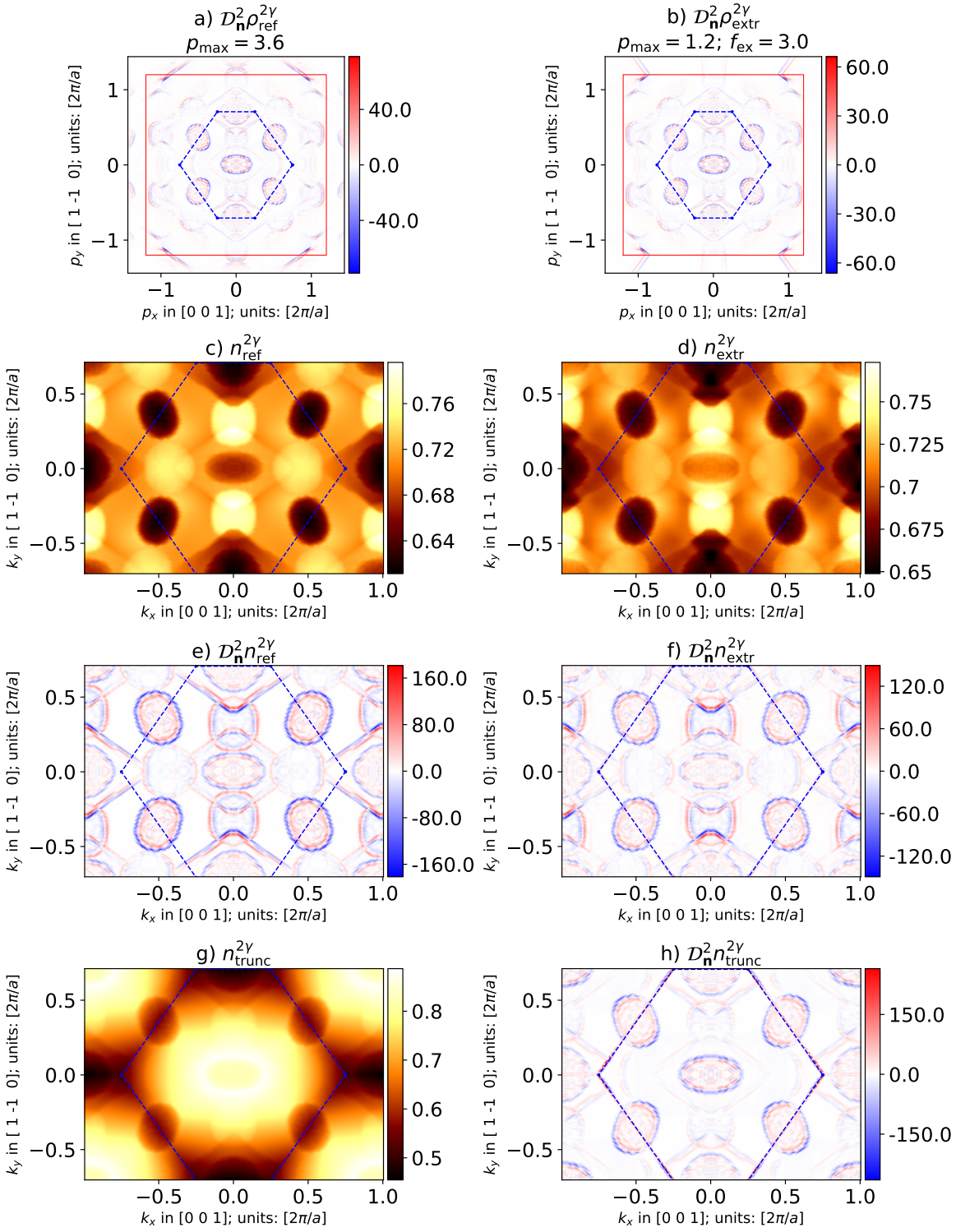

Figure 4.11.: Extrapolation artifacts in molybdenum, Elk calculation:
a, c and e) Elk calculation (subscript 'ref').
g,h) Elk calculation truncated at $p_{\max} = 1.2$ (red frame, subscript 'trunc').
b, d and f) Elk calculation truncated at $p_{\max} = 1.2$ and extrapolated to $p_{\max} = 3.6$.
Compare subplots c/g/d and e/h/f to evaluate the benefits of extrapolation. For back-folding the Voronoi cutoff scheme was applied.

Best cutoff To identify the most suitable cutoff scheme under the new perspective of extrapolation, the properties of the different cutoff schemes shall be reevaluated.

- Loss of information is not relevant:
  By adjusting the extrapolation range, an information loss by truncation does not need to be considered. We will always choose the extrapolation range such, that the full original spectrum is contained in the extrapolated spectrum after applying the cutoff.
- Convex shape effect is not relevant:
  The convex shape effect, will we corrected automatically for a large enough extrapolation scale.
- Controlling artifacts is important:
  As the artifact intensity is low at large momenta, controlling the position of artifacts becomes important. In this way an unpredictable superposition of artifacts can be prevented.

For those reasons the Voronoi cutoff is the preferable cutoff scheme, as its two disadvantages (convex shape effect and loss of data points) do not play a role for extrapolated datasets.
The choice of a specific cutoff for extrapolated data might play a negligible role in most cases, as the back-folding artifacts are small. In figures 6.1 and D.1 at $p_{\max} \approx 2$ two cases are presented, however, where the Voronoi cutoff scheme is favorable.

Benchmark When comparing the back-folding results for Voronoi cutoff with extrapolation $p_{\max} \in \{1.7, 2.1, 2.24\}$ (see figures 4.4g and B.1 i and j), we see only minor changes for increasing $p_{\max}$. The second best backfolding method is the circular cutoff with minor changes in between $p_{\max} = 2.1$ and $p_{\max} = 2.24$ (compare B.1 c and d). For $p_{\max} = 1.7$ obvious differences are still apparent. It is remarkable, that extrapolation can even for $p_{\max} = 1.7\frac{2\pi}{a}$ produce realistic results, where all other methods are barely able to produce any feature of $n^{2\gamma}(k_x,k_y)$.

Normalization Further, extrapolation improves the absolute values of $\tilde{\rho}$ and $\tilde{n}$ when the normalization condition (3.9) is applied. This might turn out as an improvement for tomographic methods [89–94] for reconstructing $\rho(\boldsymbol{p})$ as mentioned in the introduction.

4.2.3. Conclusion

General We can conclude, that extrapolation is an important new tool to increase the precision of LCW back-folding. Even though there are chances to introduce extrapolation artifact in some rare cases, extrapolation brings considerable improvements, especially for small $p_{\max}$. Extrapolation artifacts, if apparent, are clearly identifiable by the SDDn and have a smaller intensity than truncation artifacts. For symmetry reasons it is recommended to combine extrapolation with the Voronoi cutoff.

Bad counting statistics

In general, 2D-ACAR measurements are performed with a total of 200 million counts [67, 203]. There are cases however, where experiments consist of a considerable less number of counts [64, 66], for instance 8 million. The consequence is a poor signal-to-noise ratio in the tail region $\mathbb{T}$ at intermediate momenta (compare subsections 1.2.3 and 5.4.2).
In the case of bad counting statistics, it can happen, that a considerable portion of data points in the tail region $\mathbb{T}$ of $\tilde{\rho}$ are zero. An extrapolation is not possible in this case, due to the logarithms appearing in the numerator of equations (4.16) and (4.19). The concepts from this chapter can be combined in different ways to overcome this issue.

1. Application of the circular cutoff scheme:
   Even though the formation of truncation artifacts happens in an unpredictable way, the circular cutoff scheme shows the best performance if not using extrapolation.

2. Additional truncation of $\tilde{\rho}$ until $\tilde{\rho}(\boldsymbol{t}) \gg 0 \quad \forall \boldsymbol{t} \in \mathbb{T}$:
   From there on extrapolation can be used.

3. Application of some kind of averaging of $\tilde{\rho}$ in $\mathbb{T}$:
   This makes extrapolation applicable again, but bears the danger of introducing artificial steps. Further, it is questionable if extrapolation based on information with such a poor signal-to-noise ratio should be applied.

Option 2 is favorable, if just Fermi surface signatures from the small momenta region shall be identified. As additional truncation bears the danger of loosing Fermi surface signatures from the intermediate momenta region, option 1 should be applied to recover those.

4.3. Details and Implementation

We present some numerical tricks and design strategies, which were used in the implementation of the LCW back-folding code. Those lead to more readable program code, increased performance and increased precision.

4.3.1. Momentum Mesh

Remarks

Currently, there are two different types of momentum meshes (p_x,p_y) in use. The **even** and the **odd momentum mesh**, where even and odd refers to the number of mesh points used in both dimensions. Both are symmetric to the origin ($p_x = 0$,$p_y = 0$). The back-folding procedure does not change the type of momentum mesh when 'translating' from the p_x-p_y-space to the k_x-k_y-space, so the following discussion applies to both spaces. Both momentum meshes are compatible with the optimal resolution condition equation (4.2).

Even momentum mesh

The even momentum mesh originates from the beginning for the 1990s, when computational resources were a limiting factor for ACAR measurements. This made it preferable, to work with datasets with a power-of-two length. Due to symmetry, the mesh points are situated at

$$p_{x/y,i} = (N_i + \frac{1}{2}) \cdot \Delta p_{x/y} \tag{4.24}$$

with $N_i \in \mathbb{N}$. This means, that neither the origin nor the two momentum axes are included in this mesh.

High symmetry directions

Especially analyses along the coordinate axes (for example the ΓH and ΓN directions in a bcc lattice) need an additional interpolation step with this type of mesh. As pointed out in subsection 4.1.1 and section 7.3, interpolation should be avoided whenever possible, as it can lead to a shift and smoothing of the detected Fermi surface signatures.

Odd momentum mesh

Due to the advances in computational capabilities and new signal processing methods (like list mode recording [68]) in the experimental ACAR setup, the size restriction to a power of two for the number of recorded momentum channels does not hold anymore. This leads to the odd momentum mesh

$$p_{x/y,i} = N_i \cdot \Delta p_{x/y} \tag{4.25}$$

with $N_i \in \mathbb{N}$. It is more favorable to work on this mesh, as this gives interpolation free access to the Γ point and the coordinate axes.

4.3.2. Two-Dimensional Basis

In order to simplify the summation over all projections of reciprocal lattice vectors in equation (3.40), two observations should be made:

1) The distance (in p_z direction) between the reciprocal lattice vectors $\{\tilde{\boldsymbol{G}}\}$ projecting onto the same projection point ($\tilde{G}_x$,$\tilde{G}_y$) is constant and independent of the projection point ($\tilde{G}_x$,$\tilde{G}_y$). This means, that it is sufficient to identify the set of all possible projections $\{(G_x,G_y)\}$ of reciprocal lattice vectors $\{\boldsymbol{G}\}$ onto the p_x-p_y-plane. Additional information about how many $\boldsymbol{G}$s were projected onto a specific (G_x,G_y)-tuple is not needed. Projection density

2) There exists a reduced set of vectors $\boldsymbol{p_1}, \boldsymbol{p_2} \in \mathbb{R}^2$ to construct all projection points $\{(G_x,G_y)\}$ [220] 2D basis

$$\begin{aligned} \boldsymbol{p_1} &= \gcd\left(|\boldsymbol{q_1}|, |\alpha_1\boldsymbol{q_2} + \alpha_2\boldsymbol{q_3}|\right) \frac{\boldsymbol{q_1}}{|\boldsymbol{q_1}|} \quad \text{where } \boldsymbol{q_1} \parallel \alpha_1\boldsymbol{q_2} + \alpha_2\boldsymbol{q_3} \\ \boldsymbol{p_2} &= \gcd\left(|\boldsymbol{q_2}|, |\alpha_3\boldsymbol{p_1} + \alpha_4\boldsymbol{q_3}|\right) \frac{\boldsymbol{q_2}}{|\boldsymbol{q_2}|} \quad \text{where } \boldsymbol{q_2} \parallel \alpha_3\boldsymbol{p_1} + \alpha_4\boldsymbol{q_3} \end{aligned} \tag{4.26}$$

with 'gcd' denoting the greatest common divisor, α_i being integer numbers and $\boldsymbol{q_i}$ being the 2 dimensional projections of the reciprocal primitive translation vectors $\boldsymbol{b_1}$, $\boldsymbol{b_2}$, $\boldsymbol{b_3}$ onto the p_x-p_y-plane

$$\alpha_i \in \mathbb{Z} \text{ with } i \in \{1,2,3,4\} \tag{4.27}$$

$$\boldsymbol{q_j} = (b_{j,x}, b_{j,y}) \text{ with } j \in \{1,2,3\}\,. \tag{4.28}$$

With identifying this two-dimensional basis $\boldsymbol{p_1}$, $\boldsymbol{p_2}$ for constructing the projected lattice, equation (3.40) simplifies to equation (4.1). This avoids unnecessary problems with finding all projected lattice points and storing their position without rounding errors. Additionally the VP can be constructed and stored in a more compact way. Conclusion

4.3.3. Finding the Complete Set of Projections

In this section we introduce a recipe to efficiently find the complete list of projection points in a given rectangle around the origin $\mathbf{0} = (0,0)$. Aim

The set $\{(G_x,G_y)\}$ for equation (4.1) is constructed by the linear combination Linear combination

$$\{(G_x,G_y)\} = n_1\boldsymbol{p_1} + n_2\boldsymbol{p_2}\,. \tag{4.29}$$

with $n_{1/2} \in \mathbb{Z}$. This is an infinite number of points, which is not needed for backfolding. As it is sufficient to consider only those projection points ($\tilde{G}_x$,$\tilde{G}_y$), where $\tilde{\rho}(\tilde{G}_x + p_x,\tilde{G}_y + p_y)$ still reaches into the central VP/RP, we only consider projection points in the area of interest

$$\mathbb{A} \equiv \left\{(p_x,p_y) : -p_{x/y,\max} - \Delta_{x/y} \le p_{x/y} \le p_{x/y,\max} + \Delta_{x/y}\right\}. \tag{4.30}$$

$\Delta_{x/y}$ is half the size of the VP/RP in $p_{x/y}$ direction.

The question we investigate in the following is: *What is the necessary range for the* Aim

loops $-N_1 \leq n_1 \leq N_1$ *and* $-N_2 \leq n_2 \leq N_2$*, to cover all* $\{(G_x,G_y)\}$ *in the area of interest?*

Geometric consideration

We define the lines $\mathbb{L}_i$ as passing through the origin with direction $\boldsymbol{p_i}$ and $i \in \{1,2\}$.

$$\mathbb{L}_i = \left\{\mathbf{0} + \gamma_1 \boldsymbol{p_1} : \gamma_1 \in \mathbb{R}\right\}. \tag{4.31}$$

May $\mathbb{Q}$ denote the intersect of line $\mathbb{L}_1$ with the area of interest

$$\mathbb{Q} = \mathbb{L}_1 \cap \mathbb{A}. \tag{4.32}$$

The minimum number N_2 is found when there does not exist any point $\boldsymbol{q} \in \mathbb{Q}$, so that the vector sum of $\boldsymbol{q}$ and $N_2\boldsymbol{p_2}$ is still an element of the area of interest[7]

$$N_2 = \min\left(\left\{N : \boldsymbol{q} + N\boldsymbol{p_2} \notin \mathbb{A} \quad \forall \boldsymbol{q} \in \mathbb{Q}\right\}\right). \tag{4.33}$$

Implementation

This condition can be expressed in a more compact form, by just considering the edge points $\mathbb{P}$ of the area of interest $\mathbb{A}$. To determine N_2, it is sufficient to check the maximal distance d_2 in between the line $\mathbb{L}_1$ and any edge point. In a second step, we divide d_2 by the length of the part of $\boldsymbol{p_2}$, which is perpendicular to $\boldsymbol{p_1}$.

$$d_2 = \max_{\boldsymbol{p}\in\mathbb{P}} \left(\frac{|\boldsymbol{p} \times \boldsymbol{p_1}|}{|\boldsymbol{p_1}|}\right) \tag{4.34}$$

$$|\boldsymbol{p_{2,\perp}}| = \frac{|\boldsymbol{p_1} \times \boldsymbol{p_2}|}{|\boldsymbol{p_1}|} \tag{4.35}$$

$$N_2 = \left\lfloor \frac{d_2}{|\boldsymbol{p_{2,\perp}}|} \right\rfloor + 1 \tag{4.36}$$

An illustration of this construction can be found in figure 4.12. To determine N_1 this procedure is applied in an analogous way.

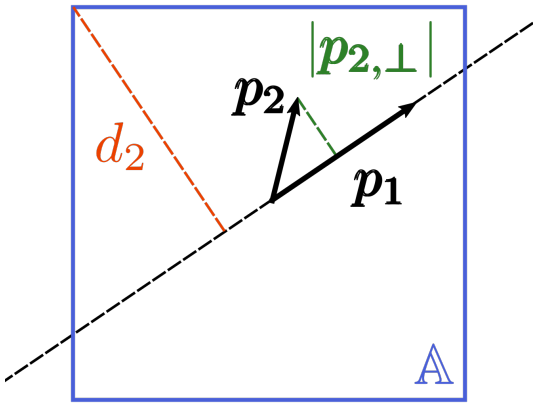

Figure 4.12.: Construction to identify the complete set of projection points (G_x,G_y) in the area of interest $\mathbb{A}$.

[7] To formulate it differently: It is impossible for $|n_2| > N_2$ that the linear combination $n_1\boldsymbol{p_1} + n_2\boldsymbol{p_2}$ is in the area of interest, independently of the choice on n_1.

4.3.4. Optimal Momentum Mesh Spacing

Integer values

As pointed out in subsection 4.1.1, the momentum mesh spacing $\Delta p_{x/y}$ should be chosen according to equation (4.2). Rounding issues are avoided by expressing $\boldsymbol{p_1}$, $\boldsymbol{p_2}$ and $\{(G_x,G_y\}$ as integer multiples of $\Delta p_{x/y}$. We denote this representation as **pixels**. Also simple expressions for the edge points of the VP are found in this representation. Other mesh spacings can break the periodicity of the VP, such that the set of momentum mesh points / pixels, expressed in relative coordinates to the corresponding projection point of the VP, slightly differs for different VPs. This leads to irregularly appearing overlap patterns of one pixel in $\tilde{n}(k_x,k_y)$, when back-folding $\tilde{\rho}(p_x,p_y)$.

4.3.5. Voronoi Plaquette Construction

VP format

The application of the Voronoi cutoff turns out to be numerically costly, if implemented in a non-optimal way. To assign the corresponding VP to each pixel is (in a naive implementation) proportional to $\mathcal{O}(|\{(p_x,p_y)\}| * N_{\mathrm{pp}}) \approx 10^9$ operations for looping over all combinations of pixels and projection points.[8]
A more efficient approach is, to calculate a list of the relative coordinates of all pixels, corresponding to the central VP, and use those as a mask to identify the VP around any projection point. The calculation of the mask is computationally cheap and explained in the next paragraph. The assignment of pixels to VPs can be performed in one loop over all projection points and another loop over the mask coordinates. This corresponds to $\mathcal{O}(N_{\mathrm{pp}} \frac{|\{(p_x,p_y)\}|}{N_{\mathrm{pp}}}) \approx 10^6$ operations.[9]

VP mask

To determine the VP mask, we first construct the VP boundary, by calculating the edge points of the VP from the vectors $\boldsymbol{p_1}$ and $\boldsymbol{p_2}$. To set up the VP mask, we start at the central pixel $\equiv$ (0,0) and check iteratively for increasing surrounding squares (1. central pixel, 2. neighboring 8 pixels, 3. next 16 pixels, ...), if the pixels belong to the central VP, i.e. the VP corresponding to projection point (0,0). As soon as no pixel of the current square belongs to the central VP, we can stop the iterative procedure and found all pixels of the VP mask.

VP boundaries

Cases appear, where a pixel can not be assigned clearly to a specific VP, as it has the same distance to two or even more 'closest' projection points. For those cases, a set of rules has to be defined, which assign this specific pixel to one of the VPs. These rules must apply in a way, that the periodicity of the VP construction is maintained, i.e. by assigning the pixels according to the VP mask around all projection points, we cover the full momentum grid in a gapless and overlap-free way. An example pseudocode for assigning VPs consistently in ambiguous cases is presented in algorithm 4.1.

[8] Assuming 2000 momentum channels for each direction and $N_{\mathrm{pp}} = 400$ projection points. Those values are typical for extrapolated spectra.
[9] The number of pixels per VP can be estimated as $|\{(p_x,p_y)\}|/N_{\mathrm{pp}}$.

1 Definition: **PPs** denotes the set Projection Points, which are situated closer to the pixel under consideration than any other projection point.
2 Is there one projection point with a smallest y-coordinate?
3 Yes: Assign the pixel to this projection point.
4 No: Reduce PPs to the projection points from PPs, which have the smallest available y-coordinate.
5 Assign the pixel to the projection point from PPs with the smallest x-coordinate.

Algorithm 4.1.: Algorithm in pseudo code for assigning a specific pixel to a VP for the case of multiple 'closest' projection points PPs.

4.3.6. Spiral Summation

Central VP

The most important speedup in the back-folding procedure is to take advantage of the VP symmetry, explained before. For that reason, it is sufficient to calculate the result of equation (4.1) not for every momentum mesh point, but just for those in the central VP. This reduces computing times by a factor of 5-1000, depending on $p_{\max}$ and the size of the VP. Considering only the central VP is a precondition for the numerically stable spiral summation.

Spiral summation

The order of the summation in equation (4.1) should be chosen such, that projections points further away from the central VP are summed up first. As $\rho^{(2\gamma)}(p_x,p_y)$ decays with increasing distance to the origin the summation at each point of the VP is performed in an numerical stable way (i.e. with increasing summand values).

4.3.7. Full Algorithm

1 Input: integer 1D arrays $\boldsymbol{p_1}_i$, $\boldsymbol{p_2}_i$ and 2D array $\tilde{\rho}_{jk}$
2 Construct projection points $\{\boldsymbol{G}_i\}$ from $\boldsymbol{p_1}_i$ and $\boldsymbol{p_2}_i$
3 Order $\{\boldsymbol{G}_i\}$ by decreasing distance to origin
4 Calculate VP as set of relative coordinate in pixels $\{\boldsymbol{q}_i\}$
5 Optional: Extrapolate $\tilde{\rho}_{jk}$ (recommended)
6 Optional: Apply a cutoff scheme to $\tilde{\rho}_{jk}$, Voronoi is recommended
7 Calculate equation (4.1) only for $(k_x,k_y) \in$ VP; Take thereby into account order of the $\{\boldsymbol{G}_i\}$

Algorithm 4.2.: Complete LCW back-folding algorithm in pseudo code

Preconditions

In algorithm 4.2 the complete pseudocode for LCW back-folding is presented. The subscript i denotes integer arrays of length two. So we assume the input to be prepared already, such that $\boldsymbol{p_1}_i$, $\boldsymbol{p_2}_i$ can be expressed as inter multiples of the optimal momentum mesh spacing $\Delta p_{x/y}$. Further we assume $\tilde{\rho}_{jk}$ to be defined on the same momentum mesh and hence shifts can be performed in step 7 without any interpolation.

Interpolation

If the input data is not available with the optimal meshing, an interpolation has to be

performed before step 1. Alternatively, step 7 can be implemented such, that the interpolation is performed there. This is not recommended however, as two different mesh spacings would appear in the code. Further, this implementation lacks the possibility to directly compare $\tilde{\rho}_{jk}$ with its interpolated version.

Part III.

Application on Realistic Systems

5. Silver (Ag): Extracting Fermi Surface Parameters

Agenda

In this section, we will parameterize the Fermi surface of silver by applying the toolbox we developed in section 3.3. Our starting point is a theoretical Elk calculation with the experimental lattice constant 7.72 a.u. = 4.08 Å, leading to

$$\frac{2\pi}{a} = 0.81\,\text{a.u.} \tag{5.1}$$

If units are not pointed out explicitly, we refer to momenta in multiple of $\frac{2\pi}{a}$. We start with a description of the Fermi surface of silver and its parameters (theoretically and experimentally). In the scope of this section, we systematically analyze the effects, which influence the experimentally measured 2D-ACAR spectrum: Staring from a purely electronic theoretical perspective, we stepwise include physical effects (positron wave function and electron-positron enhancement, section 5.3) and effects origination from the experimental realization (detector resolution and counting statistics, section 5.4). The full experimental dataset will be investigated in section 5.5.

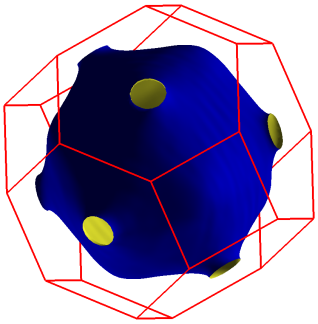

Figure 5.1.: Fermi surface of silver, Elk calculation:
Illustration of Fermi surface and Brillouin zone for further analysis.

Back-folding

In our analysis of $n^{(2\gamma)}(k_x,k_y)$ we will not investigate cuts through the spectrum across the boundaries of the VP. Hence truncation artifact formation around the VP is not a problem and we apply the Voronoi cutoff, to avoid artifacts inside the VP. For the same reason only modest extrapolation with $f_{\text{ex}} = 1.4 \approx \sqrt{2}$ is used. This ensures that the original spectrum is still contained in $\rho^{2\gamma}(p_x,p_y)$ after applying the cutoff, while keeping extrapolation artifacts to a minimum. The momentum range of the spectra is $p_{\text{max}} = 4.0\,\text{a.u.}$ (Elk) and $p_{\text{max}} = 2.9\,\text{a.u.}$ (experimental). Back-folding (i.e. truncation and extrapolation) artifacts were verified to have no influence in this analysis.

5.1. Electronic Structure of Silver

Fermi surface

The Fermi surface of silver is approximately a sphere (**belly**) with **necks** at the L-Point, where a connection is made to the neighboring Brillouin zone (compare figure 5.1). Due to its simple form, the Fermi surface is parameterized by a few parameters, being the radii of the belly in the directions [100], [110] and [112] as well as the radius of the neck. For this reason silver, along with other simple metals, has been investigated extensively, acting as a benchmark for experimental and theoretical frameworks. The results of de Haas-van Alphen measurements are known to achieve the highest precision and can be taken as a reference on an experimental level. On a theoretical level we determine the Fermi surface parameters by a band structure calculation (figure 5.2). Table 5.1 lists the theoretical and experimental results for the Fermi surface parameters.

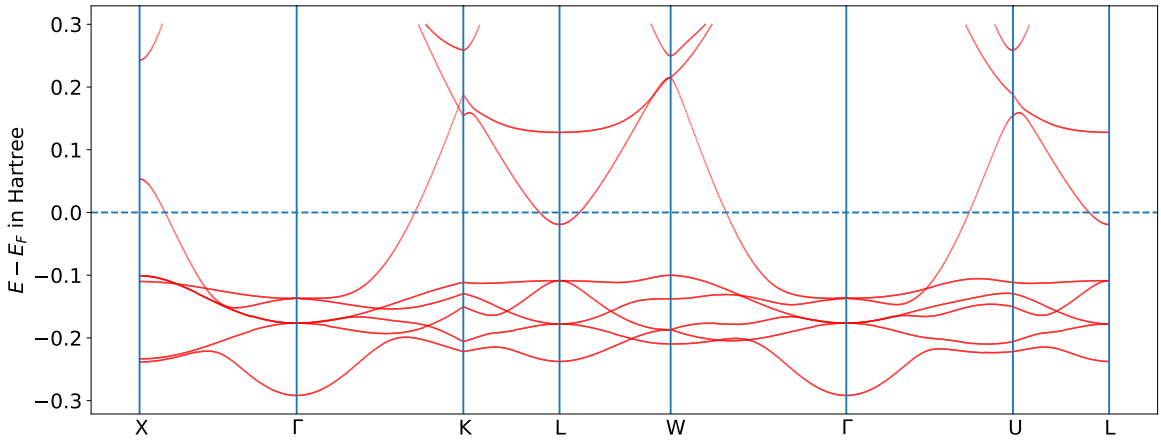

Figure 5.2.: Band structure of silver, Elk calculation: Fermi surface parameters are measured along the symmetry lines according to table 5.1.

parameter	from	to	theory	experiment
r_{100}	Γ	X	0.8406	0.8195
r_{110}	Γ	K	0.7440	0.7531
r_{112}	Γ	-	-	0.7807
r_{neck} (mean)	L	-	-	0.1064
$r_{\text{neck,LW}}$	L	W	0.1184	-
$r_{\text{neck,LK}}$	L	K	0.1307	-
$r_{\text{neck,LU}}$	L	U	0.1307	-

Table 5.1.: Fermi surface parameters of silver in units of $\frac{2\pi}{a}$:
Theoretical results from an Elk band structure calculation shown in figure 5.2. The experimentally determined parameters are averaged from references [205–208].

5.2. Fermi Surface Parameterization Based on Theoretical Data

Idea

Our target is to extract the same parameters from theoretical ACAR spectra to demonstrate our methodology. To minimize method dependent differences we perform both, the band structure and the ACAR calculation, within the Elk code [189, 190].[1]

Overview

We investigate the spectra of silver, shown in figure 5.3. The top row shows $n(k_x,k_y)$, obtained by back-folding $\rho(p_x,p_y)$. Even though $\rho(p_x,p_y)$ is experimentally not accessible, we use the freedom of theoretical simulations, to generate purely electronic back-folded spectra. Commonly the three integration directions [001] (left), [110] and $[11\bar{1}]$ (right) are investigated in 2D-ACAR. We do not present results for the [110] direction, as no FS parameter can directly be extracted from it. We determine the FS parameters, by checking for kinks in the cuts through $n(k_x,k_y)$ along the paths (a)-(f'), defined in figure 5.3.[2] The dots along the paths are put at the expected position of the Fermi surface, according to the band structure calculation for theoretical data or dHvA measurements for experimental data. For a quick analysis we present the SDDn of $n(k_x,k_y)$ in figure 5.3 c and d, where we expect the dots to be situated on sharp red curves.

FS features

The [001] projection gives us access to r_{100} denoted by (a) and (a'). The Fermi surface bellies are oriented such, that they slightly overlap at the L-points. This leads to four high intensity areas at $(k_x = \pm 0.5, k_y = \pm 0.5)$, including two neck signatures, each. Even though it might be possible to extract information about r_{neck} from this projection direction, this can be achieved with less effort from the $[11\bar{1}]$ integration direction.
For this projection the eight necks of the FS can be grouped into:

- Two **necks at the origin**, paths (c-e), pointing directly up- / down-ward and forming a completely occupied tube along the three-dimensional $\boldsymbol{k}$-space.
- Two **horizontal necks**, path (f), $(k_x = \pm\sqrt{\frac{2}{3}}, k_y = 0)$, connecting to the neighboring bellies in k_x direction.
- Four **diagonal necks**, path (f'), at $(k_x = \pm 1/\sqrt{6}, k_y = \pm 1/\sqrt{2})$, connecting to the neighboring bellies in diagonal direction. Those connections are hardly visible in figure 5.3 b and d.

The belly radius along [110] can be measured at (b). Unfortunately it is not possible to find an integration direction in silver to measure the radius of the Fermi surface belly in [112] direction. The integration along a momentum direction in combination

[1] There is no publication of the 2D-ACAR implementation in Elk, which is an extension of [190] for positrons. The first results were published in [191].

[2] Paths through k_x-k_y-space are denoted by closed brackets (...), while subplots of figures are referenced without brackets. The order of paths is given as: (a), (a'), (b), (c), (d), (e), (f), (f'). Hence, a range of paths might include primed paths. For instance (a)-(b) is equivalent to (a), (a') and (b).

with the vicinity to the neck of the Fermi surface prohibits this. We therefore have to restrict ourself to analyze the other parameters.

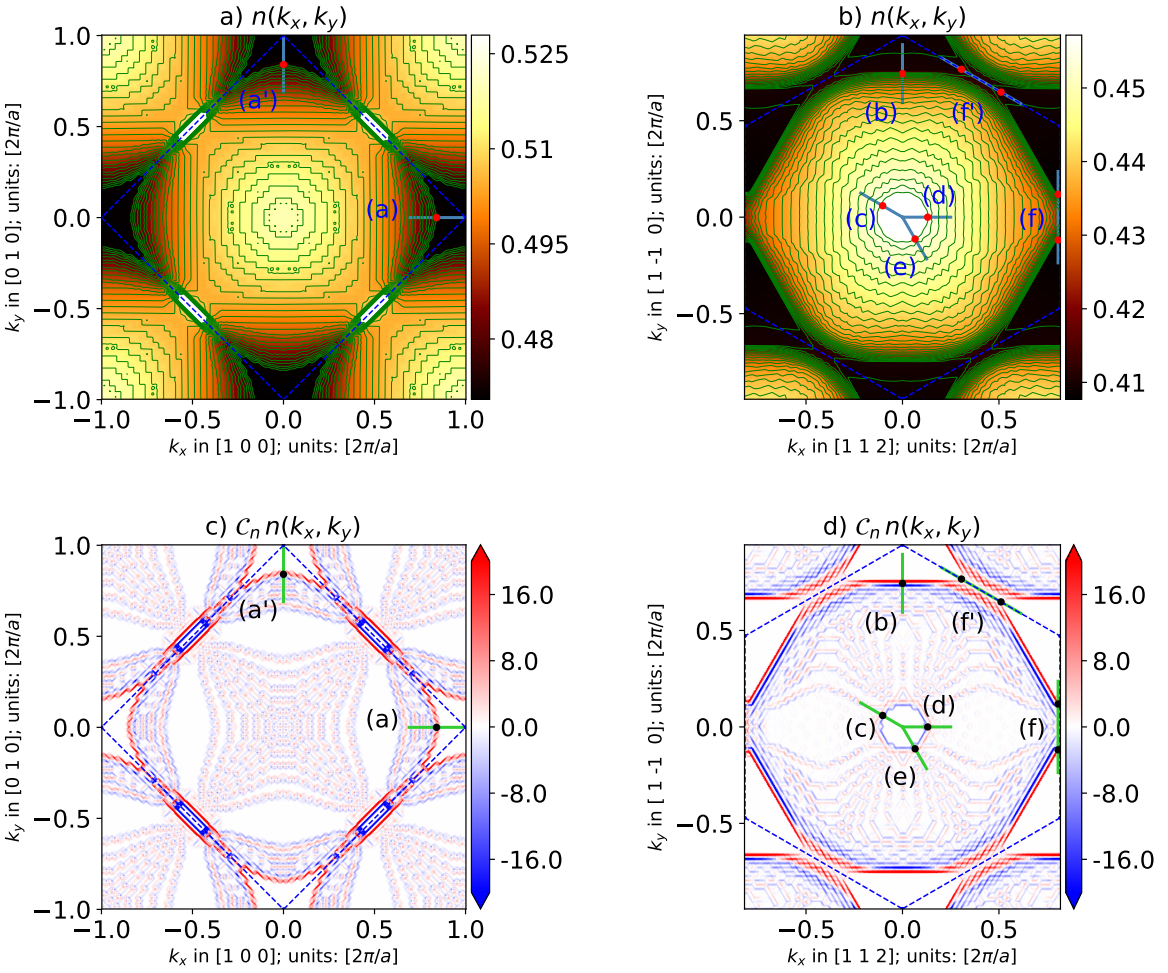

Figure 5.3.: $n(k_x,k_y)$ for silver, Elk calculation:
Dots mark the position of the expected position of the Fermi surface signatures (as calculated in the band structure calculation). Lines labeled with (a)-(f') denote paths through k_x-k_y-space, used to determine the position of the Fermi surface by finding the corresponding kink.

Analysis of L-necks

Surprisingly, we see that the diagonal and horizontal necks have a different intensity. Considering the geometry of the Brillouin zone it is expected, that these necks should be identical for this projection direction. We resolve this issue at the end of this section. We will present examples, how some Elk-code internal meshing influences the intensity distribution and the position of Fermi surface signatures. These effects are especially strong at points with a high intensity gradient, like the necks.

While we can determine the radius of the neck in LW direction from (f) and (f'), the necks at the origin allow us to measure the neck radius in all symmetry directions:

$$\begin{aligned}(\mathrm{c}) &\rightarrow r_{\mathrm{neck,LW}}\\ (\mathrm{d}) &\rightarrow r_{\mathrm{neck,LK}}\\ (\mathrm{e}) &\rightarrow r_{\mathrm{neck,LU}}\,.\end{aligned}$$

Cuts

To determine the Fermi surface parameters, we analyze $n(k_x,k_y)$ along the paths (a)-(f'). We denote this as $n(k_{\mathrm{path}})$. The results can be found in figure 5.4 as the 'ngridk=64' graph.[3] The Fermi level, as calculated by the band structure calculation, is indicated by the vertical dashed red line. We expect to see the kink of each curve (vertical dashed brown line) at the position of the Fermi level, within a range of plus/minus the momentum mesh spacing $\Delta k \equiv \Delta p \in [\Delta p_x,\Delta p_y]$. The Δk is indicated as the black line in the lower left corner for each direction. While the Fermi surface parameters in (a)-(c) are (at least approximately) captured within this precision, the parameters in (d)-(f') show a strong disagreement with the band structure result.

Dependence on ngridk

A careful analysis showed, that the Elk internal crystal momentum mesh in the irreducible wedge of the BZ, which is used for the **Linear Tetrahedron Method (LTM)** interpolation [190], is responsible for these deviations. The parameter **ngridk**, thereby defines the number of the internal $\boldsymbol{k}$-space mesh points.[4] In figure 5.4 the kinks in $n(k_{\mathrm{path}})$ are caused by interpolation between those internal mesh points. Smoother curves are created, when the path passes through areas with a low internal mesh point density.
Unfortunately, computational costs increase drastically with the value of the ngridk parameter, so ngridk=64 is the largest realizable setting. The other graphs in figure 5.4 show $n(k_{\mathrm{path}})$ for other values of the ngridk parameter. For a better overview, the vertical lines mark the position of the Fermi surface signature for each graph. We see that a larger number of internal mesh points corresponds to a higher capability to catch the exact position of the Fermi surface kink. There are exceptions, of course, where a higher ngridk parameter leads to a less favorable distribution of mesh points. In subplot f', for instance, we see a case, where the internal mesh points for ngridk=48 happens to be closer to the Fermi level, than for ngridk=64. The further theoretical analysis in this section is based on exactly those type of cuts through integrated momentum densities. Therefore, we will use the kink positions of ngridk=64 in figure 5.4 as a reference instead of the band structure calculation.

Take home message

The internal mesh, used for integrated momentum distribution calculations (like 2D-ACAR), prohibits an exact reconstruction of the Fermi level. This is concluded from the comparison with a band structure calculations from the same code. The difference between the band structure results and the 2D-ACAR spectra can be $0.03\,\frac{2\pi}{a} \approx 0.02\,\mathrm{a.u.}$

[3] 'ngridk' is an Elk internal meshing parameter, which is going to be introduced later in this subsection.

[4] The parameter 'ngridk' shall not be confused with the Elk parameter 'nints'. The latter determines the momentum mesh spacing Δp_x, Δp_y.

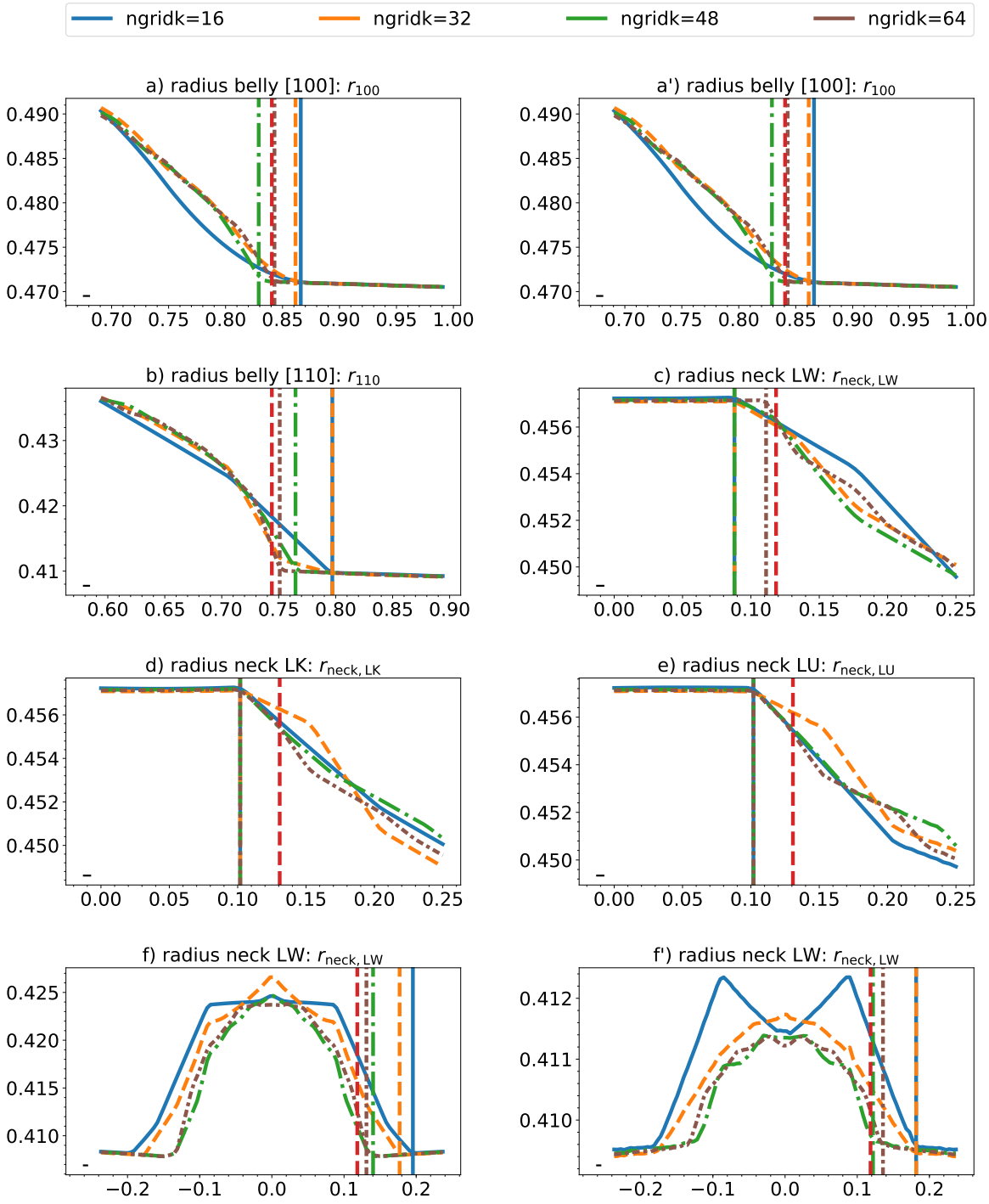

Figure 5.4.: Dependence of $n(k_{\mathrm{path}})$ on the Elk internal parameter 'ngridk' [190]: $n(k_{\mathrm{path}})$ denotes the cuts through $n(k_x,k_y)$ along the k-paths defined in figure 5.3. Vertical lines mark the kink position. The red vertical line indicates the expected position based on the band structure calculation. The momentum mesh spacing is indicated by the black bar in the lower left corner.

5.3. Including Positron Effects

Agenda

In a first step towards realistic spectra, we include the contributions of the positron. These are the weighting with the positron wave function (denoted as n^{IPM}) and the electron-positron enhancement, compare section 3.1. Both are contained in 2D-ACAR measurements. Even though we know, that the steps in $n^{2\gamma}(k_x,k_y)$ are not shifted by any of those effects, the question arises if differences occur on a practical level with the integration in one momentum direction and numerical effects taken into account.

Qualitative overview

Figure 5.5 compares $n(k_x,k_y)$, $n^{\mathrm{IPM}}(k_x,k_y)$ and $n^{2\gamma}(k_x,k_y)$, which include different positron effects. We additionally point out the differences between those quantities in figure C.1, to make a comparison in amplitude easier.
As seen already in figure 5.3, the mesh of the LTM interpolation captures only a weak signature from the L-neck at (f'). Therefore, we do not expect to see the same influences on the diagonal necks compared to the horizontal ones.

Positron wave function

To see an increase of the intensity inside the Fermi volume for $n(k_x,k_y) \rightarrow n^{\mathrm{IPM}}(k_x,k_y)$ in figure 5.5 is not surprising and in analogy to our findings in figure 3.2. The positron wave function emphasizes low momenta states in $\rho^{\mathrm{IPM}}(p_x,p_y)$, leaving less spectral weight for the area outside the FS after back-folding.
It is striking, that the L-necks get overemphasized by the positron wave function: While $n(k_x,k_y)$ has only a slightly higher density at the L-Point projection compared to the origin (compare figure 5.5a or the three-dimensional Fermi surface in figure 5.1), the intensity increase by the IPM is twice as large (compare figure C.1a). To understand this, we remember, that by Fourier transformation the intensity at the L-points originates from wave functions of the form $\Psi(\boldsymbol{r}) = \prod_i \sin(\frac{\pi}{a} r_i)$ and $\Psi(\boldsymbol{r}) = \prod_i \cos(\frac{\pi}{a} r_i)$ in real space. The positron distribution in real space is oscillating with the same period, which reinforces the sinus character of the electron-positron wave function.

Enhancement

The comparison $n^{\mathrm{IPM}}(k_x,k_y) \rightarrow n^{2\gamma}(k_x,k_y)$ in figure 5.5 presents the additional influence of enhancement, see also figure C.1 c and d. Due to the increase of the intensity directly below the Fermi level, the L-necks get particularly emphasized, as they include a large fraction of energetically high states. The intensity increase at the origin in figure C.1d is thereby stronger than the one at the position of the horizontal L-necks, as two L-necks are projected onto that point.
As pointed out in the discussion about figure 3.2, enhancement leads to a more homogeneous electron distribution. We therefore see an increase in intensity at the Γ-point and the surrounding region of small momenta. This is the inner part of the Fermi Volume, which is also increased in intensity, as we see in figures C.1 c and d.

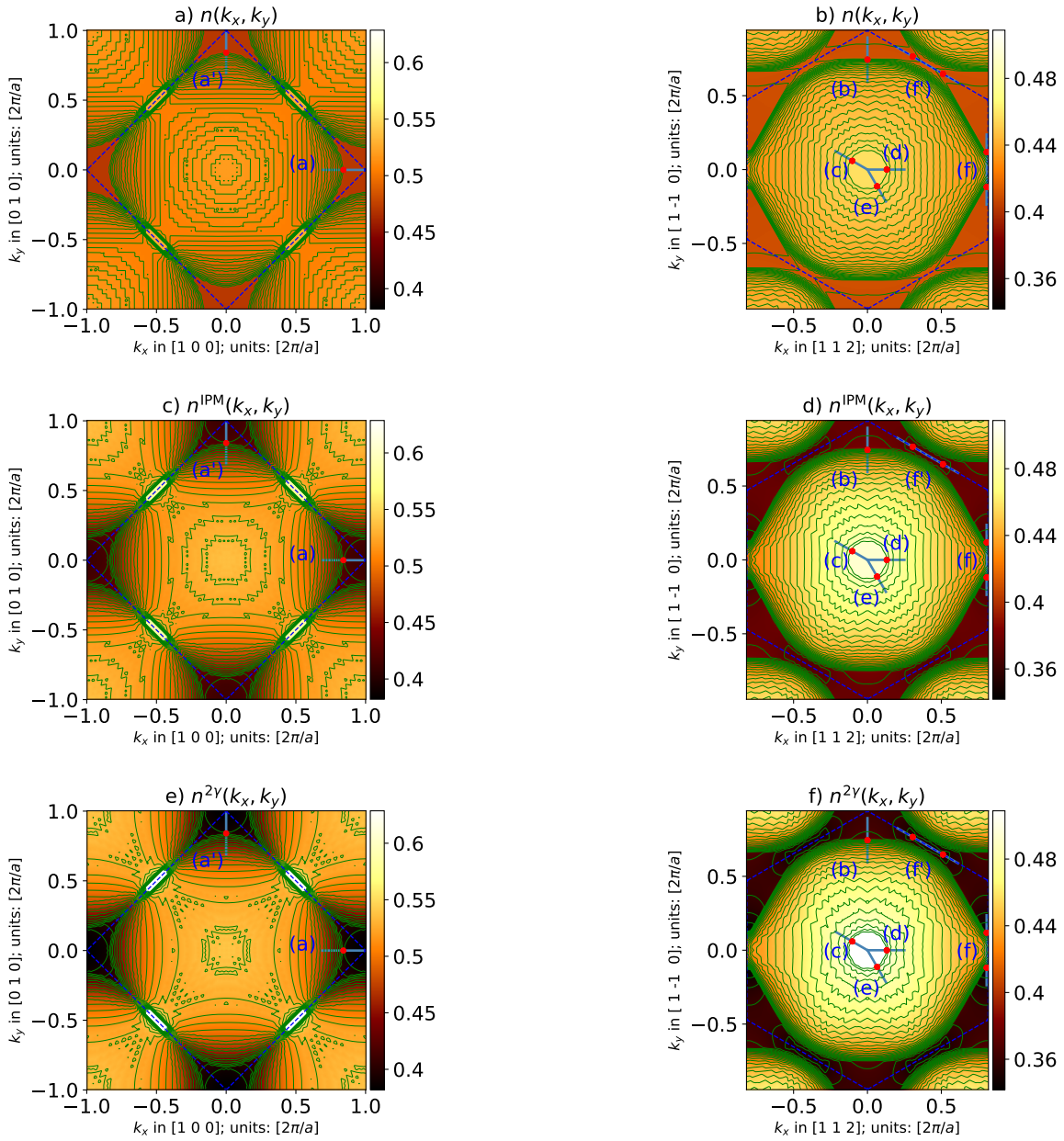

Figure 5.5.: Influence of positron wave function and enhancement, Elk calculation:
First row: No positron effects, compare figure 5.3 a and b.
Second row: Additional influence of the positron wave function;
Third row: Additional influence of electron-positron enhancement;
Note that the color scale was unified.

Spectra along paths

Figure C.2 shows cuts through $n(k_x,k_y)$, $n^{\mathrm{IPM}}(k_x,k_y)$ and $n^{2\gamma}(k_x,k_y)$ along the predefined paths (a) - (f'). For reasons of comparability the curves are rescaled to the same y-range. Detailed data (including the y-values, the curvature along the path $\partial^2_{k_{\mathrm{path}}} n^{(2\gamma)}(k_{\mathrm{path}})$ and the SDDn $[\mathcal{D}^2_n n](k_{\mathrm{path}})$) can be found in figures C.3, C.4 and C.5. The green vertical scale on the right refers to the curvatures $\partial^2_{k_{\mathrm{path}}} n^{(2\gamma)}(k_{\mathrm{path}})$ and $[\mathcal{D}^2_n n](k_{\mathrm{path}})$.

In these figures we find quantitative information about the signature from the diagonal necks: While the intensity at the horizontal necks increases with more positron effects $(1 \to 5 \to 8) \times 10^{-2}$ the intensity at the diagonal necks decreases as $(1.5 \to 1 \to 1) \times 10^{-3}$.

Influence on FS signatures

As expected, the position of the Fermi signature is not shifted. Even though the kink intensity increases with additional positron effects, the curvature within the spectrum is increased as well, due to the shift in spectral weight to low momenta. For this reason, there is only a slight improvement in the signal-to-background ratio of Fermi signatures by positron effects. We illustrate this in figure C.6, showing the SDDn of figure 5.5. One potential issue arises from the shift of spectral weight. Fermi surface signatures from bands with d and f character, contributing mainly to intermediate momenta in $\rho^{2\gamma}(p_x,p_y)$, will have less intensity. This does not concern the analysis of silver, but plays a role for molybdenum in chapter 7.

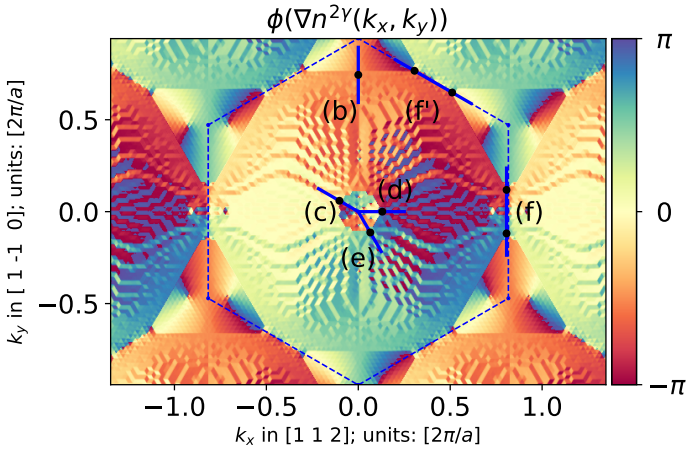

Figure 5.6.: Gradient direction for $n^{2\gamma}(k_x,k_y)$ in range $(-\pi,\pi]$, Elk calculation: The gradient direction flips by π at (f) and (f').

Curvature and SDDn

We investigate now figures C.3, C.4 and C.5 concerning $\partial^2_{k_{\text{path}}} n^{(2\gamma)}(k_{\text{path}})$ and $[\mathcal{D}^2_n n](k_{\text{path}})$. As paths (a)-(e) follow the gradient direction, it is not surprising, that the two quantities agree. An analysis is more difficult along paths (f) and (f'), as those are situated on the symmetry line between areas with opposite gradient directions (compare figure 5.6). The SDDn in not numerically stable along those paths, as the gradient direction is highly sensitive to numeric noise. This explains the differences between $\partial^2_{k_{\text{path}}} n^{(2\gamma)}(k_{\text{path}})$ and $[\mathcal{D}^2_n n](k_{\text{path}})$, which are magnified in the analysis of the curvature on the right. Differences are stronger along path (f') compared to path (f), as the amplitude of the signature is an order of magnitude smaller and the pixels are not distributed according to the symmetry of the surrounding.
Besides all problems with the LTM mesh and numerical instabilities, the SDDn, displayed in figures C.3f', C.4f' and C.5f', shows clear peaks for the Fermi surface signatures. Also in figure C.6 low intensity signatures from the L-necks along path (f') can be found (at least using a digital zoom in a pdf document). So identifying Fermi

surface signatures by extrema in the SDDn is a strategy, which also works for weak signatures.

Take home message

To summarize, we found that positron effects do not change the position of the Fermi surface signature. Both the curvature and the SDDn are suitable ways for detection. The dominant effect of the positron is an overall increase of intensity at low momenta (p_x,p_y). This includes the danger of overlooking Fermi surface signatures with d and f band character, being found at intermediate momenta of $\rho^{2\gamma}(p_x,p_y)$.

5.4. Including Experimental Circumstances

In a next step we include the experimental resolution and the counting noise into our considerations. The subscript σ denotes the additional influence of experimental resolution. As seen in figure 1.3, Fermi surface signatures can be shifted by this influence. The shift is (in the 1D model) proportional to the second derivative of $n^{(2\gamma)}(k_{\mathrm{path}})$. From the preconditions for the derivation of equation (1.29), we expect a system with a spherical Fermi surface, as silver, to be a particularly good example for demonstration.

5.4.1. Experimental Resolution

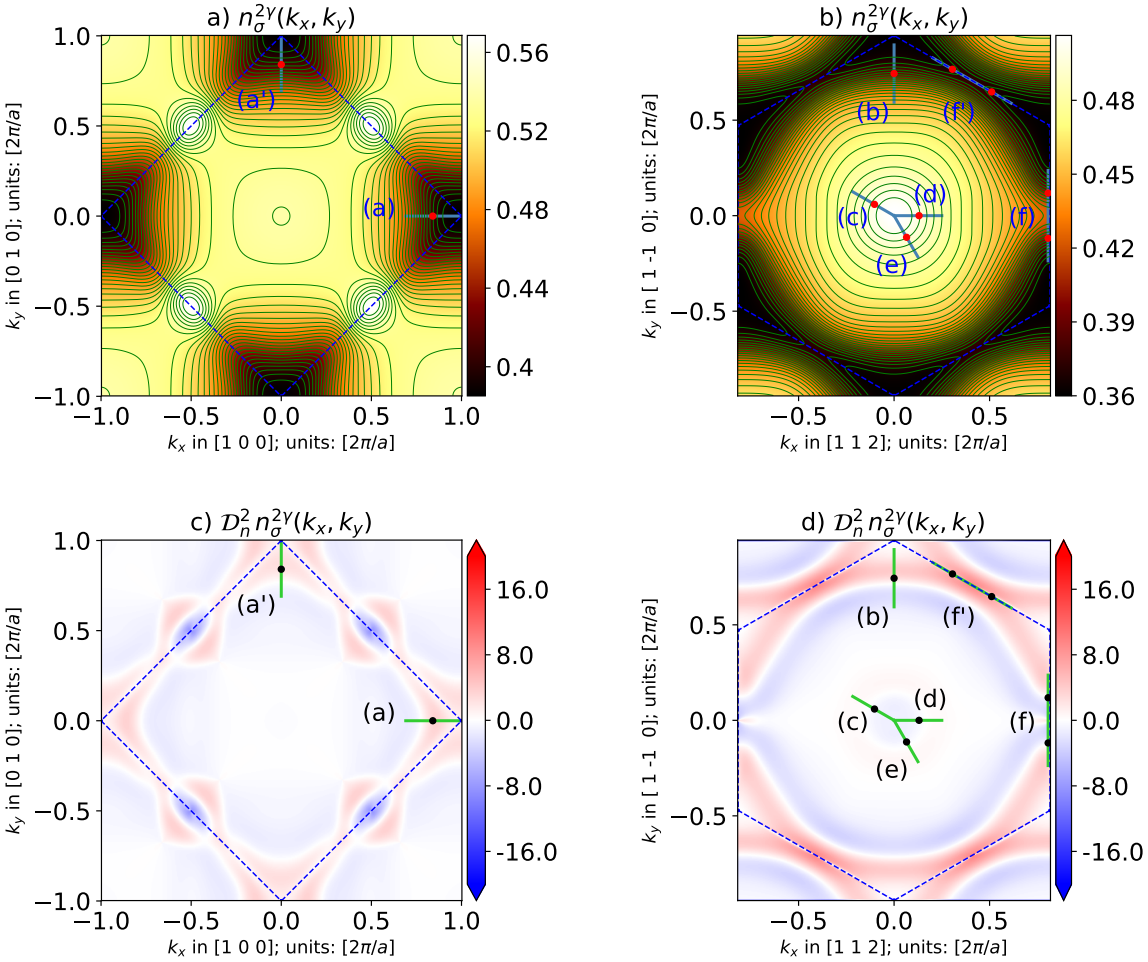

Figure 5.7.: $n_\sigma^{2\gamma}(k_x,k_y)$ for silver, Elk calculation:
Influence of the experimental resolution on $n^{2\gamma}(k_x,k_y)$, compare figure 5.3.

Experimental resolution

As mentioned in section 1.2.2, the experimental resolution is included by folding $\rho^{(2\gamma)}(p_x,p_y)$ with a two-dimensional Gaussian distribution with standard deviation

$$\begin{aligned}\sigma_0 &= 0.04654\,\text{a.u.}\\ \sigma_1 &= 0.06051\,\text{a.u.}\end{aligned} \tag{5.2}$$

and afterwards back-folding it to obtain $n^{(2\gamma)}(k_x,k_y)$. On a picture processing level this operation in known as applying a **Gaussian filter** or **Gaussian blur**. For brevity we will make use of those expressions. To stay as close as possible to the experimental conditions, we choose the following standard deviations for the Gaussian filter.
001 projection:

$$\begin{aligned}\sigma_x &\equiv \sigma_{100} = \sigma_0\\ \sigma_y &\equiv \sigma_{010} = \sigma_1\end{aligned} \tag{5.3}$$

$11\bar{1}$ projection:

$$\begin{aligned}\sigma_x &\equiv \sigma_{112} = \sigma_1\\ \sigma_y &\equiv \sigma_{1\bar{1}0} = \sigma_0\,,\end{aligned} \tag{5.4}$$

where x/y represents the horizontal/vertical direction. For the equations in subsection 1.2.2 $\sigma_{\text{l/t}}$ are constructed according to the direction of each path.

Influence

Figure 5.7 shows the influence of experimental resolution on $n^{2\gamma}(k_x,k_y)$. In comparison with figure 5.3, we see that the signatures are not only blurred, but are additionally changed in shape. This can be observed for examples in subplot a by the low intensity area around the X point at ($k_x = \pm 1, k_y = 0$) or in subplot b by the shape of the belly at ($k_x \approx \pm 0.6, k_y \approx \pm 0.4$). The resulting SDDn is not suitable for a quantitative analysis of the Fermi surface anymore, but still represents its shape. This is enough to identify the relevant k_x-k_y-space paths, as done already in figure 5.3. To correct the kink shift by experimental resolution, we will perform a fit of the available data to the two models presented in subsection 1.2.2. One of the fitting parameters, thereby, is the position of the Fermi surface.

Fitting

This procedure is demonstrated in figure 5.8. Each row shows the absolute values (left) and the curvature (right) of $n^{2\gamma}(k_{\text{path}})$ in different variations (with and without experimental resolution, model fits) along the paths (a)-(f'). As the kinks in $n^{2\gamma}(k_{\text{path}})$ are much sharper, we use a different y-scale in the right column (blue) to show its curvature. All other curves refer to the black y-axis. The two models, designed to mimic experimental resolution (i.e. 1D model and polar model), are fitted by curvature (compare next paragraph) to $n_\sigma^{2\gamma}(k_{\text{path}})$. The fitting range is marked with the black dashed vertical lines. The initial guess for the Fermi surface parameter in the fitting procedure is marked as the gray dashed vertical line. The fitting range is for all paths set to $\pm\sigma$ around this initial guess. The vertical lines with a color corresponding to a graph mark either the position of the maximal curvature ($n^{2\gamma}$ and $n_\sigma^{2\gamma}$) or the fitting parameter for the Fermi surface ('1D model' and 'polar model'). Table 5.2 contains the exact values of those parameters.

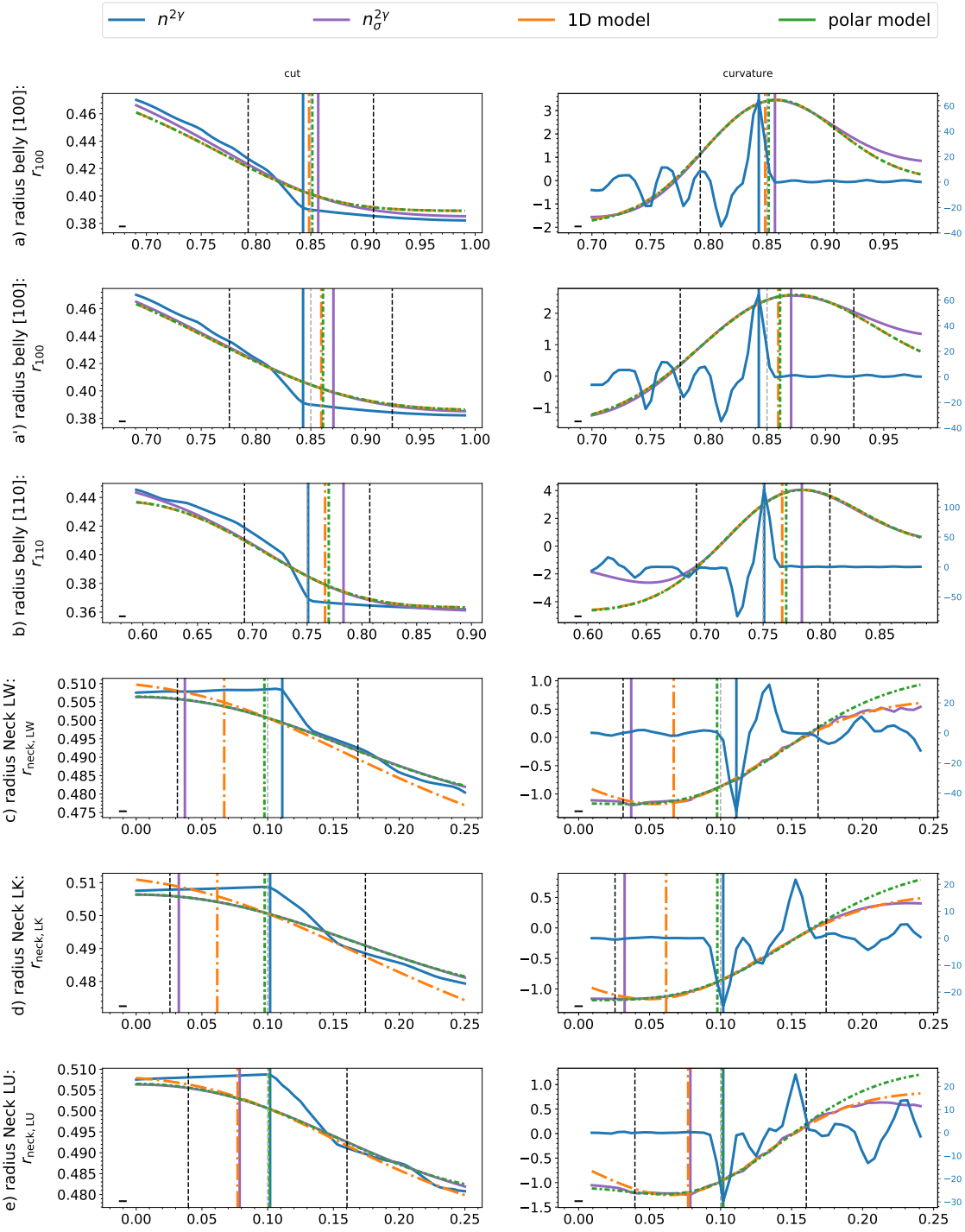

Figure 5.8.: Extraction of the Fermi surface parameters from $n_\sigma^{2\gamma}(k_x,k_y)$, Elk calculation:
Analysis based on figure 5.7.
Vertical lines:
black and gray) fitting range and initial guess for Fermi surface parameter;
blue) reference Fermi surface parameter;
purple) maximum curvature of $n_\sigma^{2\gamma}(k_{\text{path}})$ (i.e. with experimental resolution);
orange and green) reconstructed Fermi surface parameter by fitting models;

Fit by curvature

Two fitting methods were investigated:
The **fit by value** method was performed by fitting equations (1.25) or (1.36) to the spectrum along the path $n_\sigma^{2\gamma}(k_{\text{path}})$. The results of this fitting method are not presented in this work.
The **fit by curvature** is performed by fitting equation (1.28) or the twice numerically differentiated version of equation (1.36) to the curvature of the spectrum along the path $\frac{\partial^2 n_\sigma^{2\gamma}(k_{\text{path}})}{\partial k_{\text{path}}^2}$.
When evaluating both methods with respect to their ability to reconstruct $n_\sigma^{2\gamma}$ the fit by curvature is clearly favorable. It also gives better estimates for the Fermi surface parameters. The reason for this is the larger modulation in curvature, making the numerical fitting procedure more reliable.

Analysis model fits

Our objective is to reproduce the Fermi surface parameter based on the available data $n_\sigma^{2\gamma}(k_{\text{path}})$. The graphs along the paths (c)-(e) in figure 5.8 demonstrate, that the maximum in curvature can be shifted away drastically from its original position by the influence of experimental resolution, compare therefore the purple and blue vertical lines. We see along all paths an improvement for the Fermi surface parameter, suggested by the fitting models. The quality of the suggested parameter depends on the applicability in the area of $n_\sigma^{2\gamma}(k_x,k_y)$ around each cut. While both fitting models show a close agreement for the analysis along paths (a)-(b), the polar model can flexible adjust to the approximately polar symmetry of $n_\sigma^{2\gamma}(k_x,k_y)$ at paths (c)-(e). The resulting improvement compared to the 1D model is drastic. We find our prediction from equation (1.41) fulfilled. A potential disadvantage of the polar model is, that it depends on more free parameters. This makes it sensitive to **overfitting** when only a few data points are available. In the context of this work overfitting was not observed, however.

Take home message

Experimental resolution can drastically shift Fermi surface signatures. In silver, these effects can be observed very clearly for two reasons: First, due to the strong curvature of $n^{2\gamma}(k_{\text{path}})$ on one side of the Fermi surface kink. Second, due to the single Fermi surface sheet, which avoids overlapping signatures. By using a 'fit by curvature', we evaluated the two fitting models, introduced in section 1.2.2, with respect to their ability to extract the Fermi surface parameterization. Both fitting models yielded significant improvements. As expected, the numerically more demanding polar model is preferable circular Fermi surface signatures with a small radius.

5.4.2. Poisson Noise

Counting statistics

We investigate the influence of the counting statistics on the Fermi surface parameters. As Poisson noise is an influence on level of the detector signal, $n^{2\gamma}(k_x,k_y)$ is constructed from $\rho^{2\gamma}(k_x,k_y)$ by:

- removing the geometric correction,
- applying Poisson noise,
- applying a Gaussian filter (to include experimental resolution),
- taking the geometric correction back into account and
- back-fold this quantity to yield $n^{2\gamma}_{\mathrm{Pois}}(k_x,k_y)$.

For simplicity, we drop the subscript 'Pois'. We see the result of the counting statistics corresponding to 200 and 8 million counts in figures C.7 and C.8. This is the range of counts typically used in experiments [65–67, 203]. While $n^{2\gamma}_{\sigma}(k_x,k_y)$ is in reasonable agreement with the reference (figure 5.7) in the case of 200 million counts, significant deviations appear for 8 million counts. Particularly the tube structure at the origin, motivating the analysis along the k-paths (c), (d), (e), is not clearly visible in the SDDn plot anymore. Hence, from the very beginning on, a priori knowledge of the Fermi surface is needed, to perform an analysis under the influence of such a strong Poisson noise.

Symmetrizing

Even for a large number of counts a slight asymmetry is introduced into $n^{2\gamma}_{\sigma}(k_x,k_y)$, as can be seen by the contour lines in figure C.7 a and b. We symmetrize the spectrum for further analysis

$$\frac{1}{4}\left(\rho^{2\gamma}_{\sigma}(p_x,p_y)+\rho^{2\gamma}_{\sigma}(-p_x,p_y)+\rho^{2\gamma}_{\sigma}(p_x,-p_y)+\rho^{2\gamma}_{\sigma}(-p_x,-p_y)\right)\rightarrow\rho^{2\gamma}_{\sigma}(p_x,p_y) \tag{5.5}$$

as it is typically done in the post production process of experimental data.

Fermi surface

Figures C.9 and C.10 show the Fermi surface reconstruction by parameter fitting for weak and strong Poisson noise, analogue to figure 5.8. Table 5.2 lists explicitly the new positions of the Fermi surface signatures and should be used for a fast comparison of the figures 5.8, C.9 and C.10.
From experience, the influence of the Poisson noise corresponding to 200 million counts is minor and leads to negligible shifts in the extracted Fermi surface parameters. This is confirmed when comparing block b and c in table 5.2.
In the case of 8 million counts, the strong disturbance by Poisson noise can lead to strong deviations in the extracted Fermi surface parameters. For demonstrative purposes, the specific realization of noise was chosen such, that a typical range of deviations is found, when comparing the analyses along different paths. While the extracted parameterization is the same as for 200 million counts along path (c), strong changes occur along paths (b) and (d). Also average deviations can lead to an improvement or to a worsening of the Fermi surface parameterization, compare paths (a) and (a'). As

	(a) r_{100}	(a') r_{100}	(b) r_{110}	(c) $r_{\mathrm{neck,LW}}$	(d) $r_{\mathrm{neck,LK}}$	(e) $r_{\mathrm{neck,LU}}$
a) no experimental effects, reference						
$n^{2\gamma}$	0.843	0.843	0.751	0.111	0.102	0.102
b) experimental resolution only, compare figure 5.8						
$n_\sigma^{2\gamma}$	0.857	0.871	0.783	0.037	0.032	0.079
1D model	0.848	0.860	0.766	0.067	0.062	0.077
polar model	0.851	0.861	0.770	0.098	0.098	0.101
c) experimental resolution and Poisson noise (200 million counts), compare figure C.9						
$n_\sigma^{2\gamma}$	0.857	0.866	0.783	0.037	0.042	0.079
1D model	0.848	0.856	0.766	0.069	0.065	0.074
polar model	0.851	0.858	0.770	0.100	0.101	0.099
d) experimental resolution and Poisson noise (8 million counts) compare figure C.10						
$n_\sigma^{2\gamma}$	0.843	0.880	0.829	0.037	0.009	0.079
1D model	0.845	0.866	0.790	0.070	0.048	0.094
polar model	0.848	0.868	0.793	0.101	0.085	0.117
Parameters						
σ_l	0.0465	0.0605	0.0465	0.0559	0.0605	0.0491
σ_t	0.0605	0.0465	0.0605	0.0491	0.0465	0.0559

Table 5.2.: Corresponding Fermi feature positions from figures 5.8, C.9 and C.10. The reference values (from ngridk=64 in figure 5.4) are given as well. The momentum mesh spacing ≈ 0.0046 gives an estimate for the best expectable agreement.

will be discussed in section 5.5, the analysis along path (b) is numerically difficult. We see, that strong Poisson noise has a divesting influence here.

Take home message

Bad counting statistics can prevent an analysis by model fitting. 200 million counts and a symmetrized spectrum turned out to be suitable basis for extracting the Fermi surface parameters of silver. 8 million counts for a 2D-ACAR spectra can be considered as too few. The number of counts, necessary to analyze a specific feature of $n^{2\gamma}(k_x,k_y)$, depends on the position and the shape of this feature. Due to the better signal-to-noise ratio, signatures, appearing at small momenta $|(p_x,p_y)|$ in $\rho^{2\gamma}(p_x,p_y)$, can be analyzed with a smaller number of counts.
To determine the necessary number of counts for the analysis of a specific feature, this analysis should be performed (on experimental or theoretical data) under different realizations of the corresponding Poisson noise. From there, statistical error bars can be constructed.

5.5. Analysis of Experimental Results

Experimental data

We analyze the experimental $n^{2\gamma}_{\text{exp.}}(k_x,k_y)$ of silver (figure 5.9, subscript 'exp.') to extract the Fermi surface parameterization. The measurements were performed with 200 million counts at the Bristol 2D-ACAR spectrometer [132]. Before the back-folding process, we linearly interpolated $\rho^{2\gamma}(p_x,p_y)$ from 290x290 to 287x287 channels (momentum mesh points) with an optimized momentum mesh spacing.

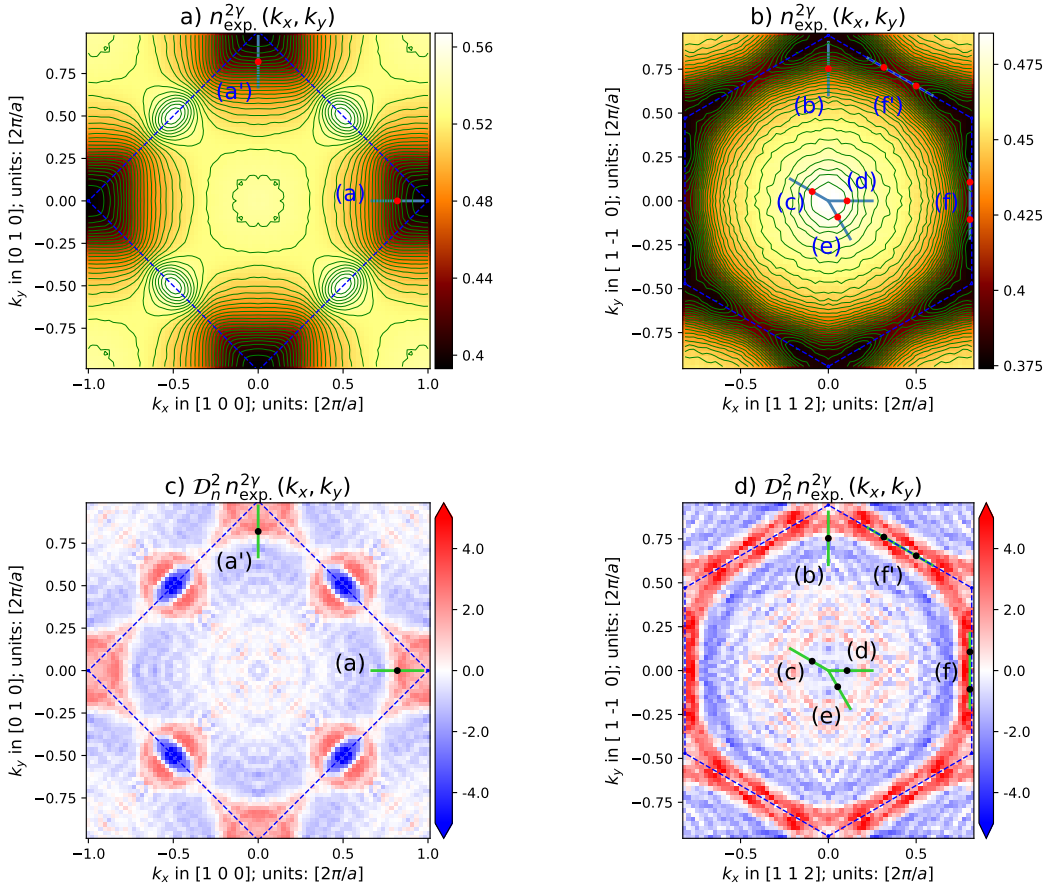

Figure 5.9.: $n^{2\gamma}_{\text{exp.}}(k_x,k_y)$ for silver, experiment:
k-paths are indicated by dots and lines. In contrast to the preceding subsections, dots refer here to the expected position of the Fermi surface signatures based on the experimental reference in table 5.1 with $r_{\text{neck,L...}} = r_{\text{neck}}$ (mean).

Interpretation

The experimental spectra looks similar to the theoretical predictions in figure C.7. The coarser resolution of the experimental data leads to less smooth contour lines. We further realize, that the intensity range of the experimental data is smaller. This might be due to contributions from completely filled bands in the experimental data [80], leading to a constant shift. We see that the horizontal and diagonal L-necks in the $[11\bar{1}]$-projection have the same intensity. We predicted this, because of symmetry reasons, but did not find in the theoretical spectra, because of the internal meshing (compare figure 5.3).

Interpolation

As for the theoretical data, we will apply the model fitting procedure for the cuts along k-paths (a)-(e). The cut and model fitting analysis of the data is presented in figure 5.10. The $n^{2\gamma}_{\text{exp.}}(k_{\text{path}})$, blue crosses, denotes the experimentally measured data points (left) and the corresponding curvature (right). As these are too sparse, performing the model fits turned out to be impractical.
We hence first interpolate the data along the cut, and perform the model fits (orange and green) based on the curvature of the interpolation result $n^{2\gamma}_{\text{interp.}}(k_{\text{path}})$, purple line. We interpolated by cubic splines and flattened the data afterwards by folding it with a Gaussian of $\sigma_{\text{int}} = 0.04\,\text{a.u.}$[5] The standard deviation parameter in the models was adjusted due to the double application of a Gaussian folding[6] by Cramer's theorem [219] ($\sigma^2_{\text{fit}} = \sigma^2_{\text{int}} + \sigma^2_{\text{l}}$). As in the preceding plots, vertical dashed lines mark the predictions for the Fermi surface parameter extracted from this dataset. The red dashed line represents the experimental reference values. If those are not precisely known (like the average L-neck radius), the standard deviation from the theoretical calculation around the mean experimental reference was marked as a red shaded area. The gray dashed line presents the center of the fitting interval (black dashed lines) with its boundaries in a distance of $\pm 1.5\sigma_{\text{l}}$. The position of this line is used as the initial value for the fitting routine and is put to a convenient value. For paths (a)-(a'), this is a multiple of $0.05\frac{2\pi}{a}$ at the expected position of the Fermi surface signature based on an analysis (by eye) of figure 5.9 a and b. For paths (b)-(e) we choose the initial value such, that the fitting interval does not cross the origin or the VP boundary. This avoids a break down of the model assumptions.

Interpretation

In comparison with figure C.9 (i.e. DFT results with experimental resolution and Poisson noise of 200 million count), we see a negative influence of the sparse momentum mesh and the additional noise on the quality of the Fermi surface parameter prediction. Nevertheless, with exception of (b), all Fermi surface parameters are extracted with a maximum deviation of $0.025\frac{2\pi}{a}$ by the polar model. This is smaller than the momentum mesh spacing, being $0.03\frac{2\pi}{a}$. The distance of the experimental Fermi surface parameter to the point of maximal curvature in the cut through the experimental data (blue dashed vertical line) is twice as large for all paths. We see though, that the polar fitting model increases the accuracy of the Fermi surface parameter significantly.

[5] Different interpolation methods will be discussed later in this subsection.
[6] σ_{l} from the experimental resolution, σ_{int} from the custom interpolation.

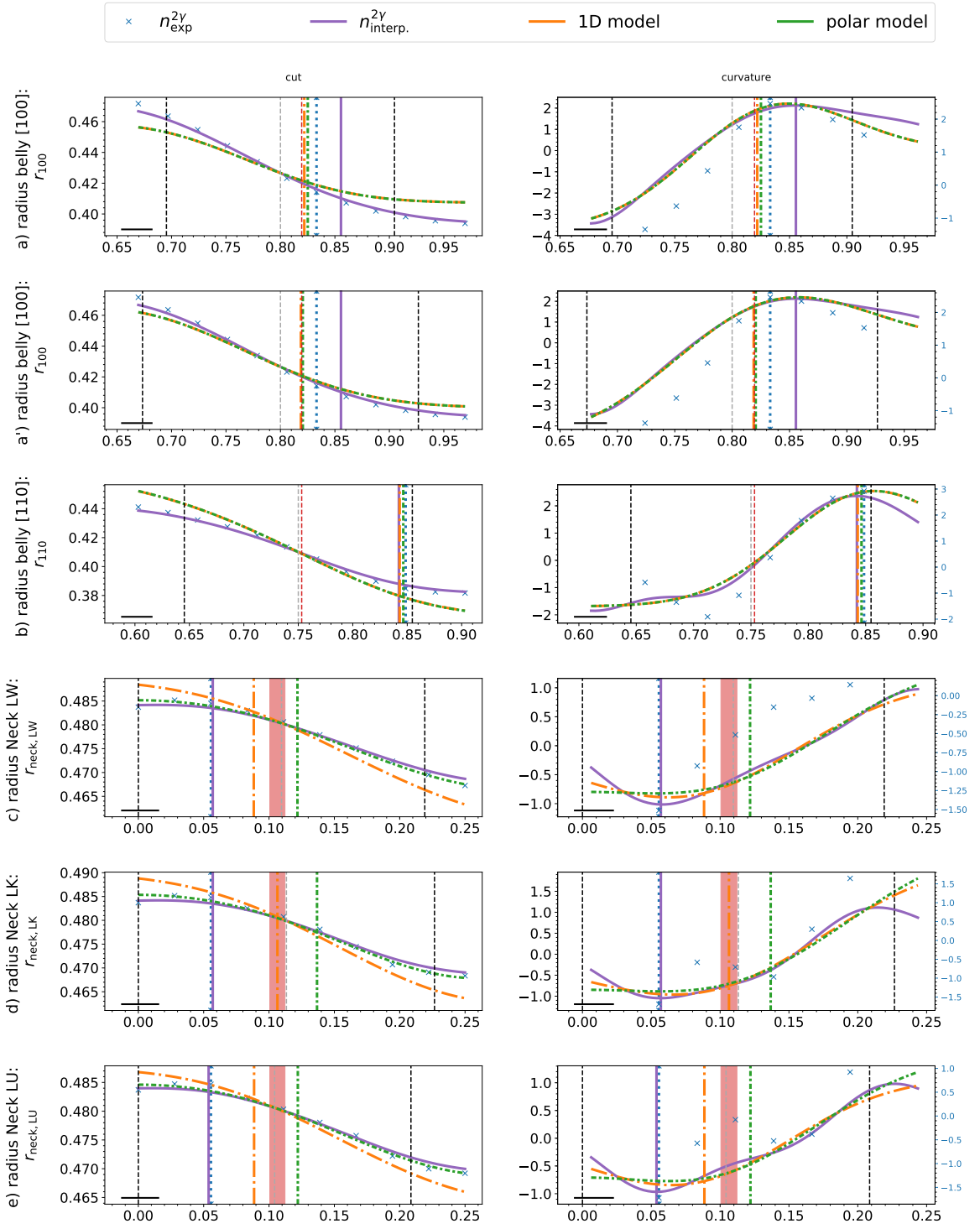

Figure 5.10.: Extraction of the Fermi surface parameters from $n^{2\gamma}_{\sigma}(k_{\mathrm{path}})$, experimental: The red vertical line denotes the experimental reference value. A shaded area is used in case of uncertainty. Otherwise analogous to figure C.9.

Path (b) The analysis in figure 5.10 along the path (b) stands out by large deviations of the observed data to the experimental reference data. The Fermi surface parameter predictions of the fitting models are at the edge of the fitting interval, which is an indicator, that the applied fitting model fails. Also, the fitting interval is not centered around the point of maximal curvature of the graph $n^{2\gamma}_{\text{exp}}(k_{\text{path}})$ to avoid crossing the VP boundary. Thereby, a periodic repetition of $n^{2\gamma}_{\text{exp}}(k_x,k_y)$ in figure 5.9 b would violate the model assumptions of the spectrum being constant on one side. Another issue with the fitting along path (b) is, that $n^{2\gamma}(k_{\text{path}})$ does not have a shape, which is well described by a parabola, as assumed in the fitting models. This is observable on a theoretical level in figure 5.8b, where $n^{2\gamma}(k_{\text{path}})$ has a second kink at $k_{\text{path}} = 0.73$. As this is not included in the fitting models, we see a deviation of the reconstructed $n^{2\gamma}_{\sigma}(k_{\text{path}})$ at $k_{\text{path}} \leq 0.64$. This is not found for the other paths in that figure. For these reasons, no satisfying reconstruction of the Fermi surface parameter r_{110} could be achieved.[7]

Other interpolation methods Other interpolation methods were tested as well to fit the models to the few experimental data points and to extract the Fermi surface parameters based on that. Among those were: Interpolation with splines of order 5, interpolation without Gaussian filtering and using a fit by value. Based on the achieved agreement of the data and its curvature with the corresponding model fits for different k-paths, we decided to present the results of this scheme. The general conclusion from those tests is, that the advantage of Gaussian filtering is to avoid sharp changes in curvature and to not recover strictly the measured data points. The last statement might sound counter-intuitive, but the measured data points are accumulated counts from a momentum range. Hence, only in the case of a linear change in $n^{2\gamma}_{\text{exp.}}(k_{\text{path}})$, the interpolated result should agree strictly with the data point.

Take home message In our example, the extraction of Fermi surface parameters from experimental data by model fitting is performed with an accuracy of $\pm 0.025\frac{2\pi}{a}$ (i.e. smaller than the momentum mesh spacing). Due to the larger momentum mesh spacing compared to the standard deviation of the experimental resolution, an additional interpolation step is necessary. The sparse grid of available data points makes the reconstruction of the Fermi surface parameters more sensitive to details as fitting range, interpolation method, noise, etc.

[7] Analyses along other paths to reconstruct r_{110} (for instance in prolongation of path (c) did not bring any improvements and faced the same issue with the end of the VP being reached.

5.6. Summary and Potential Improvements

Summary

In this chapter we systematically analyzed different influences on the determination of Fermi surface parameters from 2D-ACAR data of silver.
First of all we found that the position of kinks in $n^{(2\gamma)}(k_x,k_y)$ for simulation results is strongly influenced by the internal mesh parameters 'ngridk' in Elk, when comparing $n(k_x,k_y)$ along predefined paths to the results of a brand structure calculation.
The influences of the positron wave function and electron-positron enhancement is mainly a shift of spectral weight to small momenta $|(p_x,p_y)|$. This does not influence the signal-to-background ratio of Fermi surface sheets with s and p character, but decreases the intensity from signatures with d and f character (compare equations (3.3) and (3.4)).
In contrast to that, the experimental resolution (corresponding to a Gaussian smearing) introduces a shift of the maximal curvature. We analyzed $n^{2\gamma}(k_{\text{path}})$ along suitable paths in k-space. Instead of taking the point of maximal curvature as the position of the Fermi surface, it is preferable to perform a fit to one of the mathematical models presented in subsection 1.2.2. The Fermi surface parameter is thereby one of the fitting parameters. This technique performs well to purely reverse the Gaussian blur (figure 5.8). With increasing noise (figures C.9 and C.10) and momentum mesh spacing (figure 5.10) its accuracy decreases.
The coarse resolution in experimental data makes an interpolation between the data points necessary. A stable interpolation method was pointed out, but there might be still space for improvement. We find that model fitting improves the deviation of the extracted Fermi surface parameters, roughly by a factor of 2. Due to its more general design, the polar model thereby performs consistently better than the 1D model.

Potential improvements

In the following we want to present a collection of promising ideas to improve the methodology presented in this section:

- New fitting models:
  The development of new fitting models, could improve the Fermi surface parameter predictions, especially in figure 5.10b, where the model fitting failed. The difficulty will be, to formulate a suitable model with a small number of parameters for each individual case.

- Error bars for model fitting parameters:
  To estimate the error originating from Poisson noise, Monte Carlo Sampling for different realizations of the noise could be used. Experimental measurements could be split into several independent ones, which could be analyzed in total (mean) or separately (error bar).

- Improvement of the interpolation scheme for experimental data:
  A promising though very specific interpolation scheme is to fit the theoretical data by a shift and scaling parameter to the experimental data points. The disadvantage of this procedure is the need of a priori knowledge about the system and the risk of biasing the results.

- Truncation of noise:
  To truncate the experimentally obtained $\rho^{2\gamma}(p_x,p_y)$ at intermediate momenta, reduces the influence of Poisson noise, which is much stronger at larger momenta (compare subsection 1.2.3). Especially data with strong Poisson noise (for instance figure C.10) might profit from that.

We also want to present some ideas, how to increase the experimental resolution and decrease the momentum mesh spacing on an experimental level:

- measuring at lower temperatures,
- using a slit mask to detect only annihilation events from exactly the same position in the probe,
- increasing the detector distance to the probe and
- using detectors with a better resolution.

These suggestions should be evaluated under aspects like time resources, financial resources and available technology.

Discussion about model fitting

How reliable the extraction of Fermi surface parameters by model fitting is, strongly depends on the system under investigation. The message at this point should not be, to correct experimental resolution by model fitting, but to be aware, that experimental resolution causes a shift in the Fermi surface signatures. We used model fitting to verify this statement based on experimental evidence.
There exist two methods, intending to correct different effects, discussed in this chapter. We tested O'Brien's band pass filter [84], which did not correct the kink shift by experimental resolution. The implementation of Dugdale's maximum entropy method [83] and Hoffmann's linear and non-linear filters [82] were not available and hence not tested. It remains unclear at this point, what improvements on the kink shift issue can be obtained by these techniques.
Summarizing, we think that there is a need for a more systematic investigation of the kink shift by experimental resolution (for more than a simple system like silver) and a suitable post processing method for 2D-ACAR data.

6. Germanium (Ge): Benchmarking Back-folding Artifacts

6.1. Germanium as a Benchmarking System

Electronic properties

Germanium, being a semiconductor, has a constant $n(\boldsymbol{k})$. This can be deduced from equation (3.36), as completely filled or empty bands just result in constant contributions of one or zero. We will exploit this property, to analyze the accuracy of the different back-folding methods. Therefore, we calculate $\rho(p_x,p_y)$ of germanium for different projection directions and back-fold it. Deviations from $n(k_x,k_y)$ = constant will be assigned to artifacts, introduced by the back-folding process.

Sources of deviation

Possible reasons for a non constant $n(k_x,k_y)$ are:

- Back-folding errors: These mainly originate from the finite range issue, which is more apparent for small $p_{\max}$. A detailed discussion is presented in this chapter.
- Interpolation errors: These originate from the linear tetrahedron method [190] during the calculation of $\rho(\boldsymbol{p})$, as was presented in figure 5.4.
- Convergence of the DFT simulation: This is calculated up to a root mean square value change in the Kohn-Sham potential of $0.3 \cdot 10^{-7}$ Ha (Hartree) and an absolute change in the total energy of $0.4 \cdot 10^{-4}$ Ha. From this level of convergence, we expect this source of deviation to be minor compared to the preceding two.

Within this chapter, we will find that by increasing $p_{\max}$ the deviation from a constant $n(k_x,k_y)$ converges to a value of $\mathcal{O}(-4)$. This remaining error can be assigned to the interpolation error from the linear tetrahedron method.

Applicability

The LCW back-folding is in general performed for $\rho^{2\gamma}(p_x,p_y) \to n^{2\gamma}(k_x,k_y)$. However, this benchmark is based on $\rho(p_x,p_y) \to n(k_x,k_y)$. The key difference is, that $\rho^{2\gamma}(\boldsymbol{p})$ decays significantly faster than $\rho(\boldsymbol{p})$. This has, obviously, implications on the choice of a representative $p_{\max}$ parameter to perform this benchmark for realistic artifact intensities.

Momentum range

We will choose $p_{\max}$ such, that the center-to-boundary signal ratio $\rho(0,0)/\rho(p_{\max},p_{\max})$ resembles the ratio $\rho^{2\gamma}(0,0)/\rho^{2\gamma}(p_{\max},p_{\max})$ from 2D-ACAR experiments. In an experimental setup this ratio is typically in the range (100,1500) for $p_{\max} \approx 3.5$ a.u. This

corresponds to a suitable parameter for this benchmark of $p_{\max} \in [10\,\frac{2\pi}{a}; 18\,\frac{2\pi}{a}]$. We call this range for $p_{\max}$ the **Momentum Range of Interest (MRI)**. The calculations presented in this chapter are based on a lattice constant of $a = 10.10\,\text{a.u.}$, leading to

$$\frac{2\pi}{a} = 0.62\,\text{a.u.} \tag{6.1}$$

Germanium forms a diamond type lattice structure, which is equivalent to two fcc lattices, nested into each other and shifted by $(\frac{a}{4}, \frac{a}{4}, \frac{a}{4})$.

Indicators

We define a set of indicators to evaluate the quality of the back-folding methods in this benchmark.

- We define the maximum absolute deviation as

$$\Delta n \equiv \max_{(k_x,k_y)} n(k_x,k_y) - \min_{(k_x,k_y)} n(k_x,k_y)\,. \tag{6.2}$$

  This indicates, how well the absolute values of the back-folded spectrum agree.

- The SDDn (compare subsection 3.3.1) was used extensively during the investigation of silver in chapter 5 as an indicator for the Fermi surface. By taking the maximum over all momentum mesh points, the information of the SDDn is compressed to a scalar indicator

$$\mathcal{C}_{\boldsymbol{n},\,\max} \equiv \max_{(k_x,k_y)} |\mathcal{D}^2_{\boldsymbol{n}} n^{\text{per}}(k_x,k_y)|\,. \tag{6.3}$$

  Thereby, $n(k_x,k_y)$ is periodically (superscript 'per') replicated to enable the calculation of $\mathcal{D}^2_{\boldsymbol{n}}$ at the VP boundaries.

- For robustness with respect to saddle points, we additionally take into account the maximal SDDmax of all (k_x,k_y) points, compare subsection 3.3.1,

$$\mathcal{C}_{\boldsymbol{d},\,\max} \equiv \max_{(k_x,k_y)} \max_{\theta} |\mathcal{D}^2_{\boldsymbol{d}(\theta)} n^{\text{per}}(k_x,k_y)|\,. \tag{6.4}$$

- As described in subsection 4.2.1, the Voronoi cutoff has the property to collect truncation artifacts at the boundaries of the VP. Additionally we define VP^o as the interior of the VP. When declaring the VP boundary as a not reliable area, Fermi surface signatures in its interior can still be investigated. We hence define a second set of the SDD indicators, which act just on VP^o:

$$\mathcal{C}^o_{\boldsymbol{n},\,\max} \equiv \max_{(k_x,k_y)\in \text{VP}^o} |\mathcal{D}^2_{\boldsymbol{n}} n^{\text{per}}(k_x,k_y)| \tag{6.5}$$

$$\mathcal{C}^o_{\boldsymbol{d},\,\max} \equiv \max_{(k_x,k_y)\in \text{VP}^o} \max_{\theta} |\mathcal{D}^2_{\boldsymbol{d}(\theta)} n^{\text{per}}(k_x,k_y)|\,. \tag{6.6}$$

6.2. Overview of Different Back-folding Methods

Benchmark

The results of the benchmark for two different integration directions are presented in figures 6.1 and D.1. We see the behavior of the previously defined indicators in dependence of the maximum momentum $p_{\max}$ for different cutoff schemes and extrapolation ranges. We compare the result **without extrapolation** with **modest extrapolation**, by a factor of $f_{\text{ex}} = 1.4$, and **extreme extrapolation**, from the current $p_{\max}$ to $30\,\frac{2\pi}{a}$ (i.e. $f_{\text{ex}} = 30/p_{\max}$).[1] Those extrapolation ranges are combined with the 'no cutoff', the circular cutoff and the Voronoi cutoff schemes. All spectra are normalized to an integral value of 1 after application of extrapolation and cutoff.

Rectangular cutoff

The rectangular cutoff was not considered, due to the additional interpolation step, necessary to operate on the even momentum mesh. A comparison in this context would be misleading, compare section 4.3. Its behavior can be estimated similar to the Voronoi cutoff, as the RP coincides with the VP in this specific case. Minor differences would occur due to anisotropic contributions, which are not subtracted in the rectangular cutoff case (compare orange VPs in figure 4.8).

Results

When analyzing the results of figures 6.1 and D.1, we can distinguish roughly 4 groups. One group is formed by the cases of no and modest extrapolation for each cutoff scheme. We see that modest extrapolation yields always improvements. Those improvements are more significant for less precise back-folding schemes. The last group contains the cases with extreme extrapolation, independent of the cutoff scheme. This seems highly favorable, as even for very small $p_{\max}$ extreme extrapolation yields highly accurate results. We will discuss that case from a more critical perspective later.

No cutoff

We see that the 'no cutoff' scheme without extrapolation performs worst, by far. The Δn is an order of magnitude larger than for the other methods, over almost the complete $p_{\max}$-range. Further this is the only back-folding method, where converge is not even achieved at $p_{\max} = 30\,\frac{2\pi}{a}$. Performing the benchmark for larger $p_{\max}$, to find the exact value for convergence, is not practical from a computational point of view, due to memory limitations.
The application of modest extrapolation, reduces the artifact intensity, especially for larger $p_{\max}$, but is still not competitive with the other methods in the MRI.
The SDD indicators of the 'no cutoff' scheme are even two orders of magnitude larger compared to the other cutoff schemes with the same extrapolation. This comes from the boundaries of $\rho(p_x,p_y)$, which appear in $n(k_x,k_y)$ as horizontal and vertical steps. This is seen later in figure D.2 g, j and m.

Voronoi cutoff

The Voronoi cutoff without extrapolation is the next better scheme. A typical step pattern is found in all indicators. Only $\mathcal{C}_{\boldsymbol{n},\max}$ in figure 6.1 is influenced by numerical errors during the normalization, such that the normal direction at the VP boundary is fluctuating.

[1] This means. that for $p_{\max} \geq 21.5$ the extrapolation range of the modest extrapolation exceeds the one from the extreme extrapolation. The nomenclature is based on the behavior in the MRI.

We see, that the improvement by modest extrapolation for the Voronoi cutoff is similar to the improvement, which was gained for the 'no cutoff' scheme. The step pattern vanishes, as the decaying exponent for the extrapolation depends on the outer region of $\rho(p_x,p_y)$, which is changing with $p_{\max}$. In the MRI, the Voronoi cutoff with modest extrapolation is one of the more favorable options. In a few cases (Δn in figure 6.1) it even performs better than any other method.

Circular cutoff

Without applying extrapolation the circular cutoff turns out to be the favorable scheme. This is an important finding for spectra with strong counting noise in the tail region or extrapolation artifacts, compare subsection 4.2.2.
Its oscillating behavior in Δn origins from the overlap pattern produced by the 'circles' around each projection point. The point where a new set of circles (most probable 4) overlap just in one single point, is in general the situation producing the largest value differences in n. A situation where the 'circles' do not overlap yet, is presented in figure D.2h.
The application of modest extrapolation brings an improvement as well, which is smaller compared to the improvement in the case of the other cutoff schemes.

Interior of the VP

The property of the Voronoi cutoff scheme, to collect artifacts at the boundaries of the VP, is clearly reflected in the differences of $\mathcal{C}_{\dots}$ and $\mathcal{C}^o_{\dots}$. The Voronoi cutoff performs significantly better than the circular cutoff in the interior of the VP, but worse at the boundaries.

Extreme extrapolation

Extreme extrapolation gives very impressing results in this benchmark. From a highly truncated spectrum with $p_{\max} = 2$, extreme extrapolation produces back-folding results comparable to the output of other methods for $p_{\max} = 8$. This is mainly due to the convex shape effect (compare section 4.1), which is corrected by extreme extrapolation. In the MRI the extreme extrapolation back-folding methods perform by at least a factor of 3 better than the other methods without extrapolation. This is also true for the circular cutoff, even though at a few $p_{\max}$ values the Δn indicator is lower for the circular cutoff than for extreme extrapolation. We analyzed these cases (not presented here) and found, that the back-folding artifacts from the circular cutoff accidentally correct the rest artifacts. These rest artifacts are the artifacts, which limit the maximum level of convergence. They are found at $p_{\max} = 30$ and presented in figure D.3 n and o.
As expected, the Voronoi cutoff is the most suitable cutoff scheme for extreme extrapolation, having the highest accuracy in all indicators. A difference with the other cutoff schemes is mainly given at small $p_{\max}$, where the extrapolation procedure is less precise.
It should be mentioned though, that this level of success for extrapolation with large f_{ex} is extraordinary. It is based on $\rho(p_x,p_y)$ of germanium, which has no steps or kinks and hence, is well modeled by the extrapolation algorithm. This is not the case in common situations, where LCW back-folding is applied, to extract information about the Fermi surface.

Conclusion

We conclude from these findings, that extrapolation to large momenta in combination with the Voronoi cutoff is highly recommended. For situations, where extrapolation is not available, the circular cutoff is the preferable scheme. A cutoff should always be applied when back-folding.

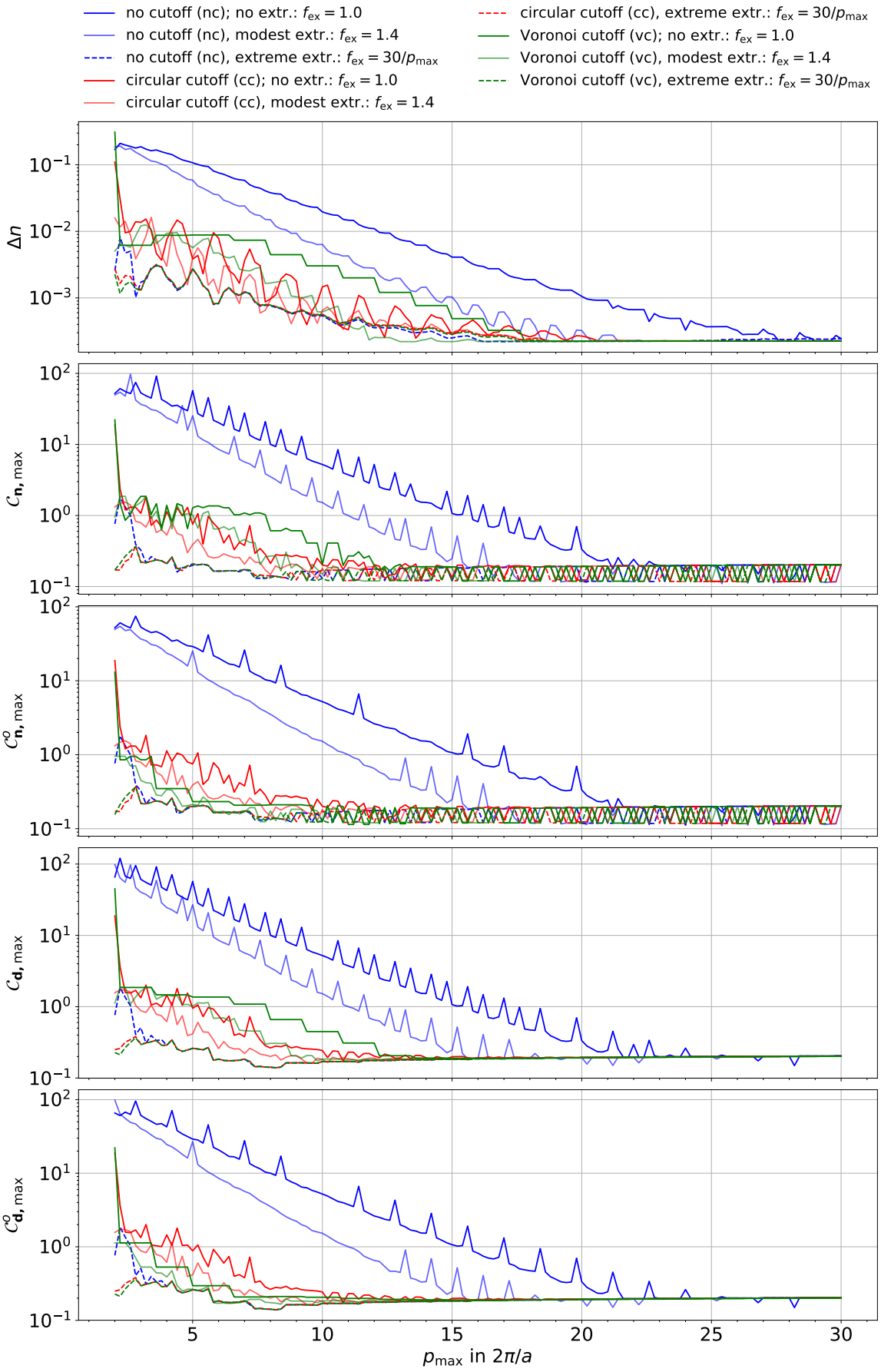

Figure 6.1.: Back-folding artifacts of Ge in the [110] vs. [1$\bar{1}$0] plane (integrated along [001]): Different cutoff schemes are investigated with and without extrapolation.

6.3. Detailed Analysis of Back-Folding Artifacts

Details 110 vs. 1-10

As an illustration, we want to point out a few situations from the plots, presented before. Figure D.2 a-f shows $\rho(p_x,p_y)$ without and with modest extrapolation after applying the cutoff. The corresponding back-folding results are presented in figure D.2 g-l. The indicators presented at $p_{\max} = 7.0$ for the solid and semi transparent lines in figure 6.1 are determined from those spectra.

No cutoff

To demonstrate the evolution of the overlap patterns from the 'no cutoff' scheme, subplots g and m-o are presented. Subplot m shows the case where contributions from four projection points just reach into the Voronoi plaquette. The corresponding regions of high intensity are found at the edges. We can deduce from this immediately, that $\rho(p_x \approx p_{\max}, p_y \approx p_{\max}) \approx 0.05$. The gap between the four high intensity regions is responsible for the large Δn values in figure 6.1. In figure D.2 g we see how the gap is reduced in size when increasing $p_{\max}$ from 6.8 to 7.0. The resolution in this example was chosen such, that the gap never closes perfectly for any $p_{\max}$.[2] The corresponding SDDn is presented in subplots n and o. Especially the large color scale in subplot o is remarkable, as the curvatures add up in the momentum mesh point at the origin. This leads to the spike in the SDD indicators in figure 6.1 at $p_{\max} = 7.0$.

Details 001 vs. 1-10

In figure D.3 a-f the back-folding results, corresponding to figure D.1, for a high level of convergence ($p_{\max} = 14.0$) are presented. The corresponding SDDn, displayed in subplots g-l, still reveals the nature of the back-folding artifacts. Figure D.3 g and j shows the typical horizontal and vertical steps for the 'no cutoff' scheme. The curved artifacts of the circular cutoff can be found in subplots h and k, where they form a red (subplot h) or white (subplot k) x-pattern on the blue background. The concentration of artifacts at the boundaries of the VP for the Voronoi cutoff can be found in figure D.3 i and l.
In subplots m - o the results of the three different truncation schemes are displayed for the largest value of $p_{\max}$. We see, that the 'no cutoff' scheme still shows its typical artifacts, while the other two agree perfectly.

[2] In such rare occasions and for the squared projected lattice, found here, the 'no cutoff' scheme would coincide with the Voronoi cutoff scheme.

6.4. Conclusion

Summary

We argued, that germanium is an excellent benchmarking system to evaluate numerical artifacts introduced by LCW back-folding.[3] We found the practical validation of our predictions made in section 4.2, concerning the advantages and disadvantages of different cutoff schemes. As expected, the combination of extreme extrapolation with the Voronoi cutoff gives the best results (compare subsection 4.2.3).

Scale of $p_{\max}$

As the benchmark is performed on the $\rho(p_x,p_y)$ of germanium (without any positron influences), larger values of $p_{\max}$ where investigated to mimic a similar center-to-boundary signal ratio as in measurements of $\rho^{2\gamma}(p_x,p_y)$. The momentum range of interest, for evaluating different back-folding methods based on the $n(k_x,k_y)$ of germanium, is hence

$$10\,\frac{2\pi}{a} \leq p_{\max} \leq 18\,\frac{2\pi}{a}\,. \tag{6.7}$$

The findings in this range can be transferred to 2D-ACAR data, truncated at 3.5 a.u.

Comments

The extraordinary benefit from extrapolation in the case of germanium (with an increase in precision by one to two orders of magnitude) profited from the absence of Fermi surface signatures in the system. We showed, however, is that the convex shape effect can be corrected by the extrapolation technique almost completely, even for small $p_{\max}$.

Recommendation

As extrapolation corrects the convex shape effect, we recommend to use a large extrapolation factor for back-folding 2D-ACAR data. At $p_{\max} \geq 12$ (i.e. $f_{\text{ex}} = 2.5$) and with extreme extrapolation a convergence of $\mathcal{O}(0.1)$ was achieved for the SDD indicators in this benchmark. This is one order of magnitude smaller than the intensity of Fermi surface signatures in molybdenum, compare figure 7.7.
Therefore, we recommend $f_{\text{ex}} \geq 2.5$ for 2D-ACAR spectra. The choice $f_{\text{ex}} = 4$, turned out to lead to a reasonable spectrum size of $\mathcal{O}(10^3 \times 10^3)$ momentum mesh points. Back-folding larger spectra is not recommended, concerning the computational effort.

[3] This is true for semiconductors in general.

7. Molybdenum (Mo): Improved Prediction of the Fermi Surface

Agenda

In this chapter we will extract the Fermi surface parameterization of molybdenum from 2D-ACAR data. Starting with a quick review of the Fermi surface from theoretical calculations with Elk in the first section, we use this a priori knowledge for analyzing theoretical ACAR spectra in the next section. The findings will be applied on experimental data in section 7.3. For simplicity all momentum quantities ($\boldsymbol{k}$, $\boldsymbol{p}$ and $p_{\max}$) and the size of Fermi surface features are given in units of $\frac{2\pi}{a}$. The theoretical and experimental results for molybdenum are based on a lattice constant of $a = 5.95\,\text{a.u.}$, leading to

$$\frac{2\pi}{a} = 1.06\,\text{a.u.} \tag{7.1}$$

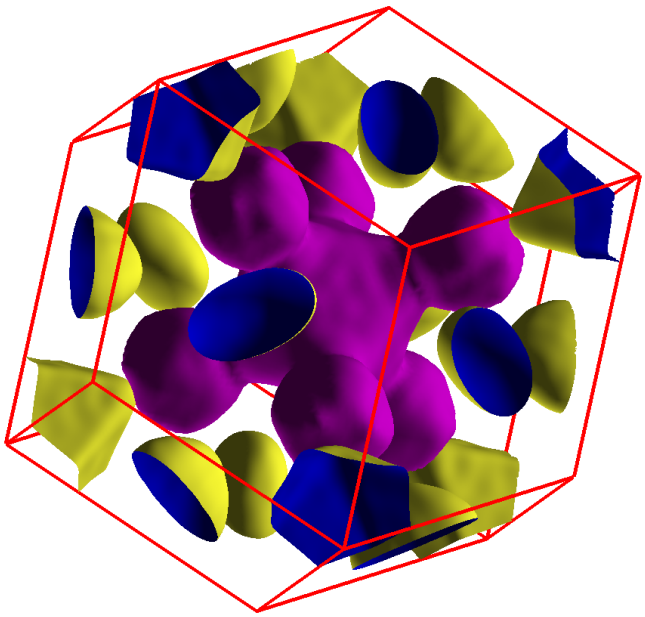

Figure 7.1.: Fermi surface of silver, Elk calculation:
Illustration of Fermi surface and Brillouin zone for further analysis.

7.1. Electronic Properties of Molybdenum

FS of Mo

The Fermi surface of molybdenum, shown in figures 7.1 and 4.3, was first predicted by Lomer [194] and Mattheiss [195]. It consists of three main structures:
The **electron jack** (purple, electron character) is centered around the origin and has in total 6 **knobs** (purple, electron character) along the [100], [010] and [001] axes. At its end each knob is almost touched by a vertex of the **H-hole octahedron** (yellow/blue, hole character), centered around the H point. Around the N symmetry points, the **N-hole pockets** (yellow/blue, hole character) are situated. These are ellipsoids with their short principal axis in NH-direction. The other principal axes are approximately of equal length. The **electron lenses** (electron character) are not visible in classical Fermi surface plots. They are situated inside the **neck**, where the octahedral shape of the electron jack and the sphere of the knobs are merged. The shape of the lens will be discussed in the context of figure E.2 and is shown for instance in [198] (figure 3). A summary of different Fermi surface parameters will be given in table 7.2 (summarizing also [196–204]). It becomes apparent in these references, that the exact size, shape and position is still under investigation.

Spin-orbit coupling

Spin-orbit coupling in molybdenum is responsible for the small spatial separation between the electron knobs and the H-hole octahedron. Calculations, which do not take spin-orbit coupling into account, predict an overlap free touching of those features. As shown in [198] (figure 3), it further leads to a shrinking of the electron lenses, such that they do not touch the neck, but instead are situated completely inside.

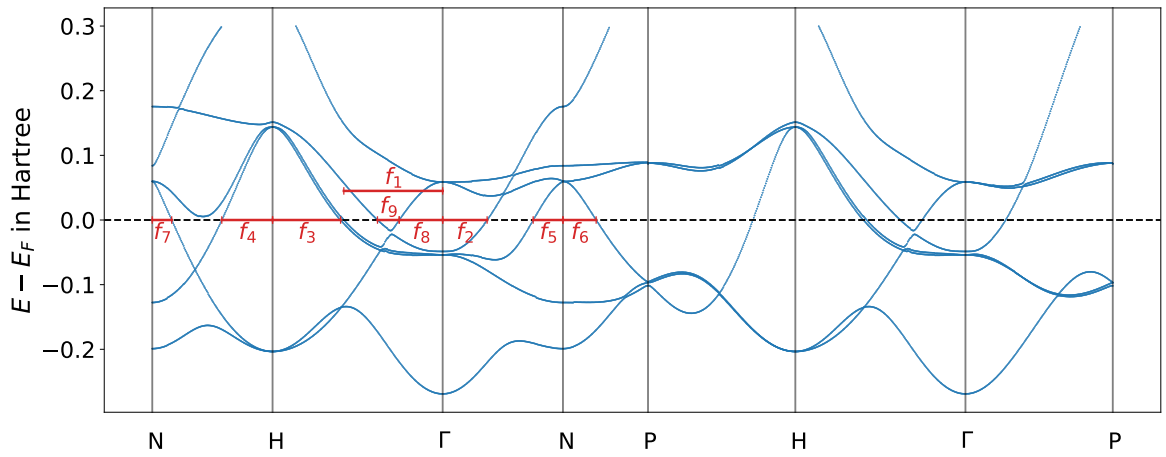

Figure 7.2.: Band structure of molybdenum, Elk calculation: Fermi surface parameters are measured along the symmetry lines, compare table 7.2.

Band structure

Figure 7.2 shows the band structure of molybdenum, where Fermi surface parameters according to table 7.2 are marked in red. We parameterize each feature by the length of its semi-axes. Only the electron lens is characterized by diameter, due to its small size and missing mirror symmetry. We will use those theoretical Fermi surface parameters as a benchmark for the analysis of 2D-ACAR spectra in curvature. By comparing

the band structure values with the extracted parameters from 2D-ACAR (both are computed within the same settings of the Elk code), we can estimate potential errors in the used methodology.

FS projection

Similar to silver, the analysis in curvature is based on cuts through the back-folded spectrum as marked in figure 7.3. In preparation for this, we discuss what Fermi surface signatures are projected onto each path:
Along the path (a) all Fermi surface features can be found, which are situated along the ΓH and the NPN symmetry direction. From the symmetry line ΓH we find signatures of the electron lens, the electron jack in knob direction and the H-hole octahedron. From the NPN line the N-hole pockets over Γ and H contribute.
Along the path (b) we expect to find the electron jack and a N-hole pocket from the ΓN line. A N-hole pocket and the H-hole octahedron contribute from the NH line. Further signatures from the lenses and the knobs, being oriented in directions [100] and [010], will be projected onto path (b) with a tilting angle of 45^o.

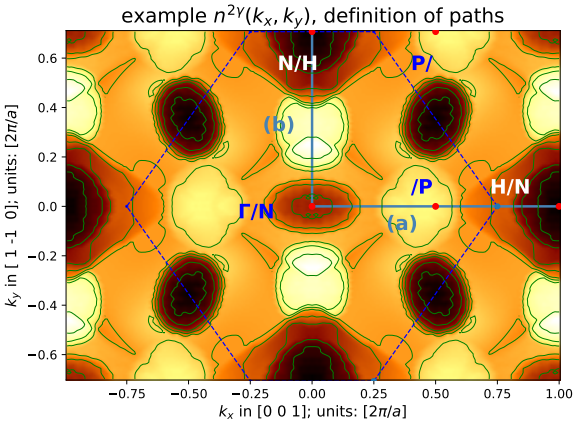

Figure 7.3.: Example 2D-ACAR spectrum of molybdenum, Elk calculation:
Overview of paths (a) and (b) and symmetry points. The first/second character refers to symmetry point in the $k_z = 0/k_z = \pm\frac{1}{\sqrt{2}}$ plane.

Expected FS signatures

Due to the integration in one momentum direction, a signature is left in $n^{2\gamma}(k_{\text{path}})$ from all parts of the Fermi surface, which are oriented perpendicular to the path. It is more practical to investigate the curvature along this path $\partial^2_{k_{\text{path}}} n^{2\gamma}(k_{\text{path}})$, as a kink along the cut is hard to see but the corresponding maximum in curvature can be found easily. Different shapes of the Fermi volume, thereby lead to different types of signatures, as can be seen in figure E.1.
An analysis of the 3D Fermi surface, as seen in figures 7.1 and 4.3, leads to the expected Fermi surface signatures as listed in table 7.1. This includes the expected positions k_i of Fermi surface signatures along each path, from what part of the Fermi surface they origin and what kind of signature is expected. Where no direct connection to the Fermi surface parameterization could be made, the expected position was determined from the numerical data of the Fermi volume. These k_i are marked by the $\approx$-symbol.

Unexpected descriptions

There are a few unexpected descriptions, as k_{b3}: 'start of knob', in table 7.1, which

Cut along the path (a)			
k_i	k_i (Elk)	description	signature in curvature
$k_{a1} = f_6$	0.195	end of N pocket NP	min
$k_{a2} = f_8$	0.255	start of Lens	max-min
$k_{a3} = f_8 + f_9$	0.383	end of Lens	max
$k_{a4} = f_1$	0.581	end of El jack (knob dir)	max
$k_{a5} = 1 - f_3$	0.600	start of H octahedron HΓ	min
$k_{a6} = 1 - f_6$	0.805	start of N pocket NP	min

Cut along the path (b)			
k_i	k_i (Elk)	description	signature in curvature
$k_{b1} = f_7$	0.114	end of N pocket NH	min
$k_{b2} \approx$	0.145	start of lens	max-min
$k_{b3} \approx$	0.145	start of knob	max-min
$k_{b4} = f_2$	0.261	end of El jack ΓN	min-max
$k_{b5} \approx$	0.280	end of lens	min-max
$k_{b6} = \frac{1}{\sqrt{2}} - f_4$	0.409	start of H octahedron HN	min-max
$k_{b7} \approx$	0.480	end of knob	max
$k_{b8} = \frac{1}{\sqrt{2}} - f_5$	0.532	start of N pocket NΓ	min

Table 7.1.: Expected Fermi surface signatures in $n^{2\gamma}(k_{\text{path}})$ along the paths (a) and (b) based on a band structure calculation in Elk.

are not interpretable from the description of the Fermi surface as given before in this chapter (the knobs are connected to the electron jack and, hence, have not start but only an end point). These origin from the Fermi surface features, which are oriented in a 45^o angle, relative to the path and integration directions. As seen for instance in figure 4.3, the double knobs, indeed have a start, due to the small diameter of the neck compared to the knob radius.

Lens projection

How an estimate for the signal of the lenses is constructed, is demonstrated in figure E.2. The subplot a shows how a simple lens model is constructed from figure 7.4d. The red points are the parameters extracted from the band structure calculation. The gray points are chosen manually, to give an estimate for the shape of the lens.
Subplot b illustrates, how the lens is oriented relative to path (b) (horizontal axes) and the integration direction (vertical axes). The curves are the diameter of the lens in integration direction with and without experimental resolution.
The corresponding signatures in curvature are shown in subplot c. When comparing the gray dashed lines with the corresponding curvature of $n^{2\gamma}_{(\sigma_0)}(k_{\text{path}})$, we find no exact relation between the maximum-minimum or minimum-maximum pattern in curvature and the position of the corresponding start or end point of the lens. For simplicity, we take the point of zero crossing in between maximum-minimum or minimum-maximum patterns as the reference for the lens signature.

7.2. Theoretical ACAR Spectra

Back-folded spectra

The results of the commonly used back-folding methods and the newly proposed back-folding (with Voronoi cutoff and extrapolation), applied to the theoretical spectrum of molybdenum, are presented in figure 7.4 a-c. Figure 7.4d shows the reference spectrum back-folded from the same $\rho^{2\gamma}(p_x,p_y)$ but with $p_{\max} = 8$. For such large momenta, the back-folding method does not play a role, as truncation artifacts are too weak. This statement will be quantified explicitly in the discussion of the red curve in figure 7.5 c and d.

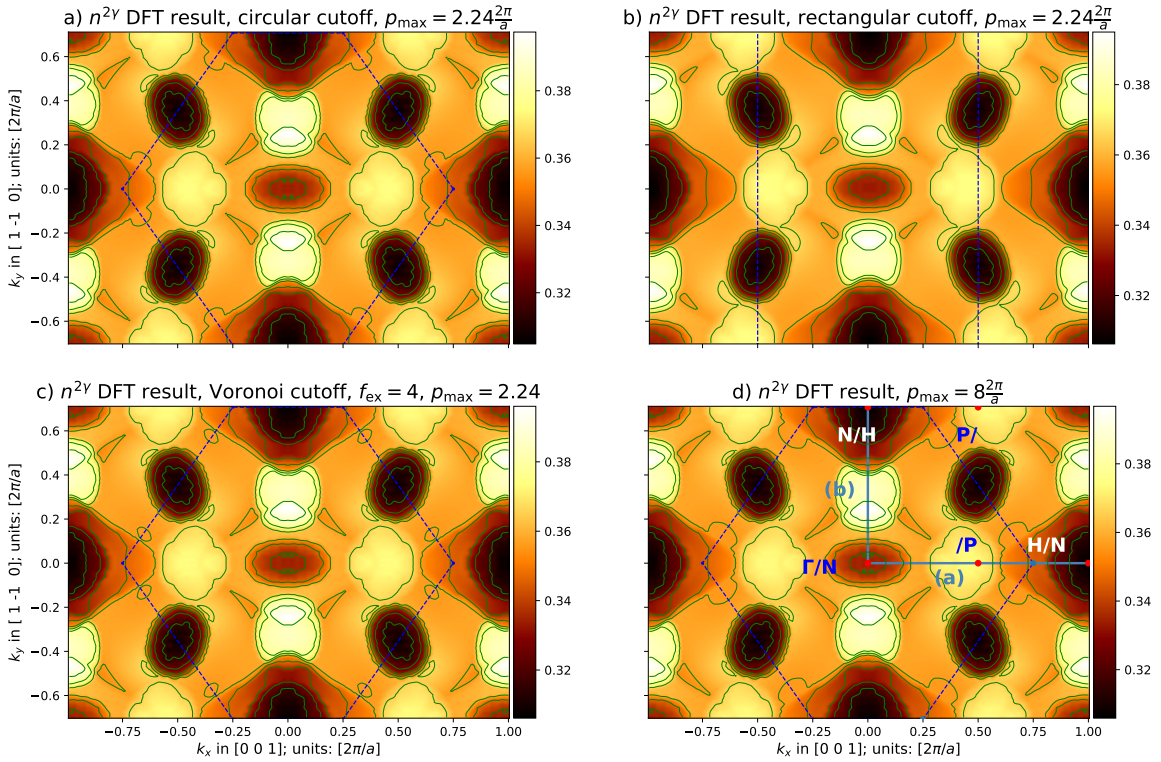

Figure 7.4.: Results of different LCW back-folding methods for molybdenum, Elk calculation:
a-c) show the results of the commonly used and the newly developed back-folding methods, corresponding to figure B.1 d, h and j.
d) shows the reference, based on $p_{\max} = 8$.

FS features

We find the structures of the Fermi surface of molybdenum, as presented in figure 4.3 (and figure 7.1), in all subplots. The **electron jack** ($k_x = 0, k_y = 0$) is limited by the **single knobs** ($k_x = \pm 0.5, k_y = \pm 0$) and the **double knobs** ($k_x = 0, k_y = \pm 0.2$). The term double knob originates from the projection of the knobs in the directions $[\bar{1}00]$, $[100]$, $[0\bar{1}0]$ and $[010]$ onto ($k_x = 0, k_y = \pm 0.2$).
The **H-hole octahedron** is the dark structure at ($k_x = \pm 1, k_y = \pm 0$) and ($k_x = \pm 0, k_y = \pm 0.7$).
In total, there are 12 **N-hole pockets** per Brillouin zone, appearing in five pairs of two pockets (being projected to the same (k_x,k_y) point) and two single pockets. Four

pairs are responsible for the ellipsoids at the VP boundaries ($k_x = \pm 0.5, k_y = \pm 0.35$). The other pair induces the low intensity areas at the origin ($k_x = 0, k_y = 0$). The single pockets are found in the center of the H-hole octahedra at ($k_x = 0, k_y = \pm 0.7$).
The signatures of the **lenses** are situated at the start of the knob structures at ($k_x = 0.25, k_y = 0$) and ($k_x = 0, k_y = 0.2$) and lead to the high intensity spot there. Due to the contour lines, this becomes particular apparent at the double knobs.

Cuts

In figure 7.5 a and b we see the cuts through the back-folded spectrum along the corresponding paths for different back-folding methods. In the lower half of each subplot, the curvature of the corresponding cut is presented. The momentum mesh points, are marked as dots. The vertical light blue lines mark the predicted position of Fermi surface signatures from table 7.1. Only those lines are labeled, which relate directly to the Fermi surface parameterization, i.e. not marked by the ≈-symbol. The vertical pink lines are drawn, where the expected signature in curvature is actually found in $\partial^2_{k_{\mathrm{path}}} n^{2\gamma}(k_{\mathrm{path}})$. In one case, no one-to-one correspondence could be made between a expected (light blue) and actual (pink) signature. This is at k_{b4} and k_{b5}. Both induce the same min-max signature in curvature, but so close to each other, that they interfere. The result is one min-max signature, which is situated at $\approx (k_{b4} + k_{b5})/2$. For that reason, only one pink marker is used.

Interpretation

We see good agreement (i.e. maximal deviation Δk) between band structure prediction and 2D-ACAR signature. The only exceptions are k_{a4},k_{a5} and k_{a6}. There are three possible sources for these deviations:

- 1) Deviating signature in curvature: The actual Fermi surface signature and the position of the signature (minimum, maximum or zero crossing) in curvature agree precisely only in a few cases, but in general are shifted by $\approx 0.5\,\Delta k$. This is due to discretization and can be seen for instance, when comparing the top and bottom row in figure E.1 for the integrated spheres (last two columns). This can explain only deviations $< \Delta k$.

- 2) Assuming the wrong Fermi volume shape: If the analysis of the Fermi volume is biased by wrong a-priori assumptions, a wrong model function (i.e. column in figure E.1) might be chosen for a specific feature. This deviation can be significant. For instance, when mistaking a p_x-p_y-integrated sphere as a step function type signature, the extracted Fermi surface parameter will be shifted by $1.5\,\Delta k$.

- 3_{theo}) LTM interpolation error: Compare the discussion about the 'ngridk' parameter in silver, especially figure 5.4, where a maximum deviation of $0.03\frac{2\pi}{a}$ was found.[1]

[1] The parameter a refers to the lattice constant of silver in this case. This is the appropriate unit and does not need to be rescaled for molybdenum, as the meshing of the LTM is with respect to the Brillouin zone.

- 3_{exp}) Curvature shift by experimental resolution: Compare the discussion of figure 1.3. This does not play a role in this example, as no experimental resolution was included, but has to be considered for the analysis of experimental data.

As k_{a1}, k_{a6} both refer to the Fermi surface parameter f_6 and show a similar deviation of $1 - 1.5\,\Delta k$, the most probable scenario is source 2. We see, that if a max-min signature for k_{a1} (meaning min-max for k_{a6}) is assumed, results with a far higher accuracy would be obtained. Chances are high, that the actual N-hole pocket in NP direction has a very steep descent and is, with respect to the signature in curvature, situated in between the 'step function' and the 'p_z-integrated sphere'.
The other explanation (source 3_{theo}), is less probable, as the issue occurs only at the parameter f_6 and at different positions in k_x-k_y-space.
Source 2 is also the most likely explanation for k_{a4} and k_{a5}. Assuming a min-max signal for k_{a4} (motivated by a steep descent) and interference with k_{a5} would lead to the signature found in figure 7.5.

Benchmarking LCW methods

Figure 7.5 c and d shows the difference of $n^{2\gamma}(k_{\text{path}})$ along the paths (a) and (b) with respect to the Voronoi cutoff with $p_{\max} = 8\,\frac{2\pi}{a}$ as a reference.
As claimed before, we see that at $p_{\max} = 8\,\frac{2\pi}{a}$ the back-folding result is cutoff independent. Both $p_{\max} = 8\,\frac{2\pi}{a}$ results agree with each other, as can be seen in the negligible amplitude of the red curve. This illustration generalizes to all cutoffs, as we compared the two cutoff methods, which induce strong artifacts at different positions.
The other graphs (blue, orange, green) present the different back-folding methods for $p_{\max} = 2.24\,\frac{2\pi}{a}$. Thereby, the rectangular cutoff shows the strongest deviations from the reference. This difference is not a smooth function and hence also visible in subplots a and b, where all curvatures coincided but the one from the rectangular cutoff. This is a serious issue, as the curvature plays an important role in identifying the Fermi surface. However, while peaks of the orange curve in figure 7.5 c and d are back-folding artifacts, strong oscillations (and the corresponding deviating curvatures) are not. This will be discussed in the next paragraph.
Considering the other two back-folding results in figure 7.5 c and d, the green curve is on average twice as close to the reference as the blue curve. This supports our findings in sections 4.2.3 and 6.2 about the optimal back-folding technique, being the Voronoi cutoff in combination with extrapolation.

Rectangular cutoff deviation

It is interesting to observe, that the rectangular cutoff differs much from all others with respect to the curvature of the back-folding result. Tests with a smaller $p_{\max}$ revealed, that these are no truncation artifacts, but originate from the different type of momentum mesh used by the rectangular cutoff. In order to compare our findings with results from existing literature, we used the original code [87] to perform back-folding with the rectangular cutoff. While our implementation is based on an odd momentum mesh, this implementation operates on an even momentum mesh. The influence of the additional interpolation step, needed for the even momentum mesh, is surprisingly strong, however. We argued in subsection 4.3.1 why our type of meshing is preferable.

Benchmarking conditions

As a final remark, we want to point out, that we used a finer momentum mesh than

common for experiments and included neither Poisson noise nor the experimental resolution for our analysis. With respect to these points, we expect the following changes for an investigation of experimental data:

- The coarser resolution will result in even larger interpolation errors. Due to the non-optimal meshing for the recorded data set, this applies to all back-folding methods. A further influence is a larger binning, i.e. the momentum interval of cumulated counts, which will reduce the overall intensity of the curvature.
- The influence of Poisson noise will be minor for a large number of counts (200 millions), but will introduce strong oscillations along the cuts for a significantly smaller number of counts.
- The experimental resolution will reduce the absolute value of curvature. This will make it harder, to identify Fermi surface signatures.

We present an explicit comparison of experimental and theoretical cuts in figure E.4. A discussion will be given in the next section.

Take home message

On a numerical level the signatures in the back-folded spectrum, can be clearly assigned to the Fermi volume. For that purpose we analyzed the curvature of cuts through the back-folded spectrum. Limitations are only reached, when different Fermi surface signatures overlap. The newly developed back-folding method, using extrapolation ($f_{\mathrm{ex}} = 4$) in combination with the Voronoi cutoff, was confirmed to be the most favorable one. The reason for this is the close agreement to results without truncation artifacts.
Further, we found, that the influence of interpolation, concerning the position of Fermi surface signatures, is not negligible. Therefore we highly recommend, to avoid interpolation on an experimental level, by choosing an odd momentum mesh with an optimal momentum mesh spacing.

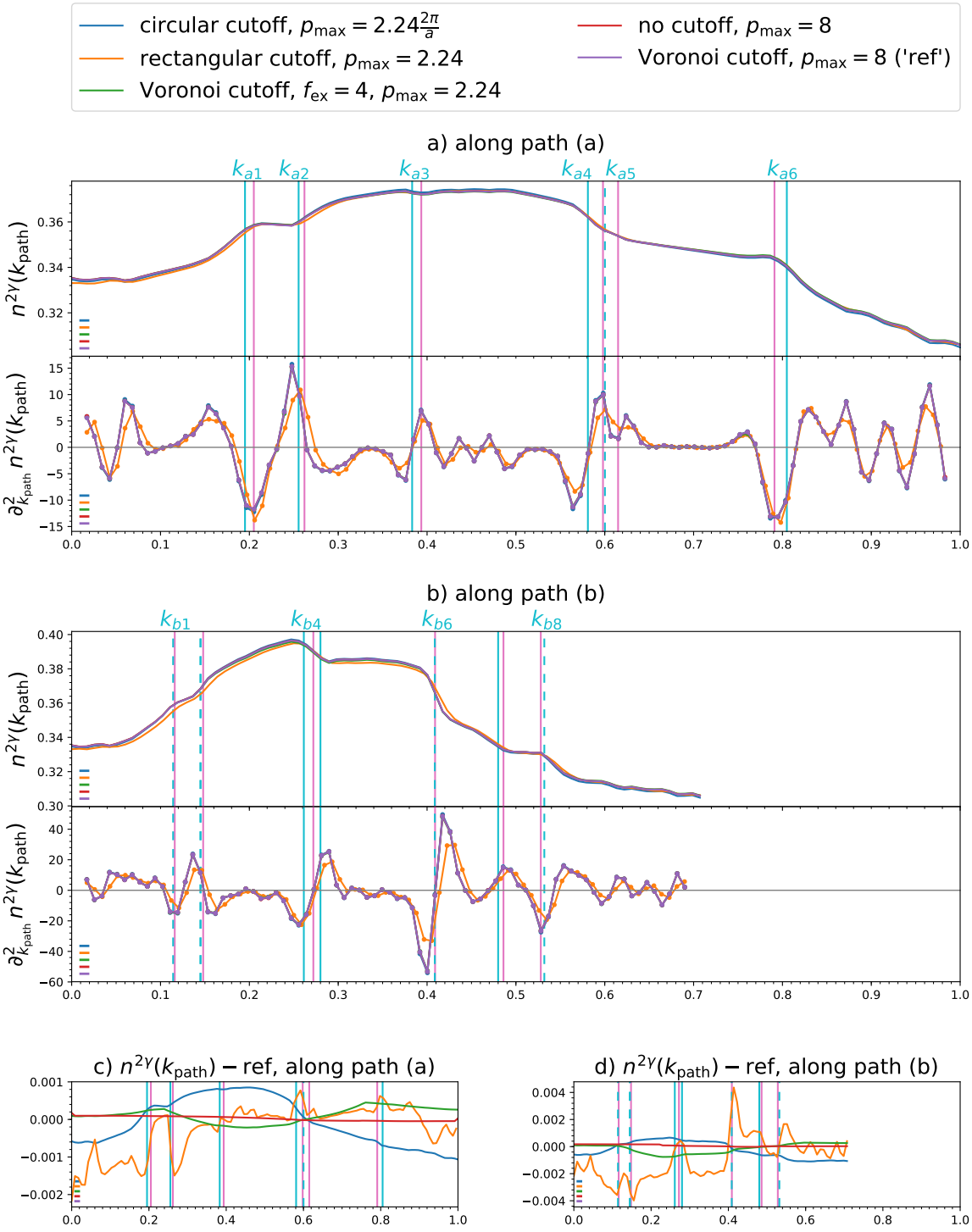

Figure 7.5.: Cuts through $n^{2\gamma}(k_x,k_y)$ of molybdenum for different back-folding methods, Elk calculation:
Light blue vertical lines: Expected signatures from band structure calculation
Pink vertical lines: Actual Fermi surface signature

7.3. Experimental ACAR Spectra

Agenda

We analyze the experimental dataset in a similar fashion to the theoretical results in the preceding section. The qualitative analysis of the experimental results was given in chapter 4 already, such that we focus on the analysis of $n_\sigma^{2\gamma}(k_{\text{path}})$. The experimental resolution of the experimental data is

$$\sigma_x = \sigma_1 \tag{7.2}$$

$$\sigma_y = \sigma_0 \tag{7.3}$$

with $\sigma_{0/1}$ being given in equation (1.18). The $\rho^{2\gamma}(p_x,p_y)$ was post-processed by the **Maximum Entropy Method (MEM)** [83, 215]. The back-folded result, using the LCW implementation [87] (rectangular cutoff), was published in [203].

Figures

In figure 7.6 we repeat some results of chapter 4 with the quantitative analysis given in figure 7.7. Similarly to the previous section the cuts along (a) and (b) through the back-folded spectrum (upper) and their curvature (lower) are presented in figure 7.7 a and b. Subplot c shows the difference between $p_{\max} = 1.7\,\frac{2\pi}{a}$ and $p_{\max} = 2.24\,\frac{2\pi}{a}$ for each of the three back-folding methods along both paths.

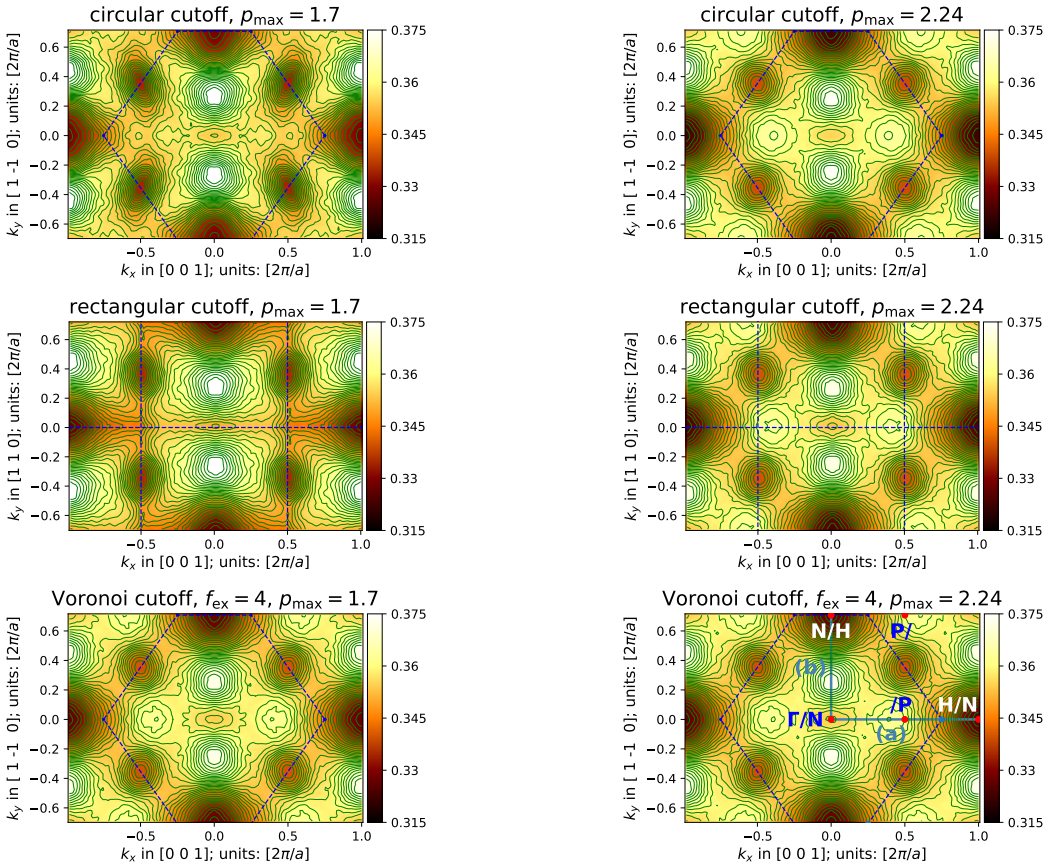

Figure 7.6.: Results of different LCW back-folding methods for molybdenum, experimental: The left column corresponds to figure 4.4 d, f and g. The right column corresponds to figure B.1 d, h and j.

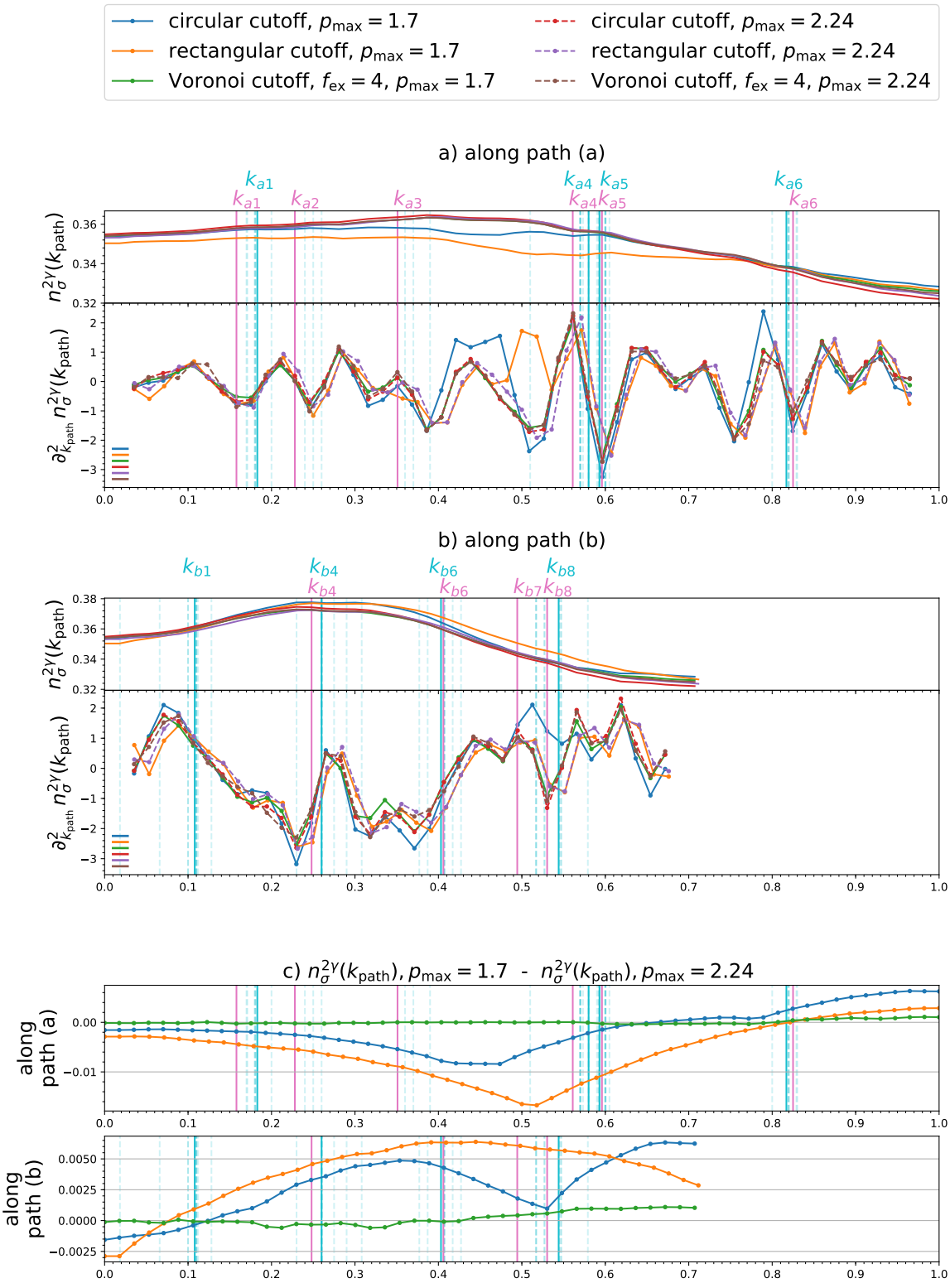

Figure 7.7.: Cuts through $n^{2\gamma}(k_x,k_y)$ of molybdenum for different back-folding methods, experimental:
a, b) cut and corresponding curvature along the momentum paths (a) and (b).
c) change of back-folding result with p_{max} along the paths.
Vertical light blue lines: Expected signatures from literature values (dashed) and reference literature values ([197] (modified) in table 7.2, solid and labeled).
Pink vertical lines: Actually found Fermi surface signatures in curvature.

Stability

In a first step, we analyze the back-folding artifacts of each method on a quantitative level, by comparing the results for $p_{\max} = 1.7$ and $p_{\max} = 2.24$. As we have no reference 2D-ACAR result, we use the stability of the back-folding result with respect to $p_{\max}$ as a criterion. As pointed out in the preceding section, there is no point in comparing the rectangular cutoff curve with the other curves, due to the disturbing influence of interpolation.
The stability can be evaluated best with respect to the curvature in figure 7.7 a and b. The circular cutoff shows artifacts at 0.45 (a), 0.8 (a) and 0.5 (b). One strong artifact is found for the rectangular cutoff at 0.5 (a). This corresponds exactly to the boundary of the RP.
The Voronoi cutoff with extrapolation has the highest stability. There are no significant differences between the different $p_{\max}$. This can be cross checked in subplot c as well. For an analysis of Fermi surface signatures, this cutoff scheme is, as expected, the most suitable.

Elk vs. experiment

When comparing the theoretical (from figure 7.5) and experimental (from figure 7.7) results for $n^{2\gamma}(k_{\text{path}})$ we see qualitative differences. This makes it not trivial to assign the Fermi surface signatures to the curvature in experimental data. To get a better overview, we show in figure E.4 a direct comparison of the theoretical data (blue) and the experimental data (red). Further the influence of increased momentum mesh spacing (orange) and experimental resolution (green) on the theoretical cuts is presented. The curves with experimental resolution, i.e. '$n^{2\gamma}_{\sigma/2}(k_{\text{path}})$; $\Delta k = 0.017$ (Elk)' and '$n^{2\gamma}_{\sigma}(k_{\text{path}})$; $\Delta k = 0.018$ (Exp)', both refer to the right y-scale in curvature, while the others refer to the left y-scale.

Experimental effects

The momentum mesh spacing has a small influence on the sharpness and position of signatures in the curvature. Small features get lost and extrema can be shifted in the order of the momentum mesh spacing.
Experimental resolution however, makes an analysis of the curvature along a path impossible, as all details in curvature get lost. The experimental resolution of $\sigma/2$ was chosen, as this shows the highest level of agreement with the experimental results in $n^{2\gamma}_{\sigma}(k_x,k_y)$. This is demonstrated in figure E.3.

MEM

Considering the demonstrated effect of experimental resolution, the clearness of different signatures in curvature for the experimental data is surprising. We see in figure E.4 that even the curvature of data with an experimental resolution of $\sigma/2$ is far smoother than the experimental. The most probable explanation is, that the MEM post-processing increases the signal clearness drastically. The exact influence of the MEM post-processing could not be investigated, as neither the raw experimental data nor the MEM code was accessible to the author.

FS parameterization

To determine the Fermi surface parameterization, we need to find the corresponding signatures along the paths from table 7.1. To identify those signatures is more challenging for experimental than for theoretical data. For that reason, we marked the position of the theoretical signatures and of reference literature values (if available,

specified later) as vertical lines (blue and gray) in figure E.4. We use those markers as a guide to identify the experimental signature (red dashed line). The resulting Fermi surface parameters are listed in the lower part of table 7.2.

Ref	jack		H oct		N pocket			lens		
Direction	ΓH	ΓN	HΓ	HN	NΓ (semi)	NP (semi)	NH (semi)	ΓH (pos)	ΓH (diam)	⊥ ΓH (diam)
Parameter	f_1	f_2	f_3	f_4	f_5	f_6	f_7	f_8	f_9	f_{10}
dHvA, [196]	0.57	0.29	0.43	0.30	0.18	0.20	0.10		0.10	0.15
dHvA, [197] (ref)	0.58*	0.26*	0.407	0.304	0.163	0.183	0.108		0.11*	0.16*
[197] modified [a] (ref)									0.14*	0.16*
LDA, [198]	0.60	0.23*	0.40*	0.29*	0.18*	0.17*	0.11*	0.24*	0.13*	0.09*
KKR (fit to [197]), [199]	0.5733	0.2602	0.3954	0.3002	0.1624	0.1808	0.1084		0.1096	0.1636
KKR, [200]	0.51*	0.26*	0.43*	0.32*	0.16*		0.11*	0.26*	0.10*	
APW, [201]	0.59*	0.26*	0.40*	0.28*	0.19*	0.18*	0.11*	0.25*	0.14*	0.19*
ACAR 1D, [201]					0.16*	0.18*	0.10*			
KKR, [202]	0.58	0.26	0.42	0.30	0.19		0.11		0.14	
model fit, KKR [192], [204]	0.57	0.260	0.395	0.300	0.162	0.181	0.108	0.280**		
model fit, KKR [193], [204]	0.57	0.275	0.408	0.330	0.190		0.112	0.256**	0.101**	
model fit, ACAR, [204]	0.60	0.066	0.408	0.399	0.128	0.171	0.128	0.284**	0.057**	
Elk (band str.), figure 7.2	0.581	0.261	0.400	0.298	0.175	0.195	0.114	0.255	0.128	
2D-ACAR Elk, figure 7.5	0.598	0.272	0.385	0.298	0.179	0.205	0.116	0.262	0.132	
						0.209				
2D-ACAR exp, figure 7.7	0.561	0.248	0.404	0.301	0.177	0.158		0.228	0.123	
						0.175				
deviation:	0.019	0.012	0.003	0.003	0.013	0.025			0.017	
2D-ACAR exp vs. ref						0.008				

Table 7.2.: Literature values of the Fermi surface parameters in molybdenum:
Values are given in units of $\frac{2\pi}{a}$.
*) Graphical determination from literature. We assume an error of $0.01\,\frac{2\pi}{a}$ for those results.
**) Unreliable estimate.

[a] without D_{4h} symmetry assumption of lens

Literature values

We consider the de Haas-van Alphen measurements of [197] in table 7.2 as the most relevant in comparison to our results, as these are the most recent ones, based on experimental evidence. We give another estimate, however, for the parameterization of the lens in the row below (compare next paragraph). In comparison with these reference results, we achieve an agreement within an error of $\pm 0.025\frac{2\pi}{a}$. The accuracy is mainly limited by the momentum mesh spacing. The only exceptions with a deviation of $\geq \Delta k$ are situated, where signatures in curvature interfere with others (f_6: k_{a1} vs. k_{a2}; f_1: k_{a4} vs. k_{a5};) and concerning the diameter of the lens.

Lens diameter

The Fermi surface parameters in [197] where constructed with Mueller's inversion scheme [8]. To apply this scheme, a D_{4h} symmetry was assumed for the electron lens, even though the authors pointed out, that it is *"rather unlikely, that the real Fermi surface exhibits this mirror symmetry"*. Theoretical literature (for example [198]) as well as our own results (figure E.2) support this point. To give a new estimate of the lens diameter, we transform one half of the ellipse into a triangle and keep the overall (experimentally validated) area constant. With this simple model we arrive at the new lens diameter specified in row ' [197] modified (ref)' of table 7.2. Our result for the lens diameter is between the original value and the new estimate.

Artifacts

At this point it becomes clear, how important the reduction of back-folding artifacts is. Even small artifacts can have a strong signature in curvature and hence can shift or modify the signatures from the Fermi surface. In figure 7.7 the truncation artifact of the 'circular cutoff, $p_{\max} = 1.7$' at 0.5 along path (b), leads to a shift of the k_{b7} and k_{b8} signatures. The only clear minimum would be found at $k_{b8} = 0.58$, leading to $f_5 = 0.127$. For the 'rectangular cutoff, $p_{\max} = 1.7$' the signature at k_{a3} gets lost, making it impossible to determine the size of the electron lens.

Take home message

We found that also for experimental spectra an analysis in curvature can be performed to extract the Fermi surface parameters. Even though, overlapping signatures can lead to deviations, the Fermi surface could be parameterized with an accuracy of roughly the momentum mesh spacing. Avoiding back-folding artifacts turned out to be important, as this prevents fake signatures in curvature. Both commonly used techniques (circular cutoff and rectangular cutoff) would have lead to fewer or wrong extracted parameters at $p_{\max} = 1.7$. For larger $p_{\max}$ it is not clear to what degree back-folding artifacts still play a role, when using those back-folding methods. This reduces the reliability of such an analysis.

7.4. Summary and Potential Improvements

Summary

We compared the two currently common back-folding methods (circular cutoff and rectangular cutoff, both without extrapolation) to the newly proposed back-folding procedure (Voronoi cutoff with extrapolation). On a theoretical level with $p_{\max} = 2.24$ we obtained minor improvements (compare figure 7.5 c and d). When investigating the experimental spectra with a higher level of truncation for $p_{\max} \in \{1.7, 2.24\}$, we found that our newly proposed method is the only one, which is stable with respect to $p_{\max}$. When analyzing the second derivative of back-folded spectra, we found that, by reducing the artifacts from back-folding, the Fermi surface parameters can be extracted directly from the back-folded spectrum. In general, complex tomographic methods need to be used for this, which introduce data processing errors on their own.

Potential improvements

In the following we propose some ideas to improve the methodology presented in this section:

- Odd momentum mesh:
  To increase the precision, in future investigations, experiment should be performed on an odd momentum mesh and with an optimal momentum mesh spacing. This has the advantage of avoiding interpolation.

- Increased detector distance:
  As both the momentum mesh spacing and experimental resolution make an analysis in curvature more difficult, our recommendation is to perform experiments with a larger distance between the detectors and the probe. This would simultaneously decrease the momentum mesh spacing and the experimental resolution, leading to an increase in precision by a factor of roughly $\frac{2.24}{1.7} = 1.3$. The disadvantage of a smaller $p_{\max}$ could be handled by the newly developed back-folding technique. Eventually occurring experimental challenges might be related to the scattering of the γ-radiation in air.[2]

- Subpixel edge detection:
  To adapt subpixel edge detection concepts [216–218] to the specific properties of 2D-ACAR data (for instance the different definitions of the edge position) is another promising path to continue. Table 2 in [216] demonstrates, how the position of a simple edge can be identified with an accuracy of about 1% of the pixel distance.[3]

All three proposals bear the potential of significantly increasing the precision of the 2D-ACAR technique. If in combination a Fermi surface signature detection with an accuracy of $0.1\Delta p_{x/y} \approx 0.002\frac{2\pi}{a}$ could be achieved, 2D-ACAR measurements would reach the precision of de Haas-van Alphen measurements, but with additional information about the position and shape of Fermi surface features.

Take home message

Analyzing the cuts along k-paths of $n^{2\gamma}$ turned out to be a reliable way, to determine the

[2] This point arose in a private conversation with Stephen Dugdale (Bristol, UK).

[3] The pixel distance corresponds in our case to the momentum mesh spacing $\Delta p_{x/y} = \Delta k_{x/y}$.

Fermi surface parameter within the accuracy of the momentum mesh spacing. The prior knowledge about the Fermi surface, necessary for such an analysis, can be obtained from calculations or tomographic methods (for instance [58, 85, 91, 92, 94, 189]). For those analyses the Voronoi cutoff in combination with extrapolation should be used for back-folding. Using an odd momentum mesh with optimal momentum mesh spacing on an experimental level, increasing the distance between the detectors and investigating subpixel edge detection methods could open the path to a new high precision method for Fermi surface measurements.

Part IV.

Conclusion and Outlook

Conclusion

Problems with back-folding algorithms

The LCW theorem plays an important role in ACAR and Compton scattering experiments. We analyzed the common implementations for numerical artifacts, which are a potential source of miss-interpretation of Fermi surface signatures in the data. The characteristic artifact patterns are pointed out, helping the reader to identify potential weaknesses in back-folded data.

Improved back-folding method

As we found out, the most precise way to perform LCW back-folding is, by first extrapolating the data and then applying a symmetry conserving (Voronoi) cutoff, before performing the shifted summation. This was not computationally affordable during the 1990s, when most of the analyzing framework for 2D-ACAR experiments was developed.

Curvature of 2D-ACAR spectra

With the new back-folding method, the curvature of the electron crystal momentum distribution can be analyzed to determine the Fermi surface. Even though, this is not applicable to all Fermi surface features (in the case of an overlap with other signatures along the integration direction), we increased the capabilities of this approach. Truncation artifacts obstructed such a detailed analysis before, so mainly qualitative analyses were performed on 2D-ACAR data from a single projection direction.

Measurement times and accuracy

The newly developed back-folding method makes it also possible, to work with data on a smaller momentum range. In this way, poor counting statistics at large momenta are no longer a limiting factor, such that experiments can be performed with a reduced number of counts and hence with shorter measurement times.
The option to work with data on a smaller momentum range also opens a new path to experimental setups with an increased probe-detector distance and hence with a smaller momentum mesh spacing. This could increase accuracy by 30%.

Elk inaccuracies

We verified the new back-folding method by applying it to several realistic systems. First we matched theoretical and experimental data of silver, as the Fermi surface of this system has a simple shape and is well investigated. We thereby encountered issues with the internal grid of the LTM in Elk (parameter 'ngridk'), being a serious source of inaccuracies on the theoretical side.

Momentum meshing

During the investigation of molybdenum it turned out, that (repeated) interpolation between data points at different stages of the back-folding process can make differences of up to the momentum mesh spacing, considering the position of Fermi surface signatures. For a precise investigation of 2D-ACAR data, interpolation should be reduced to a minimum. Therefore, when parameterizing Fermi surfaces, it is preferable to use an odd momentum mesh, including data points directly on the high symmetry lines.

Image processing methods

During this work, the application of different kinds of image processing methods was pointed out repeatedly. It should be mentioned, however, that a simple application will in general introduce a heavy additional bias. Many of those methods were developed for the manipulation of photographs and hence different definitions for basic features (for instance the exact position of an edge) apply for 2D-ACAR data. Nevertheless, the adaption of image processing methods for 2D-ACAR data is highly recommended.

Outlook

Further improvements

Together with the improvements brought by the new back-folding algorithm new options for further developments were created. The most promising are briefly summarized below.

3D-LCW

Tomographic methods [89–92, 94] in general construct $\rho^{2\gamma}(\boldsymbol{p})$ from several $\rho^{2\gamma}(p_x,p_y)$'s along different integration directions. $\rho^{2\gamma}(\boldsymbol{p})$ in then back-folded to $n^{2\gamma}(\boldsymbol{k})$ by the LCW theorem in its three-dimensional form.
With the framework, developed in this work, new options arise to increase the precision of this approach. Improvements are expected from applying extrapolation before tomographic reconstruction or from using (artifact-free) back-folded data for a tomographic reconstruction of $n^{2\gamma}(\boldsymbol{k})$.

New interpolation scheme

Common interpolation schemes are designed to avoid steps, kinks and discontinuities in higher order derivatives. This is obstructive for Fermi surface detection in the context of 2D-ACAR. As was pointed out already in figure 4.2, interpolation results in a smoothing and a shift of steps and kinks.
A suggestion for a new interpolation scheme in one dimension to evaluate a function $f(x)$ between the mesh points x_n and x_{n+1} shall be given: First we extrapolate linearly by $l_1(x) : l_1(x_{n-1}) = f(x_{n-1}) \wedge l_1(x_n) = f(x_n)$ and $l_2(x) : l_2(x_{n+1}) = f(x_{n+1}) \wedge l_2(x_{n+2}) = f(x_{n+2})$. If l_1 and l_2 intersect in the interval $(x_n; x_{n+1})$, the interpolation is performed linearly from $f(x_n)$ to the intersection point to $f(x_{n+1})$. Otherwise the interpolation is performed along l_1 and l_2 with a step at $(x_n + x_{n+1})/2$. A schematic drawing of this interpolation scheme can be found in figure 7.8. Different two-dimensional generalizations thereof should be tried and evaluated on 2D-ACAR data.

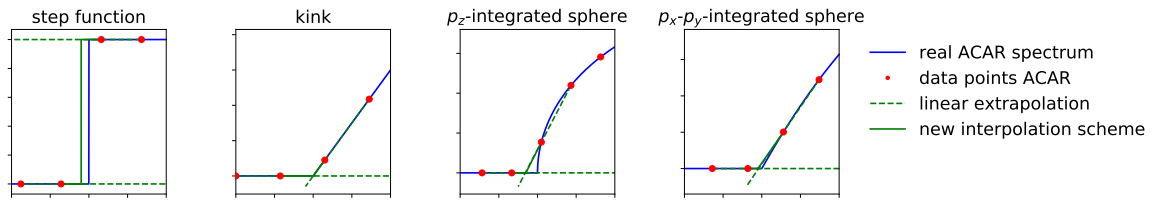

Figure 7.8.: Proposal for a new interpolation scheme

Subpixel edge detection

Using subpixel edge detection methods could also be used to determine the position of Fermi surface signatures with an increased accuracy. As pointed out in section 7.4, this technique alone could increase the precision of 2D-ACAR to the level of dHvA measurements. As mentioned earlier, this will not be possible without adjusting existing algorithms to the properties of 2D-ACAR spectra.

Correction of experimental resolution

As experimental resolution is hindering an analysis of Fermi surface signatures in curvature, the maximum entropy method (MEM) [83] is an important tool for post-processing experimental data. This method should be reviewed, concerning its influence on Fermi surface signatures in the spectrum. Further, it should be verified, that the unexpected sharpness of the experimental 2D-ACAR spectrum of molybdenum in section 7.3 is indeed a result of MEM post-processing.

Back-folding before binning

We showed that the momentum mesh should fulfill condition (4.2) in order to avoid interpolation. In modern experiments, the coincidence coordinates are recorded for each event (compare 'list mode' in [68]) and the binning[4] is performed after the measurement is completed.
Another approach might be to perform the back-folding operation with the continuous coordinates of the separate events to get the counting statistic in the VP. After that, any binning can be chosen, as the momentum mesh spacing condition (4.2) is only needed to avoid interpolation during the back-folding procedure. This would open new ways to detect the Fermi surface signatures, for instance by finer binning.
To realize this approach, a new concept for extrapolation should be developed. This could be done for instance, by first binning and extrapolating $\rho^{2\gamma}(p_x,p_y)$ as described in subsection 4.2.2. The extrapolated data points could be added then as 'fake' events to the list mode recoding, used for back-folding. This should still remain in the range of acceptable computational effort.

[4] Binning is the process of assigning the recorded coincidence events $\{(p_x,p_y)\}$ to a momentum mesh in order to construct $\rho^{2\gamma}(p_x,p_y)$. Compare page 23.

Appendix

A. A Simplified Derivation of the Lock-Crisp-West Theorem

Intention

We give a simplified proof of the LCW theorem in analogy to parts of [80] and [86]. In the previous proof of the LCW theorem (subsection 3.2.1) the majority of the complications originated from the nature of many-particle states and the additional influence of the positron. We neglect these effects and restrict ourself to the LCW theorem in its non-interacting, purely electronic version. This shall help the reader to develop an intuitive understanding of the transition from momentum space to crystal momentum space.

Approximations

We describe the electron wave function by Bloch's theorem

$$\psi^{\mathrm{e}}_{j,\boldsymbol{k}}(\boldsymbol{r}) = \sum_{\boldsymbol{G_1}} \frac{B_{j,\boldsymbol{G_1}+\boldsymbol{k}}}{(2\pi)^3} e^{i(\boldsymbol{G_1}+\boldsymbol{k})\boldsymbol{r}} \,. \tag{A.1}$$

The positron wave function is set to constant

$$\Psi^{\mathrm{p}}(\boldsymbol{r}) = 1 \,, \tag{A.2}$$

which is equivalent to having an evenly distributed positron or no positron at all.

Fourier transformation

By using the Fourier transformation

$$F(\boldsymbol{p}) = \int\limits_{\mathrm{V}} \mathrm{d}\boldsymbol{r}\, \mathrm{e}^{-i\boldsymbol{p}\boldsymbol{r}} F(\boldsymbol{r}) \tag{A.3}$$

$$F(\boldsymbol{r}) = \frac{1}{(2\pi)^3} \int\limits_{\mathrm{V}} \mathrm{d}\boldsymbol{p}\, \mathrm{e}^{+i\boldsymbol{p}\boldsymbol{r}} F(\boldsymbol{p}) \,, \tag{A.4}$$

we can express the electron wave function in momentum representation

$$\psi^{\mathrm{e}}_{j,\boldsymbol{k}}(\boldsymbol{p}) = \int\limits_{\mathrm{V}} \mathrm{d}\boldsymbol{r}\, \mathrm{e}^{-i\boldsymbol{p}\boldsymbol{r}} \psi^{\mathrm{e}}_{j,\boldsymbol{k}}(\boldsymbol{r}) \,. \tag{A.5}$$

EMD

The electron momentum distribution $\rho(\boldsymbol{p})$ is the squared amplitude of the electron wave function in momentum space. The experiment provides only information about the occupied states, giving rise to the Fermi distribution term $n_j(\boldsymbol{k})$. The vectors $\boldsymbol{p}$

and $\boldsymbol{k}$ are related by a reciprocal lattice vector, such that $\boldsymbol{k}$ is situated in the first Brillouin zone.

$$\rho(\boldsymbol{p}) = \sum_{j,k} \left| \int \mathrm{d}\boldsymbol{r}\, \psi_{j,\boldsymbol{k}}(\boldsymbol{p}) \right|^2 n_j(\boldsymbol{k}) \equiv \sum_{j,k} \rho_{j,\boldsymbol{k}}(\boldsymbol{p})\, n_j(\boldsymbol{k}) \tag{A.6}$$

Inserting equation (A.1) into (A.5) into (A.6) leads to

$$\begin{aligned}
&\rho(\boldsymbol{p}) \\
&= \sum_{j,k} \left(\int \mathrm{d}\boldsymbol{r} \sum_{\boldsymbol{G'}} \frac{B^j_{\boldsymbol{k}+\boldsymbol{G'}}}{(2\pi)^3} \mathrm{e}^{i(\boldsymbol{k}+\boldsymbol{G'})\boldsymbol{r}} \mathrm{e}^{-i\boldsymbol{p}\boldsymbol{r}} \right) \left(\int \mathrm{d}\boldsymbol{r'} \sum_{\boldsymbol{G''}} \frac{(B^j_{\boldsymbol{k}+\boldsymbol{G''}})^*}{(2\pi)^3} \mathrm{e}^{-i(\boldsymbol{k}+\boldsymbol{G''})\boldsymbol{r'}} \mathrm{e}^{+i\boldsymbol{p}\boldsymbol{r}} \right) n^j_{\mathrm{F}}(\boldsymbol{k}) \\
&= \sum_{j,k,\boldsymbol{G'},\boldsymbol{G''}} B^j_{\boldsymbol{k}+\boldsymbol{G'}} (B^j_{\boldsymbol{k}+\boldsymbol{G''}})^* \delta(\boldsymbol{p}-\boldsymbol{k}-\boldsymbol{G'}) \delta(\boldsymbol{p}-\boldsymbol{k}-\boldsymbol{G''})\, n^j_{\mathrm{F}}(\boldsymbol{k})\,.
\end{aligned} \tag{A.7}$$

Periodic summation

We calculate now the expression

$$\sum_{\boldsymbol{G}} \rho(\boldsymbol{p}+\boldsymbol{G}) \tag{A.8}$$

$$= \sum_{\boldsymbol{G}} \sum_{j,k,\boldsymbol{G'},\boldsymbol{G''}} B^j_{\boldsymbol{k}+\boldsymbol{G'}} (B^j_{\boldsymbol{k}+\boldsymbol{G''}})^* \delta(\boldsymbol{p}+\boldsymbol{G}-\boldsymbol{k}-\boldsymbol{G'}) \delta(\boldsymbol{p}+\boldsymbol{G}-\boldsymbol{k}-\boldsymbol{G''})\, n^j_{\mathrm{F}}(\boldsymbol{k}) \tag{A.9}$$

Simplification

As $\boldsymbol{k}_{\dots}$ denotes vectors of the first Brillouin zone and $\boldsymbol{G}^{\dots}_{\dots}$ reciprocal lattice vectors, we define

$$\boldsymbol{p} = \boldsymbol{G}_{\boldsymbol{p}} + \boldsymbol{k}_{\boldsymbol{p}}\,. \tag{A.10}$$

and the delta functions factorize to

$$\delta(\boldsymbol{p}+\boldsymbol{G}-\boldsymbol{k}-\boldsymbol{G'}) = \delta(\boldsymbol{k}_{\boldsymbol{p}}-\boldsymbol{k}) \delta(\boldsymbol{G}_{\boldsymbol{p}}+\boldsymbol{G}-\boldsymbol{G'})\,. \tag{A.11}$$

Equation (A.9) simplifies to

$$\sum_{\boldsymbol{G}} \rho(\boldsymbol{p}+\boldsymbol{G}) = \sum_{\boldsymbol{G},j} B^j_{\boldsymbol{k}_{\boldsymbol{p}}+\boldsymbol{G}_{\boldsymbol{p}}+\boldsymbol{G}} (B^j_{\boldsymbol{k}_{\boldsymbol{p}}+\boldsymbol{G}_{\boldsymbol{p}}+\boldsymbol{G}})^* n^j_{\mathrm{F}}(\boldsymbol{k}_{\boldsymbol{p}}) \tag{A.12}$$

$$= \sum_{\boldsymbol{G},j} B^j_{\boldsymbol{k}_{\boldsymbol{p}}+\boldsymbol{G}} (B^j_{\boldsymbol{k}_{\boldsymbol{p}}+\boldsymbol{G}})^*\, n^j_{\mathrm{F}}(\boldsymbol{k}_{\boldsymbol{p}})\,. \tag{A.13}$$

LCW theorem

So we can use the normalization condition of the wave function

$$\sum_{\boldsymbol{G}} |B^j_{\boldsymbol{k}+\boldsymbol{G}}|^2 \Big|_{j,\boldsymbol{k}} = 1, \tag{A.14}$$

to yield the **Lock-Crisp-West (LCW)** theorem for non-interacting electrons and a constant positron wave function

$$\sum_{\boldsymbol{G}} \rho(\boldsymbol{p}+\boldsymbol{G}) = \sum_{j} n^j_{\mathrm{F}}(\boldsymbol{k}_{\boldsymbol{p}}) \equiv n(\boldsymbol{k}_{\boldsymbol{p}})\,. \tag{A.15}$$

B. LCW Implementation: Supplementary Material

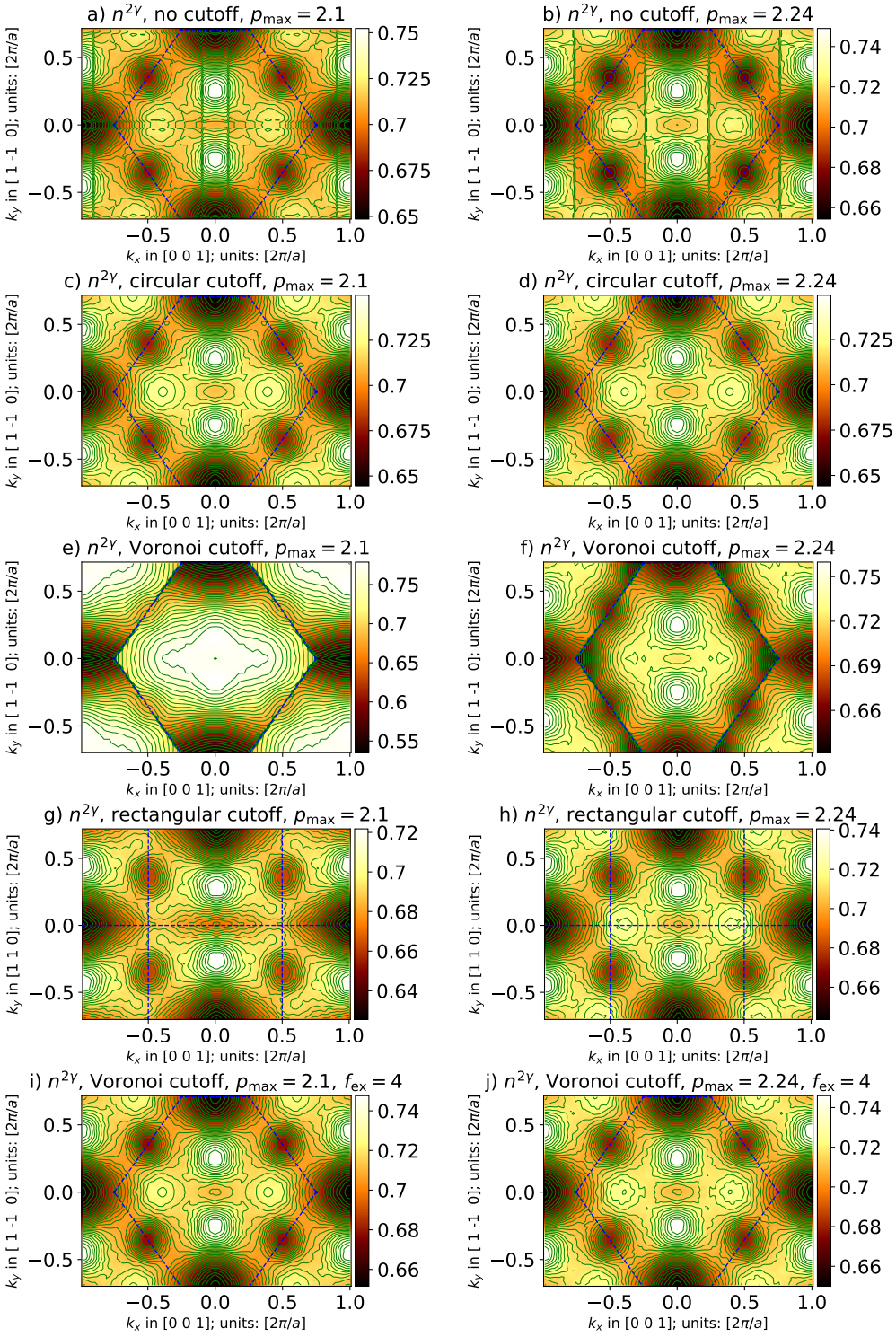

Figure B.1.: Different LCW back-folding methods applied on molybdenum, experimental:
Left column: $p_{\max} = 2.1\frac{2\pi}{a}$;
right column: $p_{\max} = 2.24\frac{2\pi}{a}$ (i.e. without truncation);
Subplot j is, by construction, identical with the reference in figure 4.4b.

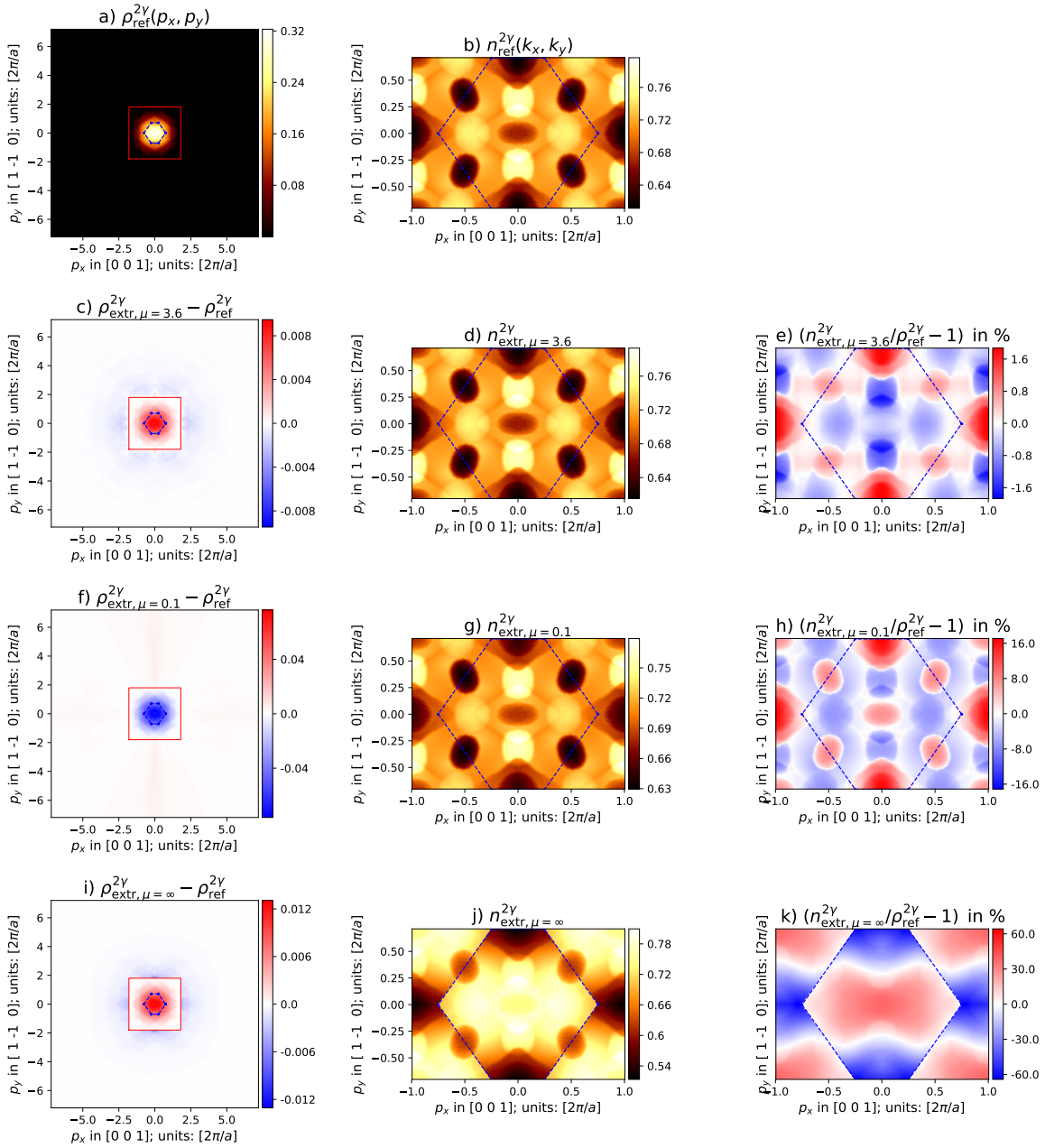

Figure B.2.: Extrapolation for an exponential scaling law with different exponents μ:
a) shows the full reference spectrum $\rho^{2\gamma}_{\mathrm{ref}}$. The extrapolation $\rho^{2\gamma}_{\mathrm{ex}}$ is performed on the data within the red box.
b) $n^{2\gamma}_{\mathrm{ref}}$, the result of back-folding $\rho^{2\gamma}_{\mathrm{ref}}$
c, f, i) difference between extrapolated and reference spectrum
d, g, j) back-folding result of extrapolated spectrum
e, h, k) the relative difference of the extrapolated back-folding result compared to the reference $(n^{2\gamma}_{\mathrm{ex}} - n^{2\gamma}_{\mathrm{ref}})/n^{2\gamma}_{\mathrm{ref}}$, i.e. subplots d, g and j compared to subplot b

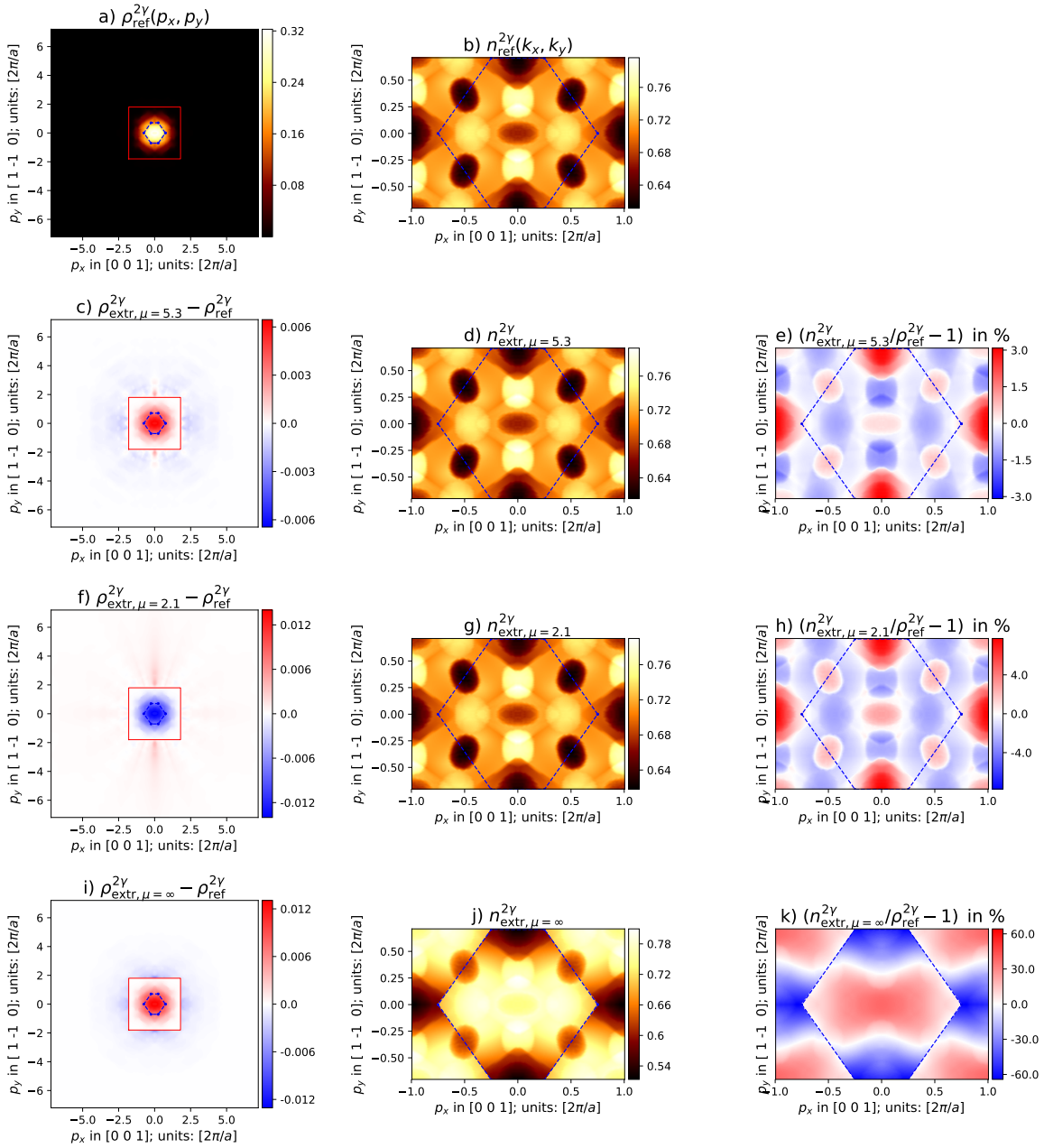

Figure B.3.: Extrapolation for a power law scaling with different exponents μ: Compare figure B.2.

C. Silver (Ag): Supplementary Material

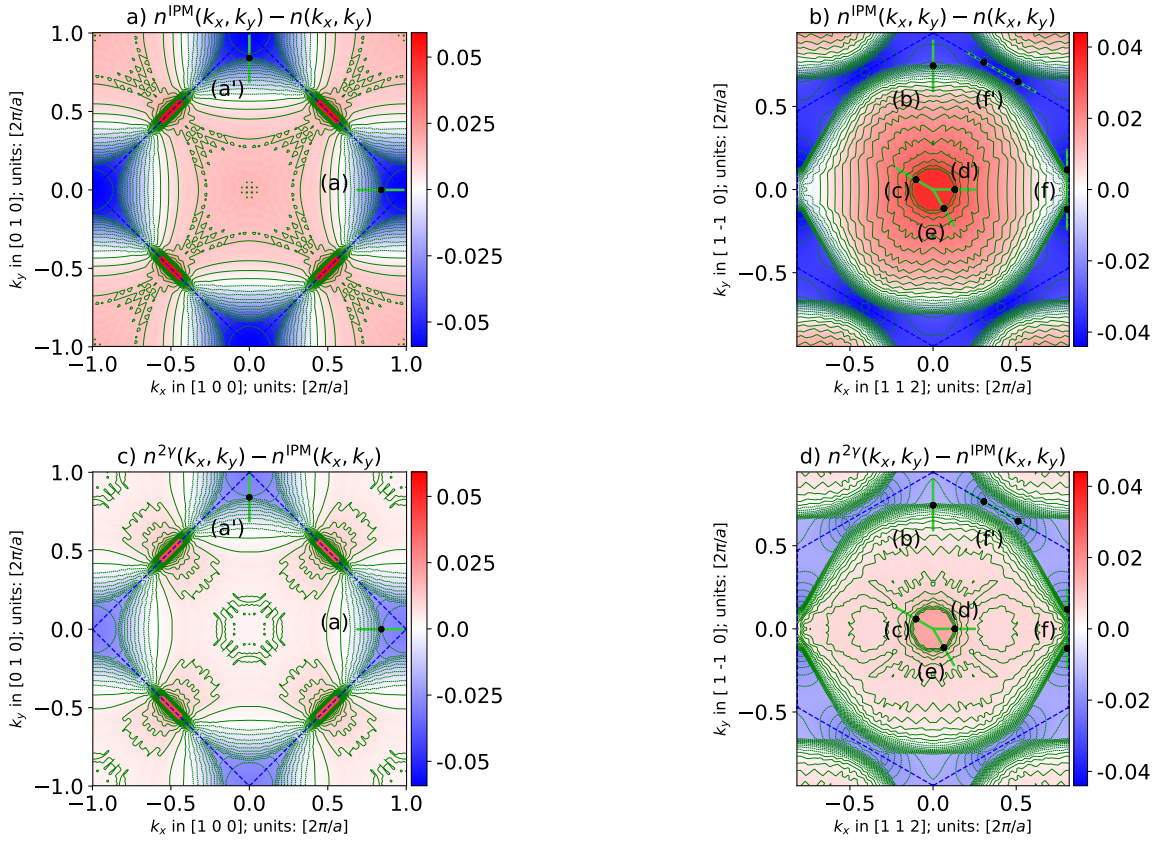

Figure C.1.: Influence of positron wave function and enhancement, Elk calculation:
Complementary illustration to figure 5.5. Change in the back-folded spectrum by the positron wave function (first row) and by electron-positron enhancement (second row).
Note that the color scale was unified.

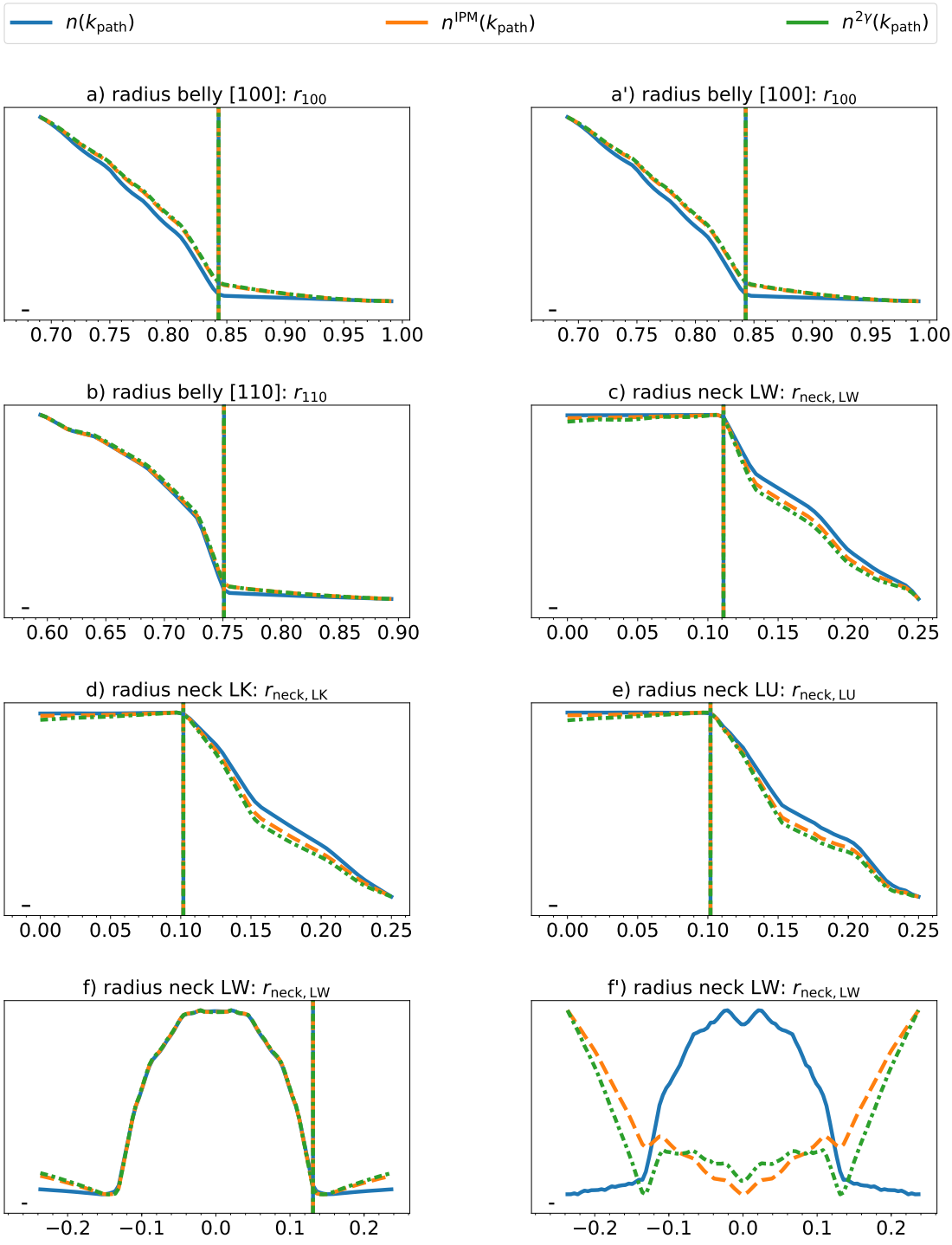

Figure C.2.: Cuts trough ACAR spectra with different positron effects taken into account, Elk calculation:
As the intensity scales are different, the y-axes was not labeled. The kink positions are independent of positron effects.

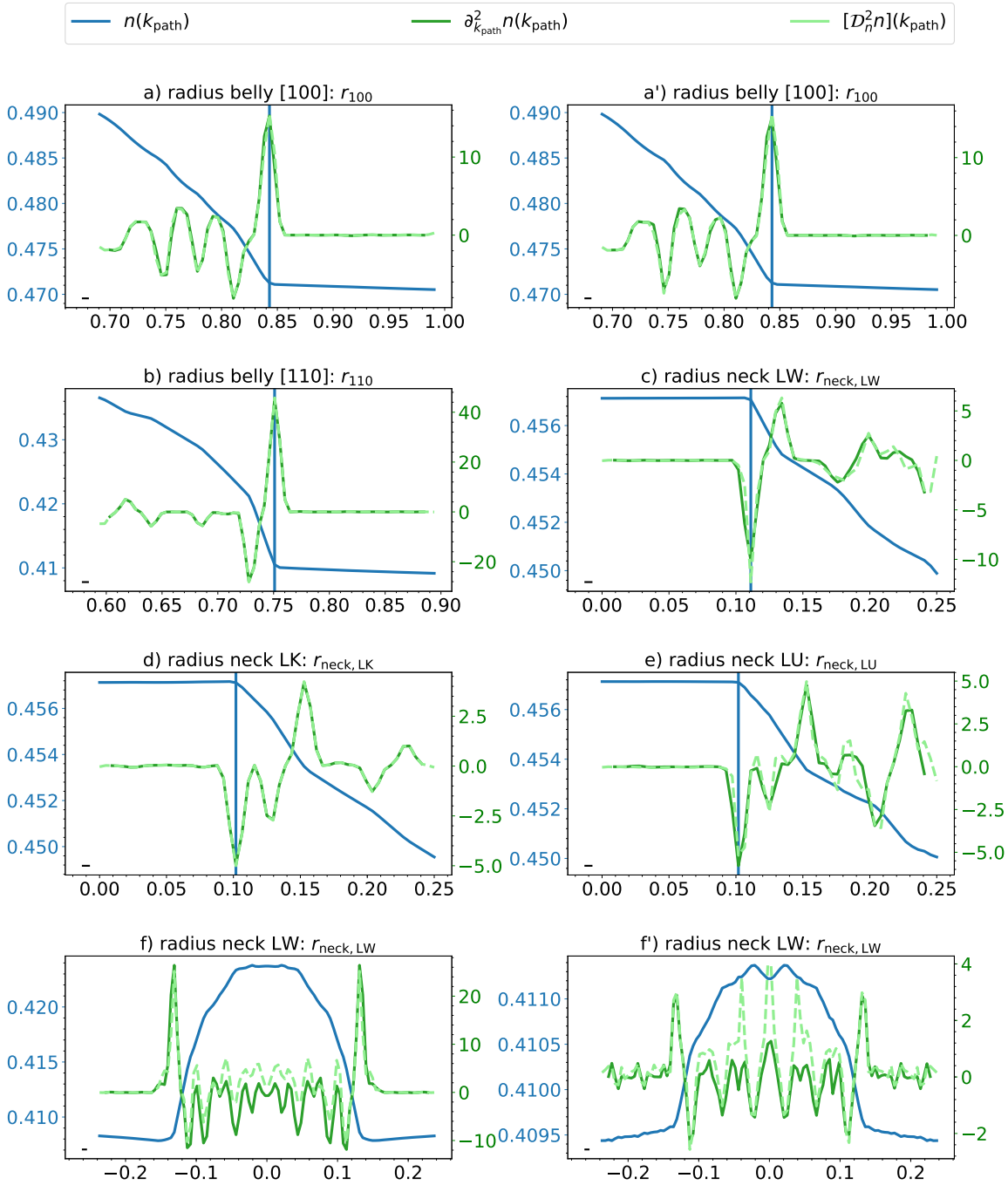

Figure C.3.: Detailed analysis of $n(k_{\text{path}})$, Elk calculation:
Shown is the spectrum along the k-path, its curvature ($\partial^2_{k_{\text{path}}}$) and the SDDn ($\hat{\mathcal{C}}_n$). Curvature and SDDn refer to the right y-scale.
The kink position is identified by extrema in curvature.

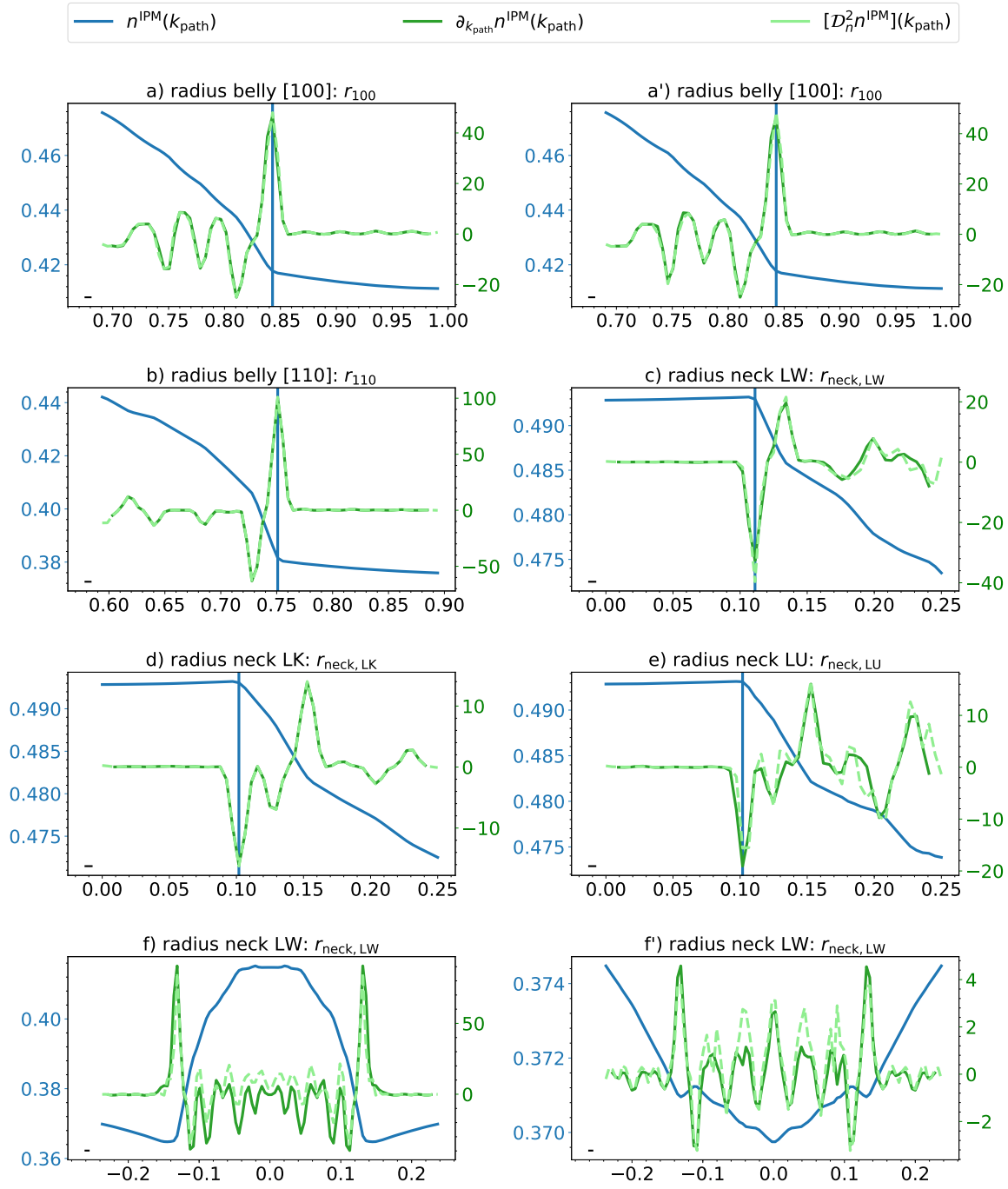

Figure C.4.: Detailed analysis of $n^{\mathrm{IPM}}(k_{\mathrm{path}})$, Elk calculation:
Compare figures C.3 and C.5 for different levels of positron effects taken into account.
This analysis includes the weighting with the positron wave function.

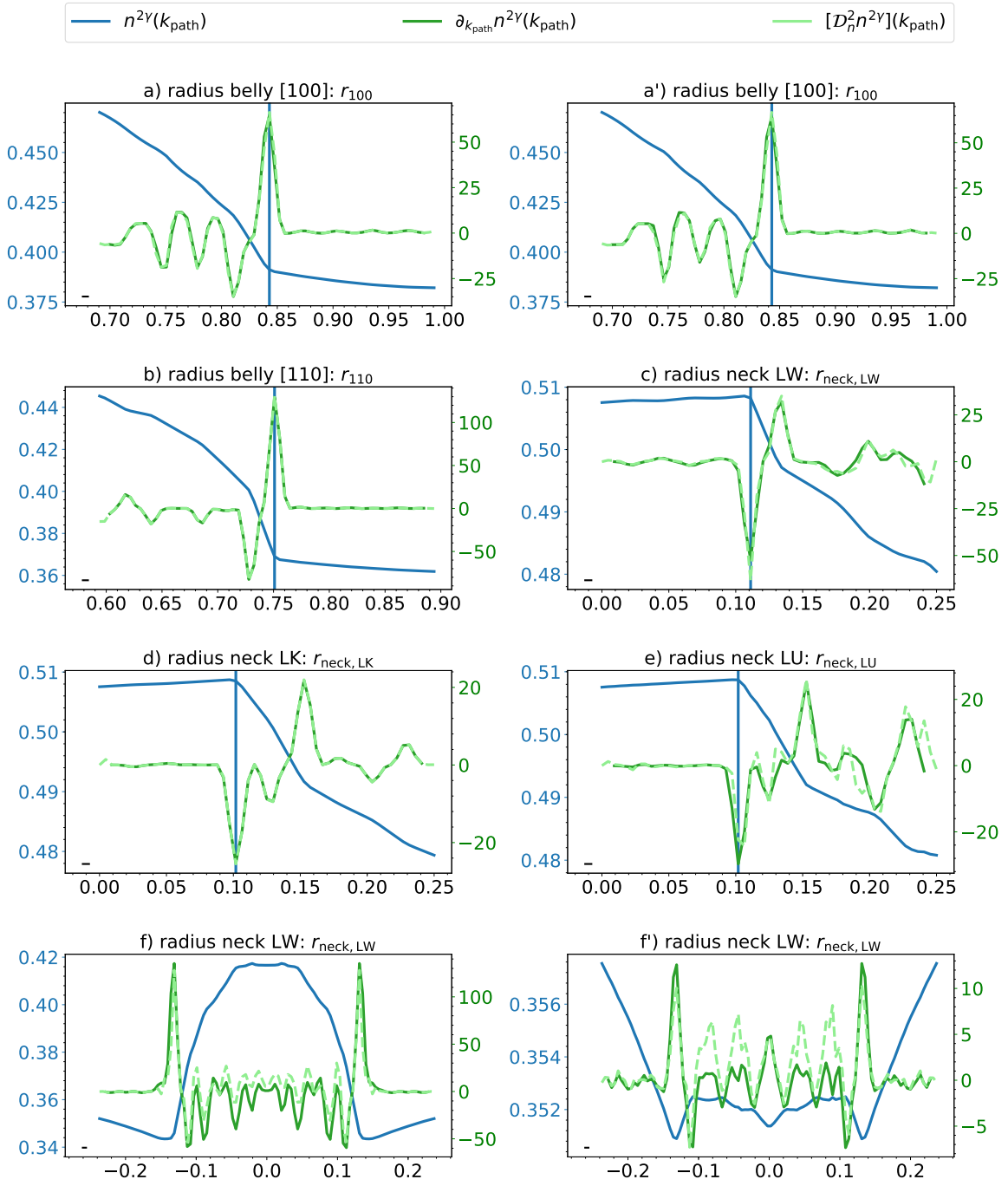

Figure C.5.: Detailed analysis of $n^{2\gamma}(k_{\text{path}})$, Elk calculation:
Compare figures C.3 and C.4 for different levels of positron effects taken into account.
This analysis includes the influence of electron-positron enhancement.

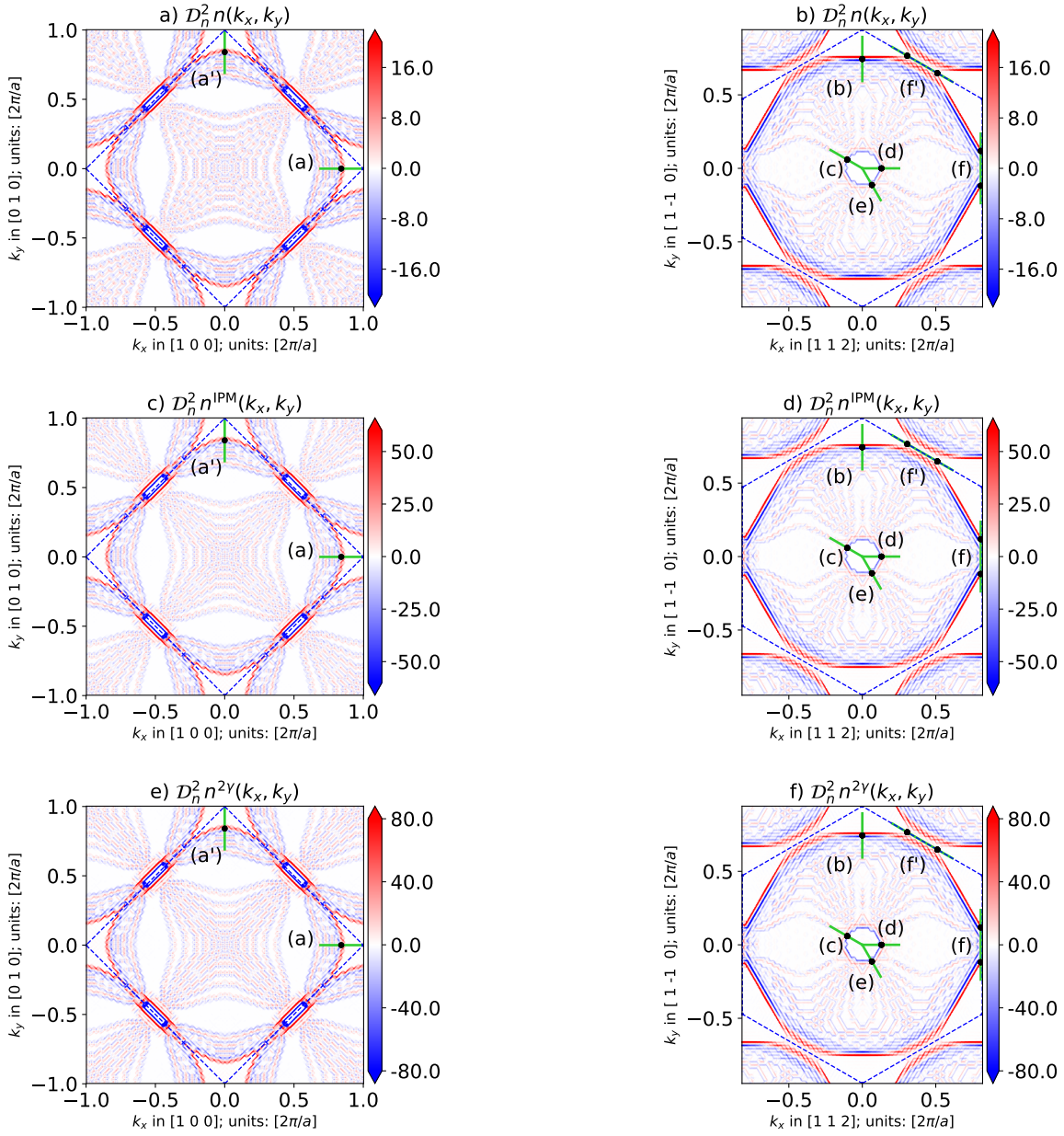

Figure C.6.: Influence of positron wave function and enhancement on the SDDn: Positron effects barely change the relative intensity of Fermi surface signatures.

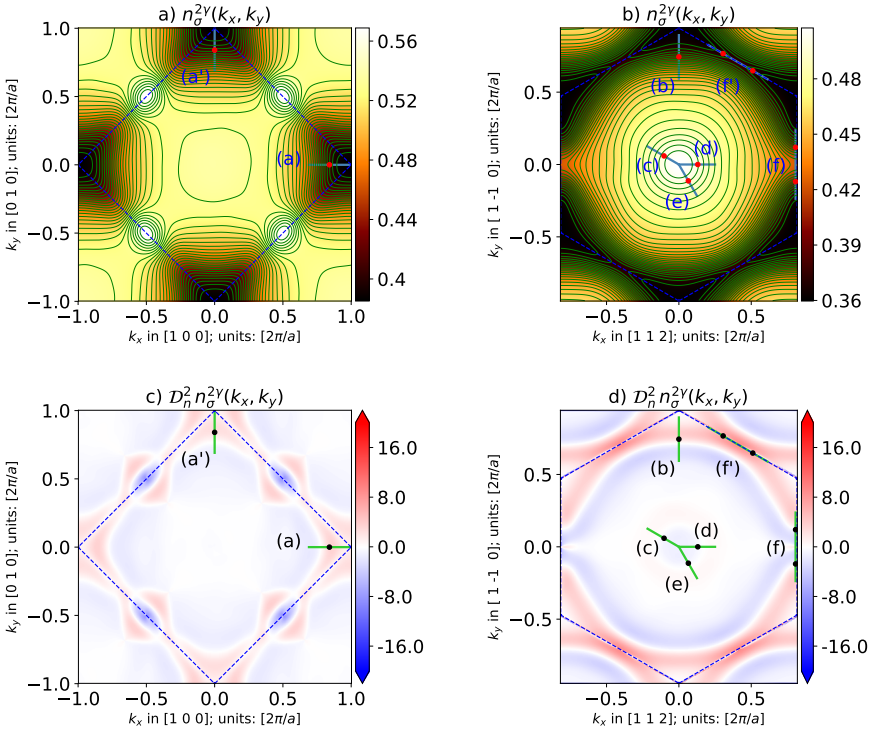

Figure C.7.: $n_\sigma^{2\gamma}(k_x,k_y)$ with strong Poisson noise (200 million counts) for silver, Elk calculation: Compare figures 5.7 and C.8 for other levels of noise.

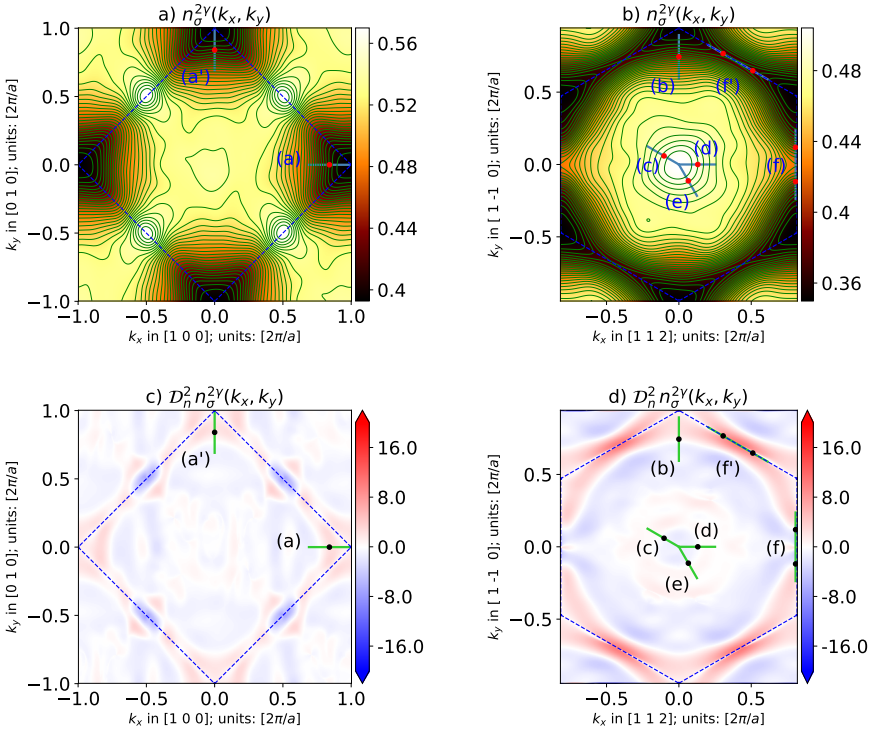

Figure C.8.: $n_\sigma^{2\gamma}(k_x,k_y)$ with weak Poisson noise (8 million counts) for silver, Elk calculation: Compare figures 5.7 and C.7 for other levels of noise.

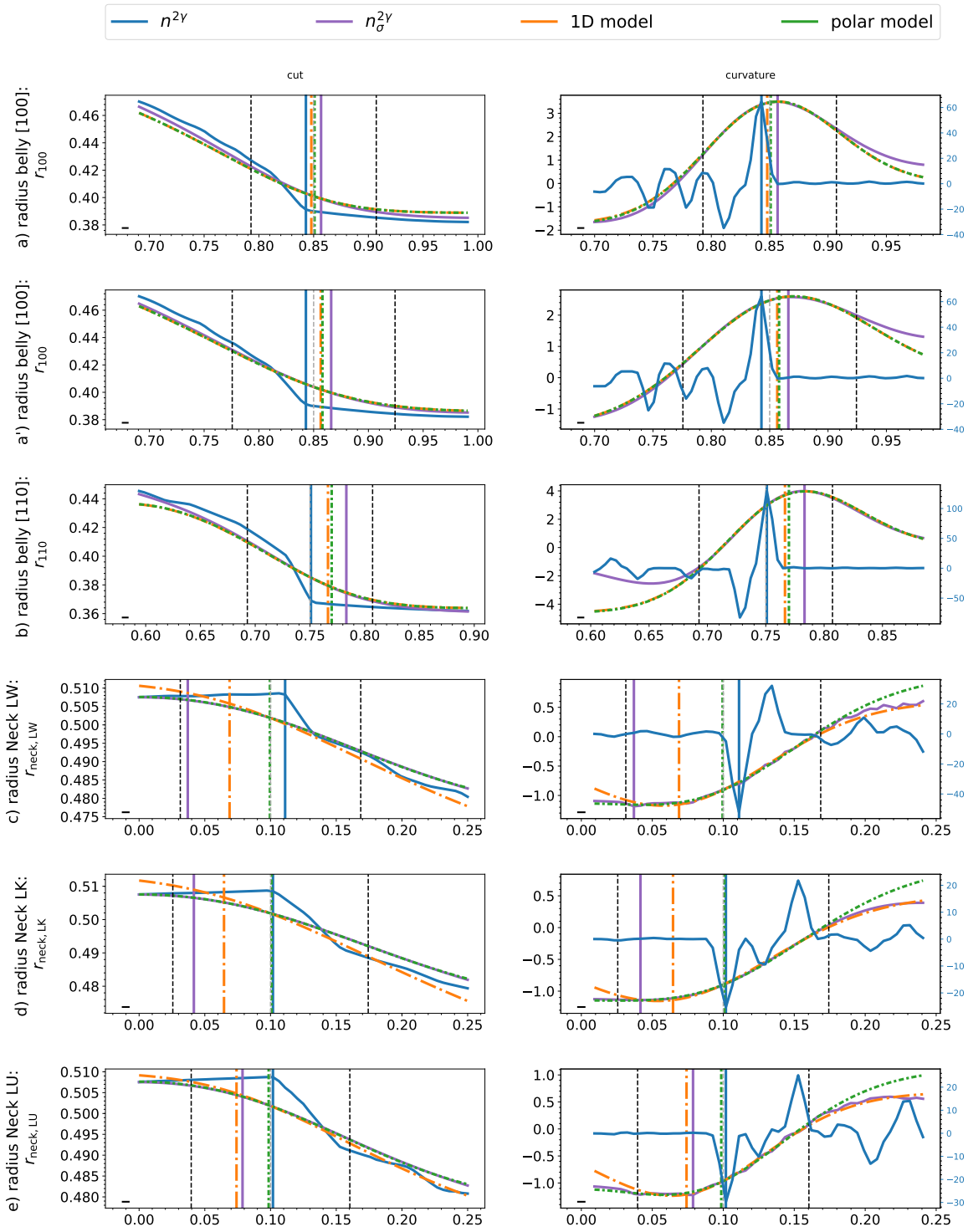

Figure C.9.: Extraction of the Fermi surface parameters from $n_\sigma^{2\gamma}(k_{\text{path}})$, Elk calculation:
Analysis based on figure C.7 (**200 million counts**).
Vertical lines:
fitting range (black) and initial guess (gray) for Fermi surface parameter; reference Fermi surface parameter (blue); maximum curvature of cut through spectrum with experimental resolution $n_\sigma^{2\gamma}$ (purple); reconstructed Fermi surface parameter by fitting models (orange, green).

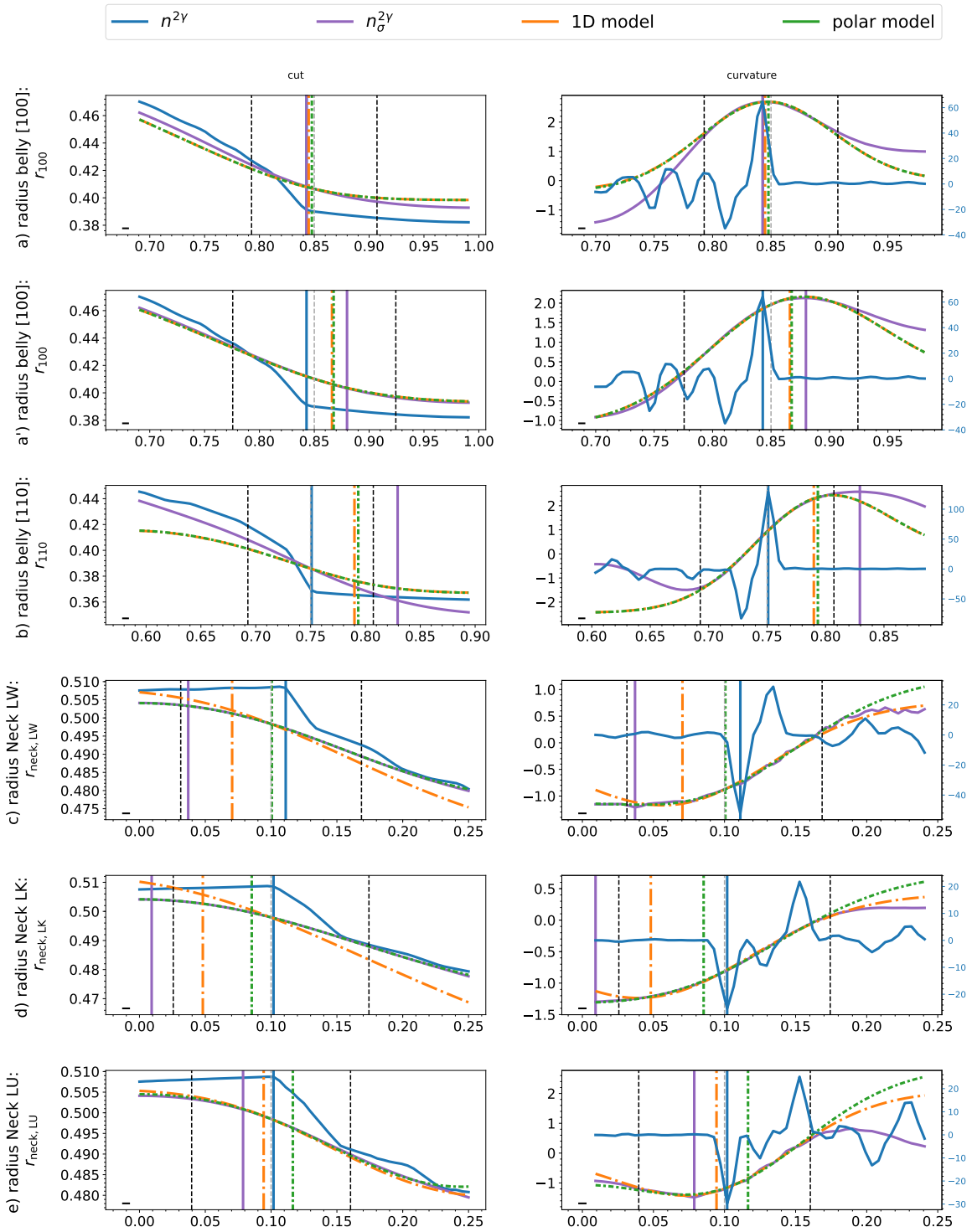

Figure C.10.: Extraction of the Fermi surface parameters from $n_\sigma^{2\gamma}(k_{\mathrm{path}})$, Elk calculation: Analysis based on figure C.8 (**8 million counts**). Analogous to figure C.9.

D. Germanium (Ge): Supplementary Material

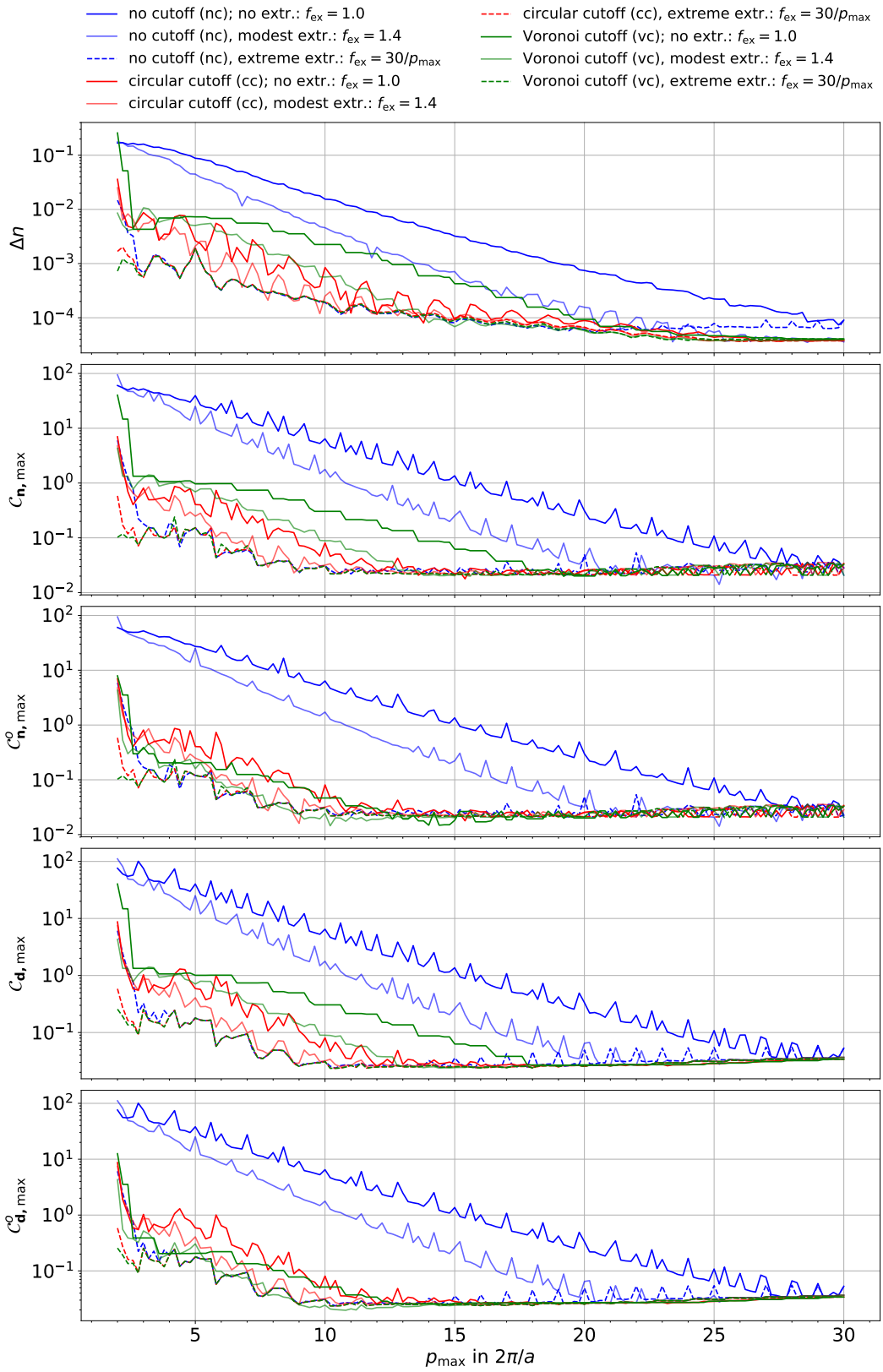

Figure D.1.: Back-folding artifacts of Ge in the [001] vs. $[1\bar{1}0]$ plane (integrated along [110]): Analogous to figure 6.1.

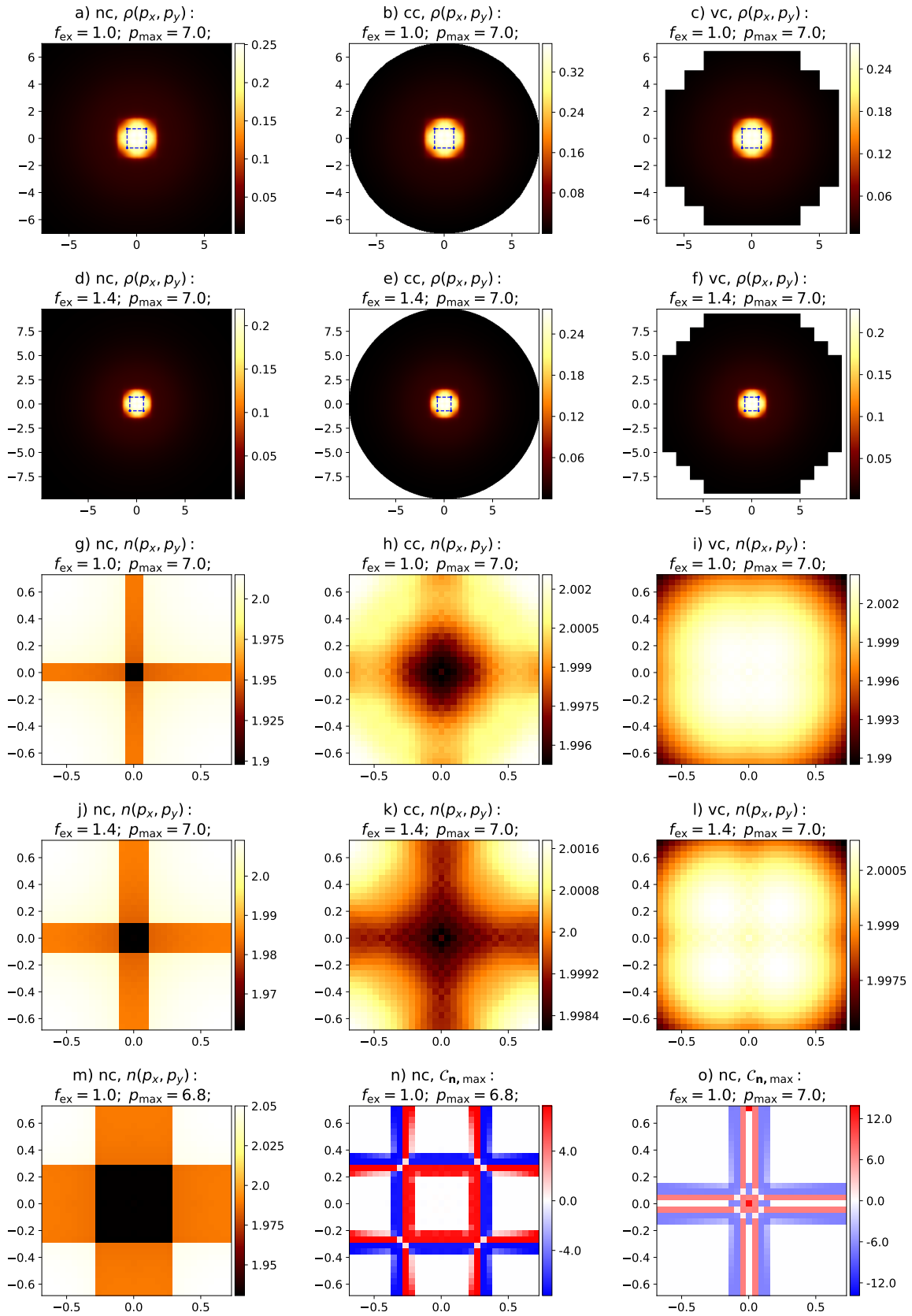

Figure D.2.: Illustration of $\rho(p_x,p_y)$ and $n(k_x,k_y)$ in the [110] (x-axis) vs. [1$\bar{1}$0] (y-axis) plane with different cutoffs, f_{ex} and p_{max}: referring to figure 6.1.

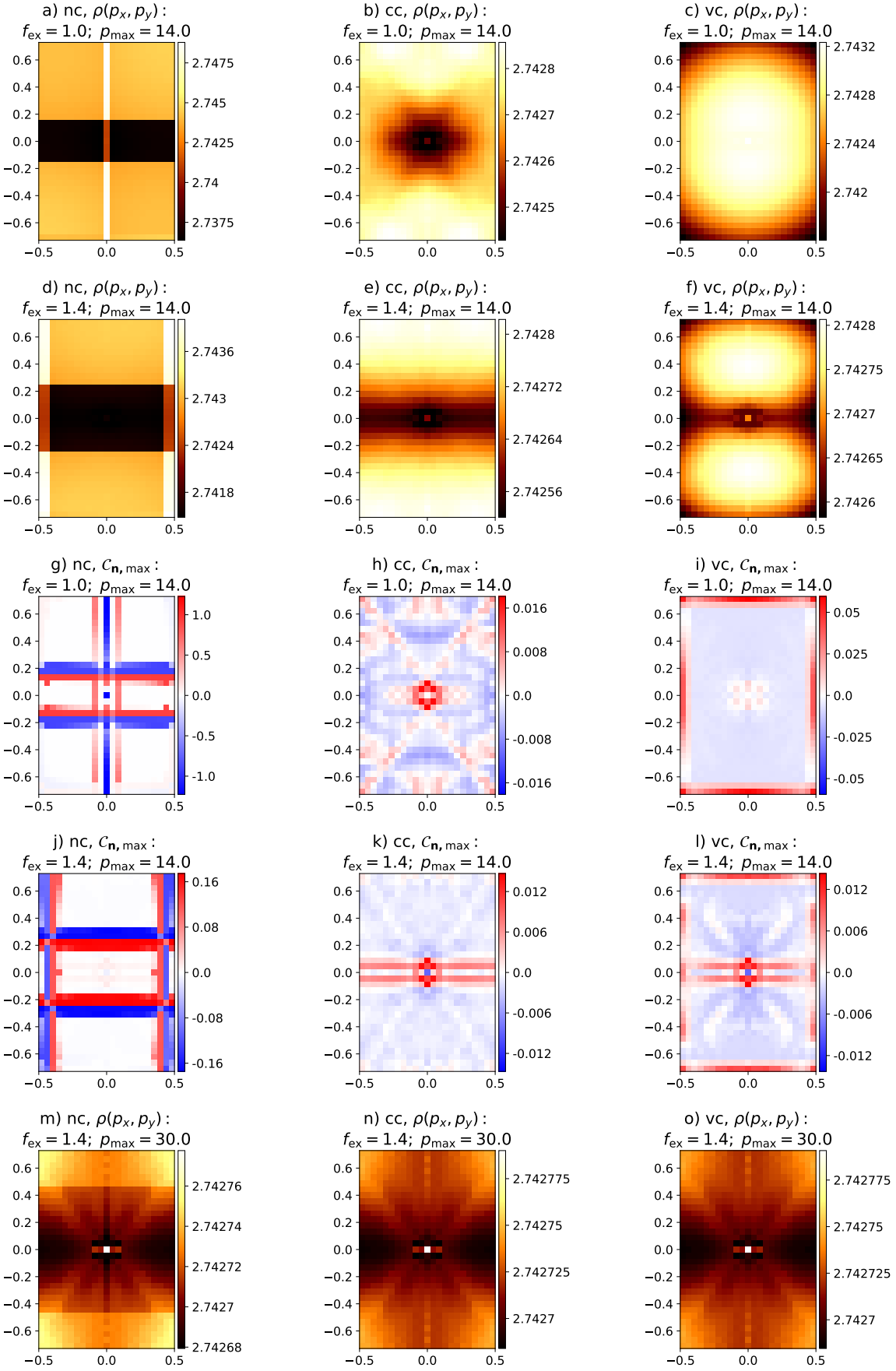

Figure D.3.: Illustration of $\rho(p_x,p_y)$ and $\tilde{n}(k_x,k_y)$ in the [001] (x-axis) vs. [1$\bar{1}$0] (y-axis) plane with different cutoffs, f_{ex} and p_{max}: referring to figure D.1.

E. Molybdenum (Mo): Supplementary Material

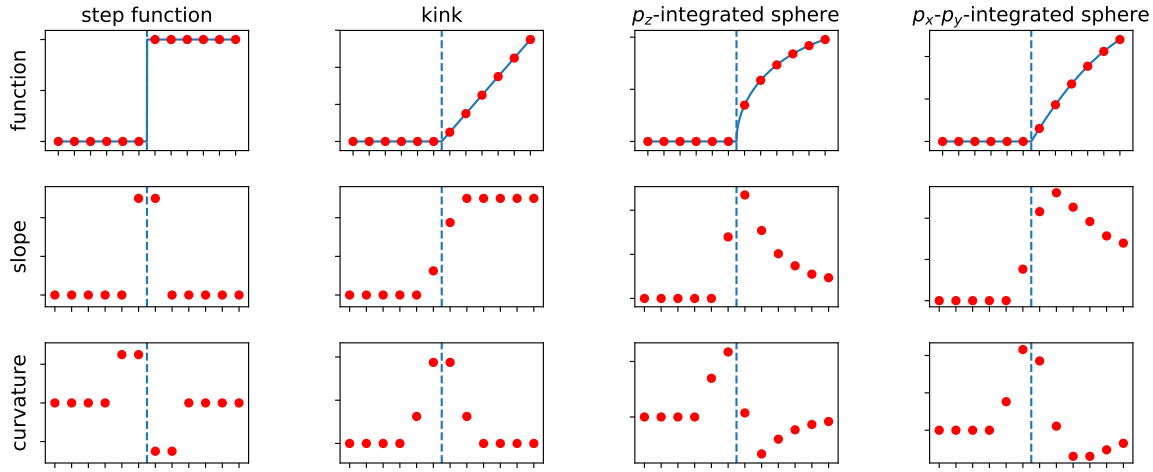

Figure E.1.: Estimated signature in curvature, model calculation:
We compare different functions, i.e. $n^{2\gamma}(k_{\text{path}})$, and the corresponding signal in the curvature, i.e. $\partial^2_{k_{\text{path}}} n^{2\gamma}(k_{\text{path}})$.

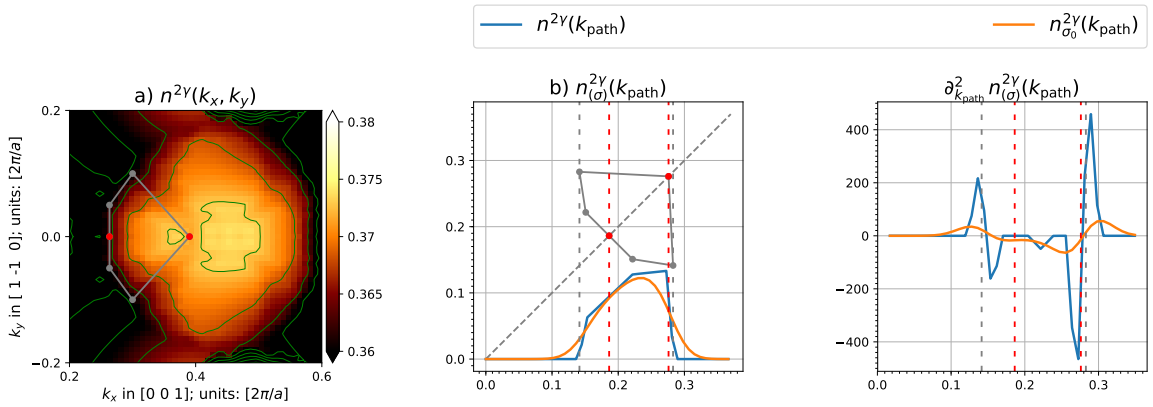

Figure E.2.: Estimated signature of the lens in $n^{2\gamma}(k_{\text{path}})$ along path (b), model calculation:
a) construction of the lens from figure 7.4d,
b) lens contribution to $n^{2\gamma}(k_{\text{path}})$ and
c) corresponding signature in curvature
with and without experimental resolution.

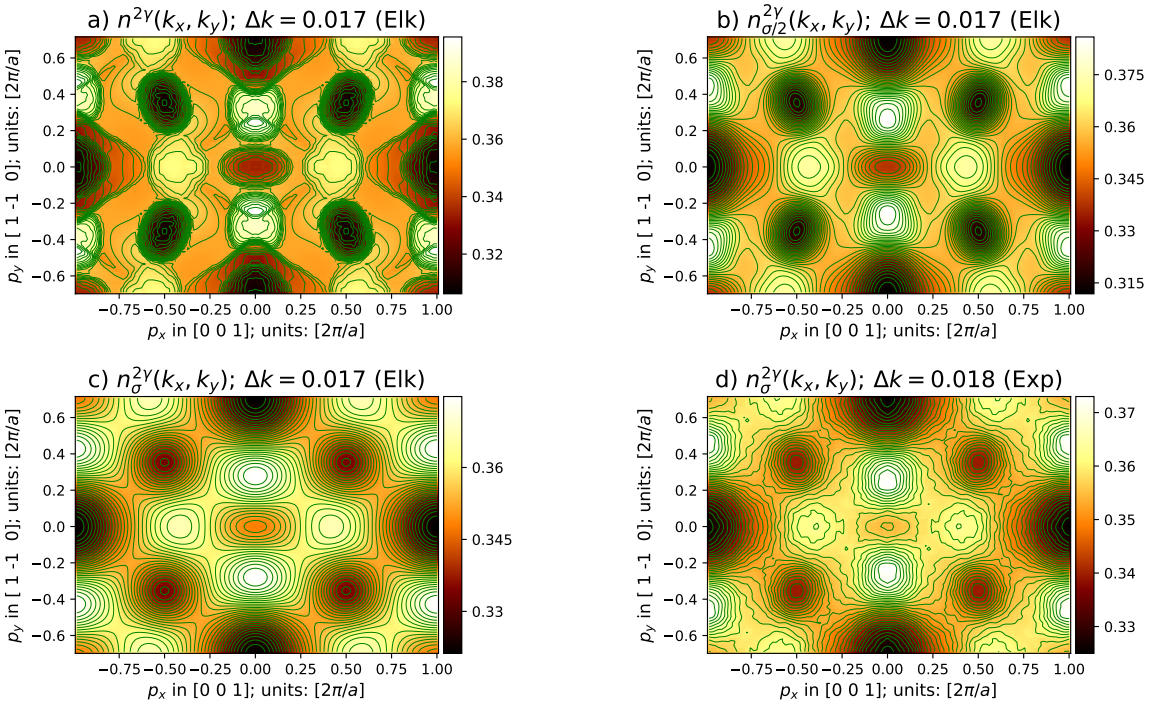

Figure E.3.: Influence of experimental resolution on $n^{2\gamma}(k_x,k_y)$ of molybdenum.
The Elk calculation is shown in subplot a. Different experimental resolutions were added in subplots b and c. The experimental spectrum (post-processed with MEM) is shown in subplot d.
In a qualitative comparison the experimental result corresponds roughly to an experimental resolution of $\sigma/2$, i.e. $\sigma_x = \frac{\sigma_1}{2}$ and $\sigma_y = \frac{\sigma_0}{2}$. The quantitative comparison in figure E.4 shows, that the MEM post-processed spectrum has a clearer structure in curvature.

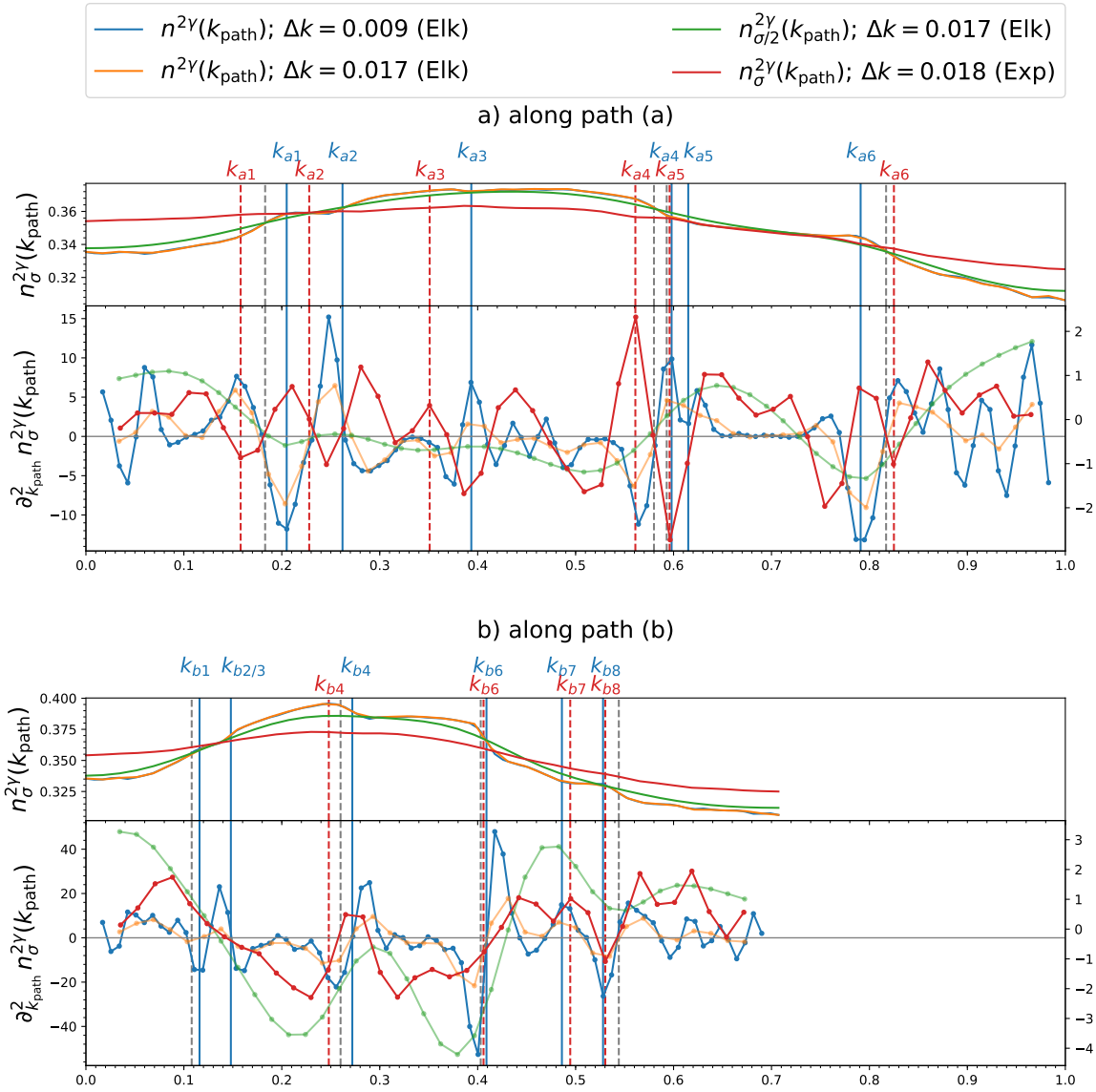

Figure E.4.: Cuts through the $n^{2\gamma}(k_x,k_y)$ of molybdenum. Comparison: Elk calculation and experiment
Left curvature axis: Cuts without experimental resolution (blue,orange).
Right curvature axis: Cuts with experimental resolution (green, red).

References

De Haas-van Alphen (dHvA)

[1] Landau, L. D. (1930). Diamagnetismus der Metalle. Zeitschrift für Physik, 64(9-10), 629-637.

[2] De Haas, W. J., & Van Alphen, P. M. (1930). The dependence of the susceptibility of diamagnetic metals upon the field. In Proc. Netherlands Roy. Acad. Sci (Vol. 33, No. 1106, p. 170).

[3] Onsager, L. (1952). Interpretation of the de Haas-van Alphen effect. The London, Edinburgh, and Dublin Philosophical Magazine and Journal of Science, 43(344), 1006-1008.

[4] Shoenberg, D. (1957). Chapter VIII The De Haas-Van Alphen Effect. In Progress in low temperature physics (Vol. 2, pp. 226-265). Elsevier.

[5] Gold, A. V. (1958). An experimental determination of the Fermi surface in lead. Phil. Trans. R. Soc. Lond. A, 251(989), 85-112.

[6] Schoenberg, D., & Roaf, D. J. (1962). The Fermi Surfaces of Copper, Silver and Gold.

[7] Vanderkooy, J., & Datars, W. R. (1967). de Haas-van Alphen Effect in Arsenic by the Torque Method. Physical Review, 156(3), 671.

[8] Mueller, F. M., & Priestley, M. G. (1966). Inversion of cubic de Haas-van Alphen data, with an application to palladium. Physical Review, 148(2), 638.

[9] Mueller, F. M. (1966). New inversion scheme for obtaining Fermi-surface radii from de Haas-van Alphen areas. Physical Review, 148(2), 636.

[10] Engelsberg, S., & Simpson, G. (1970). Influence of electron-phonon interactions on the de Haas-van Alphen effect. Physical Review B, 2(6), 1657.

[11] Falicov, L. M., & Stachowiak, H. (1966). Theory of the de Haas-van Alphen effect in a system of coupled orbits. Application to magnesium. Physical Review, 147(2), 505.

[12] Graebner, J. E., & Marcus, J. A. (1968). de Haas-van Alphen effect in antiferromagnetic chromium. Physical Review, 175(2), 659.

[13] Miller, M. M., & Reifenberger, R. (1988). Magnetic breakdown and the de Haasvan Alphen effect in Hg 1 x Fe x Se. Physical Review B, 38(5), 3423.

[14] Hall, D., Palm, E. C., Murphy, T. P., Tozer, S. W., Petrovic, C., Miller-Ricci, E., ... & Sarrao, J. L. (2001). Electronic structure of CeRhIn 5: de Haasvan Alphen and energy band calculations. Physical Review B, 64(6), 064506.

[15] Shoenberg, D. (2009). Magnetic oscillations in metals. Cambridge University Press.

Angular Resolved Photon Emission Spectroscopy (ARPES)

[16] Hertz, H. (1887). Über einen Einfluss des ultravioletten Lichtes auf die electrische Entladung. Annalen der Physik, 267(8), 983-1000.

[17] Einstein, A. (1905). Über einen die Erzeugung und Verwandlung des Lichtes betreffenden heuristischen Gesichtspunkt. Annalen der Physik, 322(6), 132-148.

[18] Seah, M. P., & Dench, W. A. (1979). Quantitative electron spectroscopy of surfaces: A standard data base for electron inelastic mean free paths in solids. Surface and interface analysis, 1(1), 2-11.

[19] Damascelli, A., Hussain, Z., & Shen, Z. X. (2003). Angle-resolved photoemission studies of the cuprate superconductors. Reviews of modern physics, 75(2), 473.

[20] Damascelli, A. (2004). Probing the electronic structure of complex systems by ARPES. Physica Scripta, 2004(T109), 61.

[21] Hüfner, S. (2013). Photoelectron spectroscopy: principles and applications. Springer Science & Business Media.

[22] Zhang, W. (2012). Photoemission Spectroscopy on High Temperature Superconductor: A Study of Bi2Sr2CaCu2O8 by Laser-Based Angle-Resolved Photoemission. Springer Science & Business Media.

[23] Doniach, S., & Sunjic, M. (1970). Many-electron singularity in X-ray photoemission and X-ray line spectra from metals. Journal of Physics C: Solid State Physics, 3(2), 285.

[24] Gadzuk, J. W., & unji, M. (1975). Excitation energy dependence of core-level x-ray-photoemission-spectra line shapes in metals. Physical Review B, 12(2), 524.

[25] Randeria, M. (1996). High-T c superconductors: New insights from angle-resolved photoemission. Journal of superconductivity, 9(4), 471-474.

[26] Hedin, L., & Lee, J. D. (2002). Sudden approximation in photoemission and beyond. Journal of electron spectroscopy and related phenomena, 124(2-3), 289-315.

[27] Kondo, T., Ochi, M., Nakayama, M., Taniguchi, H., Akebi, S., Kuroda, K., ... & Maeno, Y. (2016). Orbital-Dependent Band Narrowing Revealed in an Extremely Correlated Hunds Metal Emerging on the Topmost Layer of Sr 2 RuO 4. Physical review letters, 117(24), 247001.

[28] Miller, T., McMahon, W. E., & Chiang, T. C. (1996). Interference between bulk and surface photoemission transitions in Ag (111). Physical review letters, 77(6), 1167.

[29] Claesson, D., Lindgren, S. Å., Walldén, L., & Chiang, T. C. (1999). Drastic Photoemission Line Shape Changes in Li due to Surface-Bulk Interference and Plasmon Excitations. Physical review letters, 82(8), 1740.

Compton scattering

[30] Compton, A. H. (1923). A quantum theory of the scattering of X-rays by light elements. Physical review, 21(5), 483.

[31] de Broglie, L. (1926). Ondes et mouvements (Vol. 1). Gauthier-Villars et cie..

[32] DuMond, J. W. (1933). The linear momenta of electrons in atoms and in solid bodies as revealed by X-ray scattering. Reviews of Modern Physics, 5(1), 1.

[33] Cooper, M., Leake, J. A., & Weiss, R. J. (1965). The compton profile of lithium. Philosophical Magazine, 12(118), 797-800.

[34] Eisenberger, P., & Platzman, P. M. (1970). Compton scattering of X rays from bound electrons. Physical Review A, 2(2), 415.

[35] Cooper, M. (1971). Compton scattering and electron momentum distributions. Advances in Physics, 20(86), 453-491.

[36] Ribberfors, R. (1975). Relationship of the relativistic Compton cross section to the momentum distribution of bound electron states. Physical Review B, 12(6), 2067.

[37] Cooper, M. J. (1985). Compton scattering and electron momentum determination. Reports on Progress in Physics, 48(4), 415.

[38] Herold, H. (1979). Compton and Thomson scattering in strong magnetic fields. Physical Review D, 19(10), 2868.

[39] Daugherty, J. K., & Harding, A. K. (1986). Compton scattering in strong magnetic fields. The Astrophysical Journal, 309, 362-371.

[40] Sakai, N. (1996). Magnetic Compton scattering and measurements of momentum distribution of magnetic electrons. Journal of applied crystallography, 29(2), 81-99.

[41] Schülke, W., Stutz, G., Wohlert, F., & Kaprolat, A. (1996). Electron momentum-space densities of Li metal: A high-resolution Compton-scattering study. Physical Review B, 54(20), 14381.

[42] Hatchett, S. P., Brown, C. G., Cowan, T. E., Henry, E. A., Johnson, J. S., Key, M. H., ... & Mackinnon, A. J. (2000). Electron, photon, and ion beams from the relativistic interaction of Petawatt laser pulses with solid targets. Physics of Plasmas, 7(5), 2076-2082.

[43] Cooper, M. (2004). X-ray Compton scattering (No. 5). Oxford University Press on Demand.

[44] Dugdale, S. B., Watts, R. J., Laverock, J., Major, Z., Alam, M. A., Samsel-Czekaa, M., ... & Fort, D. (2006). Observation of a strongly nested Fermi surface in the shape-memory alloy Ni 0.62 Al 0.38. Physical review letters, 96(4), 046406.

[45] Lynn, K. G., MacDonald, J. R., Boie, R. A., Feldman, L. C., Gabbe, J. D., Robbins, M. F., ... & Golovchenko, J. (1977). Positron-annihilation momentum profiles in aluminum: core contribution and the independent-particle model. Physical Review Letters, 38(5), 241.

[46] Kaijser, P., & Smith Jr, V. H. (1977). Evaluation of momentum distributions and Compton profiles for atomic and molecular systems. In Advances in quantum chemistry (Vol. 10, pp. 37-76). Academic Press.

[47] Brandt, W. (1983). Positron Solid-state Physics: International School of Physics Enrico Fermi Course, 1981, Varenna on Lake Como: Proceedings. North-Holland

[48] Regier, P. E., Fisher, J., Sharma, B. S., & Thakkar, A. J. (1985). Gaussian vs. Slater representations of d orbitals: An information theoretic appraisal based on both position and momentum space properties. International journal of quantum chemistry, 28(4), 429-449.

[49] Al-Sawai, W., Barbiellini, B., Sakurai, Y., Itou, M., Mijnarends, P. E., Markiewicz, R. S., ... & Lin, H. (2012). Bulk Fermi surface and momentum density in heavily doped La 2 x Sr x CuO 4 using high-resolution Compton scattering and positron annihilation spectroscopies. Physical Review B, 85(11), 115109.

[50] Thakkar, A. J. (1987). Asymptotic behavior of atomic momentals. The Journal of Chemical Physics, 86(9), 5060-5062.

[51] Alatalo, M., Barbiellini, B., Hakala, M., Kauppinen, H., Korhonen, T., Puska, M. J., ... & Nieminen, R. M. (1996). Theoretical and experimental study of positron annihilation with core electrons in solids. Physical Review B, 54(4), 2397.

[52] Sekania, M., Appelt, W. H., Benea, D., Ebert, H., Vollhardt, D., & Chioncel, L. (2018). Scaling behavior of the Compton profile of alkali metals. Physica A: Statistical Mechanics and its Applications, 489, 18-27.

Angular Correlation of Electron-Positron Annihilation Radiation (ACAR)

[53] DeBenedetti, S., Cowan, C. E., Konneker, W. R., & Primakoff, H. (1950). On the angular distribution of two-photon annihilation radiation. Physical Review, 77(2), 205.

[54] Green, R. E., & Stewart, A. T. (1955). Angular correlation of photons from positron annihilation in light metals. Physical Review, 98(2), 486.

[55] Berko, S., & Plaskett, J. S. (1958). Correlation of annihilation radiation in oriented single metal crystals. Physical Review, 112(6), 1877.

[56] Stewart, A. T. (1961). Fermi Surface and Positron Annihilation in Sodium. Physical Review, 123(5), 1587.

[57] Fujiwara, K., & Sueoka, O. (1966). A precise measurement of the angular correlation of annihilation radiation in copper single crystals. Journal of the Physical Society of Japan, 21(10), 1947-1955.

[58] Mijnarends, P. E. (1967). Determination of anisotropic momentum distributions in positron annihilation. Physical Review, 160(3), 512.

[59] Murray, B. W., & McGervey, J. D. (1970). Positron Annihilation in Copper Alloys. Physical Review Letters, 24(1), 9.

[60] Berko, S., & Mader, J. (1975). Momentum density measurements by positron annihilation in metals and alloys; Recent experiments with a multicounter two-dimensional angular correlation apparatus. Applied physics, 5(4), 287-306.

[61] Hautojärvi, P. (1979). Positrons in solids. Positrons in Solids. Series: Topics in Current Physics, ISBN: 978-3-642-81318-4. Springer Berlin Heidelberg (Berlin, Heidelberg), Edited by Pekka Hautojärvi, vol. 12, 12.

[62] Mijnarends, P. E., Rabou, L. P. L. M., Hanssen, K. E. H. M., & Bansil, A. (1987). Positron-annihilation study of the electronic structure of Cu 91 Ge 9. Physical review letters, 59(6), 720.

[63] Mijnarends, P. E. (1987). Electron and positron states in disordered alloys. physica status solidi (a), 102(1), 31-46.

[64] Chan, L. P., Harshman, D. R., Lynn, K. G., Massidda, S., & Mitzi, D. B. (1991). Evidence for a fermi surface in Bi2Sr2CaCu2O8+ measured by positron 2D-ACAR. Journal of Physics and Chemistry of Solids, 52(11-12), 1557-1567.

[65] Livesay, E. A., West, R. N., Dugdale, S. B., Santi, G., & Jarlborg, T. (1999). Fermi surface of the colossal magnetoresistance perovskite La0. 7Sr0. 3MnO3. Journal of Physics: Condensed Matter, 11(25), L279.

[66] Eijt, S. W., van Veen, A. T., Schut, H., Mijnarends, P. E., Denison, A. B., Barbiellini, B., & Bansil, A. (2006). Study of colloidal quantum-dot surfaces using an innovative thin-film positron 2D-ACAR method. Nature materials, 5(1), 23.

[67] Hamid, A. S., Uedono, A., Major, Z., Haynes, T. D., Laverock, J., Alam, M. A., ... & Fort, D. (2011). Electronic structure and Fermi surface of the weak ferromagnet Ni 3 Al. Physical Review B, 84(23), 235107.

[68] Leitner, M., Ceeh, H., & Weber, J. A. (2012). Eliminating spatial distortions in Anger-type gamma cameras. New Journal of Physics, 14(12), 123014.

[69] Inoue, K., Saito, H., Nagashima, Y., Hyodo, T., Nagai, Y., Muramatsu, S., ... & Masuda, K. (2002). A position-sensitive -ray detector for positron annihilation 2D-ACAR based on metal package photomultiplier tubes. Nuclear Instruments and Methods in Physics Research Section A: Accelerators, Spectrometers, Detectors and Associated Equipment, 487(3), 471-476.

[70] Dugdale, S. B., Laverock, J., Utfeld, C., Alam, M. A., Haynes, T. D., Billington, D., & Ernsting, D. (2013). The Bristol HIDAC 2D-ACAR Spectrometer. In Journal of Physics: Conference Series (Vol. 443, No. 1, p. 012083). IOP Publishing.

[71] Ceeh, H., Weber, J. A., Leitner, M., Böni, P., & Hugenschmidt, C. (2013). The source-sample stage of the new two-dimensional angular correlation of annihilation radiation spectrometer at Technische Universität München. Review of Scientific Instruments, 84(4), 043905.

[72] Weber, J. A., Böni, P., Ceeh, H., Leitner, M., & Hugenschmidt, C. (2013). First 2D-ACAR Measurements on Cu with the new Spectrometer at TUM. In Journal of Physics: Conference Series (Vol. 443, No. 1, p. 012092). IOP Publishing.

[73] Ceeh, H., Weber, J. A., Böni, P., Leitner, M., Benea, D., Chioncel, L., ... & Hugenschmidt, C. (2016). Local electron-electron interaction strength in ferromagnetic nickel determined by spin-polarized positron annihilation. Scientific reports, 6, 20898.

[74] Ceeh, H. (2016). The new 2D-ACAR spectrometer for spin-resolved measurements of the electronic structure in correlated systems (Doctoral dissertation). Retrieved from Online Public Access Catalogue OPAC. (B3Kat-ID: BV043973230)

[75] Miller, S. C., & Love, W. F. (1967). Tables of irreducible representations of space groups and co-representations of magnetic space groups. Pruett Press.

[76] Bross, H., & Stöhr, H. (1974). MAPW calculation of the anisotropic positron annihilation in copper. Applied physics, 3(4), 307-311.

[77] Harthoorn, R., & Mijnarends, P. E. (1978). The effect of symmetry on electron momentum distributions in solids. Journal of Physics F: Metal Physics, 8(6), 1147.

[78] Hanssen, K. E. H. M., & Mijnarends, P. E. (1986). Positron-annihilation study of the half-metallic ferromagnet NiMnSb: Theory. Physical Review B, 34(8), 5009.

[79] Saito, M., Oshiyama, A., & Tanigawa, S. (1991). Anisotropic momentum distribution of positron-annihilation radiation in semiconductors. Physical Review B, 44(19), 10601.

[80] Lock, D. G., Crisp, V. H. C., & West, R. N. (1973). Positron annihilation and Fermi surface studies: a new approach. Journal of Physics F: Metal Physics, 3(3), 561.

[81] Rabou, L. P. L. M., & Mijnarends, P. E. (1984). Approximate validity of the Lock-Crisp-West theorem in positron annihilation. Solid state communications, 52(11), 933-936.

[82] Hoffmann, L., Shukla, A., Peter, M., Barbiellini, B., & Manuel, A. A. (1993). Linear and non-linear approaches to solve the inverse problem: applications to positron annihilation experiments. Nuclear Instruments and Methods in Physics Research Section A: Accelerators, Spectrometers, Detectors and Associated Equipment, 335(1-2), 276-287.

[83] Dugdale, S. B., Alam, M. A., Fretwell, H. M., Biasini, M., & Wilson, D. (1994). Application of maximum entropy to extract Fermi surface topology from positron annihilation measurement. Journal of Physics: Condensed Matter, 6(31), L435.

[84] O'Brien, K. M., Brand, M. Z., Rayner, S., & West, R. N. (1995). The enhancement of Fermi-surface images in positron ACAR spectra. Journal of Physics: Condensed Matter, 7(5), 925.

[85] Kontrym-Sznajd, G. (2009). Fermiology via the electron momentum distribution. Low Temperature Physics, 35(8), 599-609.

[86] Dugdale, S. B. (2014). Probing the Fermi surface by positron annihilation and Compton scattering. Low Temperature Physics, 40(4), 328-338.

[87] Kaiser, J. H., & Biasini, M. (1991-1992). University of Texas at Arlington. Unpublished.

[88] Unknown Authors (probably including Ceeh, H., Weber, J. A.). (2013). Technichal University of Munich. Unpublished.

[89] Cormack, A. M. (1963). Representation of a function by its line integrals, with some radiological applications. Journal of applied physics, 34(9), 2722-2727.

[90] Cormack, A. M. (1964). Representation of a function by its line integrals, with some radiological applications. II. Journal of Applied Physics, 35(10), 2908-2913.

[91] KontrymSznajd, G. (1990). ThreeDimensional Image Reconstruction with Application in Positron Annihilation. physica status solidi (a), 117(1), 227-240.

[92] Dugdale, S. B.. (1996). PhD thesis (unpublished). University of Bristol.

[93] Dugdale, S. B., Fretwell, H. M., Alam, M. A., Kontrym-Sznajd, G., West, R. N., & Badrzadeh, S. (1997). Direct observation and calipering of the webbing Fermi surface of yttrium. Physical review letters, 79(5), 941.

[94] Kontrym-Sznajd, G., & Samsel-Czekaa, M. (2000). New reconstruction method of electron momentum densities from Compton profiles. Applied Physics A, 70(1), 89-92.

Positrons

[95] Dirac, P. A. (1928). The quantum theory of the electron. Proc. R. Soc. Lond. A, 117(778), 610-624.

[96] Oppenheimer, J. R. (1930). On the theory of electrons and protons. Physical Review, 35(5), 562.

[97] Dirac, P. A. (1931). Quantised singularities in the electromagnetic field. Proceedings of the Royal Society of London. Series A, 133(821), 60-72.

[98] Anderson, C. D. (1933). The positive electron. Physical Review, 43(6), 491.

[99] Hugenschmidt, C., Kögel, G., Repper, R., Schreckenbach, K., Sperr, P., StraSSer, B., & Triftshäuser, W. (2004). The neutron induced positron source at Munich-NEPOMUC. Nuclear Instruments and Methods in Physics Research Section B: Beam Interactions with Materials and Atoms, 221, 160-164.

[100] Hugenschmidt, C., Schreckenbach, K., Stadlbauer, M., & StraSSer, B. (2005). Low-energy positrons of high intensity at the new positron beam facility NEPOMUC. Nuclear Instruments and Methods in Physics Research Section A: Accelerators, Spectrometers, Detectors and Associated Equipment, 554(1-3), 384-391.

[101] Hugenschmidt, C., Löwe, B., Mayer, J., Piochacz, C., Pikart, P., Repper, R., ... & Schreckenbach, K. (2008). Unprecedented intensity of a low-energy positron beam. Nuclear Instruments and Methods in Physics Research Section A: Accelerators, Spectrometers, Detectors and Associated Equipment, 593(3), 616-618.

[102] Djourelov, N., Oprisa, A., & Leca, V. (2016). Source of slow polarized positrons using the brilliant gamma beam at ELI-NP. Converter design and simulations. Nuclear Instruments and Methods in Physics Research Section A: Accelerators, Spectrometers, Detectors and Associated Equipment, 806, 146-153.

[103] Carbotte, J. P. (1967). Lifetime of Positrons in an Electron Gas. Physical Review, 155(2), 197.

[104] Weisberg, H., & Berko, S. (1967). Positron lifetimes in metals. Physical Review, 154(2), 249.

[105] Perkins, A., & Carbotte, J. P. (1970). Effect of the positron-phonon interaction on positron motion. Physical Review B, 1(1), 101.

[106] Berko, S., & Pendleton, H. N. (1980). Positronium. Annual Review of Nuclear and Particle Science, 30(1), 543-581.

[107] Jean, Y. C., Mallon, P. E., & Schrader, D. M. (2003). Principles and applications of positron & positronium chemistry. World Scientific.

[108] Nieminen, R. M., & Oliva, J. (1980). Theory of positronium formation and positron emission at metal surfaces. Physical Review B, 22(5), 2226.

[109] Schaefer, H. E., Würschum, R., Birringer, R., & Gleiter, H. (1988). Structure of nanometer-sized polycrystalline iron investigated by positron lifetime spectroscopy. Physical Review B, 38(14), 9545.

[110] Jensen, K. O., & Walker, A. B. (1990). Positron thermalization and non-thermal trapping in metals. Journal of Physics: Condensed Matter, 2(49), 9757.

[111] Vehanen, A., Saarinen, K., Hautojärvi, P., & Huomo, H. (1987). Profiling multilayer structures with monoenergetic positrons. Physical Review B, 35(10), 4606.

[112] Ghosh, V. J. (1995). Positron implantation profiles in elemental and multilayer systems. Applied surface science, 85, 187-195.

[113] Wright, B. T. (1953). Spectrometer measurement on the high energy positrons of sodium 22. Physical Review, 90(1), 159.

[114] Dagley, P., Grace, M. A., Hill, J. S., & Sowter, O. V. (1958). Nuclear alignment and the beta transition in cobalt-58. Philosophical Magazine, 3(29), 489-496.

[115] Hamilton, J. H., Langer, L. M., & Smith, W. G. (1958). Small Deviations Observed in Beta Spectra: Na 22. Physical Review, 112(6), 2010.

[116] Mantel, J. (1972). The beta ray spectrum and the average beta energy of several isotopes of interest in medicine and biology. The International journal of applied radiation and isotopes, 23(9), 407-413.

[117] Rabson, T. A., Bonner, T. W., Castillo-Bahena, R., Harlow Jr, M. V., Haenni, H. P., & Ranken, W. A. (1960). Gamma radiation from excited states of F18, Na22 and Ne22. Nuclear Physics, 19, 314-326.

[118] Eswaran, M. A., & Broude, C. (1964). Lifetime Measurements of States in O18 and Ne22. Canadian Journal of Physics, 42(6), 1311-1323.

[119] Jacobson, A. S. (1987). Nucleosynthesis and astrophysical gamma ray spectroscopy.

[120] West, R. N. (1973). Positron studies of condensed matter. Advances in Physics, 22(3), 263-383.

[121] Asoka-Kumar, P., Alatalo, M., Ghosh, V. J., Kruseman, A. C., Nielsen, B., & Lynn, K. G. (1996). Increased elemental specificity of positron annihilation spectra. Physical Review Letters, 77(10), 2097.

[122] Szpala, S., Asoka-Kumar, P., Nielsen, B., Peng, J. P., Hayakawa, S., Lynn, K. G., & Gossmann, H. J. (1996). Defect identification using the core-electron contribution in Doppler-broadening spectroscopy of positron-annihilation radiation. Physical Review B, 54(7), 4722.

[123] Petkov, M. P., Weber, M. H., Lynn, K. G., Rodbell, K. P., & Cohen, S. A. (1999). Doppler broadening positron annihilation spectroscopy: A technique for measuring open-volume defects in silsesquioxane spin-on glass films. Applied physics letters, 74(15), 2146-2148.

[124] Ferrell, R. A. (1956). Theory of positron annihilation in solids. Reviews of Modern Physics, 28(3), 308.

[125] Kahana, S. (1960). Positron annihilation in metals. Physical Review, 117(1), 123.

[126] Kahana, S. (1963). Positron annihilation in metals. Physical Review, 129(4), 1622.

[127] Carbotte, J. P., & Kahana, S. (1965). Positron annihilation in an interacting electron gas. Physical Review, 139(1A), A213.

[128] Boroski, E., Szotek, Z., & Stachowiak, H. (1981). Exact solution of the Kahana equation for a positron in an electron gas. Physical Review B, 23(4), 1785.

[129] Daniuk, S., Kontrym-Sznajd, G., Rubaszek, A., Stachowiak, H., Mayers, J., Walters, P. A., & West, R. N. (1987). Selective enhancement of different electron populations by electron-positron attraction: application to zinc. Journal of Physics F: Metal Physics, 17(6), 1365.

[130] Rubaszek, A., & Stachowiak, H. (1988). Self-consistent solution of the Kahana equation for a positron in an electron gas. Physical Review B, 38(6), 3846.

[131] Puska, M. J., & Nieminen, R. M. (1983). Defect spectroscopy with positrons: a general calculational method. Journal of Physics F: Metal Physics, 13(2), 333.

[132] Laverock, J., Haynes, T. D., Alam, M. A., & Dugdale, S. B. (2010). Experimental determination of the state-dependent enhancement of the electron-positron momentum density in solids. Physical Review B, 82(12), 125127.

[133] Drummond, N. D., Ríos, P. L., Needs, R. J., & Pickard, C. J. (2011). Quantum monte carlo study of a positron in an electron gas. Physical review letters, 107(20), 207402.

[134] Makkonen, I., Ervasti, M. M., Siro, T., & Harju, A. (2014). Enhancement models of momentum densities of annihilating electron-positron pairs: The many-body picture of natural geminals. Physical Review B, 89(4), 041105.

Solid State Physics

[135] Bloch, F. (1929). Über die quantenmechanik der elektronen in kristallgittern. Zeitschrift für physik, 52(7-8), 555-600.

[136] Ashcroft, N. & Mermin, N. (1976). Solid state physics. New York: Holt, Rinehart and Winston.

[137] Hoddeson, L., Baym, G., & Eckert, M. (1987). The development of the quantum-mechanical electron theory of metals: 19281933. Reviews of modern physics, 59(1), 287.

Many Particle Theory

[138] Slater, J. C. (1937). Wave functions in a periodic potential. Physical Review, 51(10), 846.

[139] Löwdin, P. O. (1955). Quantum theory of many-particle systems. I. Physical interpretations by means of density matrices, natural spin-orbitals, and convergence problems in the method of configurational interaction. Physical Review, 97(6), 1474.

[140] Löwdin, P. O. (1960). Expansion theorems for the total wave function and extended Hartree-Fock schemes. Reviews of Modern Physics, 32(2), 328.

[141] Strange, P. (1998). Relativistic Quantum Mechanics: with applications in condensed matter and atomic physics. Cambridge University Press.

Density Functional Theory (DFT)

[142] Hohenberg, P., & Kohn, W. (1964). Inhomogeneous electron gas. Physical review, 136(3B), B864.

[143] Kohn, W., & Sham, L. J. (1965). Self-consistent equations including exchange and correlation effects. Physical review, 140(4A), A1133.

[144] Gunnarsson, O., & Lundqvist, B. I. (1976). Exchange and correlation in atoms, molecules, and solids by the spin-density-functional formalism. Physical Review B, 13(10), 4274.

[145] Jones, R. O., & Gunnarsson, O. (1989). The density functional formalism, its applications and prospects. Reviews of Modern Physics, 61(3), 689.

[146] Kohn, W. (1999). Nobel Lecture: Electronic structure of matterwave functions and density functionals. Reviews of Modern Physics, 71(5), 1253.

[147] Martin, R. M. (2004). Electronic structure: basic theory and practical methods. Cambridge university press.

[148] Blügel, S. (Ed.). (2014). Computing Solids: Models, Ab-initio Methods and Supercomputing; Lecture Notes of the 45th IFF Spring School 2014; the Spring School was Organized by the Institute for Advanced Simulation and the Peter Grünberg Institute of the Forschungszentrum Jülich on March 10-21, 2014; in Collab. with Universities, Research Institutes and Industry. Forschungszentrum Jülich.

[149] Jones, R. O. (2015). Density functional theory: Its origins, rise to prominence, and future. Reviews of modern physics, 87(3), 897.

[150] Marques, M. A., Oliveira, M. J., & Burnus, T. (2012). Libxc: A library of exchange and correlation functionals for density functional theory. Computer Physics Communications, 183(10), 2272-2281.

[151] Wigner, E. (1938). Effects of the electron interaction on the energy levels of electrons in metals. Transactions of the Faraday Society, 34, 678-685.

[152] von Barth, U., & Hedin, L. (1972). A local exchange-correlation potential for the spin polarized case. i. Journal of Physics C: Solid State Physics, 5(13), 1629.

[153] Vosko, S. H., Wilk, L., & Nusair, M. (1980). Accurate spin-dependent electron liquid correlation energies for local spin density calculations: a critical analysis. Canadian Journal of physics, 58(8), 1200-1211.

[154] Ceperley, D. M., & Alder, B. J. (1980). Ground state of the electron gas by a stochastic method. Physical Review Letters, 45(7), 566.

[155] Perdew, J. P., & Zunger, A. (1981). Self-interaction correction to density-functional approximations for many-electron systems. Physical Review B, 23(10), 5048.

[156] Perdew, J. P., & Wang, Y. (1992). Accurate and simple analytic representation of the electron-gas correlation energy. Physical Review B, 45(23), 13244.

[157] Perdew, J. P., Ernzerhof, M., & Burke, K. (1996). Rationale for mixing exact exchange with density functional approximations. The Journal of chemical physics, 105(22), 9982-9985.

[158] Zhang, Y., & Yang, W. (1998). Comment on Generalized gradient approximation made simple. Physical Review Letters, 80(4), 890.

[159] Perdew, J. P., Ruzsinszky, A., Csonka, G. I., Vydrov, O. A., Scuseria, G. E., Constantin, L. A., ... & Burke, K. (2008). Restoring the density-gradient expansion for exchange in solids and surfaces. Physical Review Letters, 100(13), 136406.

[160] Andersen, O. K. (1975). Linear methods in band theory. Physical Review B, 12(8), 3060.

[161] Koelling, D. D., & Arbman, G. O. (1975). Use of energy derivative of the radial solution in an augmented plane wave method: application to copper. Journal of Physics F: Metal Physics, 5(11), 2041.

[162] Jepsen, O., Madsen, J., & Andersen, O. K. (1978). Band structure of thin films by the linear augmented-plane-wave method. Physical Review B, 18(2), 605.

[163] Hamann, D. R. (1979). Semiconductor charge densities with hard-core and soft-core pseudopotentials. Physical Review Letters, 42(10), 662.

[164] Wimmer, E., Krakauer, H., Weinert, M., & Freeman, A. J. (1981). Full-potential self-consistent linearized-augmented-plane-wave method for calculating the electronic structure of molecules and surfaces: O 2 molecule. Physical Review B, 24(2), 864.

[165] Wimmer, E., Krakauer, H., & Freeman, A. J. (1985). Theory of surface electronic structure. In Advances in electronics and electron physics (Vol. 65, pp. 357-434). Academic Press.

[166] Singh, D. J. (1994). Introduction to the LAPW Method. In Planewaves, Pseudopotentials and the LAPW method (pp. 35-43). Springer, Boston, MA.

[167] Singh, D. J., & Nordström, L. (2006). Planewaves Pseudopotentials and the LAPW Method, pringer. New York.

[168] Arponen, J., & Pajanne, E. (1979). Electron liquid in collective description. III. Positron annihilation. Annals of Physics, 121(1-2), 343-389.

[169] Gunnarsson, O., Jonson, M., & Lundqvist, B. I. (1979). Descriptions of exchange and correlation effects in inhomogeneous electron systems. Physical Review B, 20(8), 3136.

[170] Nieminen, R. M., Boronski, E., & Lantto, L. J. (1985). Two-component density-functional theory: Application to positron states. Physical Review B, 32(2), 1377.

[171] Boroski, E., & Nieminen, R. M. (1986). Electron-positron density-functional theory. Physical Review B, 34(6), 3820.

[172] Jenson, K. O., & Walker, A. B. (1988). Non-local positron-electron density functional theory and the positron surface state. Journal of Physics F: Metal Physics, 18(12), L277.

[173] Puska, M. J., & Nieminen, R. M. (1994). Theory of positrons in solids and on solid surfaces. Reviews of modern Physics, 66(3), 841.

Beyond Density Functional Theory

[174] Korringa, J. (1947). On the calculation of the energy of a Bloch wave in a metal. Physica, 13(6-7), 392-400.

[175] Kohn, W., & Rostoker, N. (1954). Solution of the Schrödinger equation in periodic lattices with an application to metallic lithium. Physical Review, 94(5), 1111.

[176] Dederichs, P. H., Drittler, B., & Zeller, R. (1992). Application of Multiple Scattering Theory to Materials Science (MRS Symposia Proceedings No 253) ed WH Butler. PH Dederichs, A Gonis and RL Weaver (Pittsburgh, PA: Materials Research Society) p, 185.

[177] Nicholson, D. M., & Faulkner, J. S. (1989). Applications of the quadratic Korringa-Kohn-Rostoker band-theory method. Physical Review B, 39(12), 8187.

[178] Drittler, B., Weinert, M., Zeller, R., & Dederichs, P. H. (1991). Vacancy formation energies of fcc transition metals calculated by a full potential green's function method. Solid state communications, 79(1), 31-35.

[179] Butler, W. H., Gonis, A., & Zhang, X. G. (1992). Multiple-scattering theory for space-filling cell potentials. Physical Review B, 45(20), 11527.

[180] Der Kellen, S. B., Oh, Y., Badralexe, E., & Freeman, A. J. (1995). Self-consistent full-potential total-energy Korringa-Kohn-Rostoker band-structure method: Application to silicon. Physical Review B, 51(15), 9560.

[181] Papanikolaou, N., Zeller, R., Dederichs, P. H., & Stefanou, N. (1997). Lattice distortion in Cu-based dilute alloys: A first-principles study by the KKR Green-function method. Physical Review B, 55(7), 4157.

[182] Asato, M., Settels, A., Hoshino, T., Asada, T., Blügel, S., Zeller, R., & Dederichs, P. H. (1999). Full-potential KKR calculations for metals and semiconductors. Physical Review B, 60(8), 5202.

[183] Zabloudil, J., Hammerling, R., Szunyogh, L., & Weinberger, R. (2005). Electron Scattering in Solid Matter. A Theoretical and Computational Treatise, vol. 147 of Springer Series in Solid-state Sciences.

[184] Metzner, W., & Vollhardt, D. (1989). Correlated lattice fermions in d= dimensions. Physical review letters, 62(3), 324.

[185] Liechtenstein, A. I., Anisimov, V. I., & Zaanen, J. (1995). Density-functional theory and strong interactions: Orbital ordering in Mott-Hubbard insulators. Physical Review B, 52(8), R5467.

[186] Georges, A., Kotliar, G., Krauth, W., & Rozenberg, M. J. (1996). Dynamical mean-field theory of strongly correlated fermion systems and the limit of infinite dimensions. Reviews of Modern Physics, 68(1), 13.

[187] Held, K., Keller, G., Eyert, V., Vollhardt, D., & Anisimov, V. I. (2001). Mott-Hubbard Metal-Insulator Transition in Paramagnetic V 2 O 3: An L D A+ D M F T (QMC) Study. Physical review letters, 86(23), 5345.

[188] Biermann, S., Aryasetiawan, F., & Georges, A. (2003). First-Principles Approach to the Electronic Structure of Strongly Correlated Systems: Combining the G W Approximation and Dynamical Mean-Field Theory. Physical review letters, 90(8), 086402.

Condensed Matter Simulations

[189] Dewhurst, K., Sharma, S., Nordstrom, L., Cricchio, F., Bultmark, F., Gross, H., ... & Chizmeshya, A. (2016). The elk FP-LAPW code. ELK, http://elk. sourceforge. net.

[190] Ernsting, D., Billington, D., Haynes, T. D., Millichamp, T. E., Taylor, J. W., Duffy, J. A., ... & Dugdale, S. B. (2014). Calculating electron momentum densities and Compton profiles using the linear tetrahedron method. Journal of Physics: Condensed Matter, 26(49), 495501.

[191] Dugdale, S. B., & Laverock, J. (2014). Recovering the Fermi surface with 2D-ACAR spectroscopy in samples with defects. In Journal of Physics: Conference Series (Vol. 505, No. 1, p. 012046). IOP Publishing.

[192] Bruno, E., Florio, G. M., Ginatempo, B., & Giuliano, E. S. (1994). Fast numerical solution of KKR-CPA equations: testing new algorithms. Journal of Computational Physics, 111(2), 248-255.

[193] Bruno, E., & Ginatempo, B. (1997). Algorithms for Korringa-Kohn-Rostoker electronic structure calculations in any Bravais lattice. Physical Review B, 55(19), 12946.

Molybdenum

[194] Lomer, W. M. (1962). Electronic structure of chromium group metals. Proceedings of the Physical Society, 80(2), 489.

[195] Mattheiss, L. F. (1965). Fermi surface in tungsten. Physical review, 139(6A), A1893.

[196] Leaver, G., & Myers, A. (1969). De Haas-van Alphen measurements in molybdenum. Philosophical Magazine, 19(159), 465-475.

[197] Hoekstra, J. A., & Stanford, J. L. (1973). Determination of the Fermi Surface of Molybdenum Using the de Haasvan Alphen Effect. Physical Review B, 8(4), 1416.

[198] Iverson, R. J., & Hodges, L. (1973). Molybdenum: Band structure, fermi surface, and spin-orbit interaction. Physical Review B, 8(4), 1429.

[199] Ketterson, J. B., Koelling, D. D., Shaw, J. C., & Windmiller, L. R. (1975). Parametrization of transition-metal Fermi-surface data. Physical Review B, 11(4), 1447.

[200] Griessen, R., Lee, M. J. G., & Stanley, D. J. (1977). Homogeneous strain response of the Fermi surface of molybdenum. Physical Review B, 16(10), 4385.

[201] Shiotani, N., Okada, T., Sekizawa, H., Wakoh, S., & Kubo, Y. (1977). Angular correlation of positron annihilation radiation in chromium and molybdenum. Journal of the Physical Society of Japan, 43(4), 1229-1236.

[202] Kaiser, J. H., Walters, P. A., Bull, C. R., Alam, A., West, R. N., & Shiotani, N. (1987). A positron study of the Fermi surfaces of the Nb-Mo system. Journal of Physics F: Metal Physics, 17(5), 1243.

[203] Dugdale, S. B., Fretwell, H. M., Hedley, D. C. R., Alam, M. A., Jarlborg, T., Santi, G., ... & Cooper, M. J. (1998). Fermiology of Cr and Mo. Journal of Physics: Condensed Matter, 10(46), 10367.

[204] Biasini, M. (2000). Study of the Fermi surface of molybdenum and chromium via positron annihilation experiments. Physica B: Condensed Matter, 275(4), 285-294.

Silver

[205] Halse, M. R. (1969). The Fermi surfaces of the noble metals. Phil. Trans. R. Soc. Lond. A, 265(1167), 507-532.

[206] Coleridge, P. T., & Templeton, I. M. (1972). High precision de Haas-van Alphen measurements in the noble metals. Journal of Physics F: Metal Physics, 2(4), 643.

[207] Shaw, J. C., Ketterson, J. B., & Windmiller, L. R. (1972). Inversion of Fermi-Surface Data Using Partial-Wave Phase Shifts and Their Derivatives: An Application to the Noble Metals. Physical Review B, 5(10), 3894.

[208] Coleridge, P. T., & Templeton, I. M. (1982). Fermi-surface radii in copper, silver, and gold. Physical Review B, 25(12), 7818.

[209] Herman, F., & Skillman, S. (1963). Atomic structure calculations. Prentice-Hall.

[210] Moruzzi, V. L., Janak, J. F., & Williams, A. R. (1978). Calculated electronic properties of metals. Elsevier.

Image Processing

[211] Kitchen, L., & Rosenfeld, A. (1982). Gray-level corner detection. Pattern recognition letters, 1(2), 95-102.

[212] Canny, J. (1987). A computational approach to edge detection. In Readings in Computer Vision (pp. 184-203).

[213] Wang, H., & Brady, M. (1994, November). A practical solution to corner detection. In Image Processing, 1994. Proceedings. ICIP-94., IEEE International Conference (Vol. 1, pp. 919-923). IEEE.

[214] Sharifi, M., Fathy, M., & Mahmoudi, M. T. (2002, April). A classified and comparative study of edge detection algorithms. In Information Technology: Coding and Computing, 2002. Proceedings. International Conference on (pp. 117-120). IEEE.

[215] Skilling, J., & Gull, S. F. (1985). Algorithms and applications. In Maximum-entropy and Bayesian methods in inverse problems (pp. 83-132). Springer, Dordrecht.

[216] Ghosal, S., & Mehrotra, R. (1993). Orthogonal moment operators for subpixel edge detection. Pattern recognition, 26(2), 295-306.

[217] Jensen, K., & Anastassiou, D. (1995). Subpixel edge localization and the interpolation of still images. IEEE transactions on Image Processing, 4(3), 285-295.

[218] Trujillo-Pino, A., Krissian, K., Alemán-Flores, M., & Santana-Cedrés, D. (2013). Accurate subpixel edge location based on partial area effect. Image and Vision Computing, 31(1), 72-90.

Further

[219] Cramér, H. (1936). Über eine Eigenschaft der normalen Verteilungsfunktion. Mathematische Zeitschrift, 41(1), 405-414.

[220] Normand, N., Servieres, M., & Guédon, J. (2005, April). How to obtain a lattice basis from a discrete projected space. In International Conference on Discrete Geometry for Computer Imagery (pp. 153-160). Springer, Berlin, Heidelberg.

[221] Cameron, A. C., & Trivedi, P. K. (2013). Regression analysis of count data (Vol. 53). Cambridge university press.

Acknowledgments

In the four years of writing this works, I had the pleasure to get to know a lot of people in this field of reseach. Thanks to all of you for the inspiring discussions. I specially want to point out a few of you, who had a key role of contributing to this work in one way or the other.
I want to thank Wilhelm Appelt: Thank you for your time, advice, patience and pointing out the right things to me, when I needed them. I did not appreciate it enough back then - now I do!
I what to thank the group of Christoph Hugenschmidt at TUM. In particular Josef Schmidbauer, who took his time to show the experimental setup to me.
I would like to express my deepest appreciation to Stephen Dugdale: Thank you for your hospitality and all kind of advice and recommendations about living in Bristol. During my visits I was able to develop a profound understanding of ACAR spectroscopy and momentum densities thanks to you. I admire your attitude to merge experiment and theoretical background by coming from both sides. The regular discussions, sharing your expertise with me and the codes and data sets you supplied me with had a huge impact on this work. I really hope to be able to return this favor one day!
I am grateful to Mikheil Sekania and Andreas Östlin, for taking you time whenever I needed to discuss aspects of condensed matter physics or the computational implementation. I also want to thank Andreas Weh and the other researchers and guests of TP3.
This work would not have been possible without my supervisor Liviu Chioncel: Thank you for a never ending supply with all kind of resources. It is a mystery to me how you did it, but whenever I needed another prolongation of my working contract, computational resources, workshops, conferences, research trips, connections to other researchers, your time or your opinion - you had it for me. Most importantly I thank you for trusting in me and my work, especially in times when I reported my progress only occasionally. This freedom helped me a lot to develop and find my way into science.
As a source of motivation and personal well being I want to mention: Andrej, Anna, Anna-Lena, Chris, Katta, Lisa, Max, Max, Manu, Padder, Richard, Steffi, Sebastian, Sebastian, Sebastian, Tobi and the other members of EP1. Thanks for refreshing lunch breaks, Schafkopf games, stupid jokes and insights into biophysics!
Also my Calisthenics partners Marc and Daniel. I enjoyed the sport sessions, the weather (mostly) and the progress we did together. You are awesome!
I further appreciate the support I got from my family and my girlfriend. Particularly from my mother, who proof-read this work! Most importantly I want to thank Flici for your positive attitude, for tolerating long working hours and for being a constant source of motivation to me.

This work was funded by the TRR80 research project.